The Tribological Effects of Lubricating Oil Containing Nanometer-Scale Diamond Particles

Matthew David Marko

Submitted in partial fulfillment of the

requirements for the degree

of Doctor of Philosophy

in the Graduate School of Arts and Sciences

COLUMBIA UNIVERSITY

2015

ABSTRACT

The Tribological Effects of Lubricating Oil Containing Nanometer-Scale Diamond Particles

Matthew David Marko

This dissertation investigates the tribological effects of diamond nanoparticles as a lubricant mineral oil additive. A numerical code was developed that models the sliding contact observed in a standard four-ball test of sliding contact. Four-ball experimental tests were conducted both of neat mineral oil and mineral oil with the diamond nanoparticle additives, varying the trial times, temperatures, nanoparticle concentrations, and loads. The numerical results matched the experimental data remarkably by adjusting the lubricant thermal conductivity to account for the enhanced conductivity of diamond; demonstrating that thermal enhancements are the primary cause of the wear reduction properties of diamond nanoparticle additives.

Table of Contents

List of Figures

List of Tables

ACKNOWLEDGEMENTS

I would like to thank my advisor, Professor Elon J. Terrell, for his unwavering support throughout the development of my doctoral thesis, and growth as an engineer and tribologist. Throughout my time in his lab, he was consistently responsive, helpful, and above-all professional, while acting as both a mentor and a friend. In addition, my fellow PhD lab mates, Emil Sandoz-Rosado, Jon Kyle, Aleks Navratil, and Yuanyuan Wang have all made my time in the lab a fun and meaningful experience. Although I was the last PhD student to enter the lab, I have always felt like I was a member since the beginning. I would also like to thank the Department Chair, Professor Jeffrey Kysar, who hosted me within his lab for the final 6 months of my PhD, where I always felt consistently welcomed by everyone. I would like to acknowledge the rest of my committee, Professors Arvind Narayanaswamy, Sinisa Vukelic, and Gautam Dasgupta, for their support and guidance. I would like to thank Dr. Blake Branson of sp3 nanotech LLC, for his collaborative efforts and for providing the diamond nanoparticle additive used so extensively in this thesis. I would like to express my appreciation to the rest of the Mechanical Engineering department, as well as those professors in Physics, Applied Physics, and Electrical Engineering for the coursework that I enjoyed and was enriched by at the early years of my PhD. There are too many others to list who work here at Columbia, from administrators, to professors, to the landscaping crew who have all contributed to my experiences as a graduate student. I have made numerous friendships with people from all over the world and everyone has enriched my experience and supported my progress. Aubrey Catalla, my parents Neil and Joy Marko, my brother Jacob, my sister Mollie, and my brother-in-law Steven Cytryn, you have all been consistently

supportive and nurturing as I progressed through this degree.

Last but not least I must give my extreme appreciation to the U.S. Navy, which since 2006 has been without a doubt the most supportive and nurturing influence of my career. Since I started over 8 years ago, I had the opportunity to work on (literally and with no ego) the most advance mechanical systems on the planet; to utilize some of the best testing and engineering equipment available; to travel all over the country; to learn and develop in new fields of sea-keeping, optical systems, radars / communication systems, electronic warfare, and naval aviation; as well as to get fully funded for both my MS degree in physics from Johns Hopkins, along with this PhD from Columbia. The Navy Postgraduate School through the Science Mathematics And Research for Transformation fellowship spared no expense as they supported my PhD, and everyone else at Lakehurst and Patuxent River has consistently supported my doctoral degree, be it financially, via equipment, or in accommodations to make this difficult challenge as smooth as possible. It would be extreme hubris on my part to think my service to the Navy in the upcoming years can really make up for the tremendous support I have received leading up to this moment, and for this I am forever grateful.

An inventor is a man who asks 'Why?' of the universe and lets nothing stand between the answer and his mind.

John Galt (Atlas Shrugged, by Ayn Rand, 1957)

Dedication

In Memory of my grandparents, Esther Marder, Max Marder, Necia Marko, and Albert Joseph Marko

Chapter 1

INTRODUCTION

INTRODUCTION

1.1 Problem Statement

Friction and wear is a problem that affects practically every field of engineering. Wear has the effect of reducing the life of materials, and causing eventual failures of the mechanical systems. A common example is the internal combustion engine, where the wear in engine cylinders reduces the effectiveness of piston ring seals, thus reducing the combustion pressure and engine power. In practically any mechanical system, any friction ends up as lost energy, reducing the overall efficiency. Finally, friction can cause runaway heating that can damage or destroy mechanical components.

Little is known about the true nature of sliding contact wear, and there are many different approaches to modeling the phenomena. Multiple effects are all at play that can affect wear rate, including elastohydrodynamic effects, pressure-viscosity effects, temperature-viscosity effects, changes to the thermal conductivity of the lubricant and surfaces, and elastic deformation as a result of the lubricant pressure fluctuations. In addition, a diamond nanoparticle additive was found to reduce the wear, which is quite counterintuitive, as diamond is a hard abrasive. Previous research into the matter shows a lot of speculation to the cause, including generating rolling contact and chemistry, but no conclusive determination as to how and why

this diamond nanoparticle additive can actually reduce the wear rate.

1.2 Archard's Wear Equation

The tribological phenomena of wear and friction is an essential design consideration for practically every mechanical device. Most of this friction is transient, occurring over an extended period of time throughout the life of the mechanical device. Friction is a dynamic and nonlinear process as the shape at the point of contact changes from the material wear; therefore it is necessary to understand the transient wear rates and the phenomena of running-in, the tribological process of friction dynamically reaching steady-state as the wear evolves in time.

Running-in is a tribological phenomenon characteristic of the physical, chemical, and geometric characteristics of the contact surface [2–14]. With this in mind, it can be clearly stated that wear rate $\dot{V}$ (m^3/s) is a function of the existing wear V (m^3). While there are several phenomena that can cause wear, one of the most profound causes are asperities in the surface. One established equation to represent wear resulting from adhesion and abrasion is the Archard's equation [3, 15]:

$$V = K_{wear} \cdot \frac{W \cdot S}{H}, \tag{1.1}$$

where W (Newtons) is the contact load, S (m) is the sliding distance, H (Pa) is the material hardness, and K_{wear} (dimensionless) is the wear coefficient. For a steady wear rate, K_{wear} is a constant, but for most applications the wear is dynamic and changing. Therefore, by taking the rate of change of Eqn. 1.1, the rate of change

for the wear is [3]

$$\dot{V} \quad = \quad f(V, \sigma, h) \cdot \frac{W \cdot U}{H}, \tag{1.2}$$

where U (m/s) is the sliding speed, and $f(V, \sigma, h)$ is a dimensionless function representing the wear rate $\dot{V}$ (m^3/s) and how it is affected by prior wear V (m^3), surface roughness σ (m), and the lubricating oil thickness h (m) from physiochemical factors [3]. One derivation of Eqn. 1.2 [15]

$$\dot{V} \quad \propto \quad K_{wear} \cdot \frac{W \cdot U}{H} \cdot \left(\frac{\sigma}{h}\right)^{n_{Archard}}, \tag{1.3}$$

where $n_{Archard}$ is an experimentally realized exponent. This is intuitive, as wear is caused by direct metal-on-metal contact that occurs when random surface asperities exceed the height of the oil film thickness.

The downside of these previous equations, however, is that they are only representative of the wear trend. This current form of Archard's equation in Eqn. 1.1 - 1.3 requires either Monte Carlo simulations [16] or a substantial amount of prior wear data [17] to fit into these equations; they are otherwise too simplistic for practical realistic wear modeling. For example, there is no clear consensus on the relationship between wear rate and both the load and the hardness; while increasing load and / or decreasing the material hardness will inherently increase the wear, the relationship is not necessarily linear [2, 18, 19]. The only tribological parameters that will have a linear relationship on the wear is the area rate of change and the average height of the surface asperities

$$\dot{V} \quad = \quad V_n \cdot \sigma \cdot U \cdot \Delta x, \tag{1.4}$$

where Δx (m) is the width of the region of contact perpendicular to the velocity U (m/s), and V_n is a dimensionless wear rate, proportional to several dimensionless ratios

$$V_n \quad \propto \quad f(\frac{\sigma}{h}, \frac{P}{H}, U_n, G_n, W_n, \kappa_{ellipse}), \tag{1.5}$$

where P (Pa) is the pressure from the load, U_n is the dimensionless speed parameter (Eqn. 2.20), G_n is the dimensionless material parameter (Eqn. 2.21), W_n is the dimensionless load parameter (Eqn. 2.22), and $\kappa_{ellipse}$ is the ellipticity of the area of contact [18–20].

It is desired to develop a practical numerical method of modeling and simulating the phenomena of asperities in sliding contact without needing substantial empirical data to start with. Such a method can be used to reduce the need for repetitive four-ball tests, which require expensive equipment and are time-consuming to perform. Finally, a reliable numerical model will help to better understand analytically and conceptually the phenomena of wear evolution, to improve on practical engineering design.

1.3 Tribological Effects of Nanoparticles

Nanometer (nm) scale particulates have garnered much recent interest as additives to lubricants. These particles are advantageous over larger additives [21–26] because of their small size and high number density. The size of nanoparticles enables them to better fit within small asperities for friction and wear mitigation than larger additives. In addition, the small size of nanoparticles allows them to be more resistant to settling than larger additives, which results in increased stability within the

lubricant [22]. Finally, provided that the particles are well dispersed within the lubricant, a large quantity of particles will exist within a given volume, even at small levels of concentration.

Several recent studies have been conducted to analyze the tribological performance of nanoparticle-containing lubricants. Nanoparticles comprised of boron nitride [27, 28], lanthanum fluoride [29], cerium fluoride [30], zinc sulfide [31], lanthanum hydroxide [32], copper oxide, and titanium oxide [23] were found to improve tribological properties when tested with a reciprocating tribotester with a flat surface sample. In addition, four-ball tests of lubricants mixed with nanoparticles of iron, copper, cobalt [24], lead sulfide [33], oleic-acid-capped lead sulfide [34], zinc sulfide [35], titanium oxide [36, 37], and calcium carbonate [25] have also shown an improvement in tribological characteristics with increased concentrations. There is much empirical evidence to show that nanoparticles can improve the tribological properties of a lubricant.

There were similar studies conducted to study the tribological effects of inorganic fullerene-like nanoparticles; these particles are known to roll, rather than slide, within a tribological interface, thus reducing friction. A ring block tester was used to study inorganic fullerene-like nanoparticles of WS_2 and MoS_2 as an additive to improve the tribological properties of powdered material, rather than oils, under friction of bronze, iron, and iron-nickel structures [26, 38–40]. These particles formed a protective film coating, usually only as thick as a single fullerene-like nanoparticle, which facilitated the shear stress of the sliding and allowed an increased load capacity of the parts in contact. Even under severe contact conditions [41], where the gap between the contact surfaces was smaller than the size of the nanoparticles, the WS_2 additives improved the tribological properties of the lubricant. While the external sheets of the outermost layers of the WS_2 nanoparti-

cles were peeled off, there were pristine layers of these fullerene-like nanoparticles found (with SEM) in the solid asperities. In a separate study [42], WS_2 and MoS_2 nanotubes were tested in comparison to spherical gold nano-objects to determine if they improved the tribological performance. An Atomic Force Microscope (AFM) was used to characterize the wear after tests with a ball-on-flat tribometer were conducted, and these nanoparticles were found to reduce wear and friction both in wet and dry conditions. These studies have helped to demonstrate how a large diversity of nanoparticles can help to improve the tribological properties of lubricants.

Diamond nanoparticles have also been investigated as lubricant additives [21, 23], and they were found to reduce friction and wear at relatively low concentrations. These previous tests were conducted with oscillating sliding conditions using a ball-on-disk apparatus; this is different from the four-ball test, which was developed to study lubricating fluids in unidirectional sliding contact [43]. The four-ball test has fixed and localized locations of wear and contact, which are not exposed to chemically affecting atmospheric changes over the duration of the test. By taking advantage of the extremely small nanometer-scale particles, large quantities of particles can be realized for a given concentration of diamond, and as a result the viscosity is minimally affected.

There are several theories to try to explain the causes of improved tribological properties with diamond and diamond-like carbons. One possible cause is that diamond nanoparticles are believed to polish away asperities (roughness) on the sliding surfaces; it is well known that the greater the initial surface roughness, the greater the coefficient of friction (COF) [44, 45]. Another theory is a smooth layer of these nanoparticles acting as "tiny ball bearings" [21, 22, 46], where there is less metal-on-metal contact and thus less wear and friction. This has been repeatedly demonstrated with fullerene-like nanoparticles [26, 38–41], which fill in nanometer-

sized holes and asperities, thus smoothing the rolling surface. Reduction in wear, however, has also been observed from particle-on-particle or dispersion diamond nanoparticles alone [22], and therefore the polishing of asperities and ball-bearing effect might not be the only cause of reduced wear and friction.

There is significant interest within the community to better understand the phenomenon of rehybridization and how it may affect tribological properties [22]. Rehybridization, which is defined by the changing back and forth from sp^2 to sp^3 atomic bonds, may cause formation of lubricious amorphous sp^2-containing carbon under high temperature friction and sliding conditions. During rehybridization, the energy resulting from grinding and high-temperatures will be high enough to exceed the activation energy needed to convert carbon sp^3-bonds (typical of hard diamond) to more amorphous carbon sp^2-bonds, thus allowing smoother sliding and less covalent bond formation that adds to the friction. This was investigated [47] on diamond ultra-crystalline coatings, and it was observed that rehybridization only occurs in temperatures greater than 600°C, thus defining an activation energy in diamond for converting sp^3-bonded carbon to sp^2-bonded carbon to be 3.5 ± 0.9 eV. For most tribological applications, the temperature is well below 600°C; the exceptions to this are concentrated stress points where the temperature may in fact exceed the rehybridization energy. Therefore, because of the high energy needed to change the carbon bonds, rehybridization is not expected to be the primary cause of improving wear and friction for the diamond nanoparticle tests of interest in this effort.

Another effort [48] was conducted to determine the comparative effects of chemistry-changing rehybridization and passivation on tribological properties of ultra-crystalline diamond surfaces. Chemical effectives were previously observed in diamond films and coatings, which are noted for their tribological properties [49–56], similar to

boron nitride [57,58] and chromium [59]. Passivation is defined as when a material becomes less reactive due to environment characteristics such as high temperatures and friction. In this effort, after the reciprocating sliding tests, spectral measurements were performed on the worn diamond surfaces. It was observed that there was no correlation from the rate of ordered graphite formed and the COF and wear rates measured. Oxidized species of the diamond coating were studied and indicated that the dangling carbon bonds were produced and then passivated. It is believed to be evidence of passivation due to the rapid dissociation times and highly favorable energetics of water (from ambient humidity) on the dangling diamond bonds. While this effort is related to ultra-crystalline diamond coatings and not necessarily diamond nanoparticles, as the diamonds nanoparticles were observed to form a definitive layer around the material [21] it is relevant as a possible tribochemical cause for reduced wear and friction as a result of diamond nanoparticle additives.

One established method to investigate the surface chemistry of tribological phenomenon is to use X-ray Photoelectron Spectroscopy (XPS). XPS is a quantitative spectroscopic technique that measures the molecular composition, chemical state, and electronic state of the elements that exist within a material on the surface (top 10 nm) of a sample of interest. Spectral data is obtained by irradiating a surface within a vacuum with X-rays while simultaneously measuring the kinetic energy and number of electrons that escape from the surface being analyzed [60]. Prior studies of diamond nanofilms have shown a peak binding energy at 398 eV for diamond films grown in a $CH_4/H_2/N_2$ mixture [61]; in a separate study the XPS spectra was found not to vary much with increasing nitrogen concentration [62]. In another prior study of diamond nanoparticles with a dimension of 5-10 nm in paraffin oil subjected to sliding friction (ball on disk test), the XPS binding energy

(284.3 eV) obtained from the contact surface is the same for both the base paraffin oil as well as the oil with the diamond nanoparticles additives; this study occurred with a significant reduction in wear volume and friction coefficient with increasing diamond nanoparticle weight concentration from 0.001% to 0.01% [21]. Because of this, it is safe to assume that a reduction in wear volume and coefficient of friction will be a mechanical, and not a chemical, phenomenon.

In an ongoing effort to determine the mechanism for improved friction/wear due to nanoparticles, this study will investigate the effect of nanoparticle concentration on tribological performance. Having this knowledge will help elucidate the underlying causes of the improved performances of diamond nanoparticle additives under sliding contact, and will help to determine the ideal concentration of nanoparticles for the optimal performance of a practical mechanical system.

1.4 Hypothesis

The hypothesis is to determine whether or not the enhanced thermal conductivity of diamond nanoparticles is the primary cause of the reduction in wear and friction. Graphite has been used as an additive to paraffin oil to enhance the thermal conductivity [63–65], and considering the very high thermal conductivity of diamond [66–69], significant enhancements in thermal conductivity can be expected with even minute mass concentrations of diamond nanoparticles [70–81]. The hypothesis proposes that this increase in the thermal conductivity is expected to reduce the lubricant film temperature [82], which will increase the viscosity [83], which will increase the lubricant film thickness [18, 20], and reduce the wear [2, 3, 15].

1.5 Intellectual Merit

This research is not only expected to greatly enhance the understanding of diamond nanoparticles, but it is expected to also provide better insight and understanding of wear, sliding contact, and elastohydrodynamic lubricant film behavior. While there have been previous efforts at modeling lubricant film thickness, it is still a new and developing field. In addition, there is very limited previous work that has investigated or modeled lubricant film thickness of worn surfaces; most studies have been performed of well-defined shapes. Finally, by having an accurate and experimentally validated numerical model of sliding contact typically seen in four-ball studies, which takes into account many tribological properties, the causes of wear can be better investigated and understood, both with the diamond nanoparticles of interest as well as future tribological studies of sliding contact.

1.6 Chapter Summaries

Chapter 2 is focused on the development of a novel numerical method to model sliding contact and wear as observed in a standard ASTM four-ball test [43]. There is first a discussion of an iterative analytical approach to determining the temperature and viscosity of the lubricant, as there are several tribological effects at play that can affect the lubricant film. Once these properties are realized, and a minimum elastohydrodynamic lubricant film thickness is obtained, the Reynolds equation is solved numerically, and the chapter discusses the detailed steps that are necessary to iterate and converge on the pressure and film thickness profile at the region of contact. Next is a discussion on how Monte Carlo simulations were used to ascertain the wear rate from the lubricant film thickness, as wear occurs when random

surface asperities exceed the film thickness height and come into contact with the opposing surface. Finally, the chapter discusses series of four-ball experimental tests with neat mineral oil in time, temperature, and load, and how the experimental results validate the numerical model. By having this numerical model, the causes of various tribological effects can be better understood.

Chapter 3 is about a purely experimental effort to investigate the wear and friction reduction properties of minute quantities of diamond nanoparticles as an additive to mineral oil. Experimental viscosity measurements of both neat mineral oil and diamond nanoparticle solution are presented and compared. Next, a series of four-ball tests are performed at consistent loads, bulk lubricant temperatures, and durations, with varying concentrations of the diamond nanoparticle additive ranging from neat mineral oil to 0.01% weight concentration. Finally, experimental XPS measurements of the surfaces of tested ball-bearings, and Dynamic Light Scattering (DLS) and Fourier Transform Infrared Spectroscopy (FTIR) measurements of tested lubricant are also discussed, in order to ascertain if any chemical reactions occurred that might affect the tribological properties of the different lubricant solutions.

Chapter 4 discusses the cumulation of the work of chapter 2 and 3, where the numerical model that was developed in chapter 2 is used to try and ascertain the cause of the wear reduction properties observed in chapter 3. Except for the lubricant thermal conductivity enhancements of the diamond nanoparticles, both the neat mineral oil and the diamond nanoparticle solution studies are simulated identically. Enhancing the thermal conductivity has the effect of reducing the lubricant film temperature, which increases the overall film thickness and reduces the wear. Four-ball experimental tests are conducted of the 0.01% weight concentration solution, varying in both duration and bulk temperature, and the experimental results

were compared to the numerical simulations in order to verify if the enhanced thermal conductivity was the primary cause of the reduction in wear from the diamond nanoparticle additive.

1.7 Specific Aims

The specific aims of this research are as follows:

- SA1: The first specific aim is to develop a novel numerical model in order to study and characterize the evolution of transient tribological wear in the presence of sliding contact. Sliding contact is often characterized experimentally via the standard ASTM D4172 four-ball test, and the numerical model was developed to simulate such a test. Finite difference methods were used to solve the Reynolds equation and find the lubricant oil pressure, and the simulation used iteration to converge on a proper film thickness profile based on this pressure and ball profile data. This film profile data can be used in conjunction with Monte Carlo simulation results in order to determine the wear rate profile as the contact evolves.

- SA2: The second specific aim involves performing four-ball experimental tests with mineral oil for varying times ranging from 10 seconds to 1 hour, as well as at varying temperatures and loads, for the purpose of verifying and validating the numerical model.

- SA3: The third specific aim is to experimentally investigate the tribological effects of diamond nanoparticles as an additive to lubricant mineral oil. The tests were run for varying concentrations ranging from pure mineral oil to 0.01% weight-concentration of diamond nanoparticles. The friction was

measured throughout the tests, and the resulting wear was measured with optical profilometry.

- SA4: The forth specific aim was to investigate the influence of nanodiamond additives on the interfacial chemical reactions during sliding contact. In order to do so, the chemical properties of the surfaces of untested ball bearings, as well as tested ball bearings from both neat mineral oil and 0.01% diamond nanoparticle solution were tested. In addition, chemical studies of used and unused lubricant were also studied. This specific aim served to identify or rule-out a chemical reaction such as rehybridization or passivation being the cause of the enhanced tribological properties from the diamond nanoparticle additive.

- SA5: The fifth specific aim focused on further investigating the wear of four-ball tests with the diamond nanoparticle additive, conducting experimental tests both in time variation and temperature variation.

- SA6: The sixth specific aim focused on investigating the possibility of thermal conductivity enhancement in the contact interface due to the diamond nanoparticles, which may lead to reduced wear. In order to do so, the numerical model was modified to simulate the enhanced thermal conductivity of the lubricant due to the addition of diamond within the lubricant, and the numerical results were compared to the experimental results in SA3 and SA5 in order to verify that the thermal effects were the primary cause of the wear reduction from the additive.

Chapter 2

NUMERICAL MODELING OF SLIDING CONTACT

TRIBOLOGICAL INVESTIGATIONS OF THE LOAD, TEMPERATURE, AND TIME DEPENDENCE OF WEAR IN SLIDING CONTACT

2.1 Chapter Abstract

An effort was made to study and characterize the evolution of transient tribological wear in the presence of sliding contact. Sliding contact is often characterized experimentally via the standard ASTM D4172 four-ball test, and these tests were conducted for varying times ranging from 10 seconds to 1 hour, as well as at varying temperatures and loads. A numerical model was developed to simulate the evolution of wear in the elastohydrodynamic regime, and is found to closely represent the experimental data and successfully model sliding contact without extensive empirical data.

2.2 Introduction

This chapter focuses on the development of a numerical elastohydrodynamic wear model, to replicate the wear observed in a four-ball sliding contact test. As was observed in Archard's Wear equation (Eqn. 1.3), the wear rate is directly proportional to the lubricant film thickness. Many elastohydrodynamic properties need to be realized, including the lubricant temperature, lubricant viscosity, elastic deflection, lubricant pressure (solved with the Reynolds equation), and the preexisting wear; all of these properties can affect the lubricant film thickness profile. These properties interplay with each other, and therefore the model must perform multiple iterative loops at each time-step in order to converge on a final set of parameters and an accurate lubricant film thickness profile. Once the film thickness is determined, only then can the principles of Archard's Wear equation be used to predict the wear rate and simulate the wear that occurs from the elastohydrodynamic sliding contact of a four-ball test.

2.3 Film Thickness Model

A numerical model was developed to solve the Archard's equation and determine the wear rate as it is distributed over the area in contact. To do this, it is clear based on Eqn. 1.3 that the wear rate is strongly proportional to the film thickness, and therefore it is necessary to realize it [18, 84–90] in order to proper predict the wear rate. The first step is to break down the area of contact into a defined two-dimensional (2D) meshed grid. It is safe to assume that throughout the entire domain of the ball bearing, surrounding the area of contact, the surface is entirely immersed in oil. With this assumption, the lubricant oil film thickness will com-

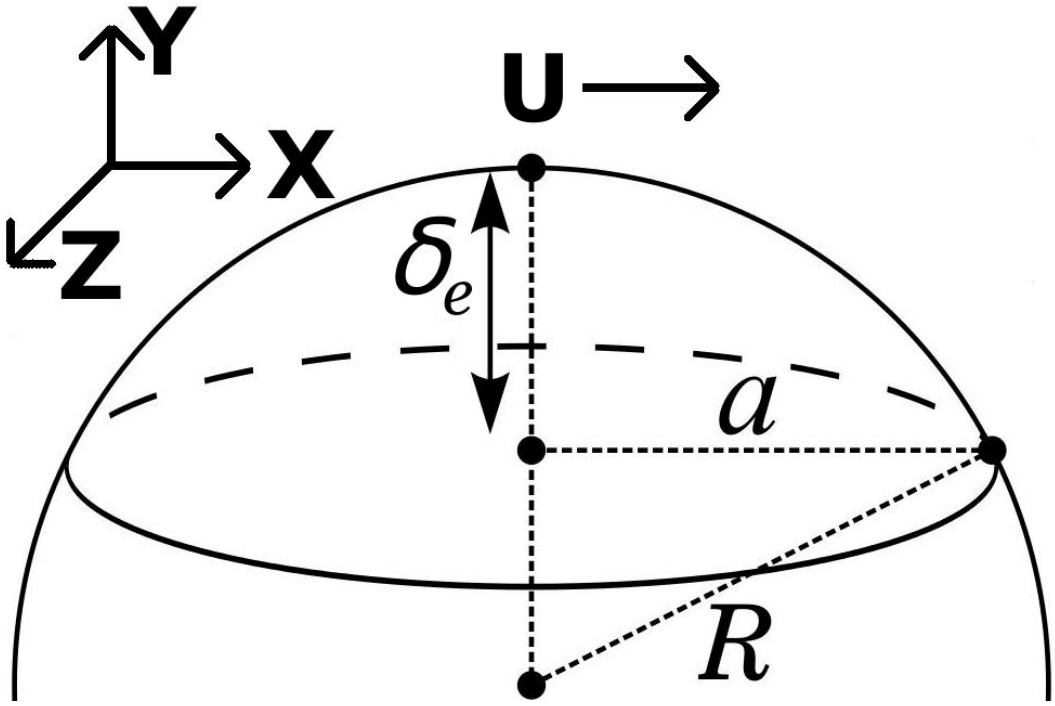

Figure 2.1: Definitions for indentation function defined by Eqn. 2.2 - 2.4, and the definition of the *x*, *y*, and *z* dimensions.

prise of the sum total of the profile of the ball bearing, elastic deflection from the pressure of contact, and any wear that may have previously occurred [91]. In addition, a minimal film thickness must exist in the presence of this elastohydrodynamic contact, and thus the oil thickness function *h* (m) is,

$$h = F_{indent} + V_y + \delta_e - min(F_{indent} + V_y + \delta_e) + h_{min}, \qquad (2.1)$$

where V_y (m) is the wear depth profile, h_{min} (m) is the minimum elastohydrodynamic film thickness, δ_e (m) is the elastic deflection, and F_{indent} (m) is the profile of the ball-bearing as is used in a standard four-ball test [1, 43]. The *min(...)* term normalizes the oil film profile, and ensures that the minimum film thickness h_{min} is consistently the minimum value of *h*.

The equation for the indentation of the ball bearing is

$$F_{indent}(x,z,R) = 2{\cdot}R{\cdot}[1-cos(sin^{-1}\frac{\sqrt{x^2+z^2}}{R})], \tag{2.2}$$

where *R* (m) is the radius of the ball bearing. Equation 2.2 can be derived by the trigonometric relationships described in Fig. 2.1,

$$F_{indent}(x,z,R) = 2{\cdot}R{\cdot}(1-cos\theta), \tag{2.3}$$

$$\theta = sin^{-1}\frac{\sqrt{x^2+z^2}}{R}, \tag{2.4}$$

where θ (radians) is defined by Eqn. 2.4. The factor of 2 is included Eqn. 2.2 and 2.3 due to the profile function F_{indent} representing both of the two ball bearings; the sample ball bearing and the top ball bearing connected by the spindle.

The next step to estimating the lubricant film thickness is to calculate the elastic deformation as a result of the lubricant pressures. To determine this deflection, the Winkler Mattress model is assumed [91], where the deflection at each finite difference node is linearly proportional to the pressure following Hooke's Law; the deflections are small compared to the total length and thus there are no significant shearing forces. The elastic deflection δ_e (m) can be easily calculated as

$$\delta_e = \frac{P}{K_h}, \tag{2.5}$$

where *P* (Pa) is the pressure; and K_h (Pa/m) is the Winkler Mattress coefficient. While there are several approaches to calculating K_h [91], this model calculates it by comparing the estimated Hertzian pressure to the estimated Hertzian deflection,

where

$$K_h = \frac{P_{Hertz}}{\delta_{Hertz}}, \tag{2.6}$$

where P_{Hertz} (Pa) is the maximum Hertzian pressure, and δ_{Hertz} (m) is the maximum Hertzian deflection, both for dry, no-wear, elastic contact.

To determine this deflection and pressure, the Hertzian contact model will be used, which assumes all-elastic dry contact between two solid spheres. To find this area, it is necessary to find [9, 20] the reduced radius (*R'*) and reduced Young's modulus (*E'*),

$$\frac{1}{R'} = \frac{1}{R_{sa}} + \frac{1}{R_{sb}}, \tag{2.7}$$

$$\frac{1}{E'} = \frac{1}{2}\left[\frac{1-p_{sa}^2}{E_{sa}} + \frac{1-p_{sb}^2}{E_{sb}}\right], \tag{2.8}$$

where *p* is the dimensionless Poisson's ratio, *E* (Pa) is the Young's modulus of the material, and *sa* and *sb* represent the two solid surfaces in contact. As all of the ball bearings in a four-ball test will have the same radius (typically 0.25 inches) and Young's modulus [43], where *sa*=*sb*, then the reduced radius and Young's modulus can be solved by:

$$R' = \frac{R}{2}, \tag{2.9}$$

$$E' = \frac{E}{1-p^2}. \tag{2.10}$$

Once these values are found, one can find the radius of the circular area of contact

a_{Hertz} (m) using Hertzian [9, 20],

$$a_{Hertz} = \left(\frac{3WR'}{2E'}\right)^{\frac{1}{3}}, \tag{2.11}$$

where W (Newtons) is the total load. Once the Hertzian contact radius is known, the pressure and deflection can be easily calculated as

$$P_{Hertz} = \frac{3}{2}\frac{W}{\pi a_{Hertz}^2}, \tag{2.12}$$

$$\delta_{Hertz} = (\frac{9}{16}\frac{W^2}{R'\cdot E'^2})^{\frac{1}{3}}, \tag{2.13}$$

and with these terms the Winkler Mattress coefficient can be determined from Eqn. 2.6. The equation for Hertzian pressure as a function of radial distance r (m) from the center of the contact is easily derived from Eqn. 2.12,

$$P_{Hertz}(r) = \frac{3}{2}\frac{W_0}{\pi a_{Hertz}^2}[1 - (\frac{r}{a_{Hertz}})^2], \tag{2.14}$$

$$r = \sqrt{x^2 + z^2}, \tag{2.15}$$

and by imposing this pressure with the Winkler Mattress coefficient determined in Eqn. 2.6, a flat profile can be observed within the radius contact in Fig. 2.2.

Due to the presence, however, of both the lubricant oil as well as the previous wear on the ball bearing profile, Eqn. 2.14 cannot be assumed for the pressure. The Reynolds equation must be solved [91] in order to get the true lubricant oil pressure and deflection. Within the Reynolds equation, the film thickness will directly affect the pressure function, which affects the elastic deformation, which affects the pressure. For this reason, an iterative solver [92–96] will be needed to converge on a solution of both the pressure and the film thickness in the presence of

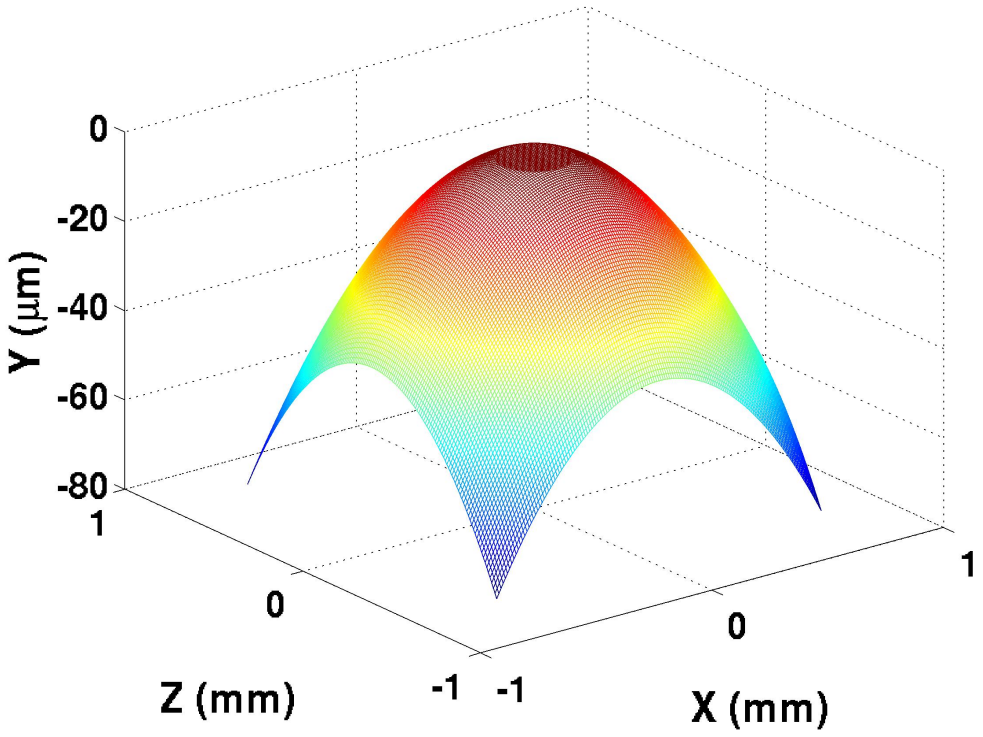

Figure 2.2: Ball bearing profile subjected to Hertzian deflection for 391 Newtons of load. The Hertzian pressure function (Eqn. 2.14) was divided by the Winkler Mattress coefficient (Eqn. 2.6), and the deflection yielded a flat surface at the region of contact.

the ball bearing profile, previous wear, and the minimum elastohydrodynamic film thickness.

In addition to the pressure and elasticity, the minimum elastohydrodynamic lubrication film thickness needs to be realized. This is a small amount of oil, typically 1 μm thick [20] or less, subjected to extreme pressures from the contact. One cause of this minimum lubricant thickness is from hydrodynamic film formation, such as boundary layer and other effects from simple hydrodynamic lubrication. A second cause of this minimum thickness is modification of the material geometry; the two surfaces deform elastically to form a quasi-parallel region for the lubricant to flow through (Fig. 2.4). Finally, according to Barus law [20, 97], the viscosity increases

exponentially with pressure

$$\nu_P = \nu_0 \cdot e^{\alpha_P P}, \tag{2.16}$$

where *P* (Pa) is the pressure, ν_P and ν_0 (mm^2/s) are the kinematic viscosity under high and atmospheric pressure respectively, and α_P (Pa^{-1}) is the pressure-viscosity coefficient (PVC) of the lubricant, [20, 98], where

$$\alpha_P = [1.216 + 4.143\chi^{3.0627} + \frac{2.848}{10^4} \cdot b_0^{5.1903} \cdot \chi^{1.5976} - 3.999\rho^{0.1162}\chi^{3.0975}] \cdot 10^8, \tag{2.17}$$
$$\chi = log_{10}\nu_0,$$

where b_0 is the ASTM slope coefficient multiplied by 5, and is determined for this oil to be 0.6363 [98]. Under the extreme pressures that occur at the point of contact, the viscosity can increase dramatically, and also contribute to the overall lubricant film thickness.

There are numerous prior studies for the lubricant oil film thickness [19, 84–90], though one of the most versatile is the study conducted by Hamrock and Dowson [18]. Film thickness profiles were studied experimentally for a large series of elastohydrodynamic profiles for varying dimensions, and optical interferometry was used to measure both the minimum and central film thickness. They used a variety of different materials, lubricants, speeds, loads, and contact dimensions, to come with a single empirical solution for the lubricant oil thickness. The Hamrock-

Dowson equations for the minimum and central film thickness [18]

$$h_{min} = 3.63R'(U_n^{0.68})(G_n^{0.49})(W_n^{-0.073})(1 - exp[-0.68\kappa_{ellipse}]), \quad (2.18)$$

$$h_c = 2.69R'(U_n^{0.67})(G_n^{0.53})(W_n^{-0.067})(1 - 0.61 \cdot exp[-0.73\kappa_{ellipse}]), \quad (2.19)$$

$$U_n = \frac{\mu_0 U}{E'R'}, \quad (2.20)$$

$$G_n = \alpha_{PVC}E', \quad (2.21)$$

$$W_n = \frac{W}{E'R'^2}, \quad (2.22)$$

where h_{min} (m) is the minimum film thickness, h_c (m) is the central film thickness, U_n is the dimensionless speed parameter, G_n is the dimensionless material parameter, W_n is the dimensionless load parameter, $\kappa_{ellipse}$ is the ellipticity of the contact area, μ_0 (Pa-s) is the dynamic viscosity of the lubricant at atmospheric pressure, and *U* (m/s) is the velocity of sliding contact of the four-ball test,

$$U = \frac{1}{2}R \cdot (\frac{2\pi}{60})\Omega_{RPM}, \quad (2.23)$$

where Ω_{RPM} is the rotation speed in revolutions per minute (r/min) of the four-ball test, and *R* (meters) is the radius of the ball bearing. It is clear that before the pressure and film thickness profile can be realized, it is necessary to determine the dynamic viscosity and the minimum film thickness, so that a proper film thickness function can be realized and the wear rate analyzed.

2.4 Viscosity Calculations

In order to realize the minimum elastohydrodynamic film thickness, it is necessary to determine the dynamic viscosity of the lubricant. The viscosity of the lubricant,

however, is affected by temperature [83, 91, 98–100], as hotter oils are inherently less viscous. A reduction in viscosity results in a reduced minimum film thickness [18], but this reduced film thickness results in a cooler oil film [82], as there is less thermal resistance from the center of the oil film to the surface of the ball bearing. As a result of this contradiction, it is necessary to use iteration in order to converge on a realistic lubricant oil temperature and viscosity, so that a minimum film thickness can be determined.

The first step is to calculate the flash temperature heating of the surface of the ball bearing. This is done by first calculating the dimensionless Peclet number [20, 82]

$$L = \frac{U \cdot a}{2\alpha_{bb}}, \tag{2.24}$$

where *a* is the radius of the area of contact, and α_{bb} (m^2/s) is the thermal diffusivity [101] of the ball bearing,

$$\alpha_{bb} = \frac{k_{bb}}{\rho_{bb} \cdot C_{P,bb}}, \tag{2.25}$$

where k_{bb} ($W/m^2 \cdot ^\circ C$) is the thermal conductivity, ρ_{bb} (kg/m^3) is the density, and $C_{P,bb}$ ($J/kg \cdot ^\circ C$) is the specific heat capacity; all of these parameters are for the ball bearing material (steel).

Once the dimensionless Peclet number *L* is known, one can calculate the average flash temperature [102–105], which is defined as the temperature that results from the high-pressure and heating. For $L < 0.1$, the friction heating is considered a *stationary* heat source, where the temperature distribution is effectively steady state, where the heat flow can be considered a flow of thermal current through a

thermal resistance of the ball bearing. For $0.1 < L < 5.0$, the friction heating is considered a *slow-moving* heat source, where there is ample time for the temperature to be conducted through the ball bearing, and for $L > 5.0$ the friction heating is considered a *high-speed* heat source [82].

The predictive analytical equation used by this model for average flash temperature can vary with Peclet number, where [20, 82]

$$\begin{aligned} \Delta T_F = & \quad \tfrac{\mu_{COF} \cdot W \cdot U}{4 \cdot k_{bb} \cdot a} & L < 0.1, \\ \Delta T_F = & \quad [0.35 + (5.0 - L)\tfrac{0.5}{4.9}]\tfrac{\mu_{COF} \cdot W \cdot U}{4 \cdot k_{bb} \cdot a} & 0.1 < L < 5.0, \\ \Delta T_F = & \quad \tfrac{0.308 \mu_{COF} \cdot W \cdot U}{4 \cdot k_{bb} \cdot a} \sqrt{\tfrac{\alpha_{bb}}{U \cdot a}} & L > 5.0, \end{aligned} \tag{2.26}$$

where μ_{COF} is the dimensionless coefficient of friction (COF), *W* (Newtons) is the load, and ΔT_F (°C) is the surface temperature increase due to friction.

The next step in realizing the elastohydrodynamic film thickness is to estimate the temperature increase of the lubricant as a result of the friction heating. This field was investigated extensively for helical gears [106] and square contact surfaces seen in cutting tools [107], and these classic theories were adjusted for circular contact by Archard in 1958 [82]. Archard's work focused on time-dependent flash heating to match experimental studies conducted by Crook [108], and an equation for the lubricant oil temperature increase $\Delta T_{L,0}$ (°C) at the center of the film ($y = \frac{h}{2}$) [82],

$$\Delta T_{L,0} = (\frac{q_v h^2}{8 k_{lub}})[1 - \frac{32}{\pi^3} \Sigma_{m=0}^{m=\infty} \frac{(-1)^m}{(2m+1)^3} (exp - \frac{\alpha_{lub}(2m+1)^2 \pi^2 t}{h^2})], \tag{2.27}$$

where q_v (Watts/m^3) is the friction energy generated per unit volume, *h* (m) is the film thickness, k_{lub} (Watts/m-°C) is the thermal conductivity of the lubricant, and

α_{lub} (m^2/s) is the thermal diffusivity [101] of the oil,

$$\alpha_{lub} = \frac{k_{lub}}{\rho_{lub} \cdot C_{P,lub}}, \tag{2.28}$$

where ρ_{lub} (kg/m^3) is the density of the lubricant, and $C_{P,lub}$ ($J/kg \cdot °C$) is the specific heat capacity of the lubricant.

The lubricant model being developed will assume steady-state heating, as the time-steps are longer than the flash temperature durations. This can be verified by determining when the first exponential term in the series in Eqn. 2.27 reaches 1%. Assuming a film thickness of h = 1 μm and a thermal diffusivity of $\alpha_{lub} = 7.73 \cdot 10^{-8}$ m^2/s, the flash temperature increase reaches steady state

$$t_{ss} = -\frac{log_N(0.01)h^2}{\alpha_{lub}\pi^2}, \tag{2.29}$$

at t_{ss} = 6 μs. This is far shorter than any time-step in the simulations, and therefore the model will treat the lubricant oil temperature increase as the result of steady-state conductive heat transfer from the center of the lubricant film to the surface of the ball bearing.

The steady-state conductive heat transfer equation [101] with heat generation from friction heating is

$$\frac{d^2T_L}{dy^2} = \frac{q_v}{k_{lub}}, \tag{2.30}$$

and thus the temperature profile of the lubricant $T_L(y)$ (°C) is

$$T_L(y) = \frac{q_v}{2 \cdot k_{lub}}[(h \cdot y) - y^2] + T_{surface}, \tag{2.31}$$

where y (m) is the film thickness position, and $T_{surface}$ (°C) is the surface temperature,

$$T_{surface} = \Delta T_F + T_B, \tag{2.32}$$

where ΔT_F (°C) is the surface temperature increase in Eqn. 2.26, and T_B (°C) is the bulk lubricant temperature. It is clear that Eqn. 2.31 is simply the steady-state ($t = \infty$) solution Eqn. 2.27. Averaging Eqn. 2.31 over the depth of the film thickness ($0 < y < h$), an average lubricant temperature T_L (°C) can be found as

$$T_L = 0.1665 \frac{q_v}{k_{lub}} \frac{h^2}{2} + T_{surface}. \tag{2.33}$$

The next step is to determine the volume rate of heat energy q_v (Watts/m^3) being dissipated into the oil from the friction heating. The friction heat energy density is assumed to be the total of the friction forces being dissipated into the lubricant, as a function of the volume of oil covering the area of contact. The power into the oil Q_{lub} (Watts) is a function of the product of the friction forces and the velocity,

$$Q_{lub} = \mu_{COF} \cdot W \cdot U, \tag{2.34}$$

where μ_{COF} is the dimensionless COF, W (Newtons) is the load, and U (m/s) is the velocity of sliding contact realized in Eqn 2.23. The volume of the oil V_{lub} (m^3) is simply the product of the area of contact and the film thickness h (m),

$$V_{lub} = h \cdot \pi a^2, \tag{2.35}$$

where a (m) is the radius of contact. With these two values, the rate of heating per

volume q_v (Watts/m^3) can be determined,

$$q_v = \frac{\mu_{COF} \cdot W \cdot U}{h \cdot \pi a^2}, \tag{2.36}$$

and with a value of q_v, the final average lubricant temperature T_L (°C) of the oil film,

$$T_L = 0.1665 \frac{\mu_{COF} \cdot W \cdot U}{\pi a^2} \frac{h}{2k_{lub}} + T_{surface}. \tag{2.37}$$

The lubricant temperature can be used to calculate the average viscosity [20,83], where

$$\begin{aligned} \nu &= \hat{Z} \text{–} exp[-0.7487 \text{–} 3.295 \cdot \hat{Z} + 0.6119 \cdot \hat{Z}^2 \text{–} 0.3193 \cdot \hat{Z}^3], \\ \hat{Z} &= 10\text{^}[10\text{^}(A - B \cdot log_{10} T_L)] - 0.7 \end{aligned} \tag{2.38}$$

where ν (mm^2/s) is the kinematic viscosity, and *A* and *B* are dimensionless coefficients derived empirically. They can be found by measuring the kinematic viscosity at two temperature points, calculating the *Z*-value [83],

$$Z = \nu + 0.7 + exp[-1.47 - 1.84\nu - 0.51\nu^2], \tag{2.39}$$

and obtaining the viscosity coefficients, where [83]

$$\begin{aligned} log_{10} log_{10} Z &= A - B \cdot log_{10} T, \\ B &= \frac{log_{10} log_{10} Z_i - log_{10} log_{10} Z_j}{log_{10} T_j - log_{10} T_i}, \\ A &= log_{10} log_{10} Z_i + B \cdot log_{10} T_i, \end{aligned} \tag{2.40}$$

where T_i, T_j, Z_i, and Z_j are the temperature (Kelvin) and *Z*-coefficients at temperature points *i* and *j*. The kinematic viscosity can be used to calculate the dynamic viscosity μ (Pa-s) of the lubricant [109],

$$\mu = \rho_{lub} \cdot \nu, \tag{2.41}$$

and this value can be used to calculate the film thickness using the Hamrock-Dowson [18] empirical equations.

According to Eqn. 2.37, it is clear that the oil temperature increase is linearly proportional to the film thickness; while Eqn. 2.18 shows how a decrease in viscosity (such as from an increase in temperature) would reduce the film thickness. For this reason, iteration is needed to converge on a final lubricant temperature, viscosity, and minimum film thickness. The Hamrock-Dowson [18] empirical equation for the central film thickness (Eqn. 2.19) can be used as an approximate central film thickness to attempt to iterate for a new temperature and viscosity. This iterative loops repeats itself until it converges at a final value for the lubricant oil temperature and viscosity. The final viscosity can be used in Eqn. 2.18 for a minimum film thickness value in order to find the full film-thickness function.

2.5 Numerical Solution of the Reynolds Equation

The Reynolds equations is a well established differential equation derived from the Navier-Stokes equation to predict the pressure distribution in a lubricating film separating two surfaces in contact [20, 91]. The general form of the Reynolds equation

is

$$\frac{\partial}{\partial x}(\frac{\rho h^3}{\mu}\cdot\frac{\partial P}{\partial x})+\frac{\partial}{\partial z}(\frac{\rho h^3}{\mu}\cdot\frac{\partial P}{\partial z})=\frac{\partial}{\partial x}[6\rho h U_x]+\frac{\partial}{\partial z}[6\rho h U_z]+12\frac{d}{dt}(\rho h), \quad (2.42)$$

where U_x and U_z (m/s) are the flow velocities in and out of the thin-film boundary in the *x* and *z* direction (see Fig. 2.1), *P* (Pa) is the pressure, *h* (m) is the film thickness, and μ (Pa-s) is the dynamic viscosity.

The Reynolds equation can be converted to a one-dimensional (1D) equation with several assumptions [91]. First, at the *z*-direction boundaries, there is no pressure change or side leakage; the flow of the fluid is only in the *x* direction, and thus

$$\frac{\partial P}{\partial z}=\frac{\partial}{\partial z}[\frac{\rho h^3}{\mu}\cdot\frac{\partial P}{\partial z}] = 0, \quad (2.43)$$

$$U_z = 0. \quad (2.44)$$

Next, it can be assumed the density ρ is constant; a reasonable assumption in most practical applications. Finally, if you assume the flow to be steady-state, where $\frac{d}{dt}=0$ the one-dimensional Reynolds equation can be written as,

$$\frac{\partial}{\partial x}(h^3\cdot\frac{\partial P}{\partial x}) = 6\mu U\cdot\frac{\partial h}{\partial x}, \quad (2.45)$$

where $U = U_x$ is determined from Eqn. 2.23 as the net *x*-direction velocity of the two surfaces in contact. Integrating this equation will yield

$$h^3\cdot\frac{\partial P}{\partial x} = 6\mu U h + C, \quad (2.46)$$

where *C* is the constant of integration. Assuming $h = h_c$ where $\frac{dP}{dx}=0$, one gets a

simple relationship for the pressure differential,

$$\frac{\partial P}{\partial x} = 6\mu U \cdot \frac{h - h_c}{h^3}, \tag{2.47}$$

where h_c is the upper boundary of the film thickness.

The next step is to discretized the Reynolds equations, including the pressure distribution. Using Taylor-Series expansion, the pressure as a function of discrete location is

$$P_{i+1} = P_i + P_{i+1}(X_{i+1} - X_i) + \hat{O}(\Delta x^2), \tag{2.48}$$

and the discretized derivatives of the pressure is [110]

$$P_i' = \frac{P_{i+1} - P_{i-1}}{2\Delta x}, \tag{2.49}$$

$$P_i'' = \frac{P_{i+1} - 2P_i + P_{i-1}}{\Delta x^2}, \tag{2.50}$$

where Δx is the length in between finite-difference nodes. These discrete terms can be plugged into Equation 2.45

$$(h^3 \cdot \frac{\partial^2 P}{\partial x^2}) + 3h^2 \frac{\partial P}{\partial x} \cdot \frac{\partial h}{\partial x} = 6\mu U \cdot \frac{\partial h}{\partial x}, \tag{2.51}$$

$$h^3 \cdot \frac{P_{i+1} - 2P_i + P_{i-1}}{\Delta x^2} + 3h^2 \frac{P_{i+1} - P_{i-1}}{2\Delta x} \cdot \frac{\partial h}{\partial x} = 6\mu U \cdot \frac{\partial h}{\partial x}, \tag{2.52}$$

$$P_{i-1}(\frac{h^3}{\Delta x^2} - \frac{3h^2}{2\Delta x}\frac{\partial h}{\partial x}) + P_i(\frac{-2h^3}{\Delta x^2}) + P_{i+1}(\frac{h^3}{\Delta x^2} + \frac{3h^2}{2\Delta x}\frac{\partial h}{\partial x}) = 6\mu U \cdot \frac{\partial h}{\partial x}, \tag{2.53}$$

$$P_{i-1}W_i + P_i a_i + P_{i+1}E_i = B_i, \tag{2.54}$$

This is the discrete form representation of the 1D Reynolds equation.

To convert this equation into a 2D format in the *x* and *z* direction ($\frac{d}{dy} = 0$), the

discrete Reynolds equation can be written as [91, 92]

$$P_{i-1,j}W_{i,j} + P_{i+1,j}E_{i,j} + P_{i,j-1}S_{i,j} + P_{i,j+1}N_{i,j} + P_{i,j}a_{i,j} = B_{i,j}, \tag{2.55}$$

where,

$$W_{i,j} = \frac{h^3}{\Delta x^2} - \frac{3h^2}{2\Delta x}\cdot\frac{\partial h}{\partial x} = \frac{h^3_{i,j}}{\Delta x^2} - \frac{3h^2_{i,j}}{2\Delta x}\cdot\frac{h_{i+1,j} - h_{i-1,j}}{2\Delta x}, \tag{2.56}$$

$$E_{i,j} = \frac{h^3}{\Delta x^2} + \frac{3h^2}{2\Delta x}\cdot\frac{\partial h}{\partial x} = \frac{h^3_{i,j}}{\Delta x^2} + \frac{3h^2_{i,j}}{2\Delta x}\cdot\frac{h_{i+1,j} - h_{i-1,j}}{2\Delta x}, \tag{2.57}$$

$$S_{i,j} = \frac{h^3}{\Delta z^2} - \frac{3h^2}{2\Delta z}\cdot\frac{\partial h}{\partial z} = \frac{h^3_{i,j}}{\Delta z^2} - \frac{3h^2_{i,j}}{2\Delta z}\cdot\frac{h_{i,j+1} - h_{i,j-1}}{2\Delta z}, \tag{2.58}$$

$$N_{i,j} = \frac{h^3}{\Delta z^2} + \frac{3h^2}{2\Delta z}\cdot\frac{\partial h}{\partial z} = \frac{h^3_{i,j}}{\Delta z^2} - \frac{3h^2_{i,j}}{2\Delta z}\cdot\frac{h_{i,j+1} - h_{i,j-1}}{2\Delta z}, \tag{2.59}$$

$$a_{i,j} = (\frac{-2h^3}{\Delta x^2}) + (\frac{-2h^3}{\Delta z^2}) = -2\frac{h^3_{i,j}}{\Delta x^2} - 2\frac{h^3_{i,j}}{\Delta z^2}, \tag{2.60}$$

and the right-hand side of this equation, in the discrete form, is

$$B_{i,j} = 6\mu U\frac{\partial h}{\partial x} = 6\mu U\frac{1}{2}[(\frac{h_{i+1,j} - h_{i-1,j}}{2\Delta x}) + (\frac{h_{i,j+1} - h_{i,j-1}}{2\Delta z})]. \tag{2.61}$$

As described in Barus Law in Eqn. 2.16, the viscosity will increase exponentially with pressure [20, 91, 98]. To implement this effect in a Reynolds solver, one could simply use a Grubin model [20, 111–114], where the pressure is substitute for a normalized pressure volume

$$q = \frac{1}{\alpha_{PVC}}[1 - exp(-\alpha_{PVC}\cdot P)], \tag{2.62}$$

$$\frac{\partial q}{\partial x} = \frac{\partial P}{\partial x}\cdot exp(-\alpha_{PVC}\cdot P), \tag{2.63}$$

and plugging in Eqn. 2.63 into Eqn. 2.47, and recalling the effective viscosity under

Barus law (Eqn. 2.16), one gets a simplified version of the 1D Reynolds equation,

$$\frac{\partial q}{\partial x} = 6\mu_0 U \cdot \frac{h - h_c}{h^3}. \tag{2.64}$$

The normalized pressure *q* (Pa) can be substituted into the Reynolds solver for lower pressures, thus simplifying the analysis for low pressure studies where Barus Law is applicable.

Barus Law, however, breaks down for high-pressures greater than 500 MPa [91], and since the region of contact can see pressures on the order of GPa, a different approach is needed to accurately model the viscosity parameter in Eqn 2.61. The approach is the *Roelands* equation [91, 115], where

$$\mu_P = \mu_0 \cdot e^{\alpha_P^* P}, \tag{2.65}$$

where

$$\alpha_P^* P = (\frac{T_i - 138}{T_B - 138})^{S_0} \cdot [(1 + \frac{P}{1.695 \cdot 10^8})^{Z_r} - 1] \cdot (log\mu_0 + 9.67), \tag{2.66}$$

$$Z_r = \frac{\alpha_{PVC} \cdot 1.695 \cdot 10^8}{(log\mu_0 + 9.67)}, \tag{2.67}$$

$$S_0 = \beta_\mu \cdot \frac{T_B - 138}{(log\mu_0 + 9.67)} \tag{2.68}$$

where β_μ is the exponential reduction in viscosity with temperature,

$$\mu(T) = \mu(T_0) \cdot e^{-\beta_\mu (T - T_0)}. \tag{2.69}$$

This model will use an iterative approach to solve the Reynolds equation, for a given input film thickness profile. A predictive guess for the pressure function is

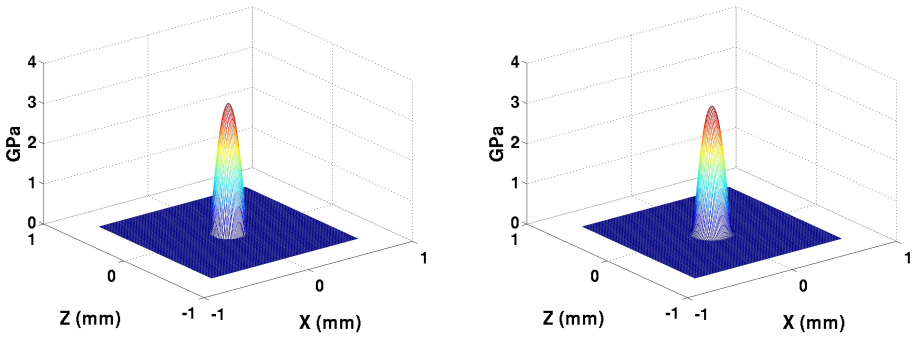

Figure 2.3: (a) Hertzian pressure distribution from Eqn. 2.14, and (b) lubricant oil pressure with no-wear.

used in Eqn. 2.55 to converge on new values of the pressure, where

$$P_{i,j} = \frac{B_{i,j} - (\hat{P}_{i-1,j}W_{i,j} + \hat{P}_{i+1,j}E_{i,j} + \hat{P}_{i,j-1}S_{i,j} + \hat{P}_{i,j+1}N_{i,j})}{a_{i,j}}, \quad (2.70)$$

where $\hat{P}$ (Pa) is an initial *guess* for the pressure at a given node. The Hertzian pressure distribution (Fig. 2.3-a) from Eqn. 2.14 is used in this model before the first time-step to ascertain the lubricant oil pressure in the absence of wear (Fig. 2.3-b). At each time-step, the initial lubricant oil pressure function with no-wear is consistently used as the initial iterative guess. At each iteration, the new pressure function is used until there is convergence.

The convergence of the pressure distribution for a given film thickness is not necessarily a final solution for the pressure. Due to elastic deformation, a change in pressure would yield a change in elastic deformation. After the first pressure convergence, the new pressure is used to find a new profile of the elastic deformation based on the Winkler Mattress Eqn. 2.5, and a new film thickness profile is developed. The film profile is normalized to the minimum film thickness realized in Eqn. 2.18, and the pressure iteration is repeated. This process repeats itself un-

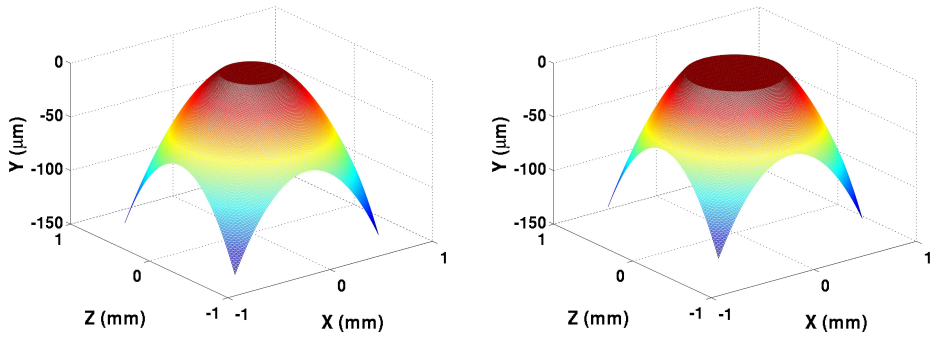

Figure 2.4: Film thickness profile after 3600 seconds of contact, at both (a) 25°C and (b) 59°C.

til the pressure, elastic deformation, and lubricant oil film thickness converge for the given ball-bearing profile and prior wear. Overwhelmingly with wear, the film thickness profile will appear flat (Fig. 2.4). Once the proper film thickness profile is determined, the wear rate can be predicted for the next time-step.

2.6 Wear Simulations

The most important part of this simulation is to figure out the sliding contact wear rate, as described in Eqn. 1.2. The first value to realize is the velocity, which is a specified parameter of the four-ball test; the hardness, which is an experimentally realized material parameter; and the pressure, which is determined with iteration and the Reynolds equation. These terms are only proportional, and a relationship between these values and the true wear rate must be realized.

As observed in Eqn. 1.3 [15], this wear is related to the ratio of the surface roughness over the lubricant thickness. The principle action of wear in the elasto-hydrodynamic regime [20,91] occurs when the material asperities exceed the thickness of the lubricant [2, 15, 116–120]; hence the larger and thicker the asperity, the

greater the wear. Certainly it is not possible to model every single asperity with infinite accuracy, but a root mean squared (RMS) value of the fluctuation of the surface can be easily measured and characterized optically.

The RMS value of the asperities assumes a normal distribution for the probability of a given peak reaching a certain height γ (m),

$$f_{normal}(\gamma, \sigma) \quad = \quad exp[-\frac{\gamma^2}{2\sigma^2}], \tag{2.71}$$

where σ (m) is the standard deviation (or RMS if the mean value is 0) of the fluctuating value γ, calculated as

$$\sigma \quad = \quad \sqrt{\Sigma_{n=1}^{N_a} \frac{(\gamma_n - \bar{\gamma})^2}{N_a}}, \tag{2.72}$$

where γ_n (m) is the height at each point, $\bar{\gamma}$ (m) is the average or arithmetic mean surface height, and N_a is the number of points within the wear scar used to calculate the RMS surface roughness σ (m).

One important consideration to calculating the wear rate is the material hardness, especially the yield stress in shear, as wear occurs when the shear stresses exceed the ultimate yield stress and material is lost. It is intuitively obvious that not all asperities that come into contact with the sliding surface will necessarily be lost as wear; some asperities will only experience elastic deflection. To get around this, a plasticity or yield length needs to be determined, where [2]

$$W_P \quad = \quad R' \cdot (\frac{G_{yield}}{E'})^2, \tag{2.73}$$

where *R'* (m) is the reduced radius (Eqn. 2.9) of the ball bearing, G_{yield} (Pa) is the ultimate yield stress, *E'* (Pa) is the reduced Young's modulus, and W_P (m) is the

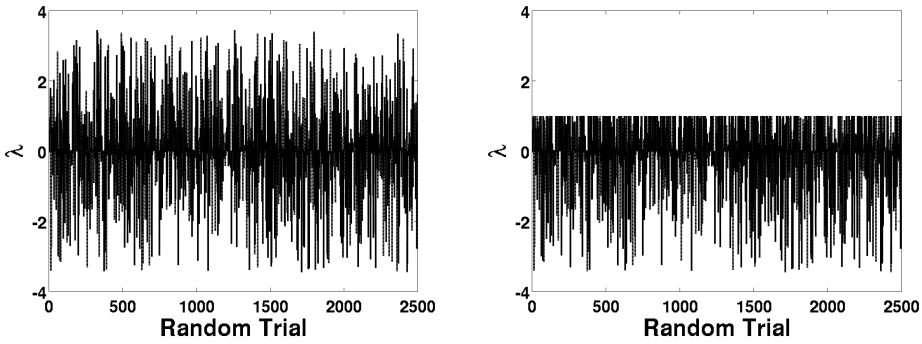

Figure 2.5: Monte Carlo data of random normalized asperities, both (a) before any wear and (b) after $\lambda_W = 1$ of contact.

yield / plasticity length.

Wear occurs when a random asperity exceeds both the film thickness height plus the yield length from Eqn. 2.73. This can be characterized as the dimensionless λ_W-value,

$$\lambda_W = \frac{h + W_P}{\sigma}, \tag{2.74}$$

and this parameter is proportional to the wear according to Archard's Wear Eqn. 1.3 [15]. Wear would occur whenever a random asperity exceeds a certain λ_W-value, which represents the ratio of roughness standard deviations that contact occurs. The lower the λ_W-value, the higher the probability of an asperity exceeding this film thickness height, and thus the more wear would occur.

A Monte Carlo simulation was conducted to attempt to predict the expected wear that would occur from a given λ_W-value, which will remove all the asperities that exceed a given ratio of standard deviations. The asperities were represented by $N = 10^9$ random numbers ranging from -1 to 1 (Fig. 2.5-a), and the standard deviation of this sequence was determined. The random sequence generated with

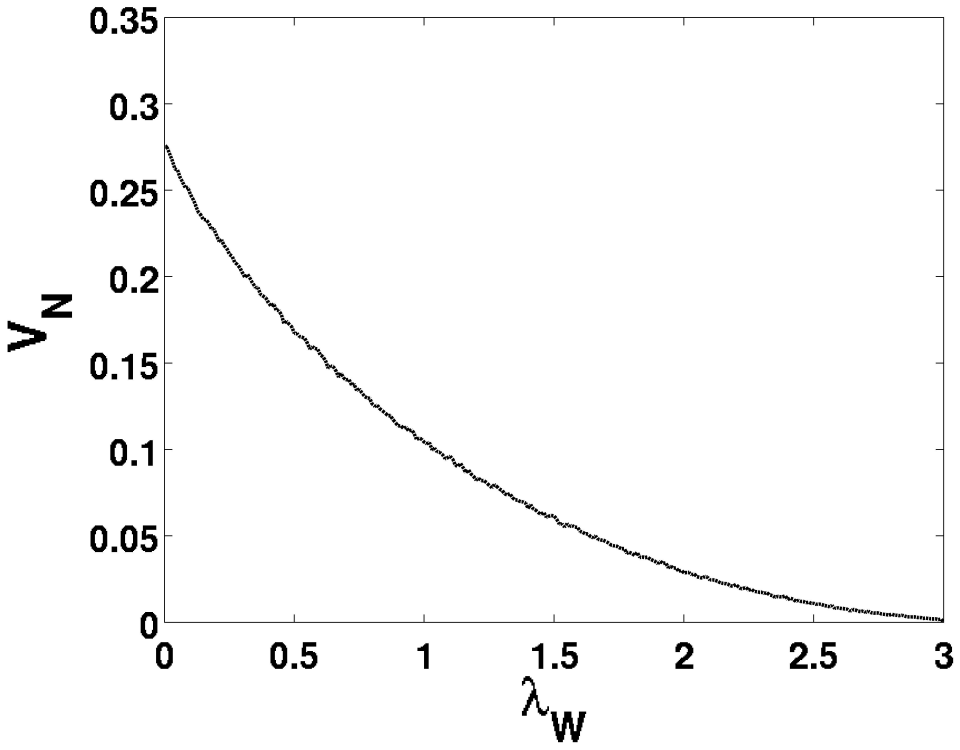

Figure 2.6: Monte Carlo data of V_N as a function of λ_W.

MATLAB was raised exponentially by a power of 5, in order that the maximum asperity height is in excess of at least 3 standard deviations. By increasing the exponential power of the sequence up to 500, λ_W-values up to 20 have been studied, though limitations of the random number generator start to yield numerical instabilities. For the purpose of establishing a trend line, as λ_W-values over 3 are expected to yield negligibly small wear, the Monte Carlo study focused up to this asperity height.

For each λ_W-value of interest, the unworn random sequence (Fig. 2.5-a) is used and all asperities that exceed the given λ_W-value (which represents the standard deviation ratio) were *worn*, where the height was reduced down to the λ_W-value

(Fig. 2.5-b). The wear can be represented as

$$V = \frac{\Delta x^2}{N}\sigma\Sigma_i^N(h_i - \lambda_W), \tag{2.75}$$

where h_i represents the normalized (dimensionless) height of each random asperity, *N* is the total number of asperities studied in the Monte Carlo simulation, Δx^2 (m^2) represents the area under contact, σ (m) represents the RMS surface roughness, and *V* (m^3) is the total wear. For each asperity, the height worn off was collected and averaged throughout all of the asperities, to yield an average wear height relative to the area of contact. The numerically obtained ratio of normalized wear for a given λ_W-value (Fig. 2.6) comes out to

$$V_N = 0.2763 \cdot exp[-1.6754 \cdot \lambda_W], \tag{2.76}$$

and the dimensionless normalized wear volume V_N can apply for the given λ_W-value regardless of the surface roughness or area of contact. The assumption that the wear rate follows an exponential function of the λ_W-value has been well established [2].

To convert the normalized volume in Eqn. 2.76 to the real wear volume in Eqn. 2.75, one simply multiplies the normalized wear by the RMS surface roughness (asperities height) and the area of contact,

$$V = V_N \cdot \sigma \Delta x^2. \tag{2.77}$$

This function assumes the total wear over a given area. In the four-ball test, how-

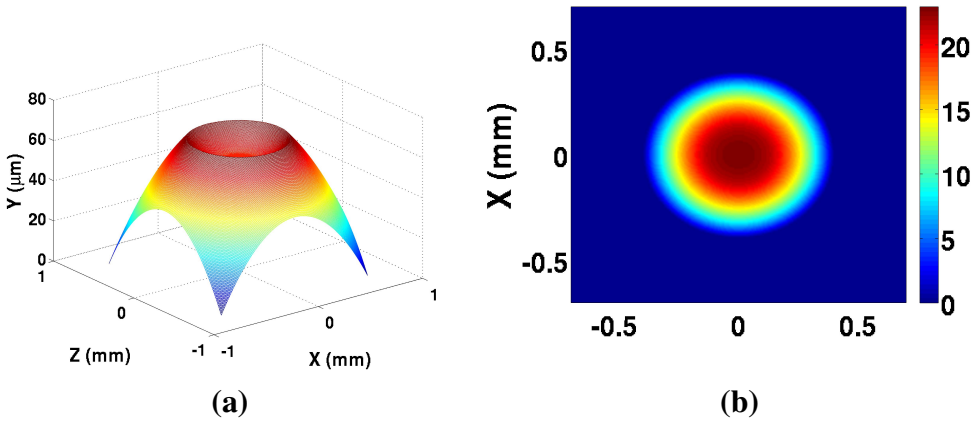

(a) **(b)**

Figure 2.7: Numerical results of wear after 1 hour of sliding contact at a bulk temperature of 59°C and a load of 391 Newtons, both (a) with and (b) without the ball bearing profile. Colorbar in (b) represents wear in μm.

ever, the contact is transient, and therefore the wear rate is

$$\dot{V} \quad = \quad V_N \cdot \sigma \Delta x \cdot U, \tag{2.78}$$

where U (m/s) is the sliding speed (Eqn. 2.23), and $\dot{V}$ (m^3/s) is the transient wear rate. By using this wear rate, and finding the λ_W obtained from the film thickness obtained with the pressure obtained by the Reynolds-function, as well as the minimum elastohydrodynamic film thickness (Eqn. 2.18), a transient wear profile can be obtained (Fig. 2.7).

2.7 Experimental Procedure

A series of four-ball [43] sliding contact tests were conducted to experimentally characterize the wear over varying temperatures, loads, and lengths of time. The four-ball tests were set to consistently run at 1200 r/min, ramped up with an angular acceleration of 100 r/min per second. Throughout all of the tests, the angular

force, and therefore the COF, was consistently recorded by a load cell within the four-ball apparatus. Three series of tests were conducted, the first in time variation, the second in load variation, and the third in temperature variation. For the first series of tests, the run time for each test was varied for different times to characterize the evolution of the wear; run-times used include 10, 60, 120, 300, 1800, and 3600 seconds after the test speed of 1200 r/min was reached. Throughout the time-variation experimental tests, the load was kept constant at 391 Newtons, and the oil was set at one of two consistent temperatures of 51°C and 59°C; PID controllers and convection fans were used to maintain the temperature in the presence of flash heating. The second series of tests were all conducted at the full run-time of 3600 seconds, and a consistent temperature of 59°C, but with a variation of the load at 258, 302, 347, and 391 Newtons. The third series of tests were all conducted at the full run-time of 3600 seconds and a load of 391 Newtons, but with a variation of the bulk oil temperature at 44°C, 51°C, 59°C, and 67°C. Finally, every test was completed twice under identical circumstances, to ensure repeatability of the results.

Before the test commenced, the kinematic viscosity of the test oil (Fig. 2.8) was experimentally measured in order to properly simulate the correct conditions. The viscosity was measured with a Brookfield Lab viscosity meter utilizing an LV2 spindle spinning at 60 r/min. After applying the proper factors, the base mineral oil was found to have (at 25°C ambient temperature) a viscosity of 107.5 mPa·s. This test was repeated for different temperatures, ranging from an ambient temperature of 25°C to 75°C. The viscosity interpolation formula (Eqn. 2.38) was verified by using the experimental data at 25°C and 75°C to find the values of coefficients A and B (Eqn. 2.40). The viscosity formula was used to predict the viscosity at all of the data points in between these two temperature points, and the error between the

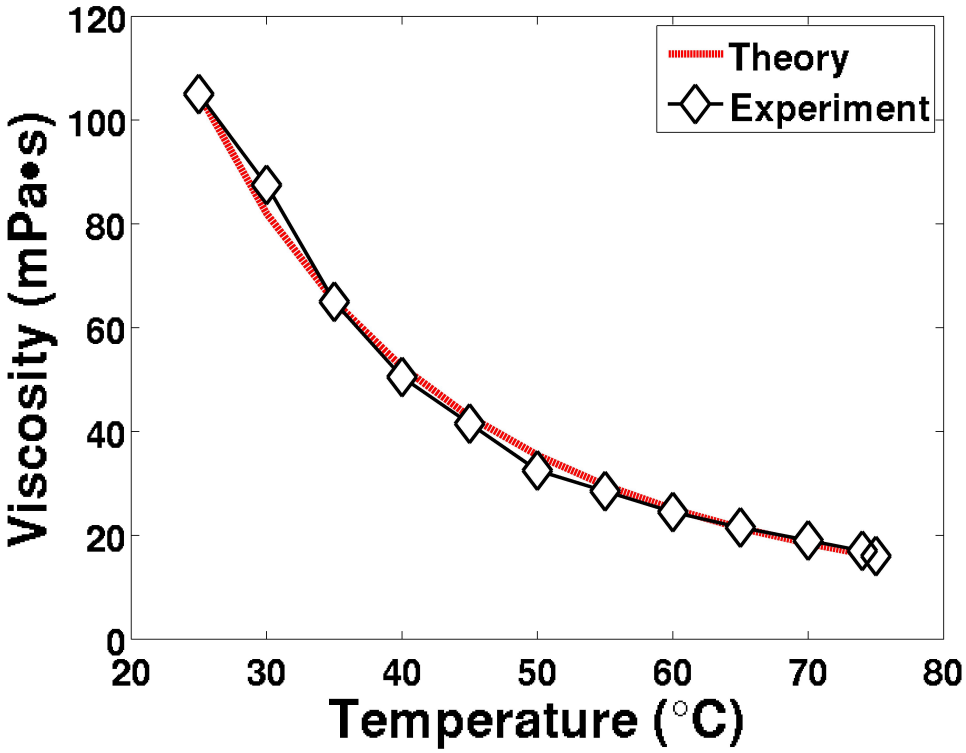

Figure 2.8: Mineral oil dynamic viscosity data.

theory and experimental data was an average of only 3.5623%, thus validating the formula. To improve accuracy, the model calculates the viscosity coefficients (Eqn. 2.40) with the data points closest to the bulk lubricant temperature.

2.8 Results

After each four-ball test, all of the ball bearings were first cleaned in acetone and isopropyl alcohol, and then measured with an optical profilometer, which provides an accurate three-dimensional (3D) model of the wear scar on the ball bearing. The Metro-Pro MX software was utilized to mask the wear scar, and remove the material of the 0.25-inch radius sphere ball bearing. This sphere-removal algorithm enabled a true measurement of the total wear loss, with far greater accuracy than the traditional method of approximating wear loss based on the wear scar diameter.

The total wear as a function of duration of the timed contact was collected at a constant load of 391 Newtons, and a consistent bulk lubricant oil temperature of 51°C (Fig. 2.10 and Table 2.1) and 59°C (Fig. 2.12 and Table 2.3). This data was compared to the numerically calculated wear, and the experimental data reflects the numerical results. In addition to the wear volume, the experimental wear scar diameters were also found to match the numerical results closely, for bulk lubricant oil temperatures of both of 51°C (Fig. 2.11 and Table 2.2) and 59°C (Fig. 2.13 and Table 2.4). The simulations show a gradual decrease in wear rate with increasing time and total wear (Fig. 2.9); this is primarily caused by a reduction in friction heating density (Eqn. 2.36) due to the increase in contact area as the wear scar diameter increases. As the friction heating density decreases, the lubricant oil temperature decreases, which causes the viscosity and film thickness to increase, and thus gradually reducing the wear. This close match is further verification and validation of

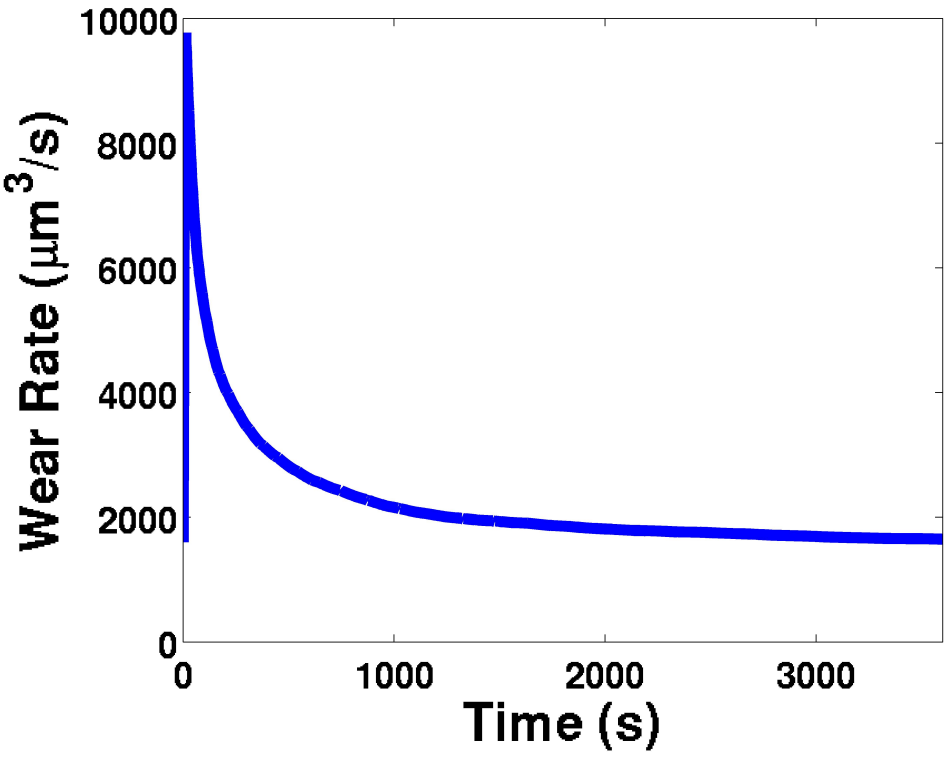

Figure 2.9: The phenomenon of running in, demonstrated from the numerical wear rate (μm^3/s) simulation results for neat mineral oil at a bulk lubricant temperature T = 59°C.

using this numerical approach as a reliable model of four-ball sliding contact tests, and strong evidence of the robustness of this model.

t	SIM	EXP	DEV
10	55	9	71.3
60	289	64	109.7
120	440	112	70.7
300	763	253	23.3
1800	2198	1320	39.2
3600	3657	3360	41.8

Table 2.1: Numerical *SIM* and experimental average *EXP* and % maximum deviation *DEV* wear (10^3 μm^3) data as a function of time (seconds) *t* for neat mineral oil at a bulk lubricant oil temperature of 51°C (Fig. 2.10).

t	SIM	EXP	DEV
60	0.383	0.37	6.3
120	0.425	0.38	7.1
300	0.481	0.44	2.1
1800	0.62	0.6	6.7
3600	0.697	0.72	4.2

Table 2.2: Numerical *SIM* and experimental average *EXP* and % maximum deviation *DEV* wear scar diameter (mm) data as a function of time (seconds) *t* for neat mineral oil at a bulk lubricant oil temperature of 51°C (Fig. 2.11).

Second, a series of 59°C, hour-long, four-ball tests were conducted at varying loads, ranging from 258 to 391 Newtons. It is expected that, with all other parameters consistent, as the load increases, the wear rate will increase, as noticed in Archard's Eqn. 1.1-1.3, and Hamrock-Dowson Eqn. 2.18 and 2.19. All of the simulation-predicted wear volumes (Fig. 2.14 and Table 2.5) and wear scar diameters (Fig. 2.15 and Table 2.6) reasonably match the experimental load-dependent wear rates, and a clear trend of increasing wear with increasing load is observed both numerically and experimentally.

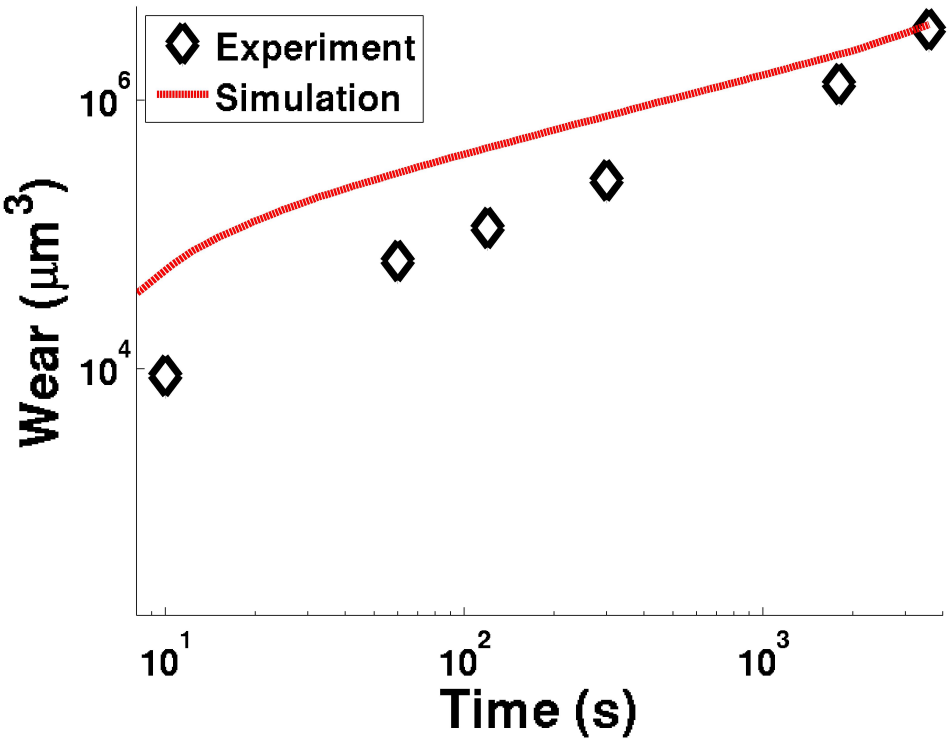

Figure 2.10: Wear (μm^3) experimental data and matching simulation results, for neat mineral oil at a bulk lubricant oil temperature of T = 51°C. Figure data in Table 2.1.

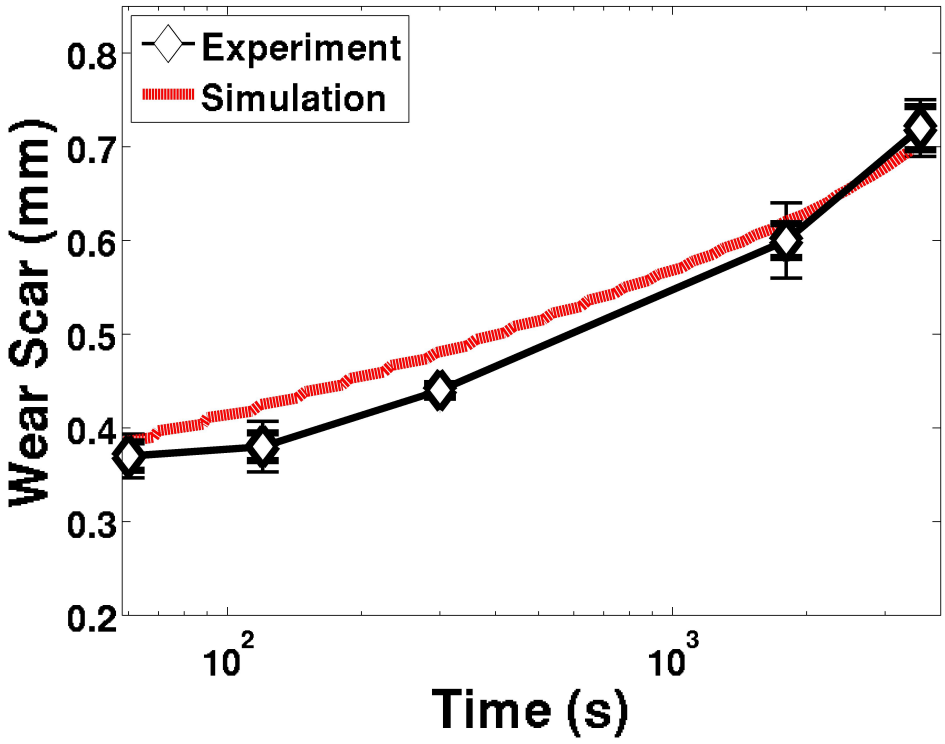

Figure 2.11: Wear scar diameter (mm) experimental data and matching simulation results, for neat mineral oil at a bulk lubricant oil temperature of T = 51°C. Diamonds represent the experimental average wear scar diameter, while error bars represent the average (thick error bars) and maximum (thin error bars) experimental variation of the wear scar diameter observed between all six samples (two repeating tests with three ball bearings each). Figure data in Table 2.2.

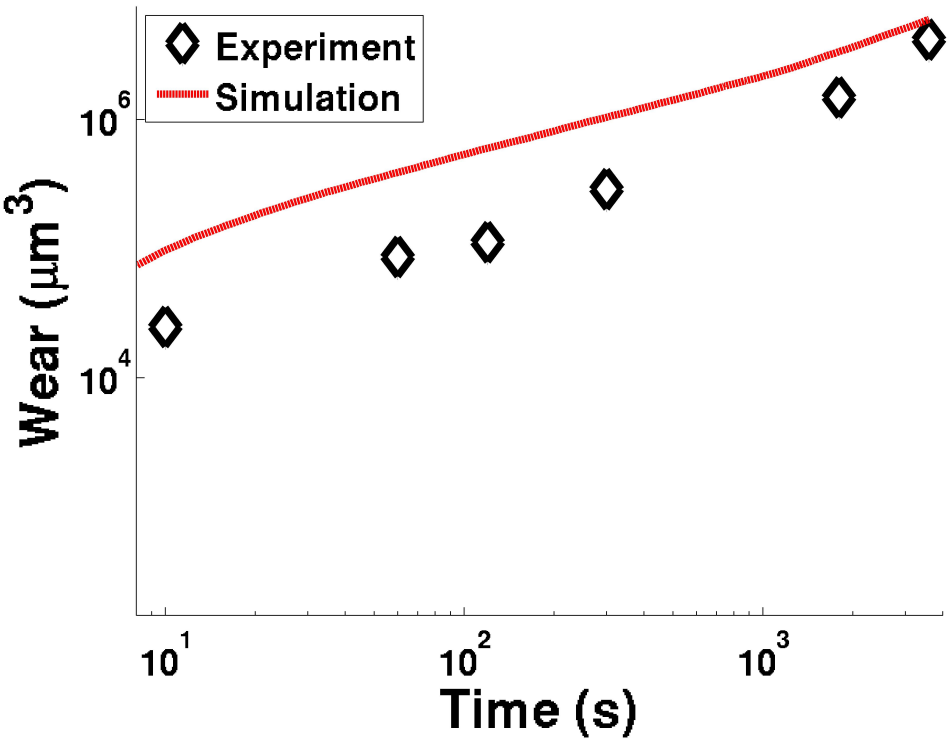

Figure 2.12: Wear (μm^3) experimental data and matching simulation results, for neat mineral oil at a bulk lubricant oil temperature of T = 59°C. Figure data in Table 2.3.

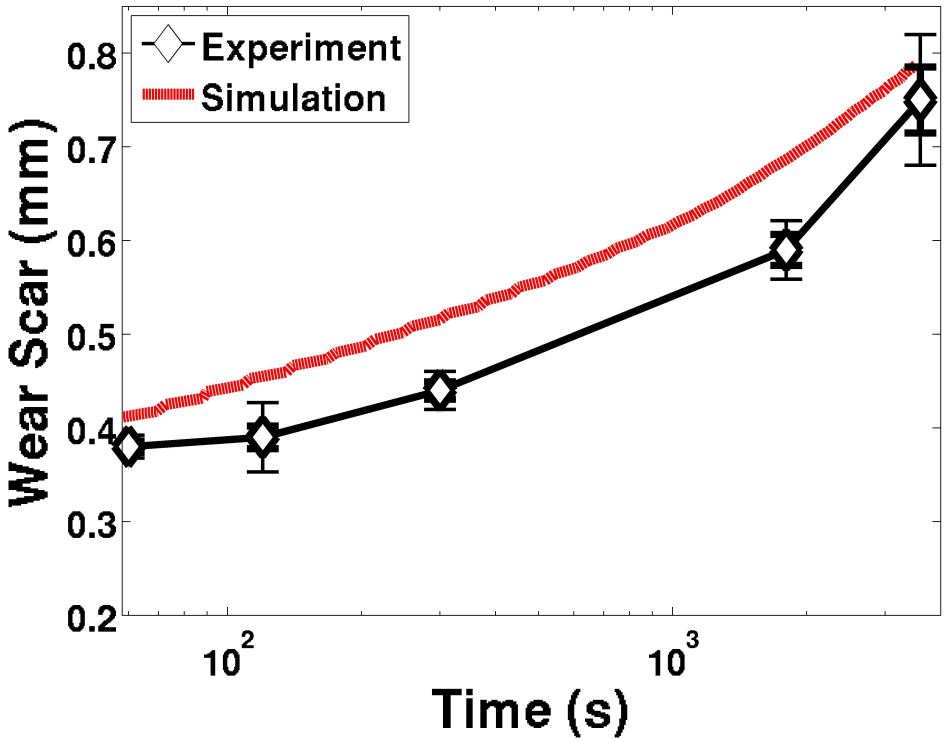

Figure 2.13: Wear scar diameter (mm) experimental data and matching simulation results, for neat mineral oil at a bulk lubricant oil temperature of T = 59°C. Diamonds represent the experimental average wear scar diameter, while error bars represent the average (thick error bars) and maximum (thin error bars) experimental variation of the wear scar diameter observed between all six samples (two repeating tests with three ball bearings each). Figure data in Table 2.4.

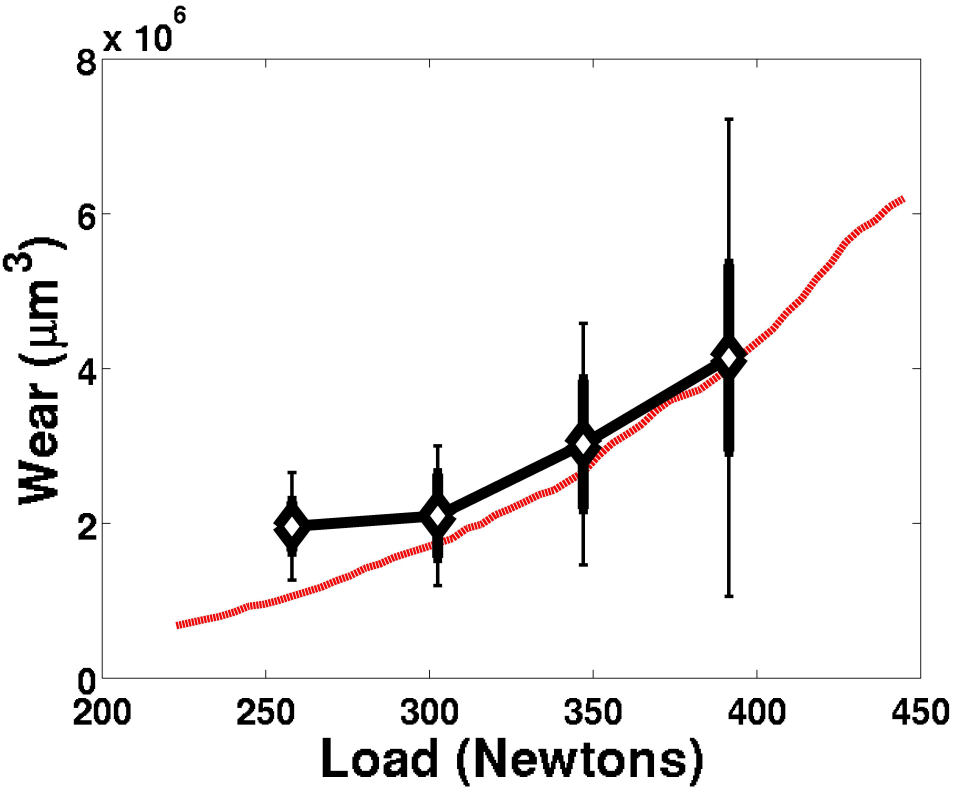

Figure 2.14: Wear (μm^3) experimental data and matching simulation results as a function of load (Newtons). Diamonds represent the experimental average total wear, while error bars represent the average (thick error bars) and maximum (thin error bars) experimental variation of the total wear observed between all six samples (two repeating tests with three ball bearings each). Figure data in Table 2.5.

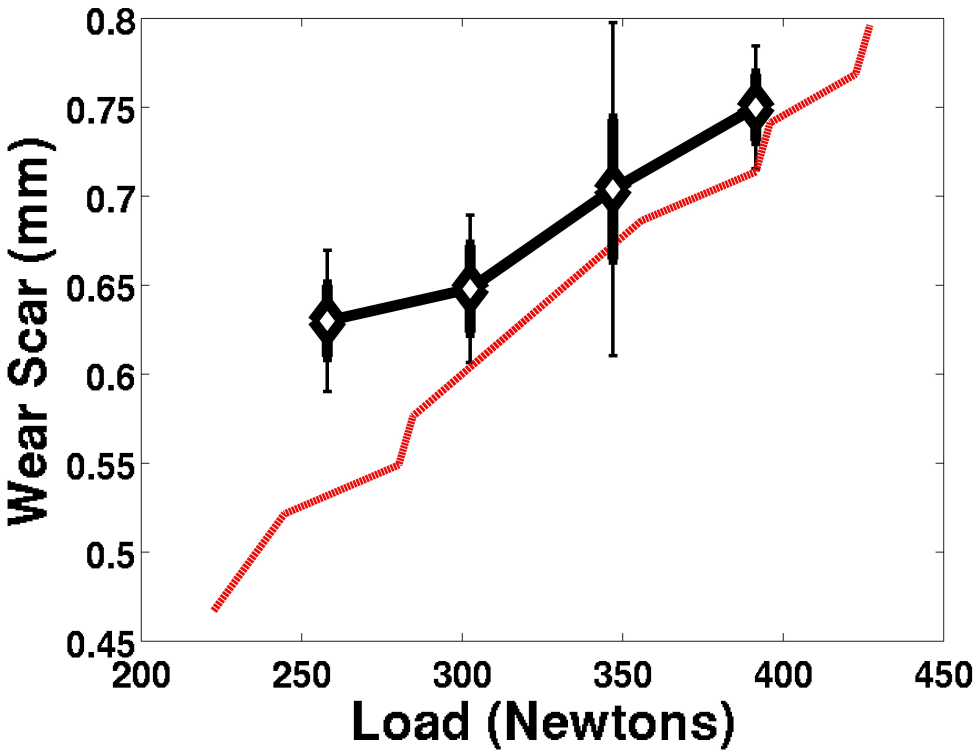

Figure 2.15: Wear scar (mm) experimental data and matching simulation results as a function of load (Newtons). Diamonds represent the experimental average wear scar diameter, while error bars represent the average (thick error bars) and maximum (thin error bars) experimental variation of the wear scar diameter observed between all six samples (two repeating tests with three ball bearings each). Figure data in Table 2.6.

t	SIM	EXP	DEV
10	96	25	84.8
60	392	86	66.7
120	602	112	103
300	1038	288	33.4
1800	3345	1480	34.1
3600	5938	4140	74.5

Table 2.3: Numerical *SIM* and experimental average *EXP* and % maximum deviation *DEV* wear (10^3 μm^3) data as a function of time (seconds) *t* for neat mineral oil at a bulk lubricant oil temperature of 59°C (Fig. 2.12).

t	SIM	EXP	DEV
60	0.411	0.38	3.2
120	0.453	0.39	9.5
300	0.515	0.44	4.6
1800	0.683	0.59	5.3
3600	0.787	0.75	9.3

Table 2.4: Numerical *SIM* and experimental average *EXP* and % maximum deviation *DEV* wear scar diameter (mm) data as a function of time (seconds) *t* for neat mineral oil at a bulk lubricant oil temperature of 59°C (Fig. 2.13).

Finally, a series of hour-long, 391 Newton load, four-ball tests were conducted at varying bulk temperatures, ranging from 44°C to 67°C. It is expected that, with all other parameters consistent, as the bulk temperature increases, the wear volume will increase. The higher temperatures oils will inherently have a reduced viscosity, and a reduction in viscosity will result in a decrease in minimum and central lubricating oil thickness, as noticed in Eqn. 2.18 and Eqn. 2.19. This trend is observed both experimentally and numerically, and the simulation-predicted wear volumes (Fig. 2.16 and Table 2.7) and wear scar diameters (Fig. 2.17 and Table 2.8) reflected the experimental data. This match helps to further establish this model as a robust representation of sliding contact within a four-ball test.

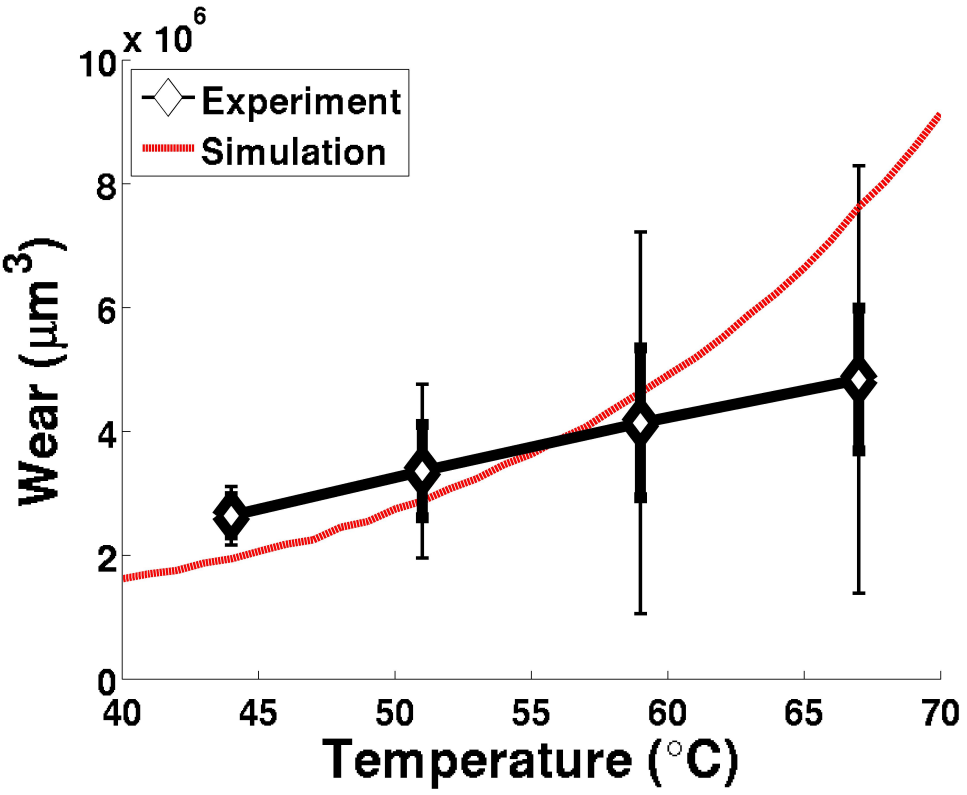

Figure 2.16: Wear (μm^3) experimental data and matching simulation results as a function of bulk lubricant oil temperature (°C). Diamonds represent the experimental average wear, while error bars represent the average (thick error bars) and maximum (thin error bars) experimental variation of the wear observed between all six samples (two repeating tests with three ball bearings each). Figure data in Table 2.7.

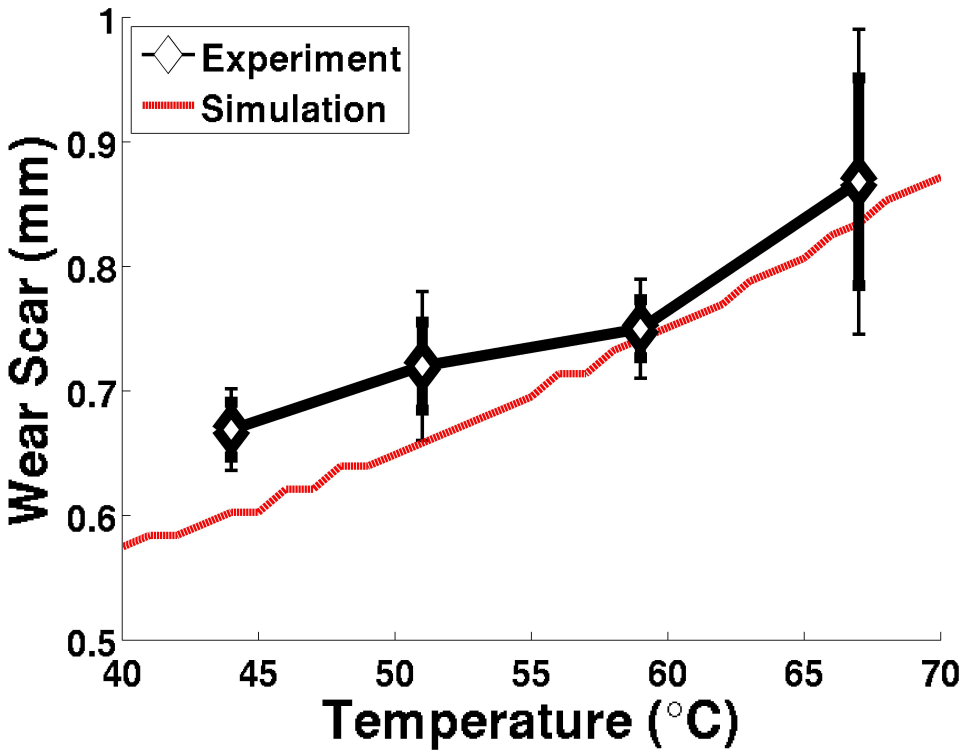

Figure 2.17: Wear scar diameter (mm) experimental data and matching simulation results as a function of bulk lubricant oil temperature (°C). Diamonds represent the experimental average wear scar diameter, while error bars represent the average (thick error bars) and maximum (thin error bars) experimental variation of the wear scar diameter observed between all six samples (two repeating tests with three ball bearings each). Figure data in Table 2.8.

W	SIM	EXP	DEV
258	1.06	1.96	35.4
302	1.74	2.1	43.0
347	2.66	3.02	51.6
391	4.01	4.14	74.5

Table 2.5: Numerical *SIM* and experimental average *EXP* and % maximum deviation *DEV* wear (10^6 μm^3) data as a function of load (Newtons) *W* (Fig. 2.14).

W	SIM	EXP	DEV
258	0.522	0.63	6.3
302	0.576	0.648	6.4
347	0.631	0.704	13.3
391	0.714	0.75	4.6

Table 2.6: Numerical *SIM* and experimental average *EXP* and % maximum deviation *DEV* wear scar diameter (mm) data as a function of load (Newtons) *W* (Fig. 2.15).

2.9 Conclusion

A novel numerical model was developed using established elastohydrodynamic principles. The numerical model used a series of iterations at each time-step in order to successfully converge at an accurate prediction of the pressure distribution, elastic deflection, lubricant film thickness, lubricant temperature, and lubricant viscosity. A Reynolds equation solver was developed to determine the pressure distribution, in conjunction with the Roelands equation to find the viscosity increase with pressure. The Winkler Mattress model was used to predict the elastic deformation of the ball-bearing surface as a result of pressure, and the Hamrock-Dowson empirical equation was used to determine the minimum elastohydrodynamic film thickness at the edge of the contact. Finally, a Monte-Carlo simulation was conducted to predict the wear rate as a result of the ratio of RMS surface roughness over the lubricant oil film thickness, and an empirical exponential equation was

T_B	SIM	EXP	DEV
44	1.9433	2.64	17.9
51	2.8774	3.36	41.8
59	4.631	4.14	74.5
67	7.627	4.84	71.3

Table 2.7: Numerical *SIM* and experimental average *EXP* and % maximum deviation *DEV* wear (10^6 μm^3) data as a function of bulk lubricant oil temperature (°C) T_B for neat mineral oil (Fig. 2.16).

T_B	SIM	EXP	DEV
44	0.603	0.669	4.9
51	0.658	0.72	8.3
59	0.742	0.75	5.3
67	0.834	0.868	14.1

Table 2.8: Numerical *SIM* and experimental average *EXP* and % maximum deviation *DEV* wear scar diameter (mm) data as a function of bulk lubricant oil temperature (°C) T_B for neat mineral oil (Fig. 2.17).

obtained from this numerical study.

A series of four-ball sliding contact tests were conducted to validate this numerical model. The simulated wear predictions reasonably matched experimental trends resulting from variations in time, load, and temperature. Over time, the total wear consistently increased, though the average wear rate would decrease with increasing total wear, primarily due to the decreased friction heating density at the enlarged area of contact. The wear was observed both experimentally and numerically to increase with increasing load, as expected based on Archard's Wear Equation. Finally, as the temperature increased, the viscosity and thus lubricant film thickness would decrease, resulting in an increase in wear; this was observed both numerically and experimentally. With this experimentally validated numerical model, an engineer can substitute extensive parametric four-ball sliding contact tests, which require expensive equipment and significant amounts of time, with cheap and straightforward

parametric simulations; this will reduce the need for excessive experiments and improve overall engineering design.

Chapter 3

DIAMOND NANOPARTICLE CONCENTRATION

TRIBOLOGICAL IMPROVEMENTS OF DISPERSED DIAMOND NANOPARTICLE ADDITIVES IN LUBRICATING MINERAL OIL

3.1 Chapter Abstract

An effort was conducted to study and characterize the effects of diamond nanoparticles as an additive to lubricating mineral oil. The tests were run for varying concentrations ranging from pure mineral oil to 0.01% weight-concentration of diamond nanoparticles. The friction was measured throughout the tests, and the resulting wear was measured with optical profilometry. It was observed that both the average friction coefficient and the wear would decrease proportionally to the concentration of diamond nanoparticles, and the 0.01% diamond nanoparticle weight concentrations was observed to improve the tribological performance of lubricating mineral oil. Chemical analysis of contacting surfaces showed no significant distinction from the diamond nanoparticle mixture versus the pure mineral oil, while particle size analysis demonstrated that the nanoparticles themselves remained intact (i.e., no

breakup) in the contact interface. This helps to conclude that a mechanical and not a chemical effect of the diamond nanoparticles helped to protect the metallic surface from wear and improve the lubricating ability of the mineral oil.

3.2 Introduction

Nanometer (nm) scale particulates have garnered much recent interest as additives to lubricants, and previous observations of diamond nanoparticles have been observed in practice to improve the tribological functions of wear. The causes of this improvement in friction and wear, however, are not well understood. To overcome this, an experimental effort was conducted to characterize the wear and friction reduction properties of varying concentrations of diamond nanoparticle additive. After the four-ball sliding-contact tests were completed, a surface chemistry analysis was conducted on the samples in order to determine if a chemical reaction is responsible for the wear reduction effects. It is hoped that by characterizing the tribological improvements of varying concentrations that a better understanding of the effects of diamond nanoparticles as a lubricant additive can be realized.

3.3 Methodology

Ultra-dispersed diamond (UDD) was obtained and heated for two hours in a 415 °C tube furnace under flowing air to enhance carboxylic acid/anhydride functionalities (ox-UDD) [121, 122]. De-aggregation of the UDD or the ox-UDD to disperse the nanodiamond was accomplished using previously reported methods [122], utilizing dimethyl sulfoxide (DMSO), oleic acid, and octane.

The ox-UDD was dispersed in the chosen mineral oil solvent by an ultrasonic

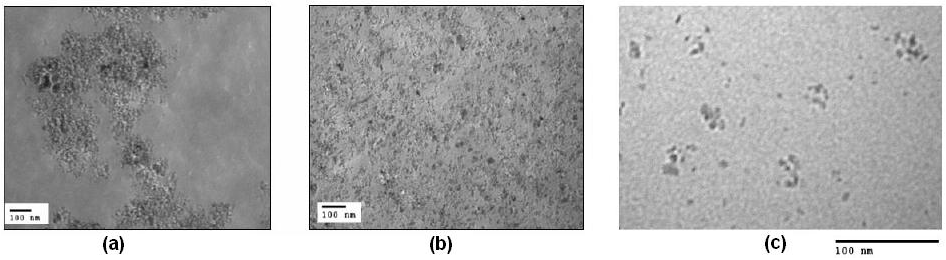

Figure 3.1: TEM images of 60 nm slices of nanocomposites with (a) UDD filler, and (b) nanodiamond filler. (c) TEM image of 40 nm microtome of the vinyl ester composite filled with 3.5% weight concentration nanodiamond-vinyltrimethoxysilane (VTMS).

bath, using a Branson 3510 bench-top sonicator; the density of the neat mineral oil was 869 kg/m^3. The particle size analysis was performed using a Microtrac Nanotrac Ultra dynamic light scattering instrument. Surface studies of the nanodiamond were conducted by Fourier Transform Infrared Spectroscopy (FTIR) on a Thermo Mattson Satellite FTIR with samples prepared in potassium bromide pellets.

A 200-mL round bottom flask was charged with 2 grams of UDD, 2 grams of oleic acid, and 63 grams of octane. The light-gray solution was placed in the ultrasonic bath for one hour. The solution was then subjected to a de-aggregation treatment [122]. This solution of deaggregated nanodiamond, now black but transparent, was combined with an appropriate amount of mineral oil and sonicated for one additional hour. The solution was then placed in a rotary evaporator with an 80°C water bath and approximately 725 mm-Hg of vacuum until the liquid condensation ceased. The final solution (Fig. 3.1) was a mineral-oil pre-blended with 0.01% weight concentration of the nanodiamond additive.

Dynamic Light Scattering (DLS) [123–125] measurements of the mixture were collected prior to tribotesting, with the measurements showing the nano-particules to the monodispersed with an average diameter of 55.7 nm (Fig. 3.2). Spectral absorption measurements were also conducted, in comparison with the clear min-

eral oil, and there was no measureable absorption for any wavelength greater than 43 nm; the smaller the particle the smaller the wavelength can propagate without being absorbed by scattering on the dissolved particles. This measurement was significantly larger than the original nanodiamond size of 5-10 nm, and may have been caused by possible aggregation of the nano-particles as well as the added size from the surfactant shell of oleic acid. Regardless, with this measured particle diameter, an average of over 1.1 trillion nanodiamond particles per mL of mineral oil can be assumed in the mineral oil. This is dramatically more particles than traditional anti-wear additives; commerical Zinc Dialkyl Dithio Phosphate (ZDDP) particles, for instance, often have a diameter of 1-5 μm [126], and thus 6 orders of magnitude fewer particles for the same weight concentration.

Before the test commenced, the viscosity of the test oils (Fig. 3.3) were experimentally measured in order to verify that any change in friction and wear was in fact the result of the diamond nanoparticles, and not necessarily simply the result of changing viscosities due to an increase in density. According to Einstein [99, 100], when solids are mixed with a liquid, the dynamic viscosity μ (Pa-s) enhancement is increased proportional to the volume concentration,

$$\mu = \mu_0(1 + 2.5\phi), \tag{3.1}$$

where ϕ is the volume concentration of the solute. At 0.01% weight concentration, according to Eqn. 3.1, the viscosity will only increase by less than $7{\cdot}10^{-5}$, and therefore no detectable viscosity increase is expected to be observed experimentally. Both the pure mineral oil and the nanodiamond mixture were tested with a Brookfield Lab viscosity meter utilizing an LV2 spindle spinning at 60 r/min. After applying the proper factors, the base mineral oil was found to have (at 25 °C

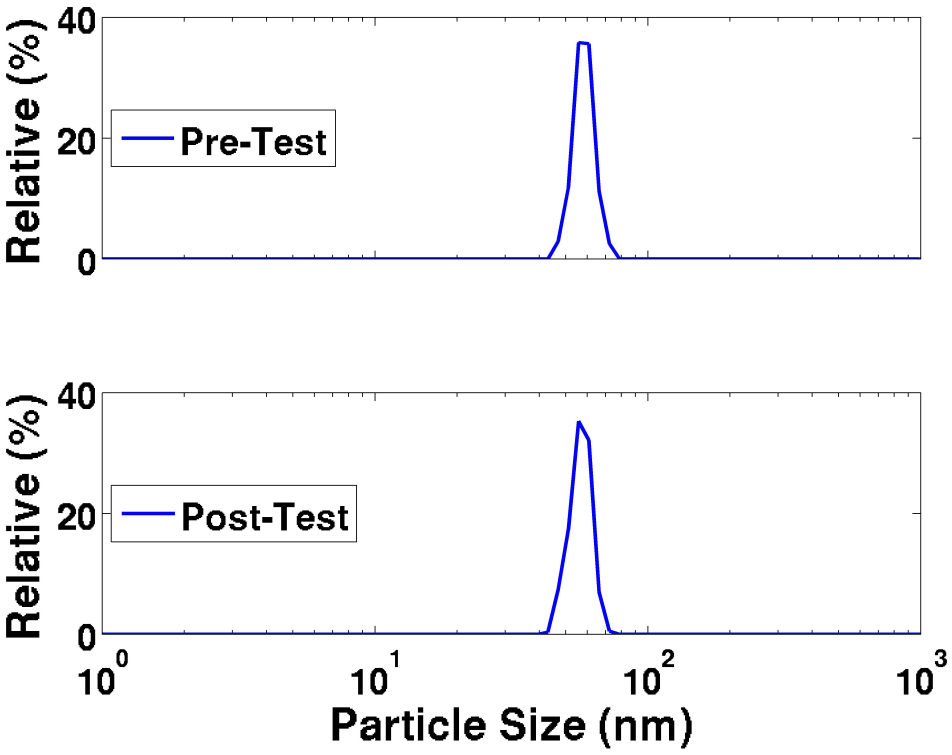

Figure 3.2: Dynamic Light Scattering (DLS) results for the nanodiamond particle diameter, both before and after a four-ball test. The DLS measurement determined both the deflection angle as well as the spectral absorption for a light propagating through the nanodiamond solution.

ambient temperature) a viscosity of 107.5 mPa·s. In contrast, the oil sample with 0.01% weight concentration of nanodiamond had a viscosity of 110.0 mPa·s at the same ambient conditions, representing a negligibly small (2%) increase in viscosity. These tests were repeated for different temperatures, ranging from an ambient temperature of 25 °C to the experimental temperature of 75 °C, and the viscosities remained fairly consistent, with an average error of 11.9%. At the test temperature of 75 °C, it was observed that the nanodiamond solution had a reduction in viscosity of 18.8%; therefore to ascertain that the reduced viscosity was not the cause of the reduction in friction, an additional mineral oil test was conducted at 79 °C, to ensure a lower viscosity. As expected, the friction increased significiantly, demonstrating that the reduction in viscosity by the diamond nanoparticle solution was not the result of the lower viscosity at the test temperature. As a result of these studies, it can be safely assumed that an observed decrease in wear and friction would in-fact be the result of the diamond nanoparticles.

T	**MO**	**ND**
25	105	118.5
30	87.5	76.5
35	65	58.5
40	50.5	43
45	41.5	36
50	32.5	30.5
55	28.5	25.5
60	24.5	24.5
65	21.5	23
70	19	16
74	17	13.5
75	16	13

Table 3.1: Experimental measurements of kinematic viscosity (mm^2/s) as a function of temperature T (°C), for mineral oil *MO* and 0.01% diamond nanoparticle *ND* weight concentration (Fig. 3.3).

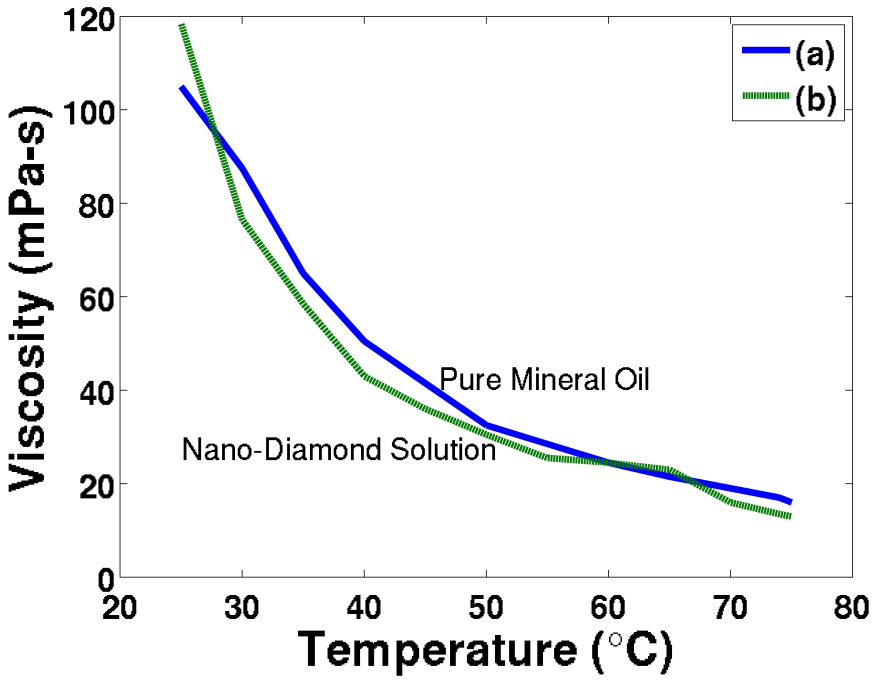

Figure 3.3: Experimental measurements of viscosity as a function of temperature, for (a) mineral oil and (b) 0.01% diamond nanoparticle weight concentration. Figure data in Table 3.1.

The test that was conducted was the American Society for Testing and Materials (ASTM) D-4172 Four-Ball Test [43]. Except for the diamond nanoparticle weight concentration in the lubricant, all of the test parameters, including duration, load, spindle speed, temperature, etc, were consistent for all the tests studied. In this test, the lubricant was varied from standard mineral oil alone to the mineral oil with 0.01% weight concentration of diamond nanoparticles; the concentration was diluted by proportional blending of standard mineral oil.

The four-ball test was set to consistently run at 1200 r/min for 60 minutes, with a load of 391 Newtons of force. The oil was set at a consistent temperature of 74 °C, and no test ever got above a maximum temperature of 77 °C. The four-ball test was conducted with the standard mineral-oil, the 0.01% weight concentration of nanodiamond, and mixtures of half, a quarter, and an eighth nanodiamond solution, to give a nanodiamond weight concentration of 0%, 0.00125%, 0.0025%, 0.005%, and 0.01%. Each test was conducted at least twice, and the base mineral-oil and 0.01% nanodiamond samples were tested at least four times. In all of the tests, COF was recorded throughout the duration of the tests.

3.4 Results and Discussion

In each of the four-ball tests, the torque was recorded in real time throughout the entire duration of the test; this torque data was used to calculate the COF between the lubricated ball bearings. Tests that had excessive variation and/or an abnormally high average COF were discarded. It was regularly observed that the COF would gradually ramp up over the first 50-100 seconds (Fig. 3.4); the top ball would reach the terminal speed of 1200 r/min in a fraction of this time. This phenomenon occurred with all the lubricants, ranging from the straight mineral-oil to

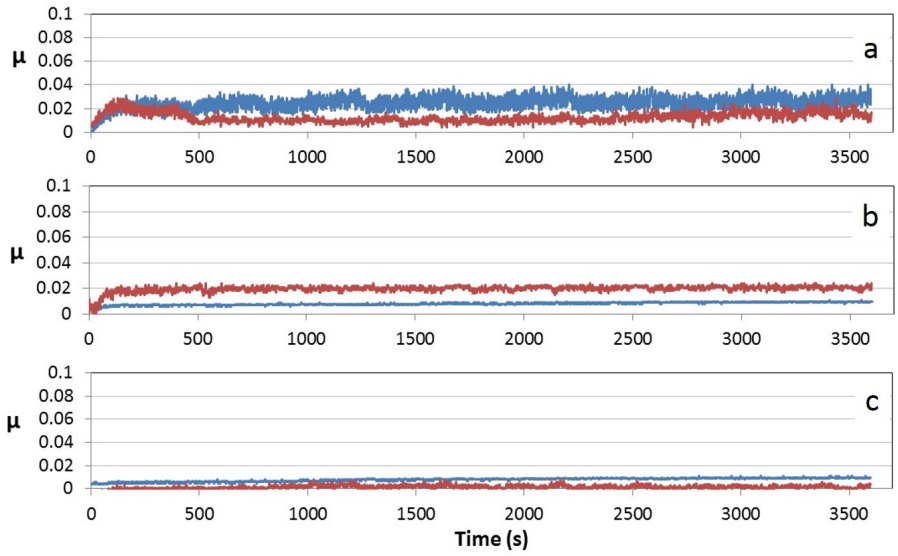

Figure 3.4: Time resolved measured COF throughout four-ball test, lubricated with (a) mineral oil, (b) mineral oil with 0.0025% nanodiamond weight concentration, and (c) mineral oil with 0.01% nanodiamond weight concentration.

the 0.01% weight nanodiamond solution, and is believed to be the result of tribological running-in between the ball bearings [10]. After this time, the frictional torque reached a steady-state level, and was constant throughout the duration of the test. The fluctuations in COF were noticeably greater for the pure mineral oil, as compared to the nanodiamond mixtures. This was most likely due to the decreased level of surface contact that occurred with the nanodiamond-containing oil.

χ	$\mu_{\mathbf{COF}}$	**STD**
0.00	0.0188556272	0.0078984959
0.125	0.0286238668	0.0086075331
0.25	0.0139575749	0.0060621476
0.50	0.0062795191	0.0017785783
1.00	0.0047925245	0.0036722504

Table 3.2: Experimentally measured COF average μ_{COF} and standard deviation *STD* as a function of nanodiamond weight concentration χ (10^{-4}); see Fig. 3.5.

An analysis of the average steady-state friction as a function of nanodiamond

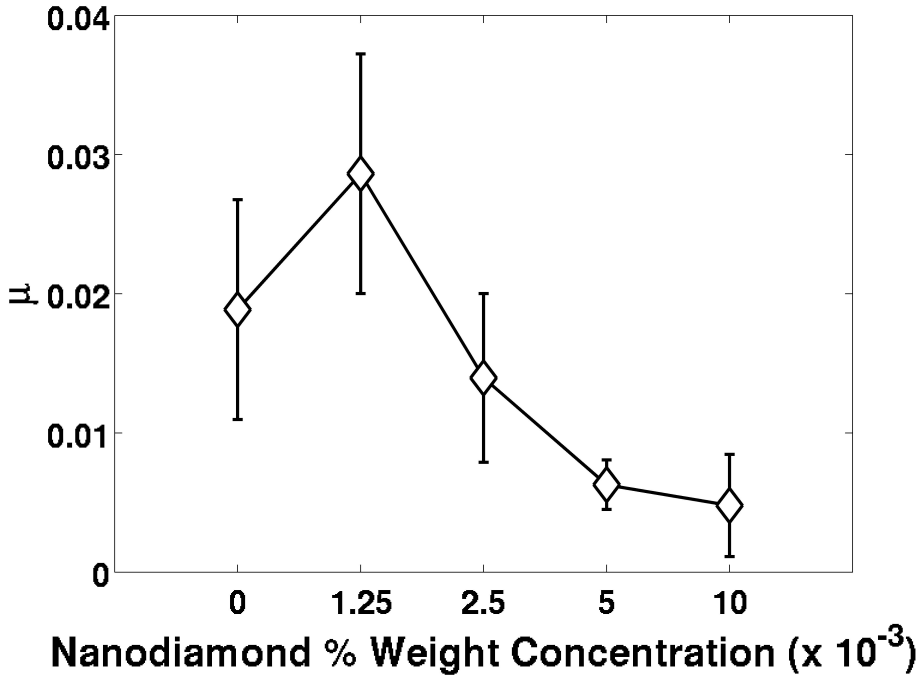

Figure 3.5: Experimentally measured COF as a function of nanodiamond weight concentration. Diamonds represent the average, and error bars represent the standard deviation of the experimental data. Figure data in Table 3.2.

concentration has demonstrated that the friction reduced proportionally with increasing concentration of nanodiamond particles (Fig. 3.5). Pure mineral-oil tests had an average COF of 0.02, whereas the 0.01% weight concentration of nanodiamond tests were reduced to less than a quarter of this friction. Increasing the nanodiamond concentration reduced the COF to a rate in between the mineral-oil and the 0.01% weight concentration. The only exception to this trend was between the straight mineral-oil and the 0.00125% weight concentration; the slight addition of nanodiamonds at first increased the friction. This increase was very small and was observed only by averaging the tests; there were specific tests where straight mineral-oil had more friction than the 0.00125% weight concentration nanodiamond. With a very low concentration of nanodiamond particles, it is plausible that an uneven pattern of hard nanodiamond particles acted as further asperities on the surface of the ball-bearings, and would explain this slight increase in the COF. Regardless, it was very clear that a 0.01% nanodiamond weight concentration as an additive to mineral oil clearly serves to reduce the friction when measured with a four ball-test.

After the tests were completed, some samples were used for FTIR surface characterizations (Fig. 3.6) on the wear scars (taking care to ensure the lubricating oil remaining on the ball). Both the 0.01% weight nanodiamond sample as well as the pure mineral-oil were studied. Comparing the FTIR spectras, it is observed that, compared to the non-processed straight nanodiamond samples (Fig. 3.6-a), the surface functionalization procedure (Fig. 3.6-b) is effective in increasing the presence of C-H bonding on the surface of the nanoparticle. The absorbance peaks at 2850 and 2900 cm^{-1} for the surface functionalized nanodiamond are much stronger than for the non-processed straight nanodiamond.

Again, these absorbance peaks associated with C-H chains is found in the min-

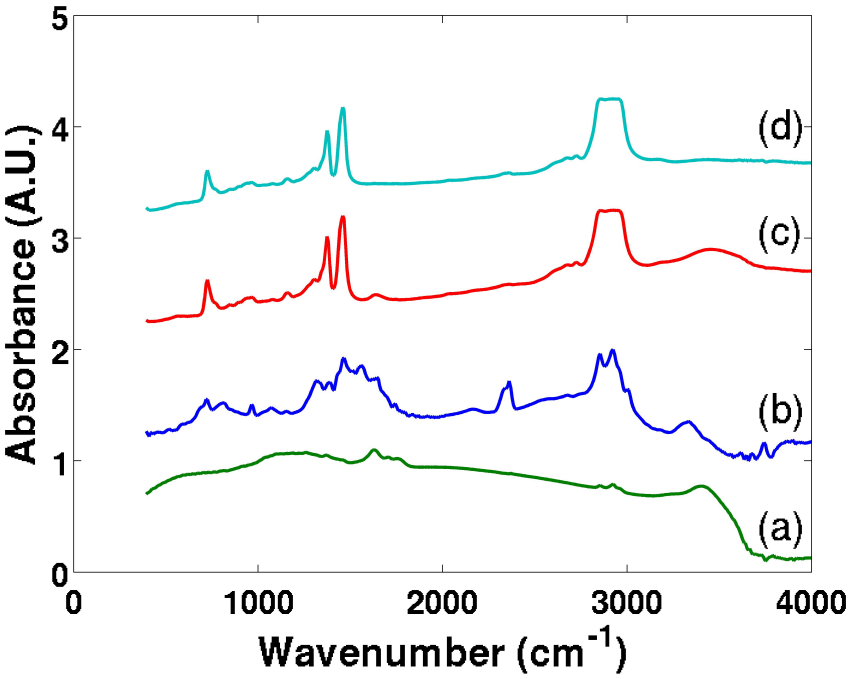

Figure 3.6: FTIR spectra of (a) straight nanodiamond as received from the manufacturer, (b) surface-functionalized nanodiamond during additive synthesis, (c) mineral oil without nanodiamond additive after four-ball testing, and (d) mineral oil containing dispersed nanodiamond particles after four-ball testing.

eral oil sample (as expected). The plateaus observed for these samples near 3000 cm^{-1} is likely due to signal saturation. The peaks at 1380 and 1460 cm^{-1} are assigned to the methyl and methylene bonds, respectively. Comparison between the spectra for (Fig. 3.6-c) and (Fig. 3.6-d), the samples of neat mineral oil without and with the nanodiamond additive, respectively, does not indicate any observable difference in the data. This is not unexpected when considering the extremely low dosing of the nanoparticles and the surface-functionalization of the nanoparticles closely matches the chemical structure of the mineral oil molecules.

In addition, the DLS measurements of the used mineral oil with the nanodiamond additive after a four-ball test was compared with pre-test solution (Fig. 3.2). The data suggested a very slight decrease in average particle size after the four-ball test; however, this change was too small to be considered a significant change. This phenomenon was noticed in both the scattering angle as well as the spectral absorption measurements.

Next, XPS measurements were conducted of the wear scars on the test samples after a four-ball test with both the pure mineral oil and nanodiamond mixture, as well as the surface of ball bearings that were never tested. The XPS results provide information of the chemical composition of the top surface (10 nm or less deep), expressed as a function of chemical excitation energy. It was observed in the wide surveying scans that both the nanodiamond mixture and pure mineral oil have extremely similar chemical composition based on identical peak excitation energy (Fig. 3.7) at 284.77 eV. This was solved using the Shirley background algorithm [127] and XPSPEAK Version 4.1. In addition, it was clear that the largest peaks for the surface compositions were around 284-286 eV, which is representative of carbon. Focusing the XPS data has demonstrated that there is very little ($<3\%$) embedded nanodiamond particles at the 285.2 eV sp2-carbon excitation en-

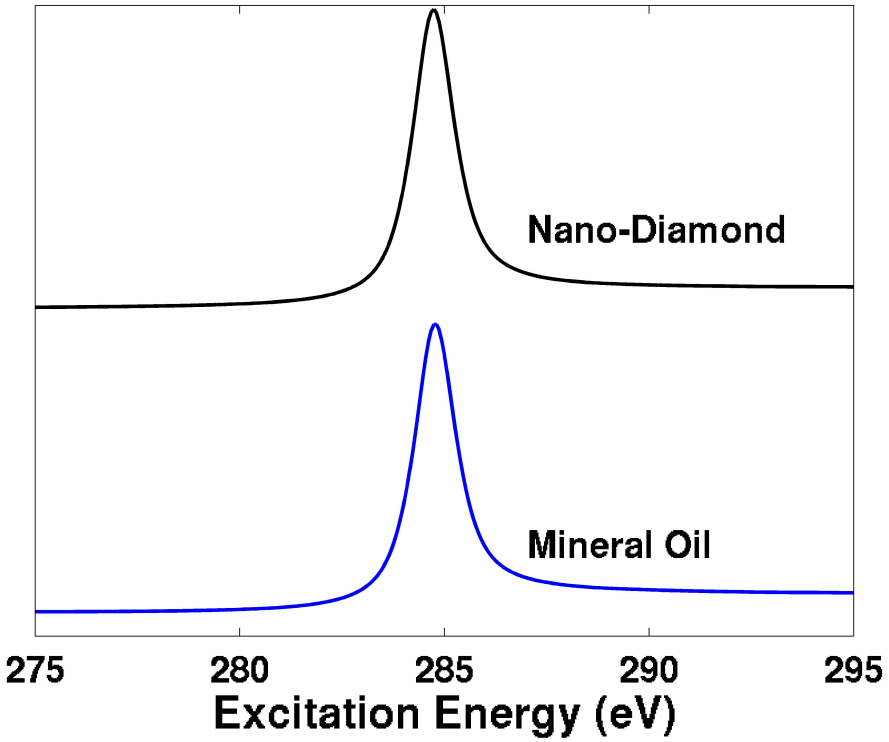

Figure 3.7: Calculated peak from high-analysis study near the excitation energy of carbon. Study includes both the wear scar after a mineral oil four-ball test (blue) and the wear scar after the nanodiamond four-ball test (black). The peaks were solved with the Shirley background function.

ergy [128, 129]. Because of this, it can be confirmed that any tribological changes between the pure mineral oil versus the the nanodiamond mixture is a result of a mechanical, and not a chemical, phenomenon.

Finally, after each test, all three ball-bearings were cleaned of oil and profiled with an optical profilometer. The wear scar diameters were measured microscopically using the profilometer's objective lenses (Fig. 3.8), in order to ensure a consistent diameter for each of the three ball bearings. If the wear-scar diameters were found to vary more than 40 μm from the average wear-scar diameter, the test was discarded. A masking algorithm was then performed on the optical profilometer

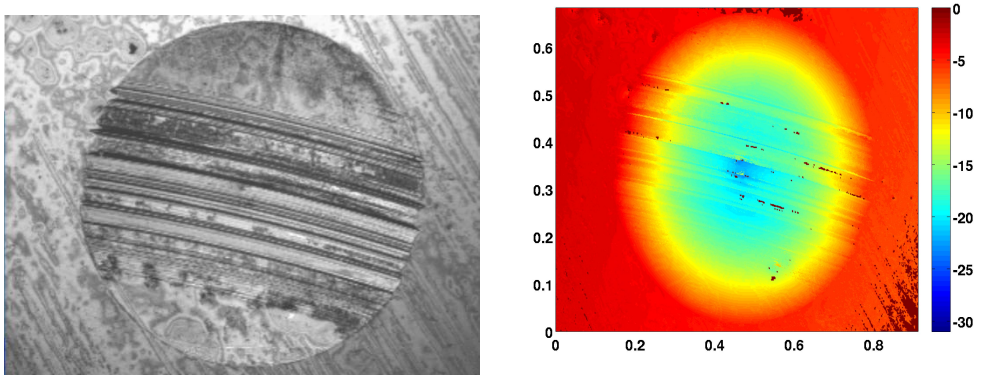

(a) **(b)**

Figure 3.8: Results of the Zygo profile-meter after a 0.01% weight concentration nanodiamond four-ball test, including (a) the microscopic image of the wear scar, (b) the 3D measured profile; X and Z labels are in millimeters, colorbar represents micrometers of wear.

data, in order to isolate the wear scar and determine the true material wear; the wear of each individual ball-bearing was averaged for each test.

It was observed in the profilometer data that, just like with the friction coefficient, the average wear followed a trend of decreasing with an increase in nanodiamond concentration (Fig. 3.9, 3.10, and 3.11). The exception to this trend, also in line with the friction analysis, was between pure mineral-oil and the 0.00125% nanodiamond weight concentrations. The wear depth typically ranged from 6 to 18 μm, and while there was a lot of variation, the depth generally followed the trend of being shallower for increased nanodiamond concentrations.

χ	**V**	**STD**
0.00	2.1608333333	0.4169904802
0.125	2.4016666667	0.6350879204
0.25	1.7616666667	0.22692877
0.50	1.5833333333	0.3854694108
1.0	1.2480049517	0.2494873936

Table 3.3: Measured wear volume ($10^6 \mu\mathrm{m}^3$) average *V* and standard deviation *STD* as a function of nanodiamond weight concentration χ (10^{-4}); see Fig. 3.10.

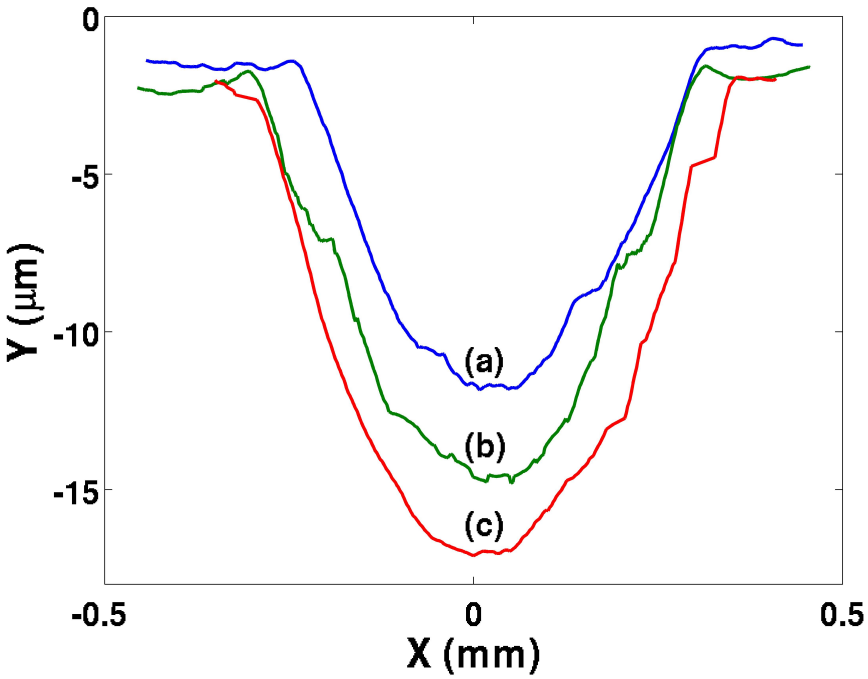

Figure 3.9: Measured profiles of wear scars, for (a) 0.01% nanodiamond weight concentration, (b) 0.0025% nanodiamond weight concentration, and (c) neat mineral oil.

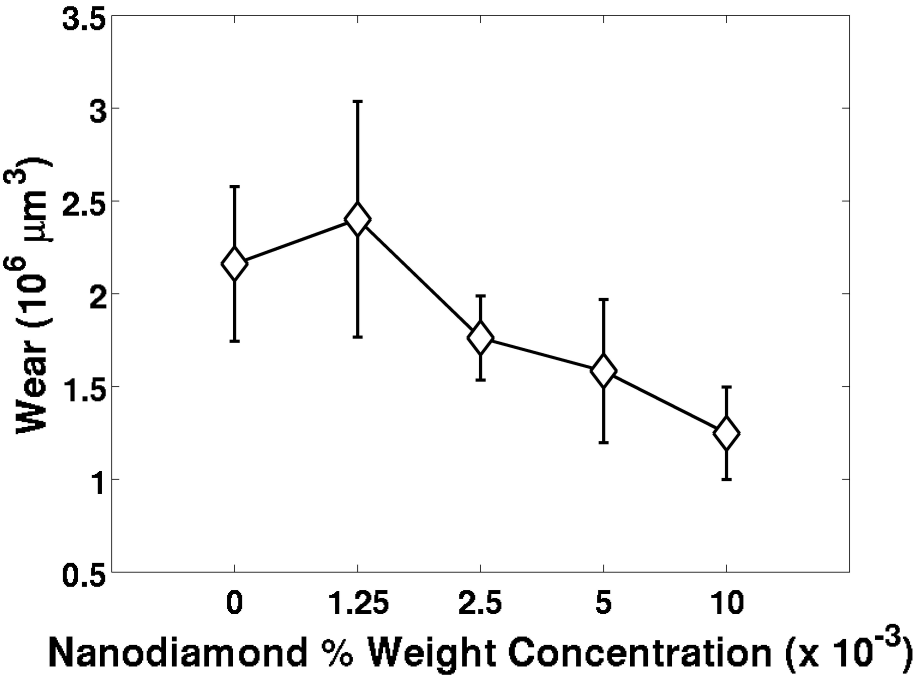

Figure 3.10: Measured wear volume as a function of nanodiamond weight concentration. Diamonds represent the average, and error bars represent the standard deviation of the experimental data. Figure data in Table 3.3.

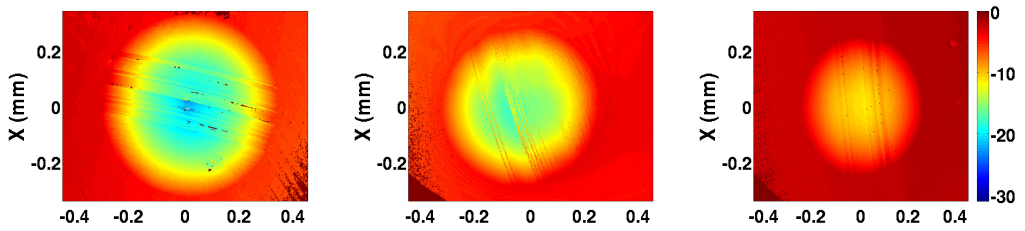

Figure 3.11: Experimental optical profilometer data of wear-scars for (a) neat mineral oil, (b) 0.005% diamond nanoparticle solution, and (c) 0.01% diamond nanoparticle solution.

The surface roughness (Fig. 3.12) was also analyzed after measurement with the optical profilometer. The RMS roughness of the wear scar was found to be 0.4135 μm for the 0.01% nanodiamond sample, as compared to 0.5876 μm for the base mineral oil. The surface roughness and standard deviation of the diluted (less than 0.01% weight concentration) samples were significantly higher; the increased surface roughness is possibly due to an increasingly uneven distribution of nanodiamond particles that may occur at lower concentrations. A two-tailed paired Student's T-test was performed on the data, and it can be concluded with a confidence of 98.68% that the 0.01% nanodiamond weight concentration reduced the surface roughness when compared to pure mineral oil.

χ	σ	**STD**
0.00	0.587583	0.1666714014
0.125	0.84583	0.2177970194
0.25	0.6285	0.1041857716
0.50	1.4067	0.5452545889
1.00	0.4135	0.0339628473

Table 3.4: RMS Surface Roughness (m) average σ and standard deviation *STD* of wear scars as a function of nanodiamond weight concentration χ (10^{-4}); see Fig. 3.12.

Additional T-tests were conducted to compare the differences in COF and wear

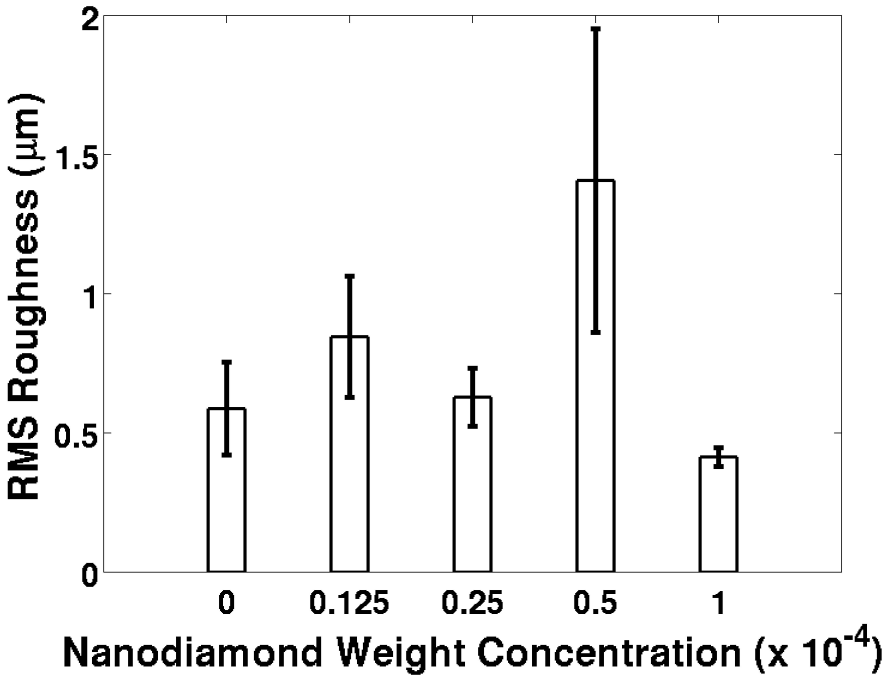

Figure 3.12: RMS Surface Roughness of wear scars. Clear bars represent average roughness, whereas error bars represent standard deviation of roughness, as a function of nanodiamond weight concentration. Figure data in Table 3.4.

between the 0.01% weight nanodiamond test-results compared to the base mineral-oil test-results. By counting the average wear of each four-ball test, and not necessarily the wear of each individual ball bearing, it was determined with over 99% confidence that the 0.01% nanodiamond weight concentration will in fact reduce COF and material wear. This four-ball study has demonstrated the practical benefits of using nanodiamond particles as an additive to lubricating mineral oil, as it was observed to reduce the friction, reduce the material wear, and improve overall tribological properties.

3.5 Conclusion

The study has demonstrated with statistical confidence that the nanodiamond particles as an additive to mineral oil can reduce wear and friction in the presence of sliding contact. Increasing the concentration of nanodiamond particles demonstrated a proportional improvement in tribological performance. This is believed to be a mechanical, and not a chemical, phenomenon; the average lubricant oil temperatures never exceeded 77°C, so rehybridization is not expected; and XPS measurements of the wear scars demonstrated that there were no chemical distinctions between tests with both pure mineral oil and the nanodiamond mixture. This experimental study demonstrated that nanodiamond additive may offer improved tribological properties of diamond to critical sliding surface interfaces.

Chapter 4

THERMAL EFFECTS OF NANOPARTICLES

NUMERICAL AND EXPERIMENTAL TRIBOLOGICAL INVESTIGATIONS OF THE THERMAL EFFECTS OF DIAMOND NANOPARTICLES

4.1 Chapter Abstract

An effort was made to study and characterize the tribological characteristics of diamond nanoparticles as compared to neat mineral oil in the presence of sliding contact typically observed in the standard ASTM D4172 four-ball test. Four-ball tests were conducted with a solution of diamond nanoparticles and mineral-oil, both at varying run times and bulk-oil temperatures, and a consistent reduction in wear rates was observed. Numerical simulations were performed; it was observed that by enhancing the thermal conductivity of the lubricant, the wear reduction rate was observed to match the diamond nanoparticles solution results remarkably. This effort provides evidence that this additive wear reduction is in-part caused by reduced lubricant temperatures due to the enhanced conductivity of diamond.

4.2 Introduction

In the preceding chapters, both a novel numerical model was developed and experimentally verified in order to simulate the sliding contact observed in a four-ball test; afterwards the effects of various concentrations of diamond nanoparticles as an additive to lubricant mineral oil were studied. This chapter is a cumulation of these two efforts, where the numerical model is used in conjunction with the diamond nanoparticle experimental data, in order to better ascertain the causes of the wear reduction properties. In addition to the concentration studies, four-ball studies with varying times and lubricant temperatures are conducted with the same 0.01% diamond nanoparticle solution fabricated in Section 3.3. With the extensive experimental data and the enhanced numerical analysis, a better understanding of the causes of wear reduction from the nanoparticle additive can be developed.

4.3 Modeling Diamond Nanoparticles

In the case of the nanoparticles fabricated in this effort [1, 122], Dynamic Light Scattering (DLS) measurements have demonstrated that the average particle diameter to be approximately 55.7 nm both before and after a four-ball test. This is significantly larger than the original diamond nanoparticles, and the increase has occurred because of an orbiting shell of the dispersant materials used in the fabrication process. Because the average RMS surface roughness of a pre-test ball bearing specimen was only 100 nm, it is not believed that the wear reduction is caused by merely filling in the voids caused by surface asperities. In addition, with this nanoparticle diameter and a diamond nanoparticle weight concentration of 0.01%, assuming a 1 μm oil film thickness (in practice even smaller) and the most evenly

spread distribution of particles on the surface, only 0.0691% of the area of contact would be coated with diamond nanoparticles; this weight concentration has been verified at significantly reducing the wear rates [1]. For this reason, this effort will focus on thermal effects and how temperature reduction for the enhanced lubricant thermal conductivity might be a significant cause for the reduction of wear by these diamond nanoparticles.

In order to better ascertain the causes of the reduction in wear due to diamond nanoparticles, this effort will seek to numerically simulate a four-ball test, and modify the model parameters to accurately reflect the enhancement in thermal conductivity of the lubricant oil as a result of the highly-conductive nanoparticle solution. This can help to better ascertain the causes of wear reduction, and help to develop an approach to numerical modeling and simulations of wear in the presence of thermally conductive nanoparticles in sliding contact.

In order to realize the elastohydrodynamic film thickness, it is necessary to determine the dynamic viscosity of the lubricant. The viscosity of the lubricant, however, is affected by temperature [83, 91, 98–100], as hotter oils are inherently less viscous. A reduction in viscosity results in a reduced minimum film thickness [18], but this reduced film thickness results in a cooler oil film [82], as there is less thermal resistance from the center of the oil film to the surface of the ball bearing. As a result of this contradiction, it is necessary to use iteration in order to converge on a realistic lubricant oil temperature and viscosity, so that a minimum film thickness can be determined.

The first step is to calculate the flash temperature heating of the surface of the ball bearing. The dimensionless Peclet number [20, 82] from Eqn. 2.24 is first calculated. Once the dimensionless Peclet number L is known, one can calculate the average flash temperature [102–105], which is defined as the temperature that

results from the high-pressure and friction heating, using the predictive analytical equation (Eqn. 2.26) used by this model for average flash temperature, which can vary with Peclet number [20, 82]. Once the surface temperature is known, the average lubricant oil temperature can be found with Eqn. 2.37, which applies to circular contacts, and it was derived by Archard in 1958 [82] in order to match experimental studies conducted by Crook [108].

The lubricant temperature can be used to calculate the average viscosity [20, 83], utilizing Eqn. 2.38. To find the coefficients of this equation, it is necessary to measure the kinematic viscosity at two temperature points, and calculating the experimental Z-value with Eqn. 2.39, and then obtaining the viscosity coefficients with Eqn. 2.40. Once the kinematic viscosity at the temperature of interest is determined, the dynamic viscosity can easily be calculated with Eqn. 2.41 [109], and this value can be used to calculate the minimum and central film thickness using the Hamrock-Dowson [18] empirical equations (Eqn. 2.18 and 2.19).

According to Eqn. 2.37, it is clear that the oil temperature increase is linearly proportional to the film thickness; while Eqn. 2.18 shows how a decrease in viscosity (such as from an increase in temperature) would reduce the film thickness. For this reason, iteration is needed to converge on a final lubricant temperature, viscosity, and minimum film thickness. An average film thickness is *guessed* with Eqn. 2.19, and the predicted temperature increase is calculated with Eqn. 2.37, which is used for the predicted viscosity (Eqn. 2.38). This iterative loops repeats itself until it converges at a final value for the lubricant oil temperature and viscosity, which is used in Eqn. 2.18 [18] for the minimum film thickness value, which is necessary for the Reynolds equation solver [84–96] in Section 2.5 in order to find the full film-thickness function, and predict the wear rate.

4.4 Temperature Modeling of Conductivity

By looking at Eqn. 2.37, it is clear that the temperature rise from friction heating at the area of contact is inversely proportional to the thermal conductivity k_{lub} of the lubricant. Neat mineral oil inherently is a thermal insulator, with a low thermal conductivity of approximately 0.14 W/m·°C [101]. Diamond, however, is one of the most thermally conductive materials on earth [66–68]; and conductivities of 2190 W/m·°C can be expected for natural diamond [69]. Much like graphite can be used as an additive to paraffin oil to enhance the thermal conductivity [63–65], it can be expected that an addition of diamond to mineral oil will enhance the lubricant thermal conductivity. It has been observed experimentally that the thermal conductivity of a liquid-liquid mixture is proportional to the mass concentration [72],

$$k_{solution} = (1-\chi)\cdot k_{solvent} + \chi \cdot k_{solute}, \tag{4.1}$$

where k_{solute}, $k_{solvent}$, and $k_{solution}$ are the effective thermal conductivities (W/m·°C) of the solute, solvent, and solution of a liquid-liquid mixture with a solute mass ratio of χ. With a 0.01% weight concentration of diamond nanoparticles, if the additive were treated as a liquid, the effective thermal conductivity of the lubricant solution can be predicted to rise to 0.359 (W/m·°C), an increase of over 150%.

For a liquid-solid particle mixture, however, the thermal conductivity enhancement is substantially less than liquid-liquid. While there are several equations for the equivalent thermal conductivity [73], probably the most well-established is the

Maxwell-Carnot [130],

$$\frac{k_{solution}}{k_{solvent}} = 1 + \frac{3(k_{pf}-1)\phi}{(k_{pf}+2)-(k_{pf}-1)\phi}, \qquad (4.2)$$
$$k_{pf} = \frac{k_{solute}}{k_{solvent}},$$

where ϕ is the volume fraction. With a weight concentration of 0.01%, which leads to a volume concentration of $2.566{\cdot}10^{-5}$, a thermal conductivity increase of only $(1 + 7.696{\cdot}10^{-5}){\cdot}k_{oil}$ is expected; effectively a negligible increase.

For nanometer scale particles, however, higher thermal conductivity enhancements significantly higher than the Maxwell-Carnot predicted rate were observed, both for aluminum and copper oxide nanoparticles [73], and even for diamond nanoparticles [70, 71]. At the nanometer scale, several phenomenons are expected to occur [74–81], such as Brownian Motion, where the nanoparticles experience random motion after collisions and interactions with the molecules of the lubricant oil solvent.

The thermal conductivity was observed for several weight concentrations, including 0.01%, and the conductivity enhancement was found to follow an Arrhenius-like temperature dependence,

$$k_{solution} = k_{solute}{\cdot}[1 + \frac{K_0}{100} exp(\frac{E'_A}{k_B T_B})], \qquad (4.3)$$

where k_B is the Boltzmann constant ($1.38{\cdot}10^{-23}$ Joules / Kelvin), E'_A (Joules) is the activation energy, T_B is the bulk lubricant temperature (must be in Kelvin), and K_0 is an experimentally realized constant. For 0.01% weight concentration, the activation energy was measured to be $E'_A = -41{\cdot}10^{-21}$ (Joules), and the constant was fitted to be $K_0 = 9{\cdot}10^4$.

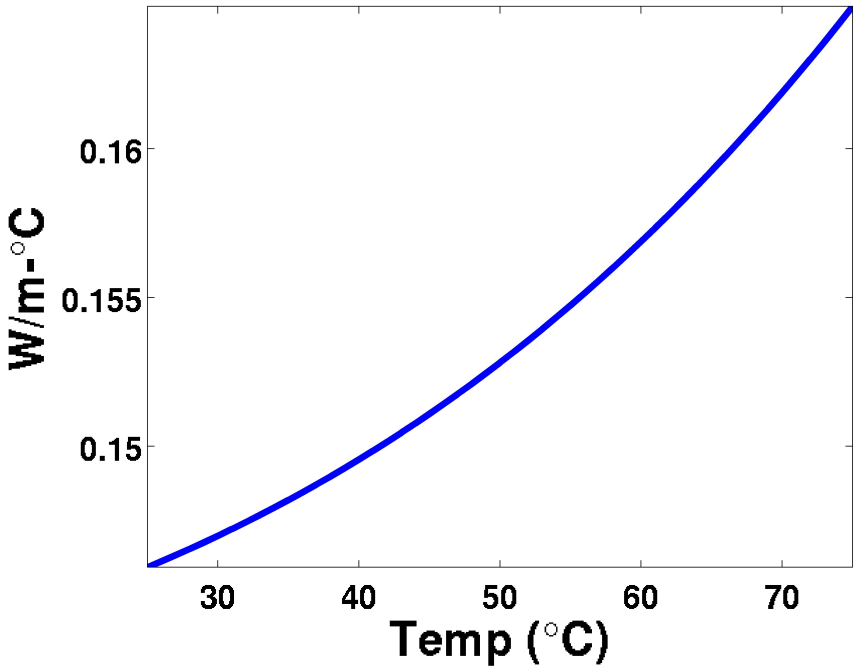

Figure 4.1: Lubricant thermal conductivity (W/m·°C) for 0.01% weight concentration of mineral oil, as a function of temperature (°C). Figure data in Table 4.1.

T	$\mathbf{k_{lub}}$
25	0.14593
35	0.14819
45	0.15109
55	0.15473
65	0.15926
75	0.16479

Table 4.1: Lubricant thermal conductivity k_{lub} (W/m·°C) for 0.01% weight concentration of mineral oil, as a function of temperature *T* (°C); see Fig. 4.1.

Part of this effort will focus on the effects of varying concentrations of diamond nanoparticles; all of the concentrations tested were fabricated by mixing proportional ratios of neat mineral oil with the 0.01% sample fabricated as described in Section 3.3. In order to determine the conductivity of a specified concentration, the model first finds the thermal conductivity for 0.01% weight concentration of diamond nanoparticle additive using Eqn. 4.3. Next, the thermal conductivity is balanced with the mixed lubricant mass ratio (Eqn. 4.1); it is valid as two liquids, the neat mineral oil and the 0.01% solution, are in fact mixed together for the final lubricant. The final thermal conductivity can thus be easily found,

$$k_{lub} = k_{oil}\cdot[1 + \frac{\chi}{10^{-4}}\frac{K_0}{100}exp(\frac{E'_A}{k_B T_B})], \tag{4.4}$$

where k_{lub} (W/m·°C) is the effective lubricant thermal conductivity, k_{oil} (W/m·°C) is the thermal conductivity of the neat mineral oil free of any diamond nanoparticle additives, and χ is the dimensionless mass concentration of the diamond nanoparticles.

Wear occurs when a random asperity exceeds both the film thickness height plus the yield length from Eqn. 2.73. This can be characterized as the dimensionless λ_W-value (Eqn. 2.74), and this parameter is proportional to the wear according

to Archard's Wear Eqn. 1.3 [15]. Wear would occur whenever a random asperity exceeds a certain λ_W-value, which represents the ratio of roughness standard deviations that contact occurs. The lower the λ_W-value, the higher the probability of an asperity exceeding this film thickness height, and thus the more wear would occur. A prior Monte Carlo study has yielded Eqn. 2.76 and 2.78, a straightforward function for the transient wear rate $\dot{V}$ (m^3/s) as a function of λ_W.

It is apparent from Eqn. 2.76 that the larger the value of λ_W, the less wear can be expected. As λ_W is directly proportional to the film thickness (Eqn. 2.74), it stands that the thicker the lubricant film, the less wear will occur; this is also represented in the variation of Archards Eqn. 1.3. One way to increase the film thickness at the region of contact is to reduce the temperature of the oil, which results in a viscosity increase that also increases the minimum (Eqn. 2.18) and central (Eqn. 2.19) film thickness, thus reducing wear. As an increase in thermal conductivity inverse proportionally reduces the average temperature increase of the film thickness (Eqn. 2.37), increasing the diamond nanoparticle concentration is expected to reduce the lubricant temperature, increase the viscosity and film thickness, and reduce the wear (Fig. 4.2).

A parametric numerical study was conducted of four-ball sliding-contact tests, at the standard [43] parameters of a bulk lubricant oil temperature of 74°C, a runtime of 3600 seconds, and a load of 391 Newtons. The effective lubricant thermal conductivity was adjusted to the mass ratio's (Eqn. 4.4) of the neat mineral oil and the diamond nanoparticle solution. The parametric study was run from no additive up to 0.01% weight concentration, and the results remarkably match the previously obtained concentration data in Fig. 4.3 and Table 4.2 [1].

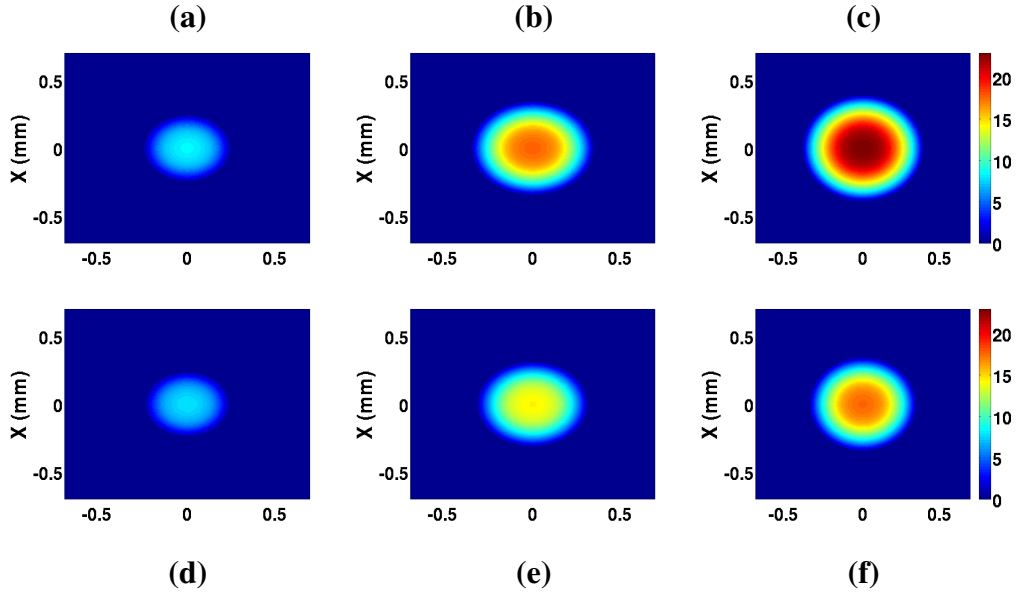

Figure 4.2: Simulation wear scar profiles after 3600 seconds of sliding contact for neat mineral oil at (a) T = 25°C, (b) T = 51°C, and (c) T = 59°C; and for 0.01% diamond nanoparticles solution at (d) T = 25°C, (e) T = 51°C, and (f) T = 59°C. Color-bar represents the wear depth in μm.

4.5 Experiment

A series of four-ball [43] sliding contact tests were conducted with both neat mineral oil and diamond nanoparticles solution to experimentally characterize the wear over varying temperatures and lengths of time. The four-ball tests were set to consistently run at 1200 r/min, ramped up with an angular acceleration of 100 r/min per second, and with a consistent load of 391 Newtons of force. Two series of tests were conducted, the first in time variation and the second in temperature variation. For the first series of tests, the run time for each test was varied for different times to characterize the evolution of the wear; run-times used include 10, 60, 120, 300, 1800, and 3600 seconds after the test speed of 1200 r/min was reached. Throughout the time-variation experimental tests, the lubricating oil, both with and without the diamond nanoparticles, was set at a consistent temperature of both 51°C and 59°C;

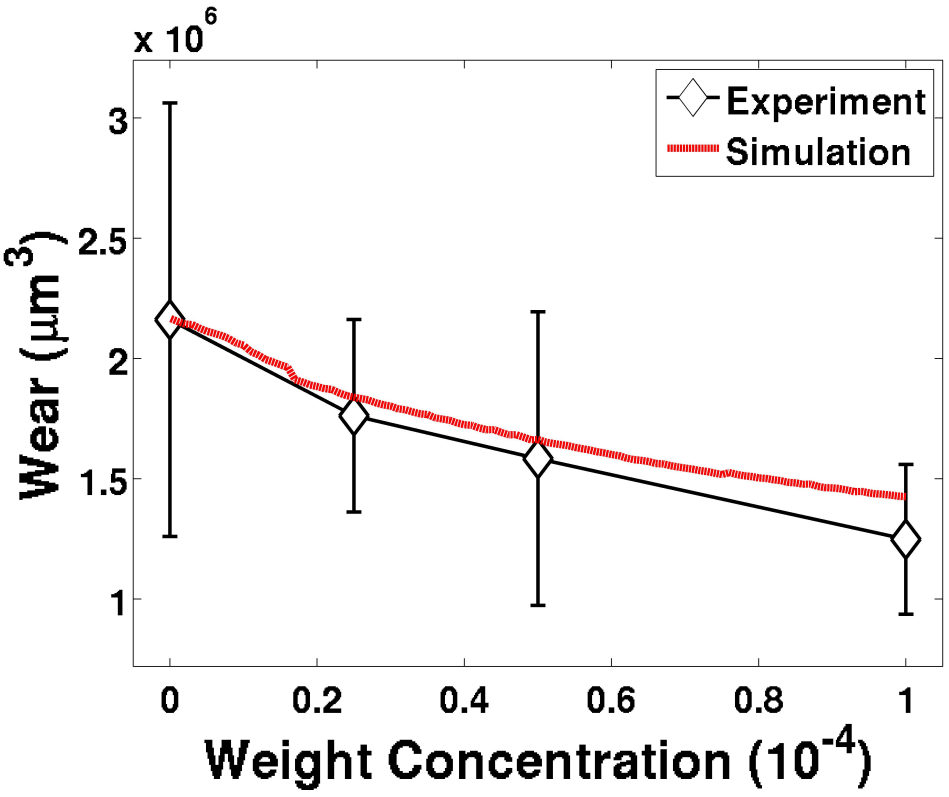

Figure 4.3: Experimental [1] and numerical wear (μm^3) data as a function of diamond nanoparticle weight concentration. Diamonds represent the average experimental wear, and error bars represent the experimental standard deviation. Figure data in Table 4.2.

χ	**SIM**	**EXP**	**STD**
0.0	2.17	2.1608	41.7
0.25	1.84	1.7617	22.7
0.5	1.66	1.5833	38.5
1.0	1.43	1.248	24.9

Table 4.2: Numerical *SIM* and experimental average *EXP* and % standard deviation *STD* [1] wear (10^6 μm^3) data as a function of diamond nanoparticle weight concentration χ (10^{-4}); see Fig. 4.3.

PID controllers and convection fans were used to maintain the temperature in the presence of flash heating. The second series of tests were all conducted at the full run-time of 3600 seconds, but with a variation of the bulk oil temperature at 44°C, 51°C, 59°C, and 67°C. Finally, every test was completed twice under identical circumstances, to ensure repeatability of the results.

4.6 Results

The numerical model, which was verified to work with neat mineral oil, was performed with the enhanced thermal conductivity of the nanoparticle solution, and the simulation results were found to match the diamond nanoparticles experimental data remarkably for both the wear volume (Fig. 4.4 and Table 4.3) and the wear scar diameter (Fig. 4.5 and Table 4.4). At all four temperature points (44°C, 51°C, 59°C, and 67°C), the predicted average wear rate from the numerical model consistently fell within the experimental variation (represented by the error bars) of the diamond nanoparticles four-ball tests. The experimental data had an average wear reduction of 35.76% (Fig. 4.6-a); the numerical simulations matched this trend (Fig. 4.6-b). This profound reduction in wear is visibly noticeable in the wear scar profile comparison in Figure 4.2.

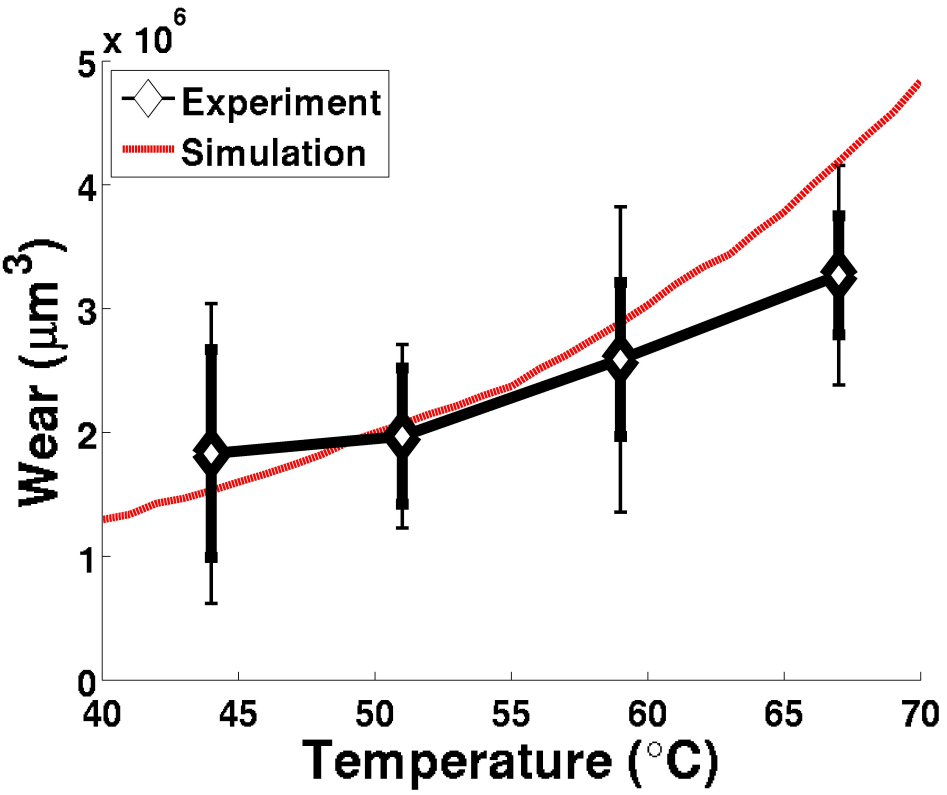

Figure 4.4: Experimental and numerical results of wear studies as a function of bulk lubricant oil temperatures ranging from T = 44°C to 67°C, for 0.01% diamond nanoparticles solution. Diamonds represent the experimental average wear, while error bars represent the average (thick error bars) and maximum (thin error bars) experimental variation of the wear observed between all six samples (two repeating tests with three ball bearings each). Figure data in Table 4.3.

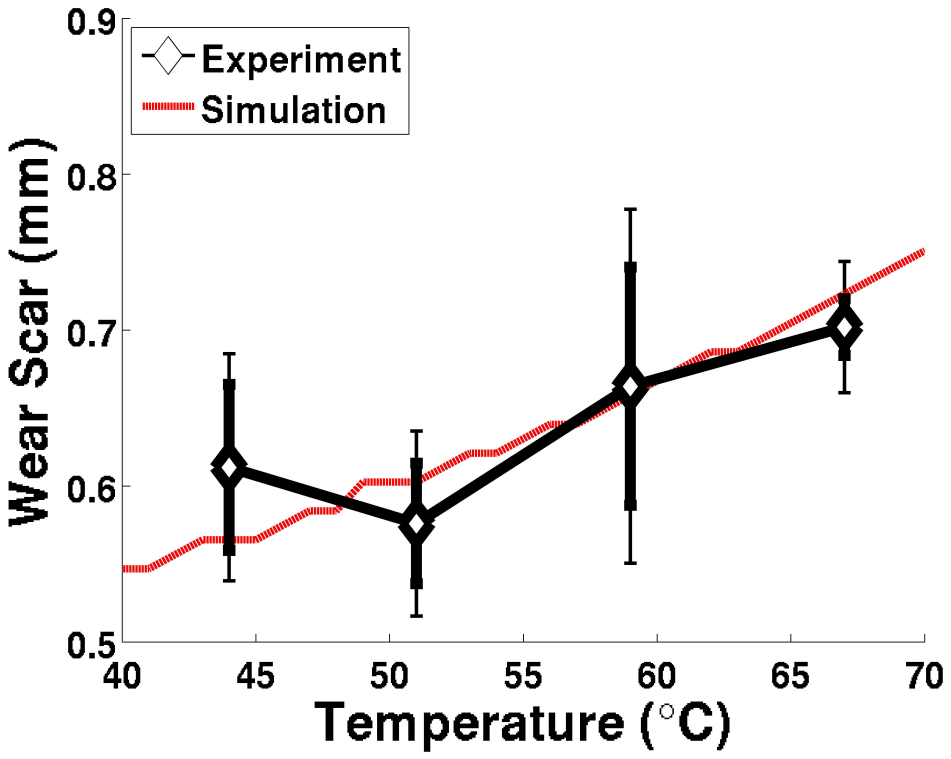

Figure 4.5: Experimental and numerical results of wear scar diameter (mm) studies as a function of bulk lubricant oil temperatures ranging from T = 44°C to 67°C, for 0.01% diamond nanoparticles solution. Diamonds represent the experimental average wear scar diameter, while error bars represent the average (thick error bars) and maximum (thin error bars) experimental variation of the wear scar diameter observed between all six samples (two repeating tests with three ball bearings each). Figure data in Table 4.4.

T_B	SIM	EXP	DEV
44	1.5311	1.83	66.2
51	2.0685	1.97	37.6
59	2.8861	2.59	47.6
67	4.1893	3.27	27.1

Table 4.3: Numerical *SIM* and experimental average *EXP* and % maximum deviation *DEV* wear (10^3 μm^6) data as a function of bulk lubricant oil temperature (°C) T_B for 0.01% diamond nanoparticle solution (Fig. 4.4).

T_B	SIM	EXP	DEV
44	0.566	0.612	11.9
51	0.603	0.576	10.3
59	0.658	0.664	17.1
67	0.723	0.702	6

Table 4.4: Numerical *SIM* and experimental average *EXP* and % maximum deviation *DEV* wear scar diameter (mm) data as a function of bulk lubricant oil temperature (°C) T_B for 0.01% diamond nanoparticle solution (Fig. 4.5).

The second phase of this experimental effort was to conduct wear evolution studies of the diamond nanoparticles solution, where four-ball tests were conducted for varying lengths of time. A series of run times ranging from 10 seconds to a full hour were conducted at both T = 51°C (Fig. 4.7 and Table 4.5) and T = 59°C (Fig. 4.9 and Table 4.7), and the numerical simulations of the 0.01% diamond nanoparticle weight concentration accurately reflected the experimental data. This numerical model was previously validated experimentally with wear evolution simulations of neat mineral oil. In addition to the wear volume, the experimental wear scar diameters were also found to match the numerical results closely, for bulk lubricant oil temperatures of both of 51°C (Fig. 4.8 and Table 4.6) and 59°C (Fig. 4.10 and Table 4.8). The close matches of this numerical model with nanoparticle-enhanced lubricant thermal conductivity provides further validation of using the thermal material properties of diamond to model the wear reducing tribological effects of diamond

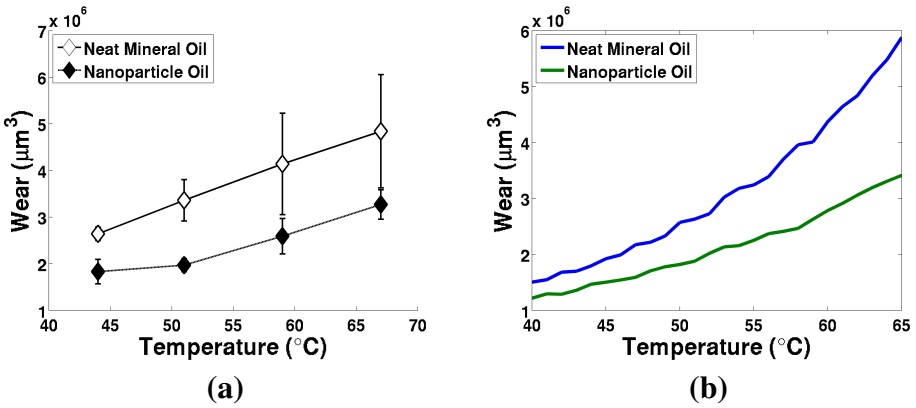

Figure 4.6: (a) Experimental and (b) numerical results of wear studies as a function of bulk lubricant oil temperatures ranging from T = 44°C to 67°C, for both neat mineral oil and 0.01% diamond nanoparticles solution. Experimental error bars represent the standard deviation.

nanoparticles as an additives to lubricating mineral oil.

t	SIM	EXP	DEV
10	34	6	109.8
60	235	61	85
120	362	115	46.8
300	612	268	24.4
1800	1655	1660	23.2
3600	2467	2590	47.6

Table 4.5: Numerical *SIM* and experimental average *EXP* and % maximum deviation *DEV* wear (10^3 μm^3) data as a function of time (seconds) *t* for 0.01% diamond nanoparticle solution at a bulk lubricant oil temperature of 51°C (Fig. 4.7).

4.7 Conclusion

This effort has managed to successfully collect four-ball experimental tests of mineral oil with an additive of diamond nanoparticles that has been demonstrated to reduce wear [1]. The experimental effort included both variating the lubricating oil bulk temperature over trials of 3600 seconds, as well as varying the run-times

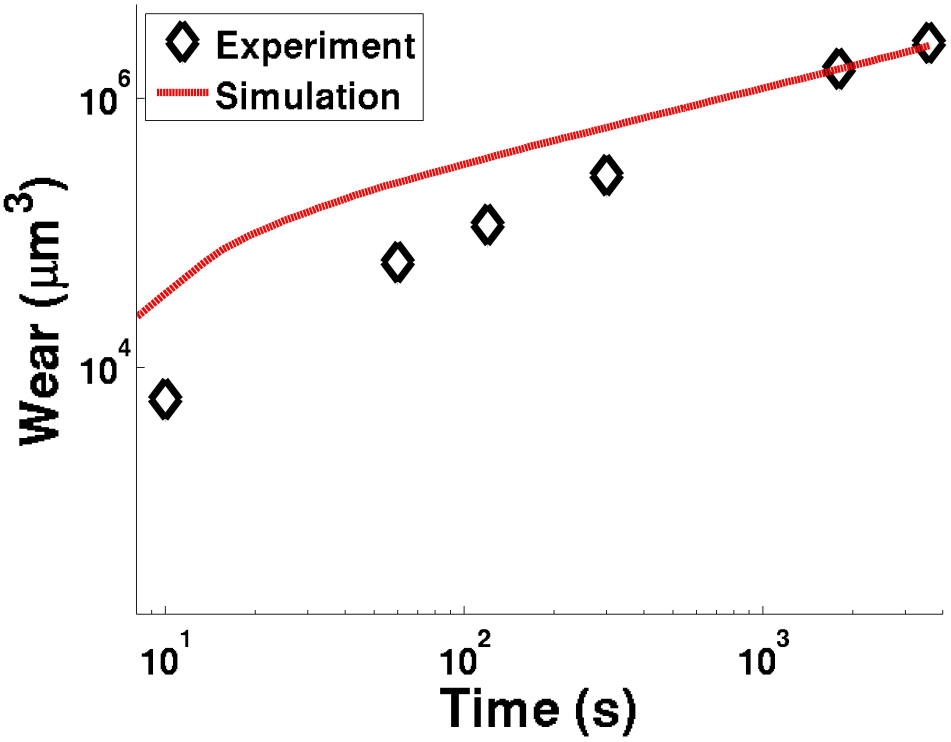

Figure 4.7: Experimental and numerical results of wear evolution studies of diamond nanoparticle solution, at a constant bulk lubricant oil temperature of T = 51°C. Figure data in Table 4.5.

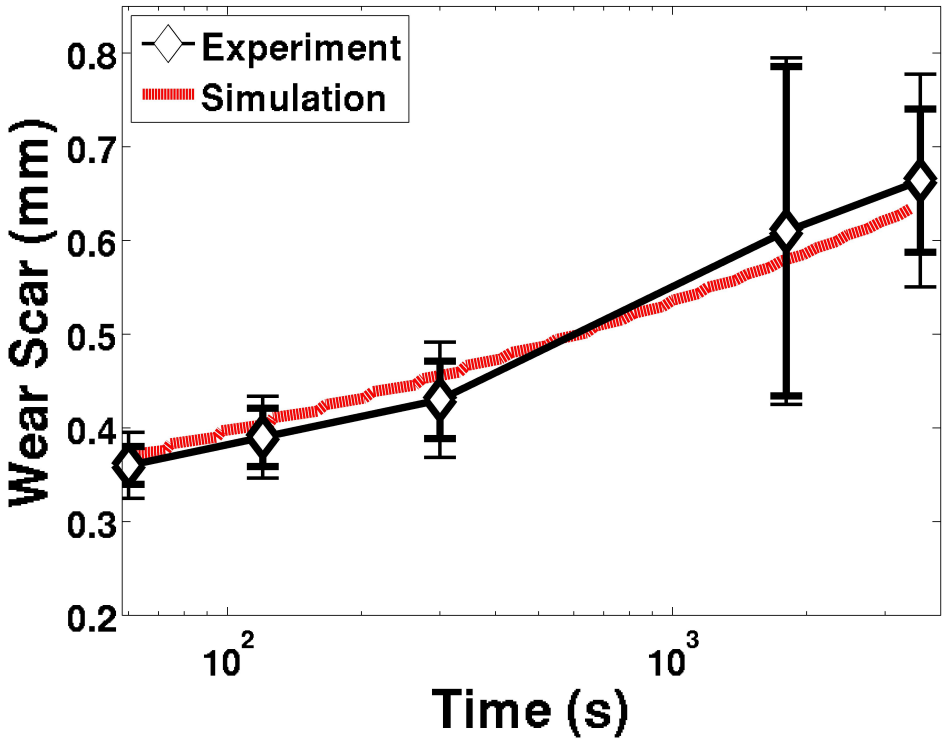

Figure 4.8: Wear scar diameter (mm) experimental data and matching simulation results, for 0.01% diamond nanoparticle solution at a bulk lubricant oil temperature of T = 51°C. Diamonds represent the experimental average wear, while error bars represent the average (thick error bars) and maximum (thin error bars) experimental variation of the wear observed between all six samples (two repeating tests with three ball bearings each). Figure data in Table 4.6.

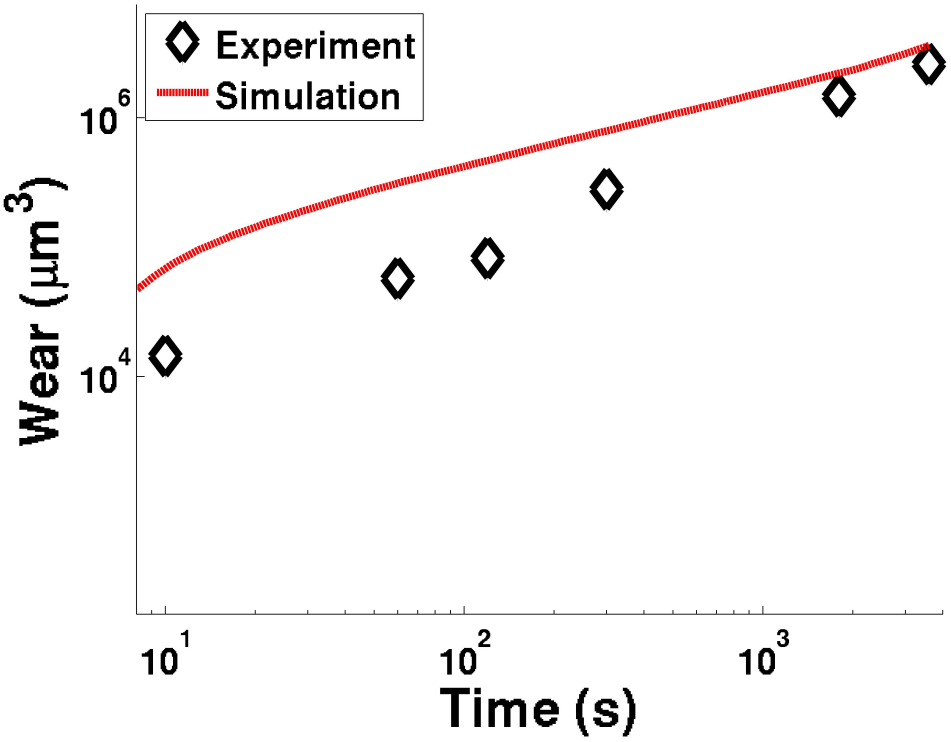

Figure 4.9: Experimental and numerical results of wear evolution studies of diamond nanoparticle solution, at a constant bulk lubricant oil temperature of T = 59°C. Figure data in Table 4.7.

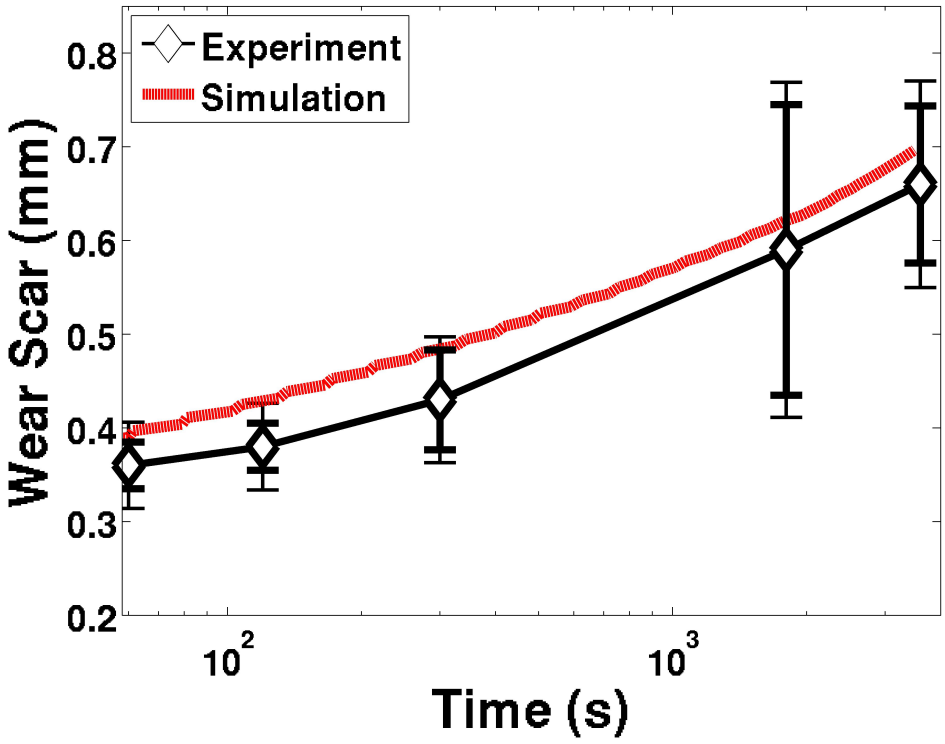

Figure 4.10: Wear scar diameter (mm) experimental data and matching simulation results, for 0.01% diamond nanoparticle solution at a bulk lubricant oil temperature of T = 59°C. Diamonds represent the experimental average wear, while error bars represent the average (thick error bars) and maximum (thin error bars) experimental variation of the wear observed between all six samples (two repeating tests with three ball bearings each). Figure data in Table 4.8.

t	SIM	EXP	DEV
60	0.369	0.36	9.8
120	0.397	0.39	11.2
300	0.453	0.43	14.3
1800	0.578	0.61	30.3
3600	0.634	0.664	17.1

Table 4.6: Numerical *SIM* and experimental average *EXP* and % maximum deviation *DEV* wear scar diameter (mm) data as a function of time (seconds) *t* for 0.01% diamond nanoparticle solution at a bulk lubricant oil temperature of 51°C (Fig. 4.8).

t	SIM	EXP	DEV
10	69	14	295.8
60	312	57	78.9
120	468	82	106.5
300	789	279	22.3
1800	2206	1460	27.6
3600	3613	2590	23.6

Table 4.7: Numerical *SIM* and experimental average *EXP* and % maximum deviation *DEV* wear (10^3 μm^3) data as a function of time (seconds) *t* for 0.01% diamond nanoparticle solution at a bulk lubricant oil temperature of 59°C (Fig. 4.9).

for consistent T = 51°C and T = 59°C lubricant temperature studies. At every data point, the diamond nanoparticles solution was found to have reduced wear compared to the neat mineral oil.

A numerical model was developed, and this model has been verified to numerically simulate the wear that occurs in four-ball tests with neat mineral oil, both in time and with fluctuating temperatures. Previous investigations of diamond nanoparticles have suggested that the reduction in wear is not the result of any chemical effects [1, 21], and prior DLS measurements of these nanoparticles both before and after a four-ball test have concluded that the dispersant shell that surrounds the diamond makes the nanoparticles too large to significantly fill up the voids caused by asperities, reduce the surface roughness, or cover the surface

t	SIM	EXP	DEV
60	0.39	0.36	12.8
120	0.425	0.38	12.2
300	0.481	0.43	15.6
1800	0.62	0.59	30.3
3600	0.697	0.66	16.7

Table 4.8: Numerical *SIM* and experimental average *EXP* and % maximum deviation *DEV* wear scar diameter (mm) data as a function of time (seconds) *t* for 0.01% diamond nanoparticle solution at a bulk lubricant oil temperature of 59°C (Fig. 4.10).

sufficiently to convert the contact from sliding to rolling. For this reason, the effort focused on the enhanced lubricant thermal conductivities due to the diamond nanoparticles.

This effort has demonstrated that by increasing the thermal conductivity of the lubricant, the lubricant temperature can expect to decrease, which results in an increase in lubricant viscosity. Based on theories of elastohydrodynamic lubrication, this increase in viscosity serves to increase the lubricant film thickness (Eqn. 2.18 and 2.19), and from Archard's equation on wear (Eqn. 1.3) the increasing film thickness serves to better protect random surface asperities and reduce wear. This numerical model of the wear with the enhanced lubricant thermal conductivity due to the diamond additive has consistently matched the experimental results within the range of experimental variation. This close correlation serves to strengthen the voracity of this theory, which may be used for future modeling of different nanoparticles as a lubricant additives and improve tribological design in this critical field of engineering.

Chapter 5

CONCLUSION

CONCLUSION

A series of four-ball sliding contact experiments were conducted for both neat mineral oil and oil with the diamond nanoparticle solution. This experimental effort utilized highly polished test-grade ball-bearings under a consistent load, speed, and temperature. Throughout the effort, experiments were conducted with varying temperature, time of contact, and diamond nanoparticle concentration. It was observed that increasing the average lubricant oil temperature increases the wear. This is expected as the temperature will decrease the viscosity of the lubricant, resulting in a thinner lubricant film thickness; the thicker the film, the less wear is anticipated. It was observed in this temperature study that the wear reduction was consistent and uniform reduction in wear with the 0.01% weight concentration nanoparticle additive was achieved. Second, at a consistent temperature it was observed that varying the nanoparticle concentration has a direct effect on proportionally reducing the wear. Finally, the time-varying studies were conducted from run-times ranging from 10 seconds to a full hour, and it was observed that increasing the time has both increased the wear (as expected), and also reduced the overall wear rate (total wear over time).

After these experimental tests were conducted, the chemical properties of the worn ball-bearing surfaces were characterized with X-Ray Photoelectric Spectroscopy, and no chemical changes were observed from the nanoparticle study, ruling out a

chemical phenomenon such as rehybridization of the carbon. In addition, with a weight concentration of 0.01%, at the optimal conditions less than 0.07% of the surface would be covered, which rules out a mechanical effect, such as the small particles converting the contact from sliding to rolling. For this reason, thermal effects are investigated, as the conductivity of the diamond is far greater than that of the oil, and temperature has been observed to directly effect the lubricant viscosity and the wear rate.

In addition to the experimental effort, a novel numerical model was developed to replicate the experimental results and provide clarification to the causes of the observed experimental trends. In this model, many tribological parameters required iteration until a final convergence was achieved for each time step. Iteration was needed to find the pressure that was solved with the Reynolds equation, and then a second iterative loop was needed to realize the elastic deformation of the ball-bearing with the Winkler Mattress model. In addition, iteration of the oil film temperature had to be performed, as a thicker oil film will inherently be hotter due to an increased thermal resistance from the center of the ball-bearing to the surface. A hotter film, however, would become less viscous, which would have the effect of reducing the film thickness. A careful balance of iteration and convergence is necessary at every time-step to keep the simulation realistic and avoid numerical errors.

Another aspect of the model was determining the rate of wear as a result of the lubricant film thickness profile, as wear occurs when random asperities exceed the oil film thickness. To properly model the wear, Monte Carlo simulations were conducted in order to determine the probability that an asperity of a given height will come into contact with the opposing surface, and what wear can be expected after a given amount of sliding contact. This data was curve fitted to an exponential

function, and it was used to determine the ratio of wear expected for a given film-thickness to surface roughness ratio.

Finally, to model the diamond nanoparticle additive, the viscosity remained unchanged (which was both theoretically expected and experimentally observed), and the thermal conductivity was increased due to the significantly (3 orders of magnitude) greater conductivity of the diamond versus neat mineral oil. It was previously reported that mixing a highly conductive material such as carbon or diamonds into a thermal insulator like lubricant mineral oil can serve to increase the thermal conductivity of the solution. For this reason, this effect will be modeled to compare the neat mineral oil with the diamond nanoparticle solution.

The numerical model managed to match the experimental data, both in time, temperature dependence, and load. Increasing the concentration of nanoparticles, thus increasing the conductivity, would result in a decrease in film temperature, which results in an increase in viscosity, which serves to increase the minimum film thickness. With an increase in film thickness, there is a reduced likelihood of random asperities coming into contact with the opposing surfaces, and thus a reduction in wear. Based on the close matching of the numerical model to the experimental data, it is a conclusion of this thesis that the thermal conductivity enhancement of the diamond nanoparticles additive is a primary cause of the reduction in wear and friction.

Bibliography

[1] Marko, M., Kyle, J., Branson, B., and Terrell, E., 2015. "Tribological improvements of dispersed nano-diamond additives in lubricating mineral oil". *Journal of Tribology,* **137**, p. 011802.

[2] Greenwood, J., and Williamson, J., 1966. "Contact of nominally flat surfaces". *Proceedings of the Royal Society of London A,* **295**(1442), pp. 300–319.

[3] Hu, Y., Li, N., and Tønder, K., 1991. "A dynamic system model for lubricated sliding wear and running-in". *Journal of Tribology,* **113**, pp. 499–505.

[4] Finkin, E., 1970. "Applicability of Greenwood-Williamson theory to film covered surfaces". *Wear,* **15**, pp. 291–293.

[5] Endo, K., and Kotani, S., 1973. "Observations of steel surfaces under lubricated wear". *Wear,* **26**, pp. 239–251.

[6] Golden, J., 1976. "The evolution of asperity height distributions of a surface seeoed to wear". *Wear,* **39**, pp. 25–44.

[7] Jahanmir, S., and Suh, N., 1977. "Surface topography and integrity effects on sliding wear". *Wear,* **44**, pp. 87–99.

[8] Shafia, M., and Eyre, T., 1980. "The effect of surface topography on the wear of steel". *Wear,* **61**, pp. 87–100.

[9] Johnson, K., 1987. *Contact Mechanics*. Cambridge University Press, 40 W 20th St, New York NY 10011.

[10] Blau, P., 2005. "On the nature of running-in". *Tribology International,* **38**, p. 1007–1012.

[11] Suzuki, M., and Ludema, K., 1987. "The wear process during the "running-ln" of steel in lubricated sliding". *Journal of Tribology,* **109**, pp. 587–591.

[12] Klapperich, C., Komvopoulos, K., and Pruitt, L., 1999. "Tribological properties and microstructure evolution of ultra-high molecular weight polyethylene". *Transactions of the ASME,* **121**, pp. 394–402.

[13] Spanu, C., Ripa, M., and Ciortan, S., 2008. "Study of wear evolution for a hydraulic oil using a four-ball tester". *The Annals of University Dunareade Jos of Galati,* **8**, pp. 186–189.

[14] Bayer, R., and Sirico, J., 1975. "The influence of surface roughness on wear". *Wear,* **35**, pp. 251–260.

[15] Sharif, K., Evans, H., Snidle, R., Barnett, D., and Egorov, I., 2006. "Effect of elastohydrodynamic film thickness on a wear model for worm gears.". *J. Engineering Tribology,* **220**, pp. 295–306.

[16] da Silva, C., and Pintaude, G., 2008. "Uncertainty analysis on the wear coefficient of Archard model". *Tribology International,* **41**, pp. 473–481.

[17] Andersson, J., Almqvist, A., and Larsson, R., 2011. "Numerical simulation of a wear experiment". *Wear,* **271**, pp. 2947–2952.

[18] Hamrock, B., and Dowson, D., 1976. "Isothermal elastohydrodynamic lubrication of point contacts, iii fully flooded results". *NASA Technical Note,* **D-8317**.

[19] Smeeth, M., and Spikes, H. A., 1997. "Central and minimum elastohydrodynamic film thickness at high contact pressure". *Journal of Tribology,* **119**, pp. 291–296.

[20] Stachowiak, G., and Batchelor, A., 2005. *Engineering Tribology* $4^{th} Edition$. Butterworth-Heinemann, Oxford, UK.

[21] Tao, X., Jiazheng, Z., and Kang, X., 1996. "The ball-bearing effect of diamond nanoparticles as an oil additive". *Journal of Physics D: Applied Physics,* **29**, p. 2932.

[22] Mochalin, V., Shenderova, O., Ho, D., and Gogotsi, Y., 2012. "The properties and applications of nanodiamonds". *Nature Nanotechnology,* **7**, pp. 11–23.

[23] Wu, Y., Tsui, W., and Liu, T., 2007. "Experimental analysis of tribological properties of lubricating oils with nanoparticle additives". *Wear,* **262**, p. 819–825.

[24] Padgurskas, J., Rukuiza, R., Prosycevas, I., and Kreivaitis, R., 2013. "Tribological properties of lubricant additives of Fe, Cu and Co nanoparticles". *Tribology International,* **60**, p. 224–232.

[25] Sunqing, Q., Junxiu, D., and Guoxu, C., 2000. "Wear and friction behaviour of $CaCO_3$, nanoparticles used as additives in lubricating oils". *Lubrication Science,* **12**, p. 205–212.

[26] Rapoport, L., Leshchinsky, V., Lapsker, I., Volovik, Y., Nepomnyashchy, O., Lvovsky, M., Popovitz-Biro, R., Feldman, Y., and Tenne, R., 2003. "Tribological properties of WS_2 nanoparticles under mixed lubrication". *Wear,* **255**, p. 785–793.

[27] Reeves, C., Menezes, P., Lovell, M., and Jen, T., 2013. "The size effect of boron nitride particles on the tribological performance of biolubricants for energy conservation and sustainability". *Tribology Letters,* **51**, pp. 437–452.

[28] Pawlak, Z., Kaldonski, T., Pai, R., Bayraktar, E., and Oloyede, A., 2009. "A comparative study on the tribological behaviour of hexagonal boron nitride (h-BN) as lubricating micro-particles—an additive in porous sliding bearings for a car clutch". *Wear,* **267**, pp. 1198–1202.

[29] Zhou, J., Wu, Z., Zhang, Z., Liu, W., and Dang, H., 2001. "Study on an antiwear and extreme pressure additive of surface coated LaF_3 nanoparticles in liquid paraffin". *Wear,* **249**, pp. 333–337.

[30] Sunqing, Q., Junxiu, D., and Guoxu, C., 1999. "Tribological properties of CeF3 nanoparticles as additives in lubricating oils". *Wear,* **230**, pp. 35–38.

[31] Chen, S., and Liu, W., 2001. "Characterization and antiwear ability of non-coated ZnS nanoparticles and DDP-coated ZnS nanoparticles". *Materials Research Bulletin,* **36**, pp. 137–143.

[32] Zhang, Z., Liu, W., and Xue, Q., 2001. "The tribological behaviors of succinimide-modified lanthanum hydroxide nanoparticles blended with zinc dialkyldithiophosphate as additives in liquid paraffin". *Wear,* **248**, pp. 48–54.

[33] Chen, S., Liu, W., and Yu, L., 1998. "Preparation of DDP-coated PbS nanoparticles and investigation of the antiwear ability of the prepared nanoparticles as additive in liquid paraffin". *Wear,* **218**, pp. 153–158.

[34] Chen, S., and Liu, W., 2006. "Oleic acid capped PbS nanoparticles: synthesis, characterization and tribological properties". *Materials Chemistry and Physics,* **98**, p. 183–189.

[35] Liu, W., and Chen, S., 2000. "An investigation of the tribological behaviour of surface-modified ZnS nanoparticles in liquid paraffin". *Wear,* **238**, p. 120–124.

[36] Xue, Q., Liu, W., and Zhang, Z., 1997. "Friction and wear properties of a surface-modified TiO_2 nanoparticle as an additive in liquid paraffin". *Wear,* **213**, pp. 29–32.

[37] Hu, Z., and Dong, J., 1998. "Study on antiwear and reducing friction additive of nanometer titanium oxide". *Wear,* **216**, pp. 92–96.

[38] Volovik, Y., and Tenne, R., 2002. "Friction and wear of powdered composites impregnated with WS_2 inorganic fullerene-like nanoparticles". *Wear,* **252**, p. 518–527.

[39] Rapoport, L., Leshchinsky, V., Lvovsky, M., Lapsker, I., Volovik, Y., Feldman, Y., Popovitz-Biro, R., and Tenne, R., 2003. "Superior tribological properties of powder materials with solid lubricant nanoparticles". *Wear,* **255**, pp. 794–800.

[40] Rapoport, L., Feldman, Y., Homyonfer, M., Cohen, H., Sloan, J., Hutchison, J., and Tenne, R., 1999. "Inorganic fullerene-like material as additives to lubricants: structure–function relationship". *Wear,* **225–229**, p. 975–982.

[41] Rapoport, L., Nepomnyashchy, O., Lapsker, I., Verdyan, A., Moshkovich, A., Feldman, Y., and Tenne, R., 2005. "Behavior of fullerene-like WS_2 nanoparticles under severe contact conditions". *Wear,* **259**, pp. 703–707.

[42] Maharaj, D., and Bhushan, B., 2013. "Effect of Mo_2 and WS_2 nanotubes on nanofriction and wear reduction in dry and liquid environments". *Tribology Letters,* **49**, pp. 323–339.

[43] "ASTM D4172-94, Standard Test Method for Wear Preventive Characteristics of Lubricating Fluid (Four-Ball Method), ASTM-International, West Conshohocken, PA, 2010, www.astm.org".

[44] Erdemir, A., and Donnet, C., 2006. "Tribology of diamond-like carbon films: recent progress and future prospects". *Journal of Physics D: Applied Physics,* **39**, pp. 311–327.

[45] Gupta, B., Malshe, A., Bhushan, B., and Subramaniam, V., 1994. "Friction and wear properties of chemomechanically polished diamond films". *Journal of Tribology,* **116**, pp. 445–453.

[46] Chin, F., and Spikes, H., 2003. "Mechanism of action of colloidal solid dispersions". *Journal of Tribology,* **125**, pp. 552–557.

[47] Grierson, D., Sumant, A., Konicek, A., Friedmann, T., Sullivan, J., and Carpick, R., 2010. "Thermal stability and rehybridization of carbon bond-

ing in tetrahedral amorphous carbon". *Journal of Applied Physics,* **107**, p. 033523.

[48] Konicek, A., Grierson, D., Gilbert, P., Sawyer, W., Sumant, A., and Carpick, R., 2008. "Origin of ultralow friction and wear in ultrananocrystalline diamond". *Physical Review Letters,* **100**, p. 235502.

[49] Sullivan, J., Friedmann, T., and Hjort, K., 2001. "Diamond and amorphous carbon MEMS". *Materials Research Society (MRS) Bulletin,* **26**, pp. 309–311.

[50] Miyoshi, K., Wu, R., Garscadden, A., Barnes, P., and Jackson, H., 1993. "Friction and wear of plasma deposited diamond films". *Journal of Applied Physics,* **74**, p. 4446.

[51] Donnet, C., Fontaine, J., Le-Mogne, T., Belin, M., Heau, C., Terrat, J., Vaux, F., and Pont, G., 1999. "Diamond-like carbon-based functionally gradient coatings for space tribology". *Surface and Coating Technology,* **120-121**, pp. 548–554.

[52] Scharf, T., Ohlhausen, J., Tallant, D., and Prasad, S., 2007. "Mechanisms of friction in diamond-like nanocomposite coatings". *Journal of Applied Physics,* **101**, pp. 063521–1 –063521–11.

[53] Gardos, M., and Soriano, B., 1990. "The effect of environment on the tribological properties of polycrystalline diamond films". *Journal of Material Research,* **5**(11), pp. 2599–2609.

[54] de Barros-Bouchet, M., Martin, J., Le-Mogne, T., and Vacher, B., 257-264. "Boundary lubrication mechanisms of carbon coatings by MoDTC and ZDDP additives". *Tribology International,* **38**, p. 2005.

[55] Tang, W., Zhu, C., Yao, W., Wang, Q., Li, C., and Lu, F., 2003. "Nanocrystalline diamond films produced by direct current arc plasma jet process". *Thin Solid Films,* **429**, pp. 63–70.

[56] Donnet, C., and Erdemir, A., 2008. *Tribology of Diamond-Like Carbon Films: Fundamentals and Applications*. Springer Science and Business Media, LLC, 233 Spring Street, New York NY USA.

[57] Miyake, S., Watanabe, S., Murakawa, M., Kaneko, R., and Miyamoto, T., 1992. "Tribological study of cubic boron nitride film". *Thin Solid Films,* **212**, pp. 262–266.

[58] Chong, Y., Ye, Q., Yang, Y., Zhang, W., Bello, I., and Lee, S., 2010. "Tribological study of boron nitride films". *Diamond and Related Materials,* **19**, p. 654–660.

[59] Dolmatov, V., Fujimura, T., Burkat, G., Orlova, E., and Veretennikova, M., 2003. "Preparation of wear-resistant chromium coatings using different types of nanodiamonds". *Powder Metallurgy and Metal Ceramics,* **42**, pp. 587–591.

[60] Siegbahn, K., and Edvarson, K., 1956. "β-ray spectroscopy in the precision range of 1:105". *Nuclear Physics,* **1**, pp. 137–159.

[61] Wanga, S., Zhanga, Q., Yoona, S., Ahna, J., Zhoua, Q., Wang, Q., Yanga, D., Lia, J., and Shanyongb, S., 2003. "Electron field emission enhance-

ment effects of nano-diamond films". *Surface and Coatings Technology,* **167**, pp. 143–147.

[62] Xu, T., Yang, S., Chen, M., Tian, J., Xue, Q., Li, J., and Guo, W., 2002. "Influence of nitrogen ion implantation on tribological properties of nanocrystalline diamond films". *Journal of Physics D: Applied Physics,* **35**(8), pp. 788–793.

[63] Zhang, Z., and Fang, X., 2006. "Study on paraffin/expanded graphite composite phase change thermal energy storage material". *Energy Conversion and Management,* **47**, pp. 303–310.

[64] Karaipekli, A., Sari, A., and Kaygusuzb, K., 2007. "Thermal conductivity improvement of stearic acid using expanded graphite and carbon fiber for energy storage applications". *Renewable Energy,* **32**, pp. 2201–2210.

[65] Sari, A., and Karaipekli, A., 2007. "Thermal conductivity and latent heat thermal energy storage characteristics of paraffin/expanded graphite composite as phase change material". *Applied Thermal Engineering,* **27**, pp. 1271–1277.

[66] Graebner, J., Hartnett, T., and Miller, R., 1994. "Improved thermal conductivity in isotopically enriched chemical vapor deposited diamond". *Applied Physics Letters,* **64**, pp. 2549–2551.

[67] Anthony, T., Fleischer, J., Olson, J., and Cahill, D., 1991. "The thermal conductivity of isotopically enriched polycrystalline diamond films". *Journal of Applied Physics,* **69**, pp. 8122–8125.

[68] Wei, L., Kuo, P., Thomas, R., Anthony, T., and Banholzer, W., 1993. "Thermal conductivity of isotopically modified single crystal diamond". *Physical Review Letters,* **70**(24), pp. 3764–3767.

[69] Anthony, T., Banhozer, W., Fleischer, J., L.Wei, Kuo, P., Thomas, R., and Pryor, R., 1990. "Thermal diffusivity of isotopically enriched ^{12}c diamond". *Physical Review B,* **42**(2), pp. 1104–1111.

[70] Taha-Tijerina, J. J., Narayanan, T., Tiwary, C. S., Lozano, K., Chipara, M., and Ajayan, P. M., 2014. "Nanodiamond-based thermal fluids". *American Chemical Society Applied Materials and Interfaces,* **6**, p. 4778−4785.

[71] Branson, B. T., Beauchamp, P. S., Beam, J. C., Lukehart, C. M., and Davidson, J. L., 2013. "Nanodiamond nanofluids for enhanced thermal conductivity". *American Chemical Society Nano,* **7**, pp. 3183–3189.

[72] Rowley, R. "A local composition model for multicomponent liquid mixture thermal conductivities". *Chemical Engineering Science,* **37**(6).

[73] Wang, X., Xu, X., , and Choi, S. U., 1999. "Thermal conductivity of nanoparticle – fluid mixture". *Journal of Thermophysics and Heat Transfer,* **13**, pp. 474–480.

[74] Keblinski, P., Phillpot, S., Choi, S., and Eastman, J., 2002. "Mechanisms of heat flow in suspensions of nano-sized particles (nanofluids)". *International Journal of Heat and Mass Transfer,* **45**, pp. 855–863.

[75] Wen, D., Lin, G., Vafaei, S., and Zhang, K., 2009. "Review of nanofluids for heat transfer applications". *Particuology,* **7**, pp. 141–150.

[76] Daungthongsuk, W., and Wongwises, S., 2007. "A critical review of convective heat transfer of nanofluids". *Renewable and Sustainable Energy Reviews,* **11**, pp. 797–817.

[77] Xuan, Y., and Roetzel, W., 2000. "Conceptions for heat transfer correlation of nanofluids". *International Journal of Heat and Mass Transfer,* **43**, pp. 3701–3707.

[78] Wang, X.-Q., and Mujumdar, A. S., 2007. "Heat transfer characteristics of nanofluids: a review". *International Journal of Thermal Sciences,* **46**, pp. 1–19.

[79] Xuan, Y., and Li, Q., 2000. "Heat transfer enhancement of nanofluids". *International Journal of Heat and Fluid Flow,* **21**, pp. 58–64.

[80] Shima, P. D., Philip, J., and Raj, B., 2010. "Synthesis of aqueous and non-aqueous iron oxide nanofluids and study of temperature dependence on thermal conductivity and viscosity". *American Chemical Society, Journal of Physical Chemistry C,* **114**, p. 18825–18833.

[81] Krishnamurthy, S., Bhattacharya, P., and Phelan, P. E., 2006. "Enhanced mass transport in nanofluids". *Nano Letters,* **6**(3), pp. 419–423.

[82] Archard, J., 1958. "The temperature of rubbing surfaces". *Wear,* **2**, pp. 438–455.

[83] "ASTM D341-09, Standard Practice for Viscosity-Temperature Charts for Liquid Petroleum Products, ASTM-International, West Conshohocken, PA, 2009, www.astm.org".

[84] Hamrock, B., and Dowson, D., 1975. "Isothermal elastohydrodynamic lubrication of point contacts, i theoretical formulation". *NASA Technical Note,* **D-8049**.

[85] Hamrock, B., and Dowson, D., 1976. "Isothermal elastohydrodynamic lubrication of point contacts, iv starvation results". *NASA Technical Note,* **D-8318**.

[86] Cameron, A., and Gohar, R., 1966. "Theoretical and experimental studies of the oil film in lubricated point contact". *Proceedings of the Royal Society of London. Series A, Mathematical and Physical Sciences,* **291**(1427), pp. 520–536.

[87] Dowson, D., 1995. "Elastohydrodynamic and micro-elastohydrodynamic lubrication". *Wear,* **190**, pp. 125–138.

[88] Archard, J., 1953. "Contact and rubbing of flat surfaces". *Journal of Applied Physics,* **24**(8), pp. 981–988.

[89] Jiang, P., Li, X., Guo, F., and Chen, J., 2009. "Interferometry measurement of spin effect on sliding ehl". *Tribology Letters,* **33**, pp. 161–168.

[90] Goodyer, C., and Berzins, M., 2006. "Adaptive timestepping for elastohydrodynamic lubrication solvers". *SIAM Journal of Science Computing,* **28**(2), pp. 626–650.

[91] Gohar, R., 2002. *Elastohydrodynamics*. World Scientific Publishing Company, Singapore.

[92] Ranger, A., Ettles, C., and Cameron, A., 1975. "The solution of the point contact elasto-hydrodynamic problem". *Proceedings of the Royal Society of*

London. Series A, Mathematical and Physical Sciences, **346**(1645), pp. 227–244.

[93] Elcoate, C., Evans, H., Hughes, T., and Snidle, R., 2001. "Transient elasto-hydrodynamic analysis of rough surfaces using a novel coupled differential deflection method". *Proceedings of the Institution of Mechanical Engineers, Part J: Journal of Engineering Tribology,* **215**(J), pp. 319–337.

[94] Jamali, H., Sharif, K., Evans, H., and Snidle, R., 2015. "The transient effects of profile modification on elastohydrodynamic oil films in helical gears". *Tribology Transactions,* **58**(1), p. 119–130.

[95] Evans, H., Clarke, A., Sharif, K., and Snidle, R., 2010. "The role of heat partition in elastohydrodynamic lubrication". *Tribology Transactions,* **53**(2), pp. 179–188.

[96] Sharif, K., Evans, H., and Snidle, R., 2012. "Modelling of elastohydrodynamic lubrication and fatigue of rough surfaces: The effect of lambda ratio". *Proceedings of the Institution of Mechanical Engineers, Part J: Journal of Engineering Tribology,* **226**(12), pp. 1039–1050.

[97] Barus, C., 1893. "Isothermals, isopiesties and isometrics relative to viscosity". *American Journal of Science,* **45**, pp. 87–96.

[98] So, B., and Klaus, E., 1980. "Viscosity-pressure correlation of liquids.". *ASLE Transactions,* **23**, pp. 409–421.

[99] Einstein, A., 1906. "Neue bestimmung der molekuldimensionen". *Ann. Physik,* **19**, pp. 289–306.

[100] Pabst, W., 2004. "Fundamental considerations on suspension rheology". *Ceramics − Silikáty,* **48**(1), pp. 6–13.

[101] Cengel, Y., 2002. *Heat Transfer, a Practical Approach, Second Edition*. Mcgraw-Hill, Texas.

[102] Abdel-Aal, H., 1997. "A remark on the flash temperature theory". *International Communication on Heat and Mass Transfer,* **24**(2), pp. 241–250.

[103] Barber, J., 1967. "Distribution of heat between sliding surfaces". *Journal of Mechanical Engineering Science,* **9**(5), pp. 351–354.

[104] Blok, H., 1963. "The flash temperature concept". *Wear,* **6**, pp. 483–494.

[105] Archard, J., and Rowntree, R., 1988. "The temperature of rubbing bodies; part 2, the distribution of temperatures". *Wear,* **128**, pp. 1–17.

[106] Blok, H., 1937. "Theoretical study of temperature rise at surfaces of actual contact under oiliness conditions". *Proceedings of the Institute of Mechanical Engineering, General Discussion on Lubrication,* **2**, pp. 222–235.

[107] Jaeger, J., 1942. "Moving sources of heat and the temperature at sliding contact". *Proceedings of the Royal Society N.S.W.,* **76**, pp. 203–224.

[108] Crook, A. "The lubrication of rollers". *Philosophical Transactions of the Royal Society of London, Series A, Mathematical and Physical Sciences,* **250**(981).

[109] White, F., 2003. *Fluid Mechanics Fifth Edition*. McGraw-Hill, Boston, MA.

[110] Garcia, A., 1999. *Numerical Methods for Physics 2nd Edition*. Addison-Wesley, Boston.

[111] Terrill, R., 1983. "On grubin's formula in elastohydrodynamic lubrication theory". *Wear,* **92**, pp. 67–78.

[112] Zhang, P., and Guo, J., 1989. "Two new formulae to calculate the film thickness in elastohydrodynamic lubrication and an evaluation of grubin's formula". *Wear,* **130**, pp. 357–366.

[113] Peiran, Y., and Shizhu, W., 1990. "A forward iterative numerical method for steady-state elastohydrodynamically lubricated line contacts". *Tribology International,* **23**(1), pp. 17–22.

[114] Conway, H., and Engel, P., April 1974. "A grubin-type formula for the elastohydrodynamic lubrication of a thin elastic layer". *Transactions of ASME, Journal of Lubrication Technology*, pp. 300–302.

[115] Roelands, C., Vlugter, J., and Waterman, H., 1963. "The viscosity-temperature-pressure relationship of lubricating oils and its correlation with chemical constitution". *Journal of Basic Engineering,* **85**, pp. 601–607.

[116] Bush, A., Gibson, R., and Keogh, G., 1976. "The limit of elastic deformation in the contact of rough surfaces". *Mechanics Research Communication,* **3**, pp. 169–174.

[117] Carbone, G., 2009. "A slightly corrected Greenwood and Williamson model predicts asymptotic linearity between contact area and load". *Journal of the Mechanics and Physics of Solids,* **57**, p. 1093–1102.

[118] McCool, J., 1986. "Comparison of models for the contact of rough surfaces". *Wear,* **107**, pp. 37–60.

[119] Bush, A., Gibson, R., and Thomas, T., 87-111. "The elastic contact of a rough surface". *Wear,* **35**, p. 1975.

[120] Persson, B., 2006. "Contact mechanics for randomly rough surfaces". *Surface Science Reports,* **61**, pp. 201–227.

[121] Osswald, S., Yushin, G., Mochalin, V., Kucheyev, S., and Gogotsi, Y., 2006. "Control of sp2/sp3 carbon ratio and surface chemistry of nanodiamond powders by selective oxidation in air". *Journal of American Chemical Society,* **128**, pp. 11635–11642.

[122] Branson, B., Seif, M., Davidson, J., and Lukehart, C., 2011. "Fabrication and macro/nanoscale characterization of aggregated and highly de-aggregated nanodiamond/polyacrylonitrile composite thick films". *Journal of Material Chemistry,* **21**, pp. 18832–18839.

[123] Goldburg, W., 1999. "Dynamic light scattering". *American Journal of Physics,* **67**, pp. 1152–1160.

[124] Schatzel, K., Drewel, M., and Ahrens, J., 1990. "Suppression of multiple scattering in photon correlation spectroscopy". *Journal of Physics: Condensed Matter,* **2**, pp. SA393–SA398.

[125] Segre, P., Megen, W. V., Pusey, P., Schatzel, K., and Peters, W., 1995. "Two-colour dynamic light scattering". *Journal of Modern Optics,* **42**(9), pp. 1929–1952.

[126] Shakhvorostov, D., Müser, M., Song, Y., and Norton, P., 2009. "Smart materials behavior in phosphates: Role of hydroxyl groups and relevance to antiwear films". *Journal of Chemical Physics,* **131**, p. 044704.

[127] Repoux, M., 1992. "Comparison of background removal methods for xps". *Surface and Interface Analysis,* **18**, pp. 567–570.

[128] Dıaz, J., Paolicelli, G., Ferrer, S., and Comin, F., 1996. "Separation of the sp^2 and sp^3 components in the c 1s photoemission spectra of amorphous carbon films". *Physical Review B,* **54**(11), pp. 8064–8069.

[129] Haerle, R., Riedo, E., Pasquarello, A., and Baldereschi1, A., 2001. "sp^2/sp^3 hybridization ratio in amorphous carbon from C 1s core-level shifts: X-ray photoelectron spectroscopy and first-principles calculation". *Physical Review B,* **65**(4), p. 045101.

[130] Maxwell, J., 1904. *Electricity and Magnetism, Part II, 3*$^{\mathrm{rd}}$ *Edition*. Clarendon, Oxford.

[131] Hoover, W., 2006. *Smooth Particle Applied Mechanics: The State of the Art*. World Scientific Publishing Company, 27 Warren St, Hackensack NJ 07601.

[132] Liu, G., and Liu, M., 2003. *Smoothed Particle Hydrodynamics: a meshfree particle method*. World Scientific Publishing Co. Pte. Ltd., Suite 202, 1060 Main Street, River Edge NJ 07661.

[133] Lai, W., Rubin, D., and Krempl, E., 2010. *Introduction to Continuum Mechanics, 4*$^{\mathrm{th}}$ *Edition*. Butterworth-Heinemann of Elsevier, 30 Corporate Drive, Suite 400, Burlington MA 01803.

Appendices

Appendix A

SYMBOLS

- V (m^3), total wear
- $\dot{V}$ (m^3/s), wear rate
- P (Pa), pressure
- S (m), total distance of sliding contact
- U (m/s), velocity of sliding contact (Eqn. 2.23)
- σ (m), RMS surface roughness
- h (m), oil thickness (Eqn. 2.1)
- F_{indent} (m), the profile function of the ball bearing (Eqn. 2.2)
- V_y (m), wear profile depth
- δ_e (m), elastic deflection of ball bearing (Eqn. 2.5)
- h_{min} (m), minimum lubricant thickness (Eqn. 2.18)

- U_n, dimensionless speed parameter (Eqn. 2.20)
- G_n, dimensionless material parameter (Eqn. 2.21)
- W_n, dimensionless load parameter (Eqn. 2.22)
- *R* (m), radius of ball bearing
- K_h (Pa/m), Winkler Mattress Coefficient (Eqn. 2.6)
- *E* (Pa), Young's Modulus
- *p*, Poisson's Ratio
- *R'* (m), reduced radius (Eqn. 2.7 and 2.9)
- *E'* (Pa), reduced Young's modulus (Eqn. 2.8 and 2.10)
- a_{Hertz} (m), radius of Hertzian elastic contact area (Eqn. 2.11)
- *a* (m), radius of contact area
- P_{Hertz} (Pa), Hertzian pressure (Eqn. 2.12 and 2.14)
- δ_{Hertz} (m), Hertzian deflection (Eqn. 2.13)
- *x*, *y*, and *z* (m), dimensions defined in Fig. 2.1
- *r* (m), radial distance from a given point to the center (Eqn. 2.15)
- Δx (m), the distance increment of each finite-difference node
- ν_0 (mm^2/s), kinematic viscosity at atmospheric pressure
- ν_P (mm^2/s), kinematic viscosity under high contact pressure (Eqn. 2.16)
- μ (Pa-s), dynamic viscosity (Eqn. 2.41)

- L, Peclet number (Eqn. 2.24)
- α_P (Pa^{-1}), pressure-viscosity coefficient (Eqn. 2.17)
- $\kappa_{ellipse}$, the wear scar ellipticity
- α_{bb} (m^2/s), thermal diffusivity of ball bearing material (Eqn. 2.25)
- α_{lub} (m^2/s), thermal diffusivity of lubricant oil (Eqn. 2.28)
- k_{bb} $(\mathrm{W/m{\cdot}^{\circ}C})$, thermal conductivity of ball bearing material
- k_{oil} $(\mathrm{W/m{\cdot}^{\circ}C})$, thermal conductivity of the additives-free neat mineral oil
- $k_{diamond}$ $(\mathrm{W/m{\cdot}^{\circ}C})$, thermal conductivity of diamond
- k_{lub} $(\mathrm{W/m{\cdot}^{\circ}C})$, thermal conductivity of lubricant oil
- k_B = $1.38{\cdot}10^{-23}$ Joules / Kelvin, Boltzmann constant
- E'_A (Joules), activation energy for Eqn. 4.3 and 4.4
- K_0, coefficient for Eqn. 4.3 and 4.4
- k_{solute}, $k_{solvent}$, and $k_{solution}$ (W/m·°C), the effective thermal conductivities of the solute, solvent, and solution of a mixture
- χ, is the diamond nanoparticle weight concentration
- ϕ, is the diamond nanoparticle volume concentration
- $C_{P,bb}$ $(\mathrm{J/kg{\cdot}^{\circ}C})$, specific heat of ball bearing material
- $C_{P,lub}$ $(\mathrm{J/kg{\cdot}^{\circ}C})$, specific heat of lubricant oil
- ρ_{bb} (kg/m^3), density of ball bearing material

- ρ_{lub} (kg/m^3), density of lubricant oil
- Ω_{RPM} (r/min), rotational speed of four-ball test
- *W* (Newtons), load
- μ_{COF}, Coefficient of Friction (Estimated in Eqn. B.4)
- ΔT_F (°C), friction temperature increase at the surface (Eqn. 2.26)
- t_{ss} (s), time for flash temperature heating to settle (Eqn. 2.29)
- $T_{surface}$ (°C), the temperature at the surfaces of the ball bearings (Eqn. 2.32)
- T_B (°C), the bulk lubricant oil temperature
- $T_L(y)$ (°C), temperature profile of the lubricant film (Eqn. 2.31)
- T_L (°C), average temperature of the lubricant film (Eqn. 2.33 and 2.37)
- Q_{lub} (Watts), power from friction forces into lubricant film (Eqn. 2.34)
- V_{lub} (m^3), volume of lubricant over area of contact (Eqn. 2.35)
- q_v (Watts/m^3), power per unit volume into lubricant (Eqn. 2.36)
- $\hat{Z}$, reduced viscosity interpolation coefficient (Eqn. 2.38)
- *Z*, viscosity interpolation coefficient (Eqn. 2.39)
- *A* amd *B*, viscosity interpolation coefficients (Eqn. 2.40)
- h_c (m), film thickness where *dP/dx* = 0 (Eqn. 2.19 and 2.47)
- U_x and U_z (m/s), flow in *x* and *z* direction, (Eqn. 2.42)
- E_i, W_i, S_i, N_i, a_i, discrete pressure relationship values (Eqn. 2.56-2.60)

- B_i, right-hand side of discrete Reynolds relationship values (Eqn. 2.61)
- q (Pa), Grubin normalized pressure (Eqn. 2.62)
- $\alpha_P^* P$, Roelands Pressure-Viscosity exponential increase (Eqn. 2.66)
- Z_r, Roelands equation parameter (Eqn. 2.67)
- S_0, Roelands equation parameter (Eqn. 2.68)
- β_μ ($^\circ C^{-1}$), Viscosity-Temperature exponential coefficient (Eqn. 2.69)
- $\hat{P}_{i,j}$ (Pa), discrete *guess* for the pressure, for iterative solver (Eqn. 2.70)
- γ (m), length of individual asperities
- $\bar{\gamma}$ (m), mean value of all asperities within the wear scar
- N_a, number of finite difference points within the wear scar
- W_P (m), yield / plasticity length (Eqn. 2.73)
- G_{yield} (Pa), shear yield strength of ball-bearing material
- λ_W, ratio of wear height over RMS asperities (Eqn. 2.74)
- V_N, normalized wear rate (Eqn. 2.76)
- *N*, total number of Monte Carlo trials performed ($N = 10^9$)
- *H* (Pa), ball bearing material hardness
- *f*, definition of a function
- θ (radians), trigonometric angle for ball-bearing indentation function
- $n_{Archard}$, Archard's coefficient for Eqn. 1.3

- K_{wear}, wear coefficient for Eqn. 1.3
- A_N, fraction of surface area that exceeds film thickness (Eqn. B.1)
- A_{wear} (m^2), surface area that exceeds film thickness (Eqn. B.2)
- F_{wear} (Newtons), tangential friction force from material wear (Eqn. B.3)
- (*m*), the dimension of length, typically meters
- (*Pa*), the dimension of pressure, typically Pascals

Appendix B

FRICTION STUDIES

An effort was conducted to determine if the numerical model can be used to predict the coefficient of friction (COF). The COF is extremely difficult to accurately predict, as it is dependent on many properties, including but not limited to the wear, the shear yield stress, the fluid shear stress, elastohydrodynamic effects, and pressure-viscosity effects [20]. In all of the simulations throughout this thesis, a consistent COF value of $\mu_{COF} = 0.1$ was used to calculate the rate of friction heating (Eqn. 2.34, 2.36, and 2.37); this value has roughly been the average friction coefficient for all of the experimental trials (Fig. B.2).

When the Monte Carlo simulations ran (Fig. 2.5 and 2.6) to find the normalized volume as a function of λ_W (Eqn. 2.76), the study also kept track of the *quantity* of asperities that came into wear contact. This quantity could be divided by the total number of random asperities, in order to find the ratio of surface area that comes into contact with the opposing surface A_N (Fig. B.2). The empirical Monte Carlo data was used to obtain an analytical exponential equation (Eqn. B.1),

$$A_N = \frac{1}{2} \cdot exp[-1.2847 \cdot \lambda_W], \tag{B.1}$$

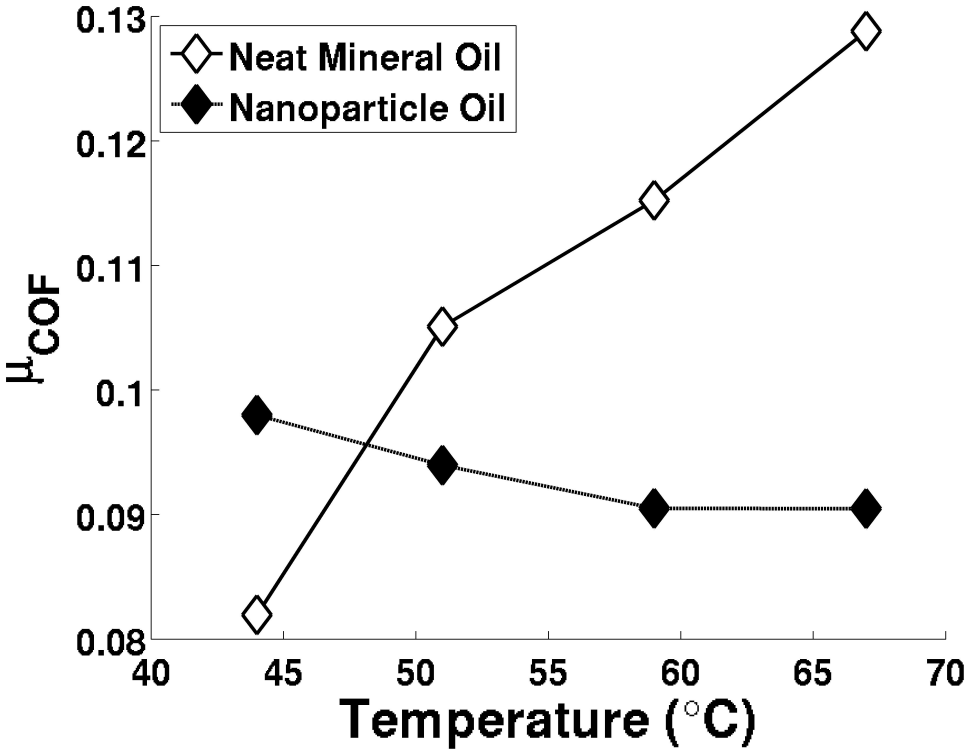

Figure B.1: Average experimental friction data as a function of temperature (°C), for a consistent contact time of 3600 seconds and a load of 391 Newtons.

where A_N is the ratio of surface area in contact with the opposing surface over the total surface area. This ratio can be used to estimate the coefficient of friction as a result of shear stress from the wear,

$$A_{wear} = \Delta x^2 A_N, \tag{B.2}$$

$$F_{wear} = G_{yield} \cdot A_{wear}, \tag{B.3}$$

$$\mu_{COF} = \frac{F_{wear}}{W}, \tag{B.4}$$

where G_{yield} (Pa) is the ultimate yield stress, A_{wear} (m^2) is the area of surface asperities in direct physical contact with the opposing surface, Δx^2 (m^2) is the total area of contact, F_{wear} (Newtons) is the tangential shear stress resulting from the wear, *W* (Newtons) is the total load, and μ_{COF} is the dimensionless coefficient of friction from the wear.

Throughout the simulations, the wear force F_{wear} was calculated at every time-step. A profile of contact area ratio A_N was calculated using Eqn. B.1 from the calculated λ_W function obtained from the film thickness profile achieved with the Reynolds equation solver. The total surface asperities area in contact A_{wear} (m^2) was easily obtained from A_N with Eqn. B.2. A wear force for each finite difference node was calculated (Eqn. B.3), and the summation of all of these forces were used to calculate the wear COF (Eqn. B.4). While rough trends were achieved, due to the highly random nature of friction, it is difficult to accurately model the friction, as observed by the discrepancies in Fig. B.3.

While an accurate prediction of the friction proved to be difficult, nevertheless trends were observed. For example, with neat mineral oil it was observed both experimentally (Fig. B.2) and numerically (Fig. B.4) that the friction would increase with increased temperatures (and wear). In addition, it was experimentally observed

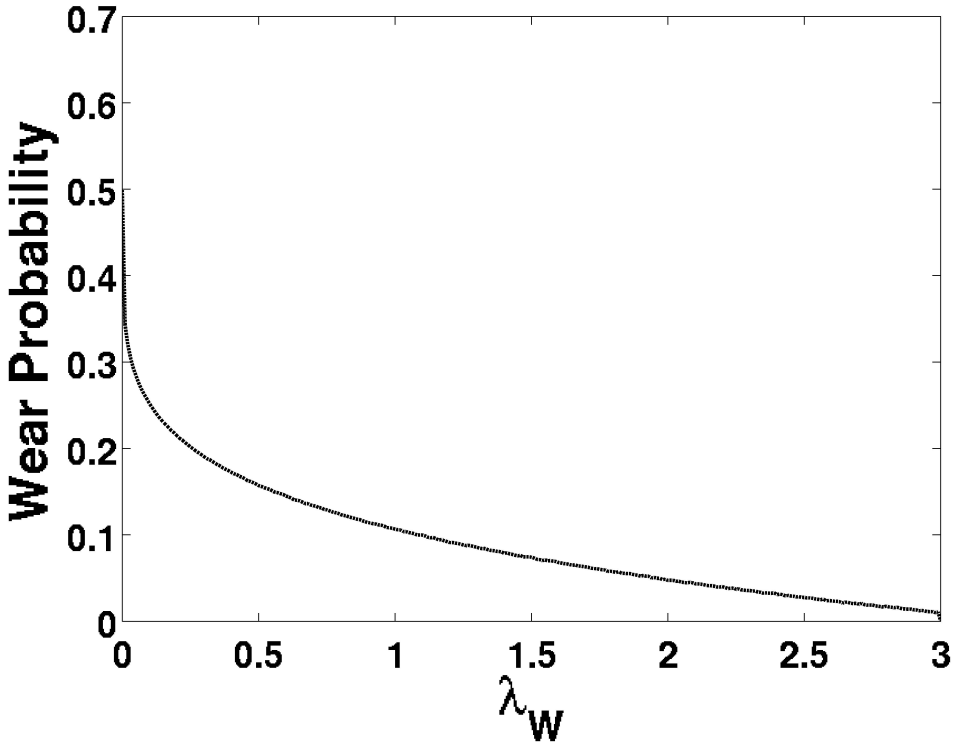

Figure B.2: Monte Carlo data of the probability of surface area coming into wear contact A_N as a function of λ_W.

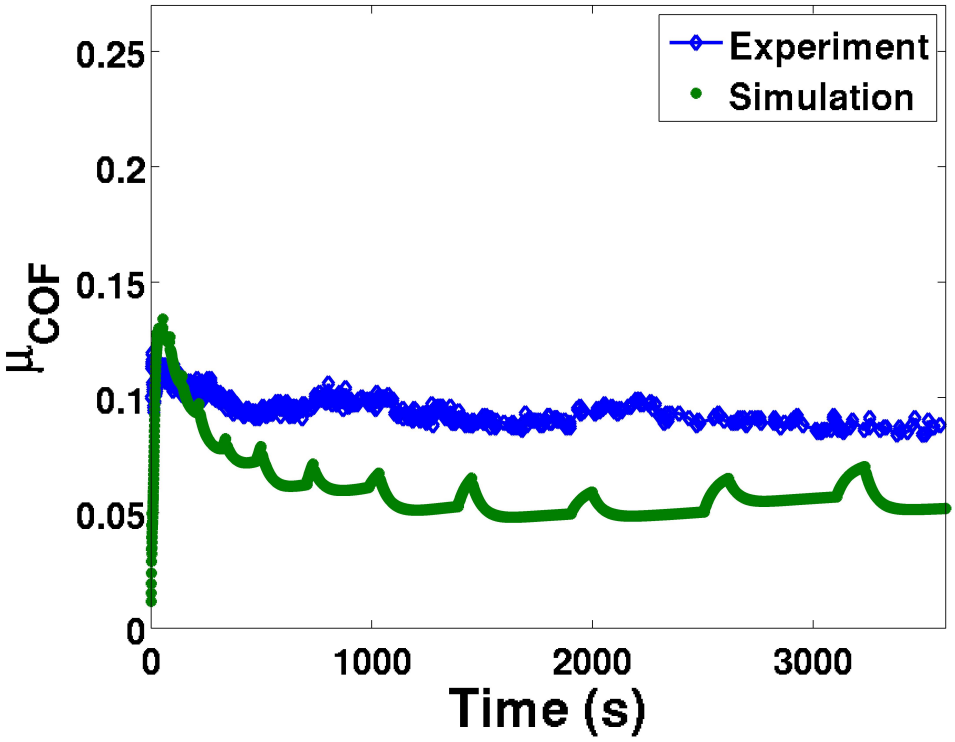

Figure B.3: Experimental and numerical coefficient of friction data, as a function of time, for a bulk lubricant temperature of T = 59°C.

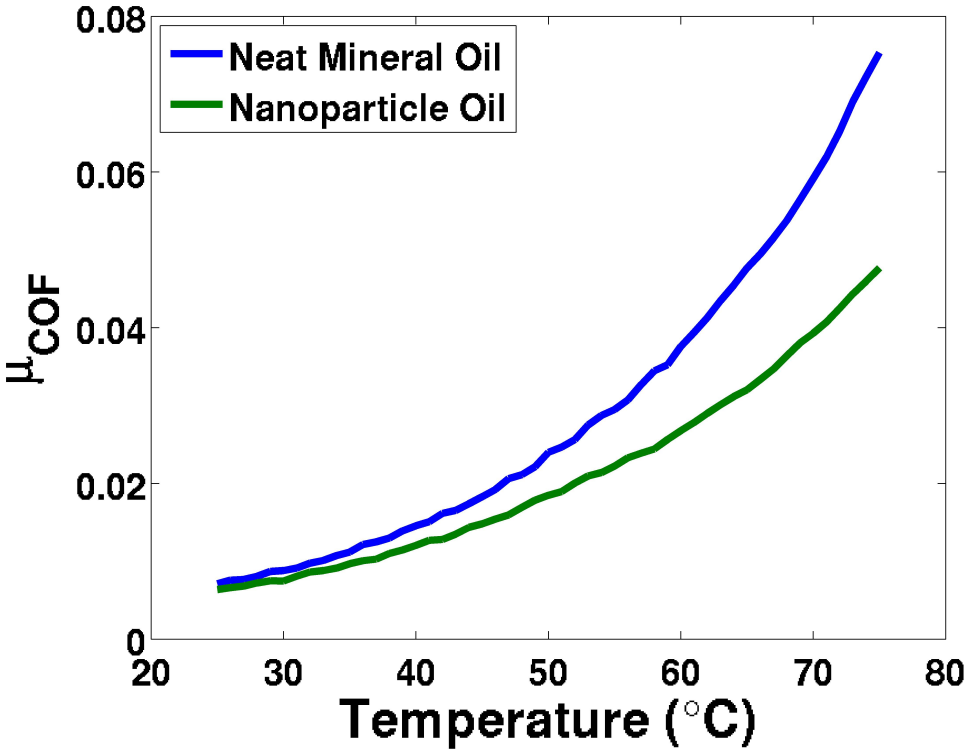

Figure B.4: Numerical friction data as a function of bulk lubricant temperature (°C), both for neat mineral oil and 0.01% diamond nanoparticle solution.

that the 0.01% weight concentration of diamond nanoparticle solution would reduce the COF [1], and this was observed in the numerical simulations (Fig. B.4 and B.5); however, unlike the predicted simulations, the experimental friction decreased very slightly with increasing temperatures. This discrepancy highlights the difficulties in accurately simulated the friction during sliding contact.

Finally, it was clearly observed (Fig 3.4) that with increasing diamond nanoparticle concentration, there would be a decrease in the fluctuation of the COF in time [1]. It was observed in the Monte Carlo simulations (Fig. B.6), that the standard deviation and fluctuations of the asperities that came into contact with the opposing surface would increase with decreasing λ_W values. As it was previously demonstrated that increasing the diamond nanoparticle concentration would

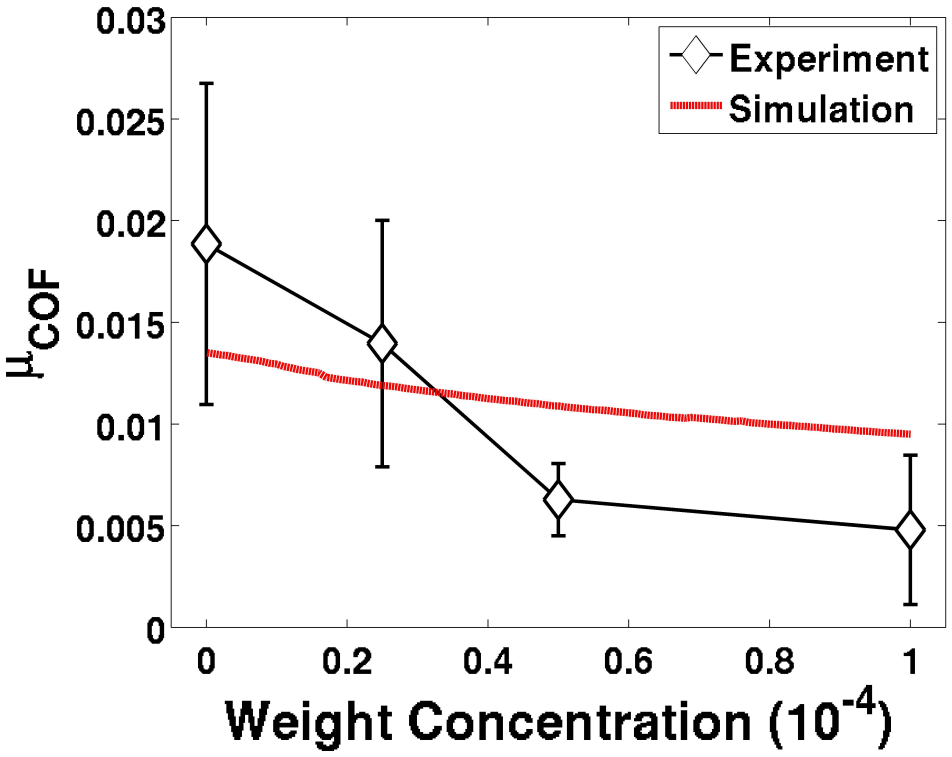

Figure B.5: Experimental [1] and numerical friction data as a function of diamond nanoparticle weight concentration. Diamonds represent the average experimental wear, and error bars represent the experimental standard deviation.

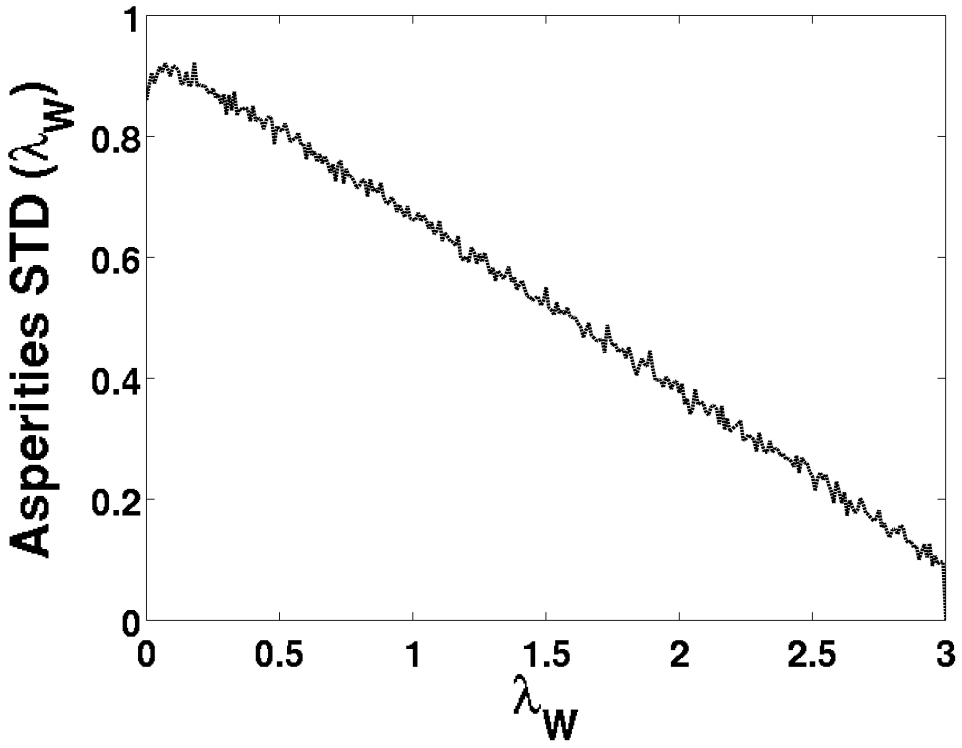

Figure B.6: Standard deviation of the normalized asperities worn off, as a function of λ_W.

decrease the lubricant temperature, causing an increase in film thickness and λ_W values; it can be expected that an increase in diamond nanoparticle concentration can result in a decrease in COF fluctuations.

Appendix C

CONCENTRATION SENSITIVITY

A series of parametric simulations were conducted, in order to determine the effects of changing diamond nanoparticle concentration on the various tribological properties. Ultimately the diamond nanoparticle concentration will affect the wear rate, with the experimental concentration data matching the numerical simulations in Fig. 4.3 and Table 4.2 [1]; however, there are many other tribological properties that change to cause this change in wear. The numerical model was conducted for three different temperatures (25°C, 50°C, and 75°C), as well as from 0 to 0.01% weight concentration of diamond nanoparticles in weight concentration increments of 10^{-6}. As expected from Eqn. 4.4, the thermal conductivity will increase with increasing nanodiamond concentration; the increase will be greater at hotter bulk lubricant temperatures (Fig. C.1). At each temperature and diamond nanoparticle concentration study, the film temperature (Fig. C.2), minimum film thickness (Fig. C.3), estimated central film thickness (Fig. C.4), average numerical film thickness at the area of contact (Fig. C.5), average and maximum pressure (Fig. C.6 and C.7), and friction coefficient (Fig. C.8) was averaged throughout the one hour simulated study, and saved as part of the parametric study.

As expected, with increasing diamond nanoparticle concentration, and thus increasing lubricant thermal conductivity, the lubricant film temperature consistently decreased (Fig. C.2). It was determined that the hotter bulk lubricant temperatures have a larger thermal conductivity improvement with temperature (Eqn. 4.3), and therefore the relative temperature increase from friction would be expected to decrease with increasing diamond nanoparticle concentrations.

Following the same trend as the temperature, with increasing diamond nanoparticle concentration, and thus increasing lubricant thermal conductivity, the analytical predictions for the minimum (Fig. C.3) and central (Fig. C.4) lubricant film thickness increases. This is expected, as the Hamrock-Dowson empirical equations [18] for film thickness show a proportional increase in film thickness with increasing lubricant viscosity (Eqn. 2.18 and 2.19); this occurs with decreasing temperature. This increase in empirically predicted thickness was thus more profound for hotter bulk lubricant temperature studies, which have more profound thermal conductivity enhancement from the diamond nanoparticles with increasing temperatures.

The average film thickness at the area of contact (Fig. C.4), however, with increasing concentrations of diamond nanoparticles is observed to increase at the cooler 25°C and decrease at the hotter 75°C study. This is plausible, as with hotter temperatures, and thus greater wear, the deviation in the film thickness from the minimum film thickness will be more profound. As most of the wear occurs along the edge of the boundary where the film thickness is at a minimum, and the wear rate will decrease exponentially with increase film thickness, this variation does not have a significant impact of the wear rate predictions.

An investigation of the average pressure over the region of contact shows that, with increasing diamond nanoparticle concentrations, the average pressure (Fig.

C.6) will increase while the maximum pressure (Fig. C.7) will decrease. This is expected, as with thicker lubricant oil film, the greater the pressure is expected to increase from the no-pressure boundary; this was realized by the Reynolds equation that was numerically modeled in Section 2.5. With increasing average pressures, however, the maximum pressure would have to decrease, as the total pressure must remain proportional to the total load; this is observed in Fig. C.7.

Finally, the simulated friction coefficients were studied (Fig. C.8), and as observed both experimentally and numerically (Fig. 3.5 and B.5), increasing nanoparticle concentrations result in less friction. This phenomenon was significantly greater at the hotter bulk lubricant temperature, where the thermal conductivity enhancement would be more profound. This numerical study offers further evidence that the increasing lubricant thermal conductivity caused by the diamond nanoparticle additive is the primary cause of the reduction in friction and wear.

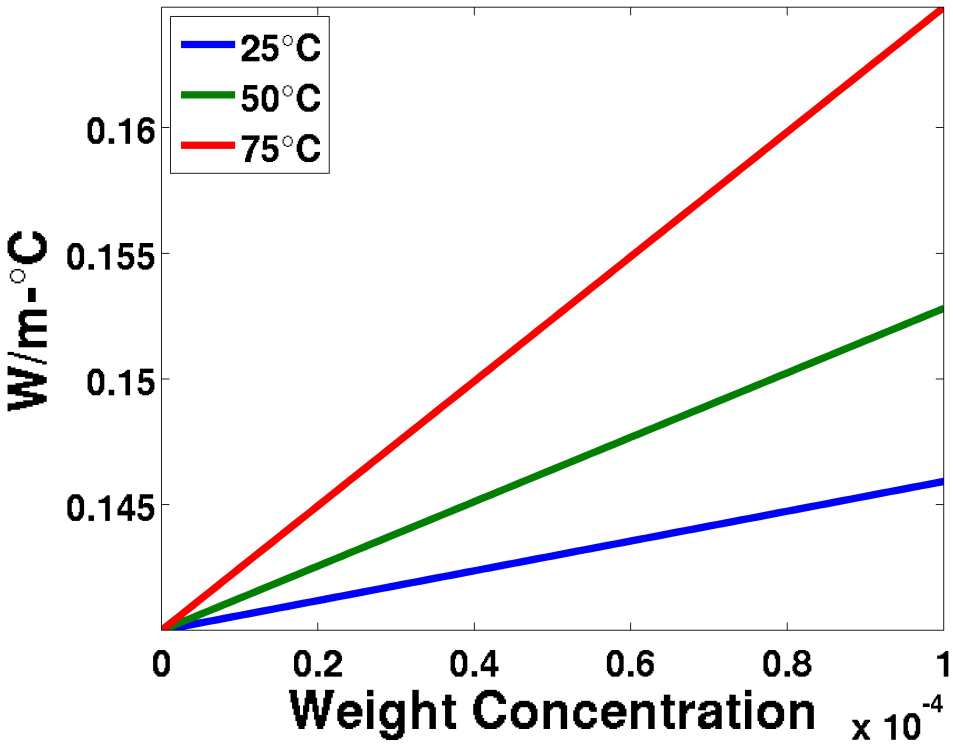

Figure C.1: Numerical sensitivity of the lubricant thermal conductivity (W/m·°C) as a function of diamond nanoparticle concentration.

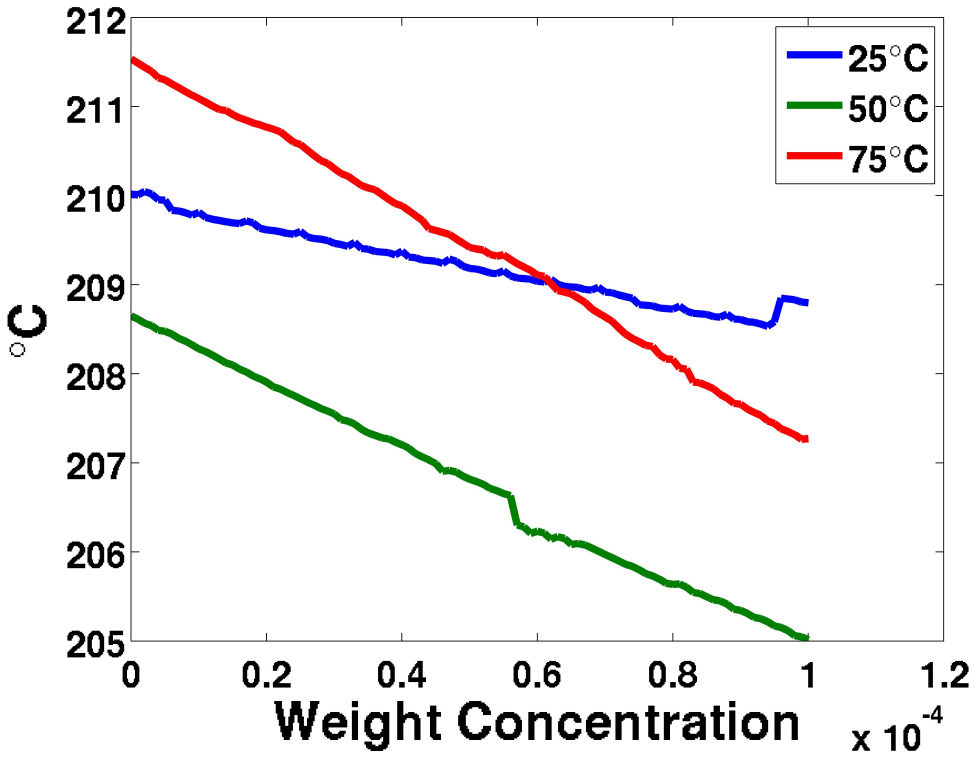

Figure C.2: Numerical sensitivity of the average film temperature over the region of contact as a function of diamond nanoparticle concentration.

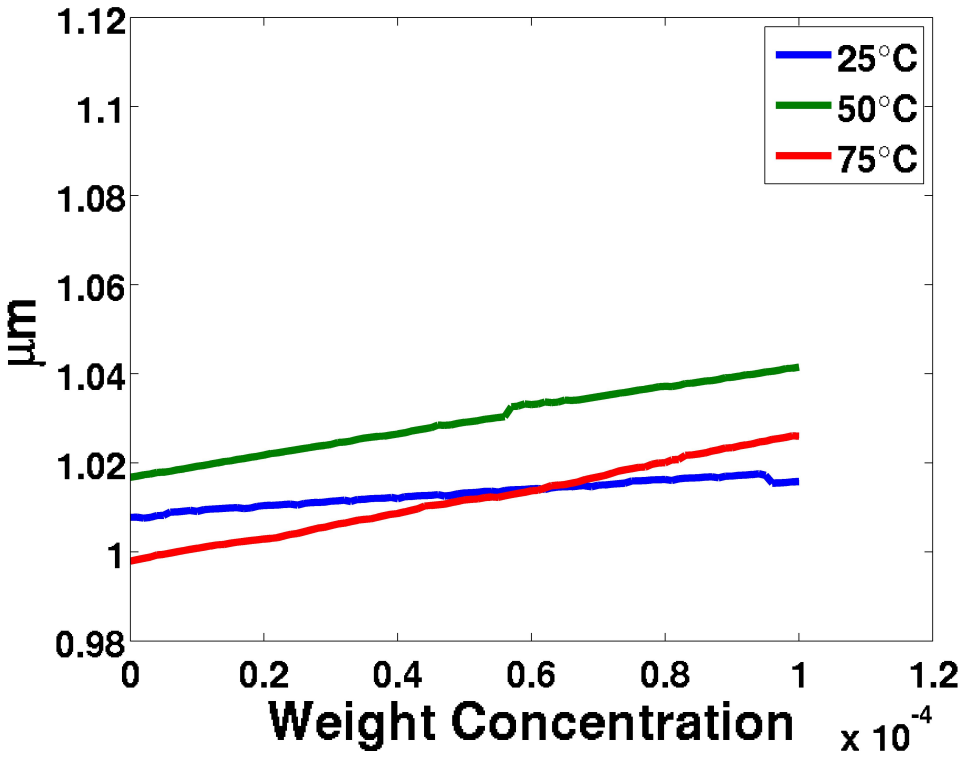

Figure C.3: Numerical sensitivity of minimum film thickness (μm) from Hamrock-Downson (Eqn. 2.18) as a function of diamond nanoparticle concentration.

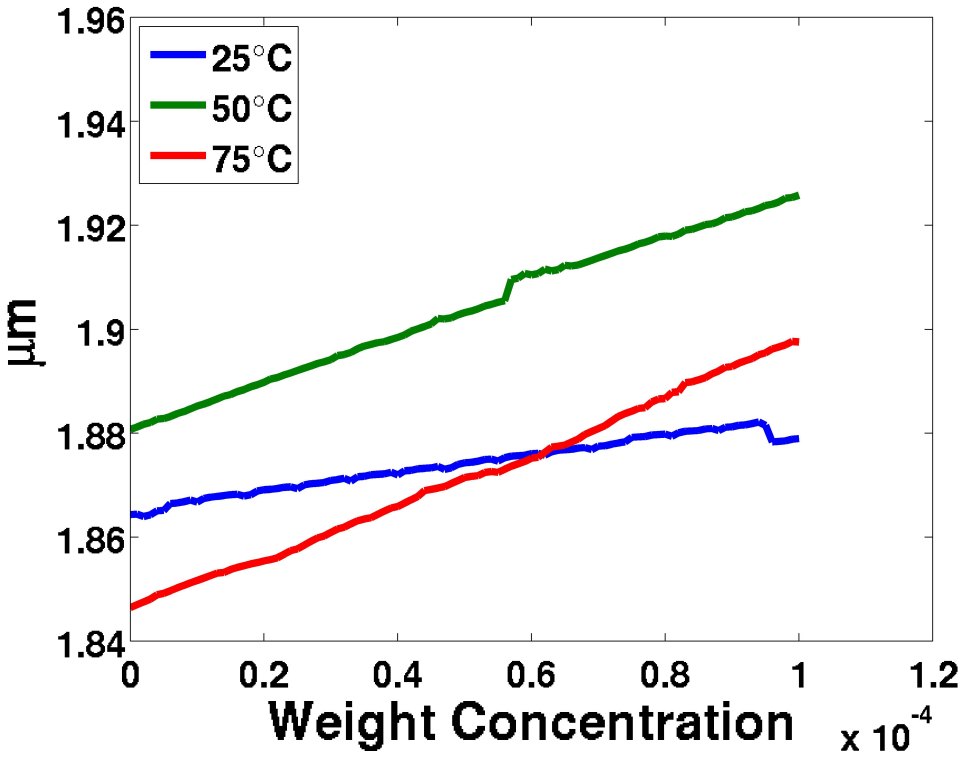

Figure C.4: Numerical sensitivity of the central film thickness (μm) from Hamrock-Downson (Eqn. 2.19) as a function of diamond nanoparticle concentration.

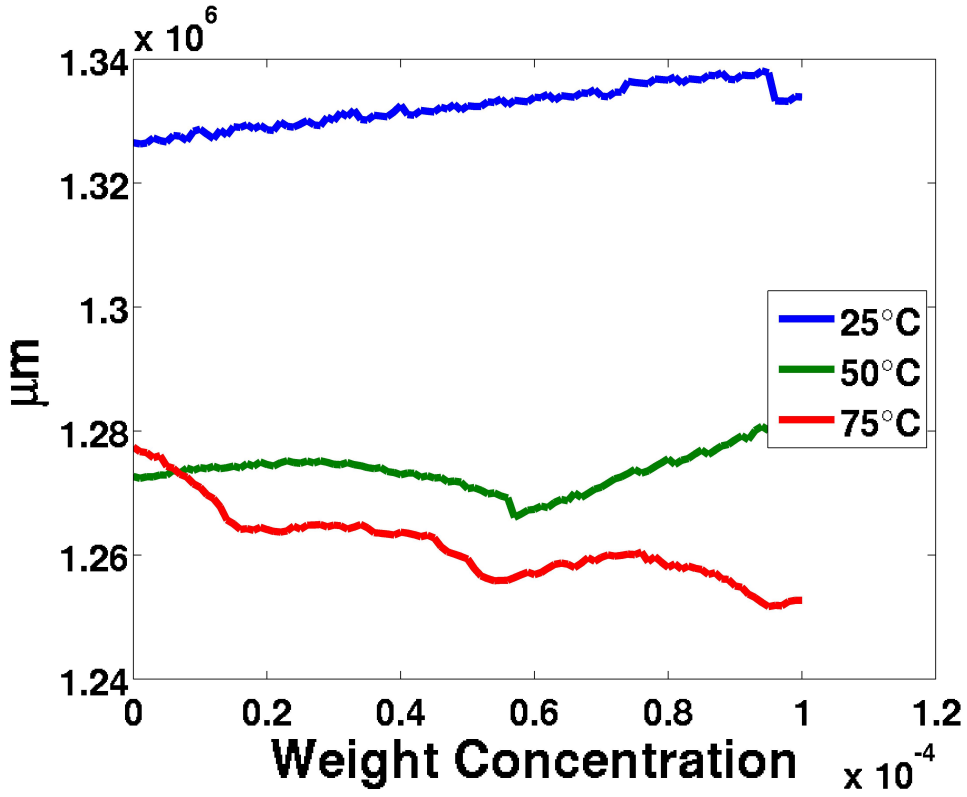

Figure C.5: Numerical sensitivity of average film thickness (μm) over the region of contact as a function of diamond nanoparticle concentration.

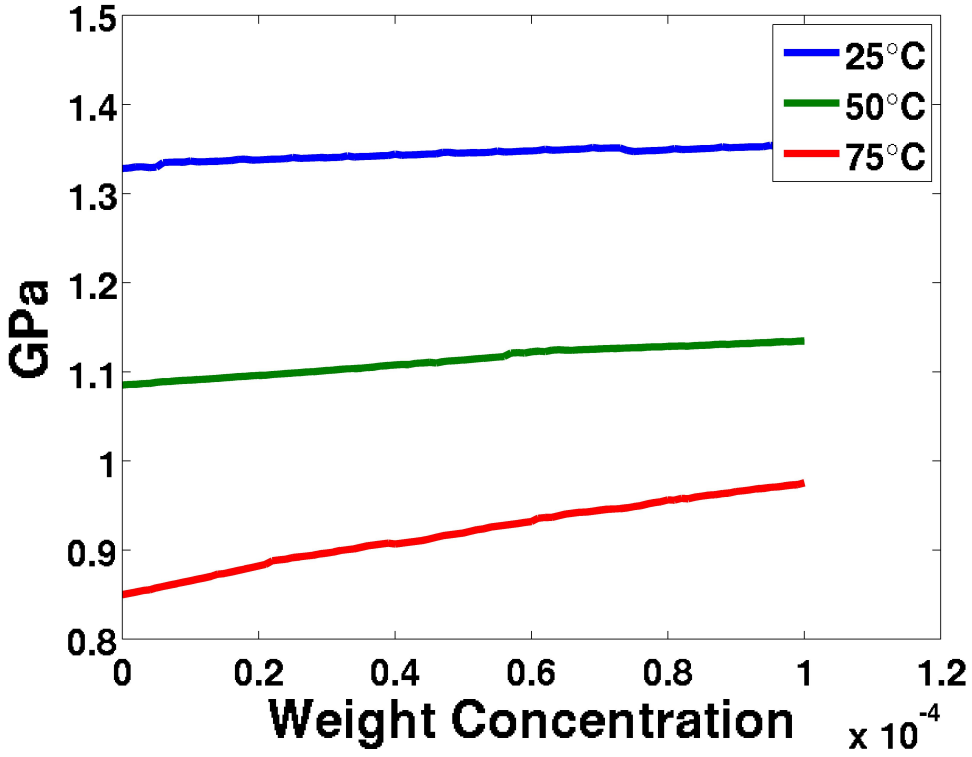

Figure C.6: Numerical sensitivity of the average pressure over the region of contact, solved with the Reynolds equation from Section 2.5, as a function of diamond nanoparticle concentration.

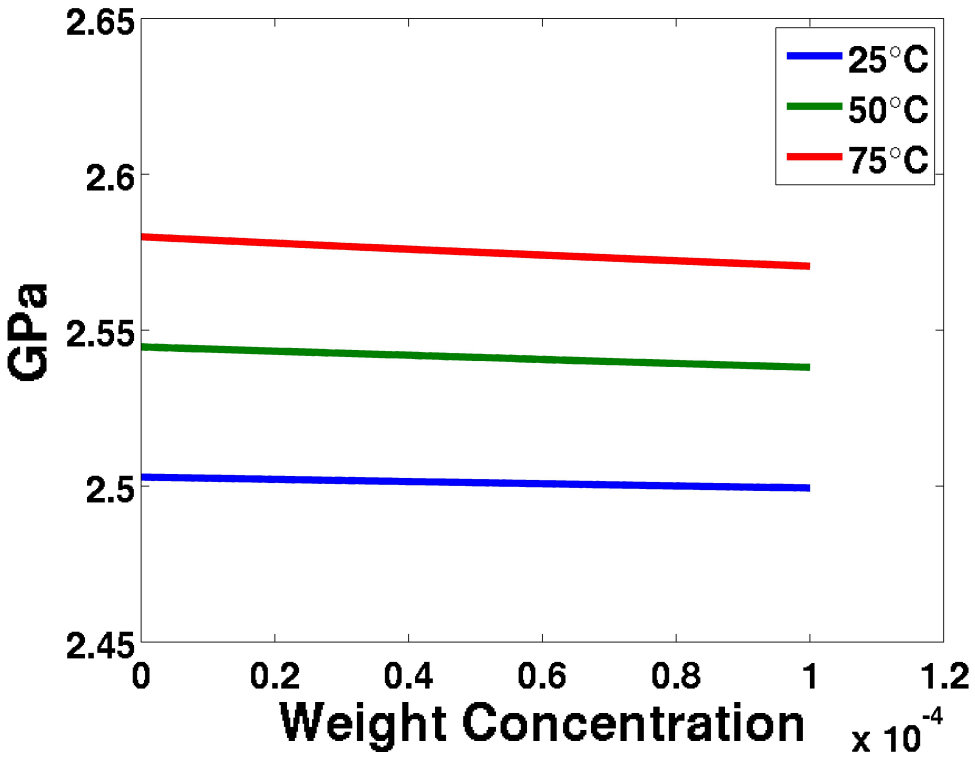

Figure C.7: Numerical sensitivity of the maximum pressure of contact, solved with the Reynolds equation from Section 2.5, as a function of diamond nanoparticle concentration.

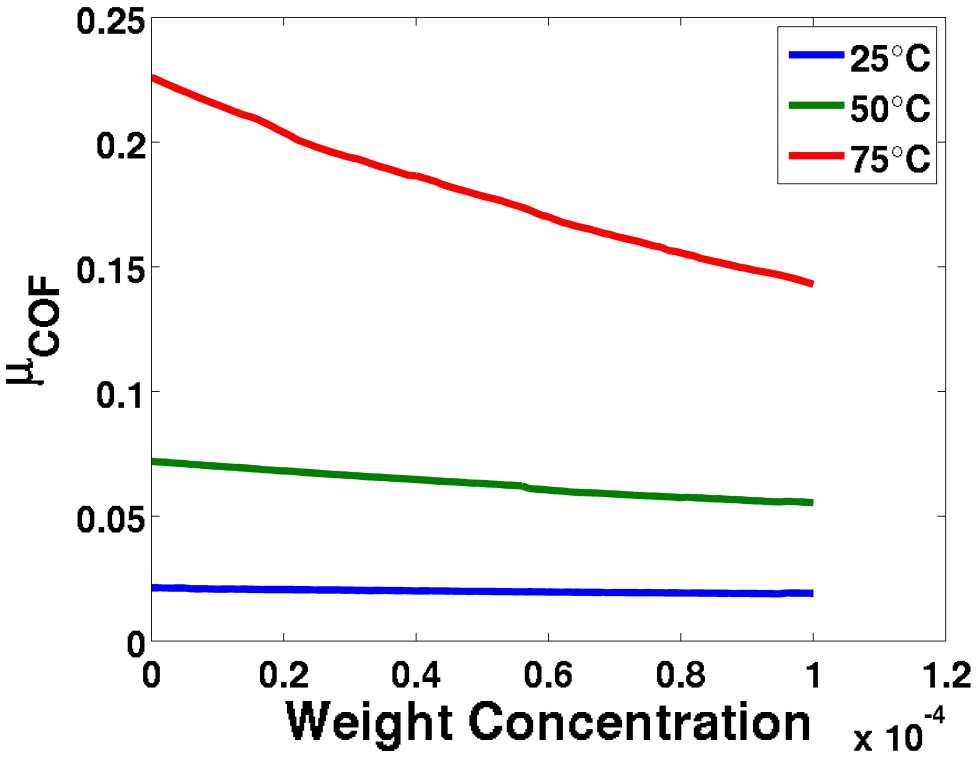

Figure C.8: Numerical sensitivity of friction coefficient μ_{COF} as a function of diamond nanoparticle concentration.

Appendix D

ANALYTICAL WEAR PREDICTION

An effort was made to determine if the probability of wear could be realized analytically, rather than relying on the Monte Carlo empirical solution in Eqn. 2.76. The assumption would be to treat the probability of a given asperity to reach a certain height to follow a normal Gaussian distribution (Eqn. 2.71). If this is the case, the volume of wear that would be lost for a given λ_W value is

$$V_N(\lambda) = \lambda \cdot exp[-\frac{\lambda^2}{2}], \tag{D.1}$$

and therefore the total normalized volume wear is

$$V_N(\lambda_W) = \int_{\lambda_W}^{\infty} \lambda \cdot exp[-\frac{\lambda^2}{2}] d\lambda. \tag{D.2}$$

This equation can be easily solved by partial integration, where

$$\begin{aligned} V_N &= -\int exp[u] du, \\ u &= -\frac{\lambda^2}{2}, \end{aligned} \tag{D.3}$$

and thus

$$V_N(\lambda_W) = [-exp(-\frac{\lambda^2}{2})]_{\lambda_W}^{\infty}, \quad \text{(D.4)}$$

$$V_N(\lambda_W) = exp(-\frac{{\lambda_W}^2}{2}), \quad \text{(D.5)}$$

$$V(\lambda_W) = (\Delta x^2 \sigma) \cdot exp(-\frac{{\lambda_W}^2}{2}), \quad \text{(D.6)}$$

where Δx^2 (m^2) represents the area under contact, σ (m) represents the RMS surface roughness, and V (m^3) is the total wear.

This analytical equation was simulated numerically, but was found to not match the experimental data. This is not surprising, as it requires the assumption that the asperities accurately follows a normal distribution. Unfortunately, the resolution of the optical profilometer is insufficient to realistically get enough asperity data of the surface of untested ball bearings to ascertain the true distribution profile of the surface height. For this reason, the exponential function in Eqn. 2.76, which was verified to accurately simulated four-ball test, is used throughout this study.

Appendix E

MATLAB SOURCE CODE

E.1 WearStudy.m

```
clear
tic

Tb=59;            % Bulk Lubricant Temperature (Centigrade)
maxdepth=5e-8;    % Maximum depth of wear per cycle
maxdt=1e0;        % Maximum time step per cycle
Mx=201;           % X and Z Nodes
W0=88;            % Applied load in lbs for four ball tester
Ra0=15.0e-8;      % Initial surface roughness of ball bearing
nd=0e-4;          % weight fraction of diamond nanoparticles
```

```
totaltime=3600;  % Total Wear Time (seconds)
Ey=210e9;        % Young's Modulus of the tested material in Pa
poisson=.3;      % Poisson Ratio of tested material
R = 0.25;        % Radius of ball bearings in inches
RPM=1200;        % Speed of spindle in rpm
COF=0.10;        % COF of interest
dt0=0e0;         % Initial starting time step (s)
Bw=0.0014;       % Bearing width (meters)
UTC=5e8;         % Ultimate tensile stress of steel (Pa)
SC=0.6;          % Ultimate shear stress coefficient for steel
Ea=-41e-21;      % Diamond Nanoparticle Activation Energy (J)
K0=900;          % Therman Conductivity Constant
k_boltz=1.38e-23; % Boltzman Constant

k=46.6;          % Thermal Conductivity of Material (W/m-K) - Steel
rho=7810;        % Material Density (kg/m^3) - Steel
Cp=475;          % Specific Heat of Material (J/kg-K) - Steel

k_d=2190;        % Thermal Conductivity of Material (W/m-K) - Diamond
rho_d=3530;      % Material Density (kg/m^3) - Diamond
Cp_d=519;        % Specific Heat of Material (J/kg-K) - Diamond

k_oil=0.140;     % thermal conductivity of oil (W/m-K)
Cp_oil=2000;     % specific heat of oil (J/kg-K)
rho_oil=905.75;  % Density of Lubricant (kg/m^3)
```

```
%%%%%%%%%%%%%%%%%%

if mod(Mx,2)==0
    Mx=Mx+1;
end
dx=Bw/Mx;
Xfct=linspace(-Bw/2,Bw/2,Mx);
W=W0*4.44822162/3;  % Divide by 3 and convert to Newtons
R=R*2.54/100;
Rp=R/2;
Eyr=Ey/(1-(poisson^2));
aHertz=((3/2)*W*Rp/Eyr)^(1/3);
omg=RPM*(2*pi/60);
U=0.5*omg*R; % Contact Speed (m/s)
ndx=nd*(1e4);
k_nd=(1+(K0*exp(Ea/(k_boltz*(Tb+273.15)))))*k_oil;
k_lub=(k_oil*(1-ndx))+(k_nd*ndx);
Cp_lub=(Cp_oil*(1-nd))+(Cp_d*nd);
rho_lub=1/(((1-nd)/rho_oil)+(nd/rho_d));
TD=k/(rho*Cp); % Thermal Diffusivity (m2/s)
TD_lub=k_lub/(rho_lub*Cp_lub); % Thermal Diffusivity of oil (m2/s)
kellip=1;                % Elliptical Parameter = a/b
oo=ceil(Mx/2);
Wp=Rp*((UTC*SC/Eyr)^2);
PmaxH=((1.5*W)/(pi*(aHertz^2)));
delH=1.31*(((W^2)/((Eyr^2)*Rp))^(1/3));
```

```
Kh=4*PmaxH/delH;
Rw=Rp*((2*pi*R/(0.5*Bw/4.5)));

% Viscosity
VcSt0=ViscFct(Tb);
b0=0.6363/0.2; % Taken
PVC=(1.216 + (4.143*((log10(VcSt0))^3.0627))+...
((2.848e-4)*(b0^5.1903)*((log10(VcSt0))^1.5976))...
-(3.999*((log10(VcSt0))^3.0975)*((rho_lub/1000)^0.1162)))*(1e-8);

% Calculate initial film thickness
Vpas0=VcSt0*rho_lub*(1e-6);
Vpas=Vpas0;

%%%%%%%%%%%%%%%%%%%

a=aHertz;
L=U*a/(2*TD); % Peclet Number (dimensionless)
if L<0.1
    Tf=0.25*COF*W*U/(k*a);
elseif L>0.1 && L<5
    foo=0.35+((5-L)*(0.5/4.9));
    Tf=foo*0.25*COF*W*U/(k*a);
else
    Tf=(0.308*COF*W*U/(k*a))*(sqrt(TD/(U*a)));
end
```

```
foo=0:0.001:1; foo=foo-(foo.^2); foo=mean(foo);
HcHD=Rw*2.69*((U*Vpas/(Eyr*Rp))^0.67)*((PVC*Eyr)^0.53)*...
((W/(Eyr*(Rp^2)))^-0.067)*(1-(0.061*exp(-0.73*kellip)));
HcHD0=HcHD; Fluc=1; ct=0;
while Fluc>(1e-2)
    ct=ct+1;
    dT=foo*COF*(W/(pi*(aHertz^2)))*HcHD*U/(2*k_lub); Ti=Tb+Tf+dT;
    VcSt=ViscFct(Ti); Vpas=VcSt*rho_lub*(1e-6);
    HcHD=Rw*2.69*((U*Vpas/(Eyr*Rp))^0.67)*((PVC*Eyr)^0.53)*...
    ((W/(Eyr*(Rp^2)))^-0.067)*(1-(0.061*exp(-0.73*kellip)));
    Fluc=abs(HcHD-HcHD0)/HcHD0;
    HcHD0=HcHD;
    FlucFct(ct)=Fluc;
    if ct>10000
        Fluc=0;
        ['Trouble!!!']
    end
end

H0HD=Rw*3.63*((U*Vpas/(Eyr*Rp))^0.68)*((PVC*Eyr)^0.49)*...
((W/(Eyr*(Rp^2)))^-0.073)*(1-(exp(-0.68*kellip)));

wear=zeros(Mx,Mx);
```

```
% Indent Function
indent=zeros(Mx,Mx);
for ii=1:Mx
    for jj=1:Mx
        rrp=sqrt((Xfct(ii)^2)+(Xfct(jj)^2));
        theta=asin(rrp/R);
        indent(ii,jj)=R*(1-(cos(theta)));
    end
end
Rfct=zeros(Mx,Mx);
for ii=1:Mx
    for jj=1:Mx
        Rfct(ii,jj)=sqrt((Xfct(ii)^2)+(Xfct(jj)^2));
    end
end

%%%%%%%%%%%%%%%%%

% Find a default pressure function to start iteration
[aa,bb]=find(Rfct<aHertz); Laa=length(aa);
PfctH=zeros(Mx,Mx);
for uu=1:Laa
    ii=aa(uu); jj=bb(uu);
    PfctH(ii,jj)=PmaxH*(1-((Rfct(ii,jj)/aHertz)^2));
end
```

```
[h0,Pfct00]=gethfct(indent,wear,dx,Vpas,Vpas0,H0HD,U,...
PfctH,R,Kh,PVC,Tb,Ti);

h=h0; havg=h;
Pfct0=Pfct00; Pfct=Pfct00;

a=aHertz;
time=0;
dTavg=0;
NL=['\n'];
TS=0;

dt=dt0;
while (time<totaltime)
    TS=TS+1;
    time=time+dt;

    [a0,kellip]=wearscar(wear,dx,Ra0/2);
    aD=a0*2; a=a0;
    if (a<aHertz)
        a=aHertz;
    end

    %%%%%%%%%%%%%%%%%%%%%%%%%%%%
```

```
L=U*a/(2*TD); % Peclet Number (dimensionless)
if L<0.1
    Tf=0.25*COF*W*U/(k*a);
elseif L>0.1 && L<5
    foo=0.35+((5-L)*(0.5/4.9));
    Tf=foo*0.25*COF*W*U/(k*a);
else
    Tf=(0.308*COF*W*U/(k*a))*(sqrt(TD/(U*a)));
end

foo=0:0.001:1; foo=foo-(foo.^2); foo=mean(foo);
HcHD=Rw*2.69*((U*Vpas/(Eyr*Rp))^0.67)*((PVC*Eyr)^0.53)*...
((W/(Eyr*(Rp^2)))^-0.067)*(1-(0.061*exp(-0.73*kellip)));
HcHD0=HcHD; Fluc=1; ct=0;
while Fluc>(1e-2)
    ct=ct+1;
    dT=foo*COF*(W/(pi*(aHertz^2)))*HcHD*U/(2*k_lub); Ti=Tb+Tf+dT;
    VcSt=ViscFct(Ti); Vpas=VcSt*rho_lub*(1e-6);
    HcHD=Rw*2.69*((U*Vpas/(Eyr*Rp))^0.67)*((PVC*Eyr)^0.53)*...
    ((W/(Eyr*(Rp^2)))^-0.067)*(1-(0.061*exp(-0.73*kellip)));
    Fluc=abs(HcHD-HcHD0)/HcHD0;
    HcHD0=HcHD;
    FlucFct(ct)=Fluc;
```

```
    if ct>10000
        Fluc=0;
        ['Trouble!!!']
    end
end

H0HD=Rw*3.63*((U*Vpas/(Eyr*Rp))^0.68)*((PVC*Eyr)^0.49)*...
((W/(Eyr*(Rp^2)))^-0.073)*(1-(exp(-0.68*kellip)));

%%%%%%%%%%%%%%%%%%%%%%%%%%%%%

[aa,bb]=find(Rfct<(a-dx)); Laa=length(aa);

PfctHt=zeros(Mx,Mx);
for uu=1:Laa
    ii=aa(uu); jj=bb(uu);
    PfctHt(ii,jj)=((1.5*W)/(pi*(a^2)))*(1-((Rfct(ii,jj)/a)^2));
end

[h,Pfct]=gethfct(indent,wear,dx,Vpas,Vpas0,H0HD,U,Pfct00,R,...
Kh,PVC,Tb,Ti);

[aa,bb]=find(Rfct<a); Laa=length(aa);
```

```
RaOP=Ra0; MW=(mean(mean(wear(aa,bb))));
for uu=1:Laa
    ii=aa(uu); jj=bb(uu);
    RaOP=RaOP+((wear(ii,jj)-MW)^2);
end
RaOP=2*sqrt((RaOP/Laa)+(Ra0^2));
RaExp=((0.0027125069*time) + (0.8618890914))*(1e-6);

Ra=Ra0;

LamFct=(h+Wp).*(Ra.^-1);
LamRat=0.2763*exp(-(1.6754)*LamFct);
wearrate=(LamRat.*Ra.*(U*dx))/(dx^2);
for ii=1:Mx
    for jj=1:Mx
        if wearrate(ii,jj)<0
            wearrate(ii,jj)=0;
        end
    end
end
% The wear rate is in m/s in this model
WRt=(sum(sum(wearrate)))*(dx^2)*(1e18);
WRavg=(sum(sum(wear)))*(dx^2)*(1e18)/time;
```

```
maxwearrate=max(max(wearrate));
if maxwearrate>0
    dt=maxdepth/maxwearrate;
else
    dt=totaltime;
end
if (dt>maxdt)
    if (mod(time,maxdt)~=0)
        dt=maxdt-(mod(time,maxdt));
    else
        dt=maxdt;
    end
end
wear=wear+(wearrate*dt);

COFrat=0.5*exp(-1.2847*LamFct);
F_wear=UTC*SC*(sum(sum(COFrat)))*(Bw^2)/3;
COFw=F_wear/W;

WearData(TS)=(dx^2)*sum(sum(wear));
WearRateData(TS)=(dx^2)*sum(sum(wear))/time;
WearRateSimData(TS)=(dx^2)*sum(sum(wearrate));
COFdata(TS)=COFw;
aData(TS)=aD;
kellipData(TS)=kellip;
TimeData(TS)=time;
```

```
    RaData(TS)=mean(mean(Ra));
    RaOPdata(TS)=RaOP;
    RaExpData(TS)=RaExp;
    PressureMaxData(TS)=max(max(Pfct));
    PressureAvgData(TS)=mean(mean(Pfct));
    PressureScarData(TS)=mean(mean(Pfct(aa,bb)));
    hminData(TS)=H0HD;
    TempData(TS)=Ti;
    LamData(TS)=mean(mean(LamFct(aa,bb)));
    LamDataMax(TS)=max(max(erfc(LamFct(aa,bb))));
    hData(TS)=mean(mean(h(aa,bb)));
end

if nd==0
    filestr=['DataT' num2str(Tb) '.mat'];
else
    ndx=(1e-4)/nd;
    filestr=['DataT' num2str(Tb) 'd' num2str(ndx) '.mat'];
end

save(filestr)
toc
```

Figure E.1: Highest level flowchart of four-ball test wear model. The process takes place within the *WearStudy.m* script.

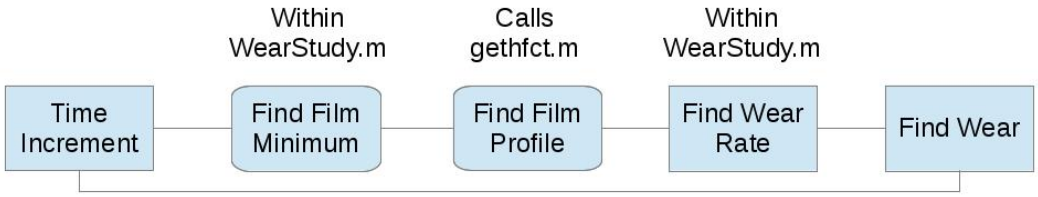

Figure E.2: Flowchart representation of a single time-step. The process takes place within the *WearStudy.m* script.

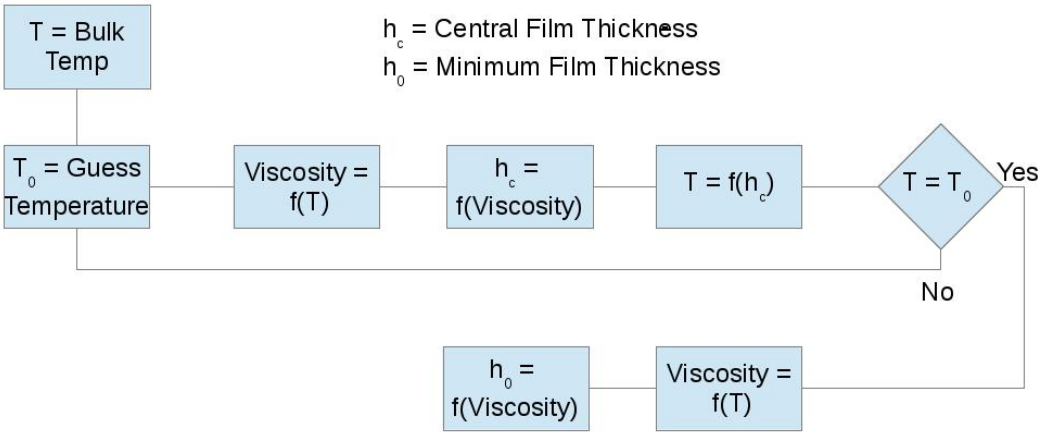

Figure E.3: Flowchart representation of the iterative process of determining the lubricant film temperature, viscosity, and minimum thickness. The process takes place within the *WearStudy.m* script.

E.2 gethfct.m

```
function [hOut,PfctOut]=gethfct(indent,wear,dx,Vpas,Vpas0,...
H0HD,U,Pfct00,R,Kh,PVC,Tb,Ti)

Pfct0=Pfct00;

Mx=length(Pfct00); %oo=ceil(Mx/2);
ElastFct=zeros(Mx,Mx);

wear2=zeros(Mx,Mx);
for ii=1:Mx
    foo=(sum(wear(ii,:)))*(dx/(pi*R));
    for jj=1:Mx
        wear2(ii,jj)=foo;
    end
end

testbreak=0; del=1;
while del>1e-1
    testbreak=testbreak+1;
    ElastFct0=ElastFct;
    hFoo=wear+wear2+(indent*2)+ElastFct;
    h=hFoo-(min(min(hFoo)))+H0HD;
```

```
    [Pfct]=findP(h,Mx,dx,Vpas,Vpas0,Tb,Ti,U,PVC,Pfct0);
    ElastFct=Pfct/(Kh);

    del=abs(mean(mean(ElastFct-ElastFct0)))/(mean(mean(ElastFct)));
    Pfct0=Pfct;
    if testbreak<5
        del=1;
    elseif testbreak>25
        del=0;
        fprintf('Failure to Converge!!!!!!!');
    end
end

hFoo=wear+wear2+(indent*2)+ElastFct;
h=hFoo-(min(min(hFoo)))+H0HD;

hOut=h;
PfctOut=Pfct;

end
```

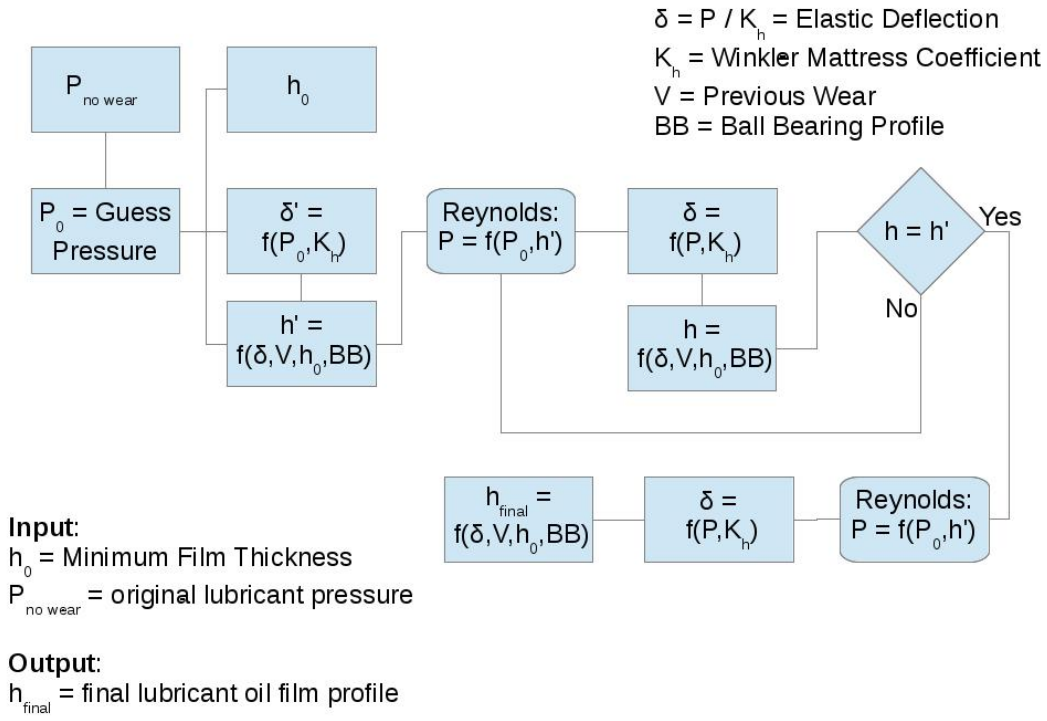

Figure E.4: Flowchart representation of the determination of the lubricant film-thickness profile, which is performed within the *gethfct.m* function.

E.3 findP.m

```
function [PfctOut]=findP(h,Mx,dx,Vpas,Vpas0,Tb,Ti,U,PVC,Pfct0)

Pfct=Pfct0; DifMat=zeros(Mx,Mx,5);
AP=Roelands(Tb,Ti,PVC,Vpas,Vpas0,Pfct0);

for ii=2:(Mx-1)
    for jj=2:(Mx-1)
        uu1=(h(ii,jj)^3)/(dx^2);
        uuX=((1.5/dx)*(h(ii,jj)^2)*((h(ii+1,jj)-h(ii-1,jj))/(2*dx)));
        uuY=((1.5/dx)*(h(ii,jj)^2)*((h(ii,jj+1)-h(ii,jj-1))/(2*dx)));
        DifMat(ii,jj,1)=-((2/(dx^2))*(h(ii,jj)^3))-((2/(dx^2))*...
        (h(ii,jj)^3));              % A
        DifMat(ii,jj,2)=uu1+uuX;    % E
        DifMat(ii,jj,3)=uu1-uuX;    % W
        DifMat(ii,jj,4)=uu1+uuY;    % N
        DifMat(ii,jj,5)=uu1-uuY;    % S
    end
end
```

```
for ii=2:(Mx-1)
    for jj=2:(Mx-1)
        BB=6*Vpas*U*(((h(ii+1,jj)-h(ii-1,jj))/(2*dx))+...
        ((h(ii,jj+1)-h(ii,jj-1))/(2*dx)))*0.5;
        BB=BB*(exp(AP(ii,jj)));
        foo=(DifMat(ii,jj,2)*Pfct0(ii-1,jj));
        foo=foo+(DifMat(ii,jj,3)*Pfct0(ii+1,jj));
        foo=foo+(DifMat(ii,jj,4)*Pfct0(ii,jj-1));
        foo=foo+(DifMat(ii,jj,5)*Pfct0(ii,jj+1));
        Pfct(ii,jj)=(BB-foo)/(DifMat(ii,jj,1));
    end
end

PfctOut=abs(Pfct);
end
```

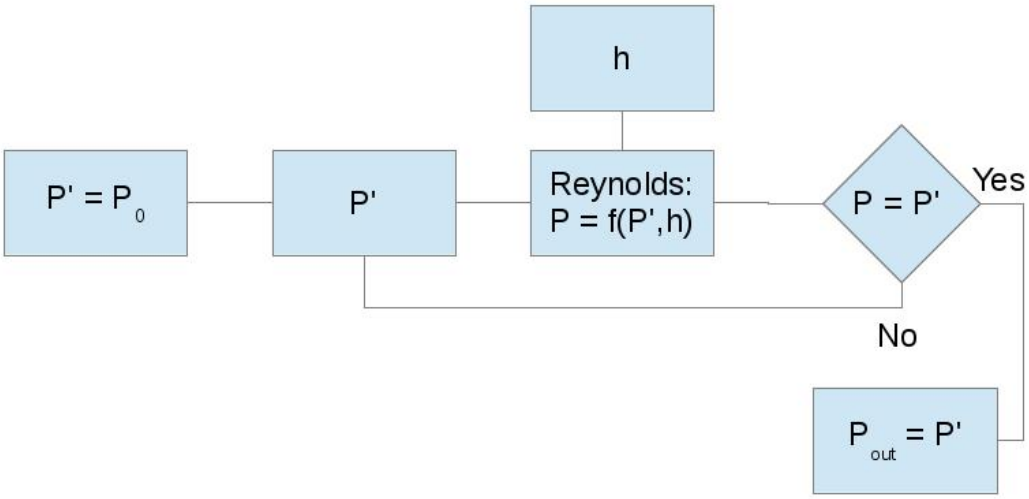

Figure E.5: Flowchart representation of the determination of the lubricant pressure profile with the Reynolds equation, which is performed within the *findP.m* function.

E.4 Roelands.m

```
function [AP]=Roelands(TbC,TiC,PVC,Vpas,Vpas0,Pfct)

Ti=TiC+273.15; Tb=TbC+273.15;

foo=((log(Vpas))+9.67);
foo0=((log(Vpas0))+9.67);

Z=PVC/((5.1e-9)*foo0); %Z=0.68;
beta=GetBeta;
S0=beta*(Tb-138)/foo;
AP=(((Ti-138)/(Tb-138)).^-S0).*(((1+(5.1e-9*Pfct)).^Z)-1)*foo;

end
```

E.5 GetBeta.m

```
function [beta]=GetBeta

Tfct=25:5:75; LL=length(Tfct);
ViscDat=[105 87.5 65 50.5 41.5 32.5 28.5 24.5 21.5 19 16];

ViscRat=ViscDat(2:LL)/ViscDat(1);
ViscLog=log(ViscRat);
dTemp=Tfct(2:LL)-Tfct(1);

BetaFct=-ViscLog.*(dTemp.^-1);

beta=mean(BetaFct);

end
```

E.6 ViscFct.m

```
function [VcSt]=ViscFct(Tc)

T=Tc+273.15;
Tfct=25:5:75;
ViscDat=[105 87.5 65 50.5 41.5 32.5 28.5 24.5 21.5 19 16];

Tfct=Tfct+273.15;
foo=abs(T-Tfct);
a=find(foo==min(foo)); a=a(1);

if min(foo)==0
    b=a;
else
    if a==1
        b=2;
    elseif a==length(Tfct)
        b=length(Tfct)-1;
    else
        fooT=((T-Tfct(1))/5)+1;
        a=floor(fooT);
        b=ceil(fooT);
    end
end
```

```
if a==b
    VcSt=ViscDat(a);
else
    T1=Tfct(a); v1=ViscDat(a);
    T2=Tfct(b); v2=ViscDat(b);
    Z1=v1 + 0.7 + exp((-1.47-(1.84*v1)-(0.51*(v1^2))));
    Z2=v2 + 0.7 + exp((-1.47-(1.84*v2)-(0.51*(v2^2))));
    B=((log10(log10(Z1)))-(log10(log10(Z2))))/...
    ((log10(T2))-(log10(T1)));
    A=(B*log10(T1))+(log10(log10(Z1)));

    Z=10^(10^(A-(B*(log10(T)))));
    VcSt=(Z-0.7)-exp(-0.7487-(3.295*(Z-0.7))+...
    (0.6119*((Z-0.7)^2))-(0.3193*((Z-0.7)^3)));
end

end
```

E.7 wearscar.m

```
function [a,kellip]=wearscar(wear,dx,Ra0)


th=Ra0/2;
Xfct=max(wear); var=find(Xfct>th);
if length(var)>1
    deltX=(max(var)-min(var)+1)*dx;
else
    deltX=dx;
end
Xfct=max(wear'); var=find(Xfct>th);
if length(var)>1
    deltY=(max(var)-min(var)+1)*dx;
else
    deltY=dx;
end
a=(deltX+deltY)/2; kellip=deltX/deltY;
if kellip>1
    kellip=1/kellip;
end


end
```

Introduction:

The purpose of this model is to numerically simulate with finite difference the process of sliding contact similar to what occurs during an ASTM D-4172 four-ball test. It was written in the Matlab programming language. By running this simulation, it is feasible to numerically predict the evolution of wear from sliding contact in a lubricated four-ball test.

Definition of Files:

- WearStudy.m:
  - This is the main program script for the model, running through all of the steps to determine the wear rate and total wear
  - This script can be converted to a function for a parametric study, if needed
  - Function calls on the “gethfct.m” function to determine the film thickness profile
- gethfct.m:
  - This function is used to iterate for the film-thickness profile
  - Function calls on the “findP.m” function to determine the pressure as it iterates for the film thickness profile
  - The function takes the guess for the pressure, predicts the film thickness, determines the pressure for the given film-thickness profile, and use the pressure to adjust the film-thickness; this iteration runs until there is convergence on the lubricant film-thickness and pressure
  - Output:
    - hOut: output final lubricant film-thickness profile
    - PfctOut: output final lubricant film pressure profile
- findP.m:
  - Determines the pressure for an input lubricant film-thickness profile
    - Assumes the film thickness is constant within the function
  - Uses a “guess” pressure for the nearest-neighbor pressure values to solve for the new pressure value at a given finite difference node
    - Iteration is used until the function converges on a pressure profile
  - Function calls on the “Roelands.m” function to determine the pressure-viscosity exponential coefficient, to calculate the true pressure as a function of the “guess” pressure during the iterative step
  - Output:
    - PfctOut: the output pressure function

- Roelands.m:
  - Calculates the pressure-viscosity exponential increase
    - $\mu = \mu_0 e^{\alpha * P}$
  - Determines the change in viscosity as a function of pressure
  - Calls on the “GetBeta” function
  - Output:
    - AP: the α*P term as a function of pressure
- GetBeta.m:
  - Calculates the viscosity-temperature exponential decay coefficient
    - $\mu(T) = \mu_0 e^{\beta(T - T_0)}$
  - Uses experimental data for the lubricant oil embedded into the function
  - Output: beta
- ViscFct.m:
  - Determines the kinematic viscosity for a given input temperature (in Centigrade)
  - Uses experimental viscosity-temperature data embedded in the function
  - Output:
    - VcSt: the kinematic viscosity in centistokes
- wearscar.m:
  - Determines the wear profile, and calculates the wear scar size and ellipticity
  - Wear is recognized when the wear exceeds the RMS surface roughness
  - The ellipticity consistently remains 1 throughout the model
  - Output:
    - a: the radius of the wear scar
    - kellip: the ellipticity of the wear scar (consistently 1)

Layout of the Code:

- Input Parameters
  - This is where the material and simulation parameters are inputted by the user
  - The first set are separated, as sometimes Matlab functions can be built with this information
    - These parameters, versus the function line, can be commented out if the script will be used as a function
    - Tb=59; % Bulk Lubricant Temperature (Centigrade)
      - This is the bulk lubricant oil temperature
      - The model will calculate localized heating from the pressure
    - maxdepth=5e-8; % Maximum depth of wear per cycle
      - The time step will adjust itself to ensure no more than this much wear (in meters of depth) will occur in a given time step
    - maxdt=1.0e0; % Maximum time step per cycle
      - The maximum time step in seconds, if a longer time step is calculated for the maximum wear depth per time step
    - Mx=201; % X and Z Nodes
      - The number of finite difference nodes in the X and Y direction (for Mx^2) nodes total
    - W0 = 88; % The load (in lbs) of the 4-ball test
    - Ra0=15.0e-8; % Initial surface roughness of ball bearing
    - nd = 0; % weight fraction of diamond nanoparticles
      - Set to 1e-4 for the standard 0.01% weight concentration
- Other model parameters
  - totaltime=3600; % Total Wear Time (seconds)
    - The total time (in seconds) of the sliding contact of the four-ball test
  - Ey=210e9; % Young’s Modulus of the ball-bearing material (Pa)
  - poisson=.3; % Poisson Ratio of ball-bearing material
  - R = 0.25; % Radius of ball bearings in inches
    - Code will convert it to metric later
  - RPM=1200; % Speed of spindle in rpm
  - COF=0.10; % COF of interest

- dt0 = 0e0; % Initial starting time-step
- Bw=0.0014; % Bearing width (meters)
  - This is the length of the domain being analyzed
  - If it is made larger, the finite difference units will have lower resolution unless more nodes are added (which increases computational resources exponentially)
- UTC=5e8; % Ultimate Tensile Strength of Steel (Pa)
- SC = 0.6; % Ratio of ultimate strength in shear over ultimate tensile stress
- Ea=-41e-21; % Diamond Nanoparticle Activation Energy (J)
- K0=900; % Therman Conductivity Constant
- k_boltz=1.38e-23; % Boltzman Constant (Joules / Kelvin)

- Input of ball-bearing material properties
  - k=46.6; % Thermal Conductivity of Material (W/m-K) – Steel
  - rho=7810; % Material Density (kg/m^3) – Steel
  - Cp=475; % Specific Heat of Material (J/kg-K) – Steel
- Input of diamond nanoparticle material properties
  - k_d=2190; % Thermal Conductivity of Material (W/m-K) – Diamond
  - rho_d=3530; % Material Density (kg/m^3) – Diamond
  - Cp_d=519; % Specific Heat of Material (J/kg-K) – Diamond
- Input of oil thermal properties
  - k_oil=0.140; % thermal conductivity of oil (W/m-K)
  - Cp_oil=2000; % specific heat of oil (J/kg-K)
  - rho_oil=905.75; % Material Density (kg/m^3) – Oil

- Calculate Parameters from Input
  - Make *Mx* an odd number
    - This assures there is a finite difference node that is at the center of the domain
    - if mod(Mx,2)==0
      Mx=Mx+1;
      end
  - dx=Bw/Mx;
    - The distance increment (meters) between each finite difference node

- Xfct=linspace(-Bw/2,Bw/2,Mx);
  - Generates distance function, used to calculate the oil film thickness
- W=W0*4.44822162/3; % Divide by 3 and convert to Newtons
  - Convert the force in pounds to Newtons, and divides by 3 because the force is evenly distributed over 3 ball bearings
- R=R*2.54/100;
  - Converts the radius of each ball bearing from inches to meters
- Rp=R/2;
  - $\frac{1}{R'}=\frac{1}{R_A}+\frac{1}{R_B}$, and $R_A=R_B=R$, therefore $R'=\frac{R}{2}$
  - 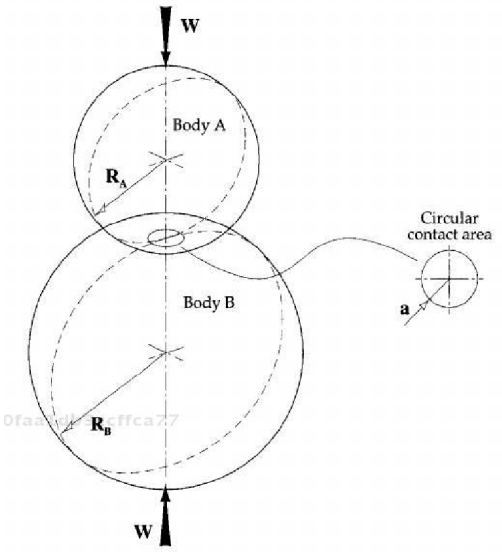

  - Reduced Radius, for Hertz Contact calculations
- Eyr=Ey/(1-(poisson^2));
  - $\frac{1}{E'}=\frac{1}{2}[\frac{1-\nu_A^2}{E_A}+\frac{1-\nu_B^2}{E_B}]$, and $E_A=E_B=E$, $\nu_A=\nu_B=\nu$, therefore $E'=\frac{E}{1-\nu^2}$
  - Calculates the reduced Young's modulus, for solving Hertzian contact equations
- aHertz=((3/2)*W*Rp/Eyr)^(1/3);
  - Uses Hertz's contact equations to calculate the radius of the area of contact, assuming all elastic deformation
  - $a=(\frac{3WR'}{2E'})^{\frac{1}{3}}$

- omg=RPM*(2*pi/60);
  - Converts the top-ball speed from revolutions per minute to radians per second
- U=0.5*omg*R; % Contact Speed (m/s)
  - Calculates the linear speed of sliding contact at the full specified speed
- ndx=nd*(1e4);
  - Determines the equivalent mass ratio of the 0.01% diamond nanofluid solution to neat mineral oil necessary to get the equivalent mass ratio of the lubricant being simulated
- k_nd=(1+(K0*exp(Ea/(k_boltz*(Tb+273.15)))))*k_oil;
  - Determines the thermal conductivity of the 0.01% weight concentration diamond nanoparticle solution only
  - Based on experimental studies, and follows an Arrhenius-like temperature dependence
- k_lub=(k_oil*(1-ndx))+(k_nd*ndx);
  - Thermal conductivity of lubricant with diamond nanoparticles
  - Derived as an average of mass functions of the neat mineral oil and the 0.01% weight concentration of diamond nanoparticles, to achieve the desired concentration of interest
- Cp_lub=(Cp_oil*(1-nd))+(Cp_d*nd);
  - Specific heat of lubricant with diamond nanoparticles (derived analytically)
- rho_lub=1/(((1-nd)/rho_oil)+(nd/rho_d));
  - Density of lubricant with diamond nanoparticles (derived analytically)
- TD=k/(rho*Cp); % Thermal Diffusivity (m^2/s)
  - The thermal diffusivity of the ball bearing, calculated from the input conductivity, heat capacity, and density
- TD_lub=k_lub/(rho_lub*Cp_lub); % Thermal Diffusivity of oil (m^2/s)
  - Uses lubricant parameters to allow for mixing of diamond nanoparticles
- kellip=1; % Elliptical Parameter = a/b
  - The initial ellipticity of the contact area
- oo = ceil(Mx/2);
  - Find the array position in the center of the contact area
  - Mx will consistently be an odd number

- Calculate the assumed added length W_P (meters) to take into consideration the shear yield stress of the ball bearing material (Greenwood Williamson theory)
  - $W_P = R'\left(\frac{G_{yield}}{E_y'}\right)^2$
    - where G_{yield} is the shear yield strength of the ball-bearing material (Pa)
- Maximum Hertzian pressure
  - $P_{Hertzian} = \frac{3}{2}\frac{W}{\pi a_{Hertz}^2}$
- Calculate the Hertzian deflection
  - $\delta_{Hertz} = \left(\frac{9}{16}\frac{W^2}{Ey'^2 R'}\right)^{\frac{1}{3}}$
- Calculate the ratio of deflection for pressure
  - $K_h = \frac{P_{Hertzian}}{\delta_{Hertz}}$
  - Uses the Winkler Mattress model to calculate the elastic deformation for a given fluid pressure by this ratio
  - 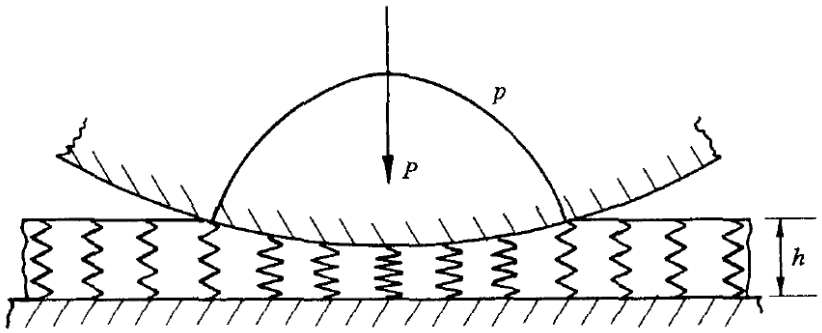

- Calculate the normalized radius R_w
  - To find the equivalent reduced radius, to normalize the dimensionless film thickness
    - To take into account that the contact is stationary sliding; Hamrock-Downson assumes moving rolling contact
  - Rw=Rp*((2*pi*R/(0.5*Bw/4.5))); $R_w = R'\frac{2\pi R}{0.5\frac{B_w}{4.5}}$
  - Ratio of the length of a revolution of the ball, over the approximate wear scar length
    - 4.5 is the minimum ratio of wear scar over total domain width (required to meet the Swift-Steiber boundary condition)

- Calculate the pressure-viscosity coefficient (See viscosity section for details)
  - $\alpha_{PVC} = 1.216 + 4.143(\log_{10} v)^{3.0627} + (\frac{2.848}{10^4} b_0^{5.1903})(\log_{10} v)^{1.5976} + 3.999\,\rho_{density}^{0.1162}(\log_{10} v)^{3.0975}$
    - where v is in cSt, and b_0 is the ASTM slope coefficient times 5
  - For this oil, the ASTM slope coefficient b_0 is found to be 0.6363
  - The viscosity is calculated with the viscosity function (see Viscosity section)
  - This coefficient is used to find the viscosity changes with pressure following Barus' law:
    - $v = v_0 \exp[\alpha_{PVC} P]$
    - Breaks down when P < 0.5 Gpa
      - Roeland's theory is used for the Reynolds Equation Solver, where the pressure can exceed this level (See Roeland's Equation section)
- Calculate the initial minimum and central film thickness (see loop for details of equation)
  - The minimum film thickness is used in the iterative solver to find the film thickness function
    - Determined from the Hamrock Dowson empirical equations
    - $h_{min} = 3.63\,R_w(\frac{\mu_0 U}{E_y' R'})^{0.68}(\alpha_{PVC} E_y')^{0.49}(\frac{W}{E_y' R'^2})^{-0.073}(1 - \exp[-0.68\kappa_{ellipse}])$
  - Calculated at the beginning of each time-step throughout the simulation
    - Instabilities may occur if changes are too dramatic
      - With increasing temperature, viscosity decreases, and thus the minimum film thickness would decrease
      - With the minimum film thickness decreasing (such as from a temperature increase), the thermal resistance decreases (the oil is an insulator), and thus the temperature decreases
      - As a result of the temperature increase, the temperature decreases, which can cause numerical instabilities unless iteration for a proper average temperature is found
    - This new version assumes steady temperatures throughout each time-step
      - The only parameter that changes this minimum film thickness is the wear scar radius
      - As the wear scar diameter increases, the contact area increases, thus the friction heating density decreases, thus the temperature decreases, and thus the minimum film thickness increases, resulting in less wear
      - Temporally the wear rate decreases slowly in time (after initial running in)

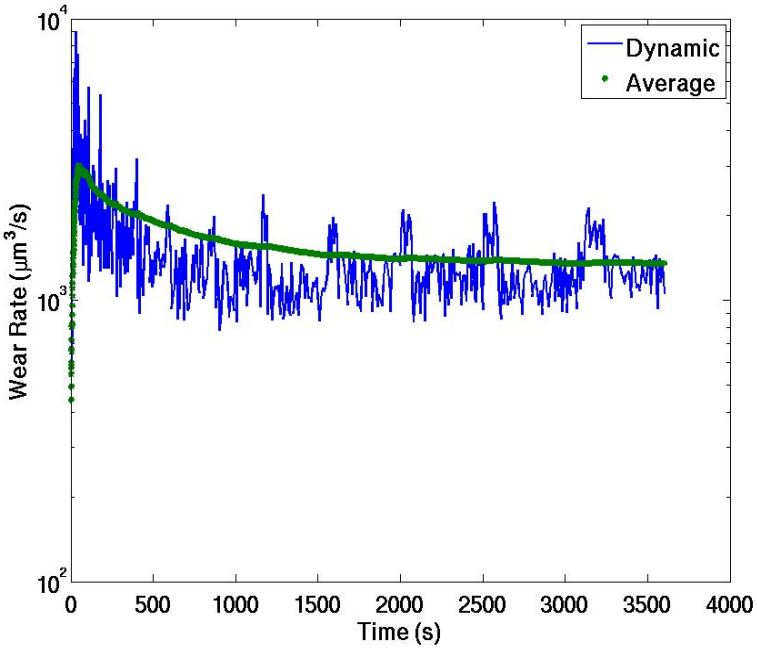

- First step is to calculate the flash temperature heating at the surface of the ball bearing
  - If Pecelt Number L < 0.1
    - $T_f = \frac{\mu_{COF} W U}{4 k a}$, where μ_{COF} is the coefficient of friction
    - Friction is considered a stationary heat source
  - If Pecelt Number 0.1 < L < 5
    - $T_f = [0.35 + (5 - L)\frac{0.5}{4.9}]\frac{\mu_{COF} W U}{4 k a}$
    - Friction heating is considered a slow-moving heat source
  - If Pecelt Number L > 5
    - $T_f = \frac{0.308\,\mu_{COF} W U}{4 k a}\sqrt{\frac{\alpha}{U a}}$
    - Friction heating is considered a fast-moving heat source
- Next step is to calculate the temperature distribution within the oil film
  - For steady-state heat transfer with heat generation (effectively from the friction)
    - $\frac{d^2 T}{dx^2} = \frac{-\dot{g}}{k_{lub}} \rightarrow \dot{g} = \frac{\dot{Q}}{\pi a_{Hertz}^2} = \frac{\mu_{COF} W U}{\pi a_{Hertz}^2}$

- $T(x)=\frac{\dot{g}}{2k_{lub}}[hx-x^2]+T_f$
- $T_{avg}=0.1665\frac{\dot{g}}{2k_{lub}}h^2+T_f$
  - where $\dot{g}$ is the equivalent heat generation (W/m^3), k_{lub} is the thermal conductivity of the oil, and h is the film thickness

- The next step is to use this average temperature to calculate the viscosity
  - See viscosity section
  - The bulk-temperature is used for the oil film thickness to start the iterations
- When a viscosity is determined, a central film thickness is estimated to calculate the new temperature profile
  - An analytical equation based on empirical data is used:
  - $h_c=2.69\,R_w\left(\frac{\mu_0 U}{E_y' R'}\right)^{0.67}\left(\alpha_{PVC}E_y'\right)^{0.53}\left(\frac{W}{E_y' R'^2}\right)^{-0.067}\left(1-0.061\bullet\exp[-0.73\kappa_{ellipse}]\right)$

- The iterations occur until there is convergence, looping through the following steps
  - Take the most recent central film thickness based on Dowson's equation
    - For the initial start of the iterative loop, use the viscosity estimated at the bulk temperature to estimate this thickness
  - Use the film thickness to determine the increase in oil film temperature
  - Determine the total film temperature by adding the flash temperature increase and the bulk temperature
  - Calculate the new viscosity based on the newly calculated lubricant temperature
  - Calculate the new central film thickness
  - If the error between the latest film thickness and the previous thickness is less than 1%, end the loop, and utilize this temperature and viscosity throughout the simulation
    - After 1000 iterations, the loop brakes and an alert is prompted

- Determine the minimum film thickness from the viscosity calculated by the converged temperature of the oil film, and use this initial minimum thickness throughout the simulation

- Calculate the viscosity
  - The viscosity is found through a separate viscosity Matlab function
  - Coefficients are first found before the time-steps start
    - It is necessary to know the viscosity of the lubricant at two temperature points, and for this to be declared; for example
      - T1=297.15; v1=638;
      - T2=363.15; v2=25;
    - In the separate function, the *A* and *B* terms are found for the two closest experimental data points, to reduce interpolation error when the theoretical viscosity is found
    - Find the value of *Z* at these temperatures
      - $Z = v + 0.7 + \exp(1.47 - 1.84v - 0.51v^2)$
      - ν is in cSt or mm^2/s
    - Find the coefficients of viscosity for the lubricating oil
      - $\log_{10}\log_{10} Z = A - B\log_{10} T$
      - $B = \frac{\log_{10}(\log_{10} Z_1) - \log_{10}(\log_{10} Z_2)}{\log_{10} T_2 - \log_{10} T_1}$, or $B = \frac{\log_{10}(\log_{10} Z_1) - \log_{10}(\log_{10} Z_2)}{\log_{10} T_2 - \log_{10} T_1}$
      - $A = \log_{10}\log_{10} Z_i + B\log_{10} T_i$, where *i* could be either 1 or 2
  - At each time step, find the new dynamic viscosity
    - Calculate the kinematic viscosity
      - Z = 10^(10^ $(A - B\log_{10} T_F)$)
      - $v = (Z - 0.7) - \exp[-0.7487 - 3.295(Z - 0.7) + 0.6119(Z - 0.7)^2 - 0.3193(Z - 0.7)^3]$
        - v is in cSt, T_f is in Kelvin
      - To calculate changes in viscosity
    - Convert to dynamic viscosity
      - $\mu(Pa - s) = \frac{v(cSt)}{10^6}\rho_{density}$
- Declare the arrays
  - In Matlab, if arrays are not pre-declared (as empty matrices), then creating and recreating the matrix size dynamically will dramatically increase the computational time

- Most matrices are set as Mx by Mx arrays of zero, where Mx is the number of finite difference points in the X and Z direction
  - wear=zeros(Mx,Mx);
  - indent=zeros(Mx,Mx);
- Indent is an array to represent the changing depth of the oil thickness as a result of the curvature of the ball bearing
  - $r' = \sqrt{X^2 + Y^2} = R\sin\theta$, and $R - I = R\sin\theta$, therefore
    - $I = R[1 - \cos(\sin^{-1}\frac{r'}{R})]$
  - 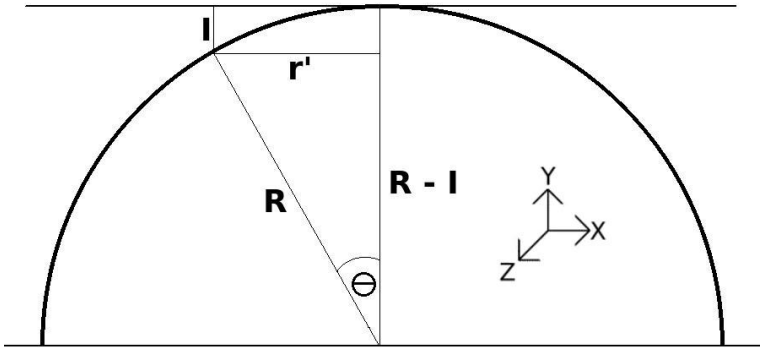

- Rfct
  - Determines the distance from the center of the domain to the location of each finite difference node
  - Rfct(ii,jj)=sqrt((Xfct(ii)^2)+(Yfct(jj)^2));
  - This is to be used for determining when a finite difference node is within the domain of the wear scar
- Determine the basis of the pressure function starting with Hertzian pressure
  - Determine the Hertzian pressure function
    - $P_{Hertzian}(r) = \frac{3}{2}\frac{W}{\pi a_{Hertz}^2}[1 - (\frac{r}{a_{Hertz}})^2]$
  - Iterate the Reynolds solver to find the correct no-wear pressure distribution of the oil
    - See chapter on deflection and film thickness model

- Set up parameters for the start of the simulation
  - Set *a* as the radius of the contact area, starting at the Hertzian minimum
  - Set *TS* (the time step count) at 0

- Set *time = 0* at the start of full spindle acceleration
- Set *dt* to *dt0*

- Run the simulation (for each time step)
  - Calculate the new wear scar radius
  - Calculate the lubricant film temperature, lubricant viscosity, and the minimum elastohydrodynamic film thickness
  - Solve the Reynold's Equation with finite difference to determine the detailed lubricant profile
  - Calculate the asperities-film thickness ratio profile and resulting wear rate
  - Adjust the time-step
  - Calculate the total wear
- Save data

<u>At each time-step</u>:

- Calculate the size of the wear scar
  - Adjust scar diameter based on where there is some wear
  - If the wear scar is smaller than the Hertzian radius, adjust to the Hertzian radius
    - Hertzian is considered a valid assumption for a low or no-wear contact with an oil film thickness (ex. Grubin)
- Calculate the minimum film thickness
  - Uses Hamrock Dowson film-thickness
  - This will adjust as the temperature increases, and thus the atmospheric pressure (μ_0) decreases
- Calculate the oil thickness function
  - Iterate for the proper film thickness:
    - Determine the deflection based on oil pressure, utilizing the Winkler Mattress model
      - $\delta(x,z)=\frac{P(x,z)}{K_h}$
    - Determine the oil film thickness
      - $h(x,z)=2\bullet I(x,z)+\delta(x,z)+Wear(x,z)-min[2\bullet I(x,z)+\delta(x,z)+Wear(x,z)]+h_{min}$
      - This assures that the minimum film thickness is the calculated minimum film thickness
      - In this equation and model *Wear(x,z)* is in meters, not volume

- Determine the pressure with the Reynolds solver
- Adjust the deflection function δ, and repeat the iteration until there is convergence
  - Require a minimum of 5 iterations, and a maximum of 25 iterations

- Reynolds Solver
  - If the film thickness is very thin (at the area of contact), it is reasonable to assume there is negligible Y directional changes
  - The Reynolds Equation:
    - $\frac{\partial}{\partial x}(\frac{\rho h^3}{\mu}\frac{\partial P}{\partial x})+\frac{\partial}{\partial z}(\frac{\rho h^3}{\mu}\frac{\partial P}{\partial z})=\frac{\partial}{\partial x}[6\rho h(U_x)]+\frac{\partial}{\partial z}[6\rho h(U_z)]+12\frac{d}{dt}(\rho h)$
  - If the flow is 1D, the Reynolds equation can be treated as 1D, where
    - $\frac{\partial P}{\partial z}=\frac{\partial}{\partial z}(\frac{\rho h^3}{\mu}\frac{\partial P}{\partial z})=0$
  - and therefore:
    - $\frac{\partial}{\partial x}(h^3\frac{\partial P}{\partial x})=6\mu U\frac{\partial h}{\partial x}$
      - Unidirectional Reynold's Equation
      - This equation can be used for both Pressure and the Grubin reduced Pressures
  - This can be derived into:
    - $\frac{\partial P}{\partial x}=6\mu U\frac{h-h_c}{h^3}$
    - where h_c is the upper film thickness where $\frac{\partial P}{\partial x}=0$, typically at the center of the region of contact
  - Convert the pressure differential into a discrete series with Taylor Series Expansion
    - $P(X_{i+1})=P(X_i)+P'(X_{i+1})(X_{i+1}-X_i)+\bar{O}(\Delta X^2)$
    - $P'(X_i)=\frac{P(X_{i+1})-P(X_{i-1})}{2\Delta x}$
    - $P''(X_i)=\frac{P(X_{i+1})-2P(X_i)+P(X_{i-1})}{\Delta x^2}$

- Using this, we can write the Reynold's equation in discrete linear form
  - $h^3\frac{\partial^2 P}{\partial x^2}+3h^2\frac{\partial P}{\partial x}\frac{\partial h}{\partial x}=6\mu U\frac{\partial h}{\partial x}$
  - $h^3\frac{P(X_{i+1})-2P(X_i)+P(X_{i-1})}{\Delta x^2}+3h^2\frac{\partial h}{\partial x}+\frac{P(X_{i+1})-P(X_{i-1})}{2\Delta x}=6\mu U\frac{\partial h}{\partial x}$
  - $P_{i-1}(\frac{h^3}{\Delta x^2}-\frac{3h^2}{2\Delta x}\frac{\partial h}{\partial x})+P_i(\frac{-2h^3}{\Delta x^2})+P_{i+1}(\frac{h^3}{\Delta x^2}+\frac{3h^2}{2\Delta x}\frac{\partial h}{\partial x})=6\mu U\frac{\partial h}{\partial x}$
  - $(P_{i-1}W_i)+(P_ia_i)+(P_{i+1}E_i)=B_i$
- This same 1D equation can be converted to 2D for this simulation
  - $(P_{i-1,j}W_{i,j})+(P_{i+1,j}E_{i,j})+(P_{i,j-1}S_{i,j})+(P_{i,j+1}N_{i,j})+(P_{i,j}a_{i,j})=B_{i,j}$
  - $W_{i,j}=(\frac{h^3}{\Delta x^2}-\frac{3h^2}{2\Delta x}\frac{\partial h}{\partial x})=\frac{h(i,j)^3}{\Delta x^2}-\frac{3h(i,j)^2}{2\Delta x}(\frac{h(i+1,j)-h(i-1,j)}{2\Delta x})$
  - $E_{i,j}=(\frac{h^3}{\Delta x^2}+\frac{3h^2}{2\Delta x}\frac{\partial h}{\partial x})=\frac{h(i,j)^3}{\Delta x^2}+\frac{3h(i,j)^2}{2\Delta x}(\frac{h(i+1,j)-h(i-1,j)}{2\Delta x})$
  - $S_{i,j}=(\frac{h^3}{\Delta z^2}-\frac{3h^2}{2\Delta z}\frac{\partial h}{\partial z})=\frac{h(i,j)^3}{\Delta z^2}-\frac{3h(i,j)^2}{2\Delta z}(\frac{h(i,j+1)-h(i,j-1)}{2\Delta z})$
  - $N_{i,j}=(\frac{h^3}{\Delta z^2}+\frac{3h^2}{2\Delta z}\frac{\partial h}{\partial z})=\frac{h(i,j)^3}{\Delta z^2}+\frac{3h(i,j)^2}{2\Delta z}(\frac{h(i,j+1)-h(i,j-1)}{2\Delta z})$
  - $a_{i,j}=-2\frac{h(i,j)^3}{dx^2}-2\frac{h(i,j)^3}{dz^2}$
- It is of course necessary to watch for boundaries, and leave out empty data for boundary nodes that do not have a node to a directional border
- The right-hand side of this equation can discretely be solved as:
  - $B_i=6\mu U\frac{\partial h}{\partial x}=(6\mu U)\frac{1}{2}[(\frac{h(i,j+1)-h(i,j-1)}{2\Delta x})+(\frac{h(i,j+1)-h(i,j-1)}{2\Delta z})]$
- Iterate to solve for the normalized pressure based on the older function for P
  - $P_{i,j}=\frac{B_{i,j}-[(P_{i-1,j}W_{i,j})+(P_{i+1,j}E_{i,j})+(P_{i,j-1}S_{i,j})+(P_{i,j+1}N_{i,j})]}{a_{i,j}}$
  - All finite difference nodes at the boundary are set to 0
    - Assumed that far from the wear scar the oil pressure is practically nonexistent
  - Require a minimum of 2 iterations, and a maximum of 1000

Dry Contact Pressure (Hertzian) **Oil Pressure (Reynolds)**

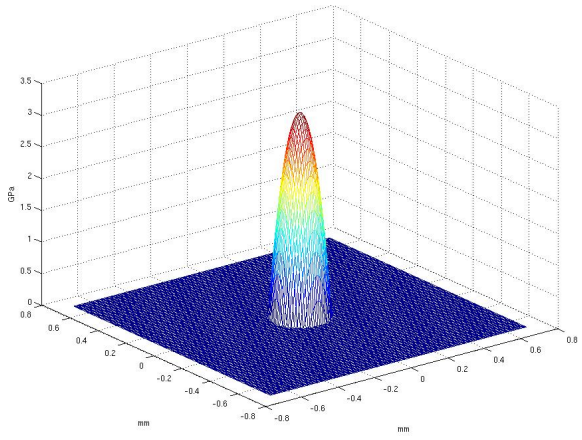

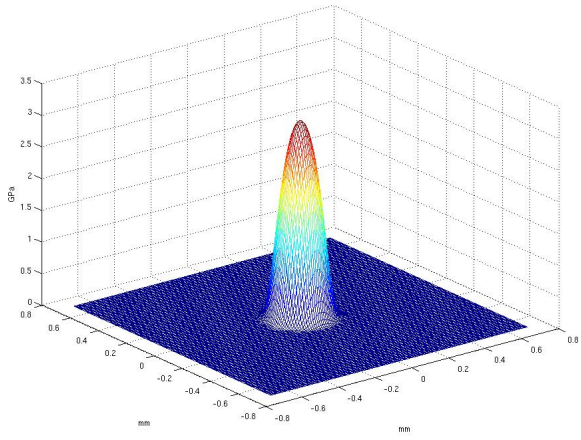

- Determine the pressure-viscosity effects
  - Barus' Law breaks down after 500 MPa; many pressures of interest exceed this level
  - Roelands equation is used to estimate the equivalent viscosity at each point when solving the Reynolds equation
    - $v = v_0 \exp[\alpha^x P]$
    - $\alpha^x P = \left(\frac{T_i - 138}{T_b - 138}\right)^{-S_0} \left[\left(1 + \frac{P}{1.9608 * 10^8}\right)^{Z_0} - 1\right][\log(\mu) + 9.67]$
    - $Z_0 = \frac{\alpha_{PVC}}{(5.1 \cdot 10^{-9})[\log(\mu_0) + 9.67]}$
      - Note: uses dynamic viscosity at the bulk-temperature (as the PVC coefficient was found at the bulk temperature)
      - All other equations use the viscosity at the lubricant film temperature
    - $S_0 = \beta \frac{T_b - 138}{[\log(\mu) + 9.67]}$
      - where β is obtained from the experimental viscosity-temperature data $v(T) = v(T_0)\exp[-\beta(T - T_0)]$
- Have a final determination for the pressure and film thickness function
  - The pressure can be used to determine the elastic deformation to calculate the film thickness
  - The film thickness will appear very flat at the area of contact

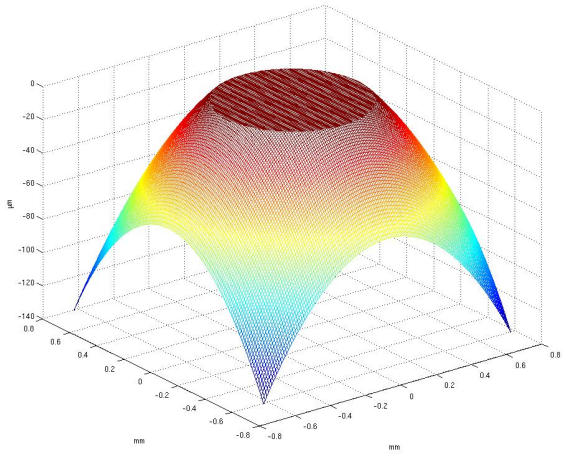

- Determine which data nodes are in the region of the wear scar
  - Done by taking the radius of each data node (found earlier), and determining which are less than the calculated wear scar radius
  - The wear scar radius is defined as the region where wear exceeds the original RMS surface roughness of the ball bearings
- Calculate the new RMS surface roughness σ
  - Calculated as the RMS of the different wear values as compared to the average wear depth for finite difference nodes within the wear scar
  - This total summation of the difference in wear is squared, summed up, divided by the total number of finite difference nodes in the wear scar, and square rooted
  - The original RMS value is then added to this newly calculated value, and it is multiplied by two, as there are two surfaces in contact (the sample ball bearing and the spinning ball bearing)
    - $$\frac{\sigma}{2}=\sigma_0+\sqrt{\frac{\Sigma\left[W\left(i,j\right)-\bar{W}\right]^2}{N_{nodes}}}$$
  - If σ is ever calculated to be less than σ_0, set $\sigma = \sigma_0$
  - This is not used for the numerical model, only for tracking and comparison to the optical profilometry data
- Find the ratio of asperity contact
  - A study was conducted to determine the ratio of wear for a given lambda-value (λ_W)
    - $\lambda_W=\frac{h+W_P}{\sigma}$, where σ is the standard deviation of the asperities height, h is the height of the oil film thickness, and W_P is the Greenwood Williamson height

- Monte Carlo was used to simulate the asperities
  - Asperities were represented by a series of random number from -1 to 1, which was then normalized by the standard deviation of the random number generator
    - This normalization was set so that a random height of 1 represents the RMS asperities height (σ)
      - No actual real values were used in this prior numerical Monte-Carlo study
    - The random series were multiplied by an odd exponential power when it was necessary to decrease the standard deviation
      - An odd power was necessary to ensure both negative and positive asperities
  - All asperities in excess of the specified lambda-value were removed

Before Wear

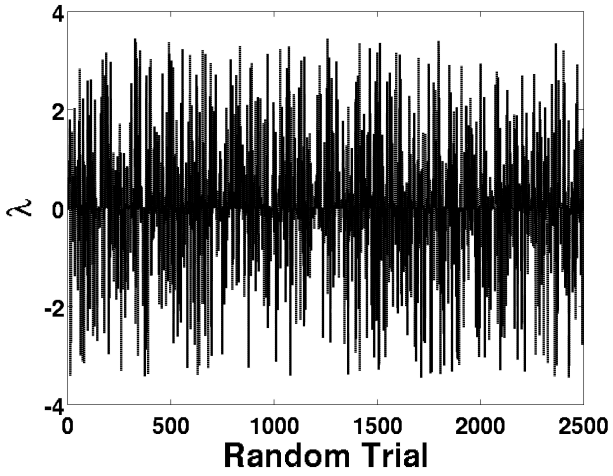

After Wear (λ_w = 1)

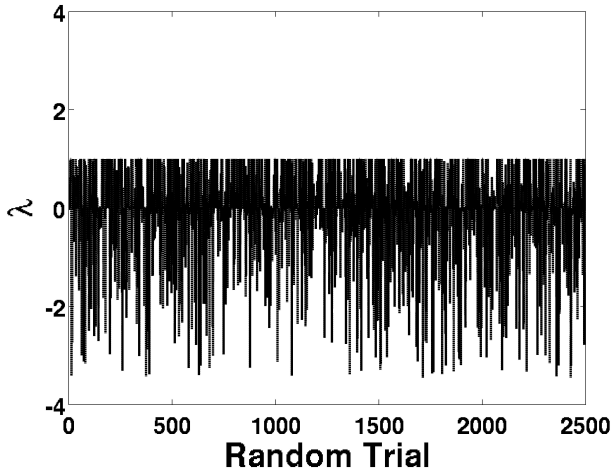

- Every time this happened, a count was recorded, to compare to the total number of random trials, to validate the area ratio
- Every time an asperities exceeded the λ_W value, the height in excess was recorded
  - This total height represents the total wear
  - Wear Volume: $V=\left(\frac{\Delta x^2}{N}\right)\sigma\,\Sigma_i^N\left(h_i-\lambda_W\right)$ (m^3)
  - where N is the total number of random asperities, and h_i represents all random normalized "asperities" in excess of λ_W; all other random asperities are set to zero
  - The total normalized wear was determined to follow (with reasonable error) an exponential decay function, where:
    - $V_N=0.2763\cdot\exp\left[-1.6754\,\lambda_W\right]$, where $V=V_n\cdot\Delta x^2\cdot\sigma$ (m^3)
  - The wear rate at each finite difference node is simply: $\dot{V}=V_n\cdot\Delta x\cdot U\cdot\sigma$ (m^3/s)
- Calculate the time-step to ensure:
  - It is small enough that there would not be a wear depth increase exceeding the user specified maximum wear per time-step, where $dt=dW_{max}/\left(\frac{dW}{dt}\right)_{max}$
  - The calculated time-step is not longer than a user-specified maximum time-step duration
    - Once the max-wear calculated time-step exceeds the maximum time-step, the time-step is rounded down once so that the net time function is a clean integer of maximum time-steps
    - This is not necessary for anything except clean organization of data
- Save all the data within arrays

Appendix F

MONTE CARLO MATLAB SOURCE CODE

- *runsim.m*: run the parametric Monte Carlo study
- *crunch.m*: function to complete a Monte Carlo study for a given λ_W-value
- *analyze.m*: determine the empirical equation (Eqn. 2.76) for the normalized wear from the Monte Carlo empirical data
- *analyzeCOF.m*: determine the empirical equation (Eqn. B.1) for the coefficient of friction from the Monte Carlo empirical data

F.1 runsim.m

```
clear
tic

LambdaFct=0:0.01:3.0; ct=length(LambdaFct);
SubLoop=5;

WearRat=zeros(1,ct); RatErfc=zeros(1,ct);

for ii=1:(ct-1)
    Lambda=LambdaFct(ii);
    wearX=zeros(1,SubLoop); RatErfcX=zeros(1,SubLoop);
    for jj=1:SubLoop
        [wearX(jj),RatErfcX(jj)]=crunch(Lambda);
    end
    WearRat(ii)=mean(wearX); RatErfc(ii)=mean(RatErfcX);
end

save MCdata
toc
```

F.2 crunch.m

```
function [wear,RatErfc]=crunch(Lambda)

% Lambda = (hc + Wp) / Ra

Mx=1e4; pw=5;
if mod(pw,2)==0
    pw=pw+1;
end
StdRng=((2*rand(Mx,1))-1).^pw; StdRng=std(StdRng);
if Lambda>(1/StdRng)
    fprintf(['ALERT - Increase PW!!!!' '\n']);
end

Dat=((((2*rand(Mx^2,1))-1).^pw))/StdRng;
aa=find(Dat>Lambda); ct=length(aa);
RatErfc=ct/(Mx^2);

wear=0;
for ii=1:ct
    wear=wear+(Dat(aa(ii))-Lambda)*((1/Mx)^2);
end

end
```

F.3 analyze.m

```
clear

load MCdata

Decline=WearRat(ct-1)/WearRat(1);

coeff=-(1/LambdaFct(ct-1))*log(Decline);
Fct=WearRat(1)*exp(-coeff*LambdaFct);

plot(LambdaFct,WearRat,LambdaFct,Fct)

Error=(abs((Fct.*(WearRat.^-1))-1)); Error=mean(Error(1:(ct-1)));
```

F.4 analyzeCOF.m

```
clear

load MCdata

Decline=RatErfc(ct-1)/RatErfc(1);

coeff=-(1/LambdaFct(ct-1))*log(Decline);
Fct=RatErfc(1)*exp(-coeff*LambdaFct);

plot(LambdaFct,RatErfc,LambdaFct,Fct)

Error=(abs((Fct.*(RatErfc.^-1))-1)); Error=mean(Error(1:(ct-1)));
```

Appendix G

SMOOTHED PARTICLE APPLIED MECHANICS

Introduction

Part of my doctoral thesis effort was to investigate *Smooth Particle Applied Mechanics* (SPAM) [131], a mesh-less solid mechanics numerical method that has its origins from *Smooth Particle Hydrodynamics* [132]. A numerical method such as finite element or finite difference utilizes a mesh of regions in space, and tracking the flow of mass in and out of these defined regions; a mesh-less approach tracks *particles* of mass and how the particles interact with each other. Whereas a meshed numerical method can be considered an *Eulerian* approach, a mesh-less numerical model is a *Lagrangian* approach.

A mesh-less numerical method can be advantageous for simulations that require a large spatial domain, such as in the presence of large deformations, explosions, or fluid flow; there is no need to build a larger and larger mesh, which consumes

computational resources, as the spatial domain increases. The disadvantage is that particles must track each other, and large particles counts can increase the computational domain exponentially. This limitation can be overcome with link-lists and other computational methods of optimization, but with enhanced complexity in the coding. Whether one uses a meshed or mesh-less numerical method should be dependent on the application involved.

There is very little research conducted in SPAM to date; SPH has been investigated much more thoroughly, as fluids tend to have much more profound deformations. It was previously observed that to use the equations of SPH directly for a solid often yields tensile instabilities, causing the numerical model to fail. Various schemes were attempted to make SPAM and SPH work for solids, of limited effectiveness. This approach to date uses a separate array to record all particles connected in tensile contact, and the model will apply a tensile forces to keep them together; repulsive compressive forces, however, will be applied to any two particles in proximity to each other. This numerical approach was applied to model the Hertzian contact of a cylindrical disk on a flat surface, and the results closely match the analytical model for all scales and sizes.

While this effort is not a major component of this doctoral thesis, the work will continue at my place of employment, the Navy Air Systems Command at Joint-Base McGuire-Dix-Lakehurst, as part of an *In-house Laboratory Independent Research* (ILIR) project titled *Smooth Particle Applied Mechanics*. An emphasis will focus on fluid-solid interactions; existing SPH and finite element models can only approximate the stresses from the fluid to model the solid (or vice versa). The ability to model both liquids and solids together can have a host of applications, such as

a lubricant film separating two solids in contact, as well as the water brake for the existing steam catapult launching system on the Nimitz-class aircraft carrier. This effort will continue beyond this PhD, up till at least the end of the 2016 calendar year.

About the Study:

- The purpose of this study is to better verify and validate the Smoothed Particle Applied Mechanics (SPAM) model as it applies to Hertzian contact-mechanics.
- While the simulation is capable of 3D studies, only a 2D layer of particles are studied.
- The model will be represented by an inelastic disk being in contact with a elastic flat plate.
- The fixed 2D disk will be comprised of the same Lagrangian particles as the flat plate.
- The disk will be forced down at a user-specified velocity and then stay in place for a specified number of time steps.
- The plate will rest on a boundary of fixed solid particles beneath it.
- This effort will ensure that the deflection length is less than one tenth the disk radius.

Hertzian Equations for Comparison of SPAM:

- $P_{max} = |T_{22}|$ for the Top Center Particle
- $\delta = |Y(t) - Y(0)|$ for the Top Center Particle
- $a = R \sin\left(\cos^{-1}\left(\frac{R-\delta}{R}\right)\right)$
  - R = Radius of Disk
  - a = half length of (theoretical) contact area
- Reduced Modulus:
  - $\frac{1}{E} = \frac{1-\nu_1^2}{E_{y,1}} + \frac{1-\nu_2^2}{E_{y,2}}$
    - Ey = Young's Modulus of Elasticity (Pa)
    - ν = Poisson's Ration
    - 1 and 2 represent the parameters of the disk and plate respectively
  - The disk is assumed to be rigid and inelastic, and thus is assumed to have a Young's Modulus of infinity. Based on the assumptions taken for the disk radius, though it is safe to assume the disk is rigid, and thus the Young's Modulus is infinite, therefore:
    - $E = \frac{E_y}{1-\nu^2}$
- $Weight_N(N/m) = \frac{a^2 \pi E}{4R}$
  - This is the normalized weight, or the weight per unit length of the disk
- The calculated maximum stress is found via:
  - $Max\,Stress_{calculated} = \frac{2\,Weight_N}{\pi a}$
- Simulated Weight
  - $Weight = \Sigma_N(T_{22} * dx^2)$
  - Taken for all the fixed particles at the bottom of the flat disk
- The simulated weight is compared to a calculated total weight based on the simulated (with SPAM) maximum stress at the center of the top of the flat.
  - $Max\,Stress_{SPAM} = \frac{Weight}{\pi a\, dx} \quad \rightarrow \quad Weight = \pi a\, dx\,(Max\,Stress_{SPAM})$

Model:

- Steel: Young's Modulus at 207 GPa, Poisson's Ratio at 0.3
- Color Code:
  - Red: Rigid Disk
  - Blue: elastic solid
  - Green = Fixed boundary
- 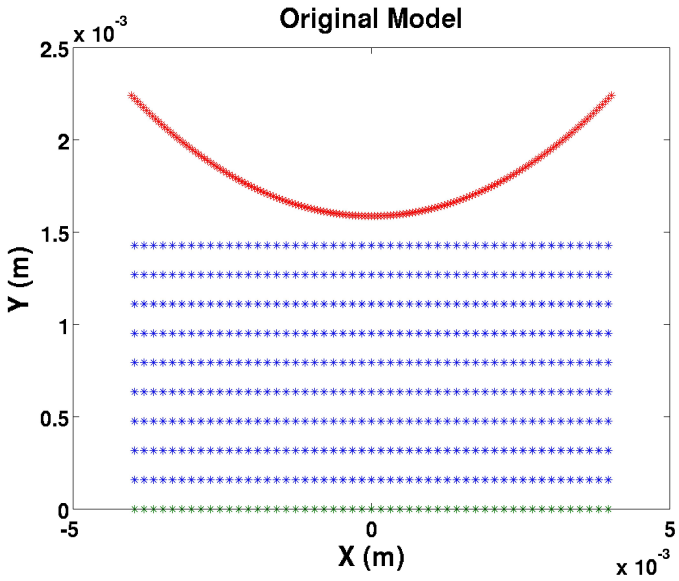

Results of Simulation:

- Calculated Contact Area Half-Length (a) = 1.6501 meters
  - a / R = 8.78%
- Simulated Deflection: -0.0125 inch
- Stress (MPa) Tensor of Top Center Particle (Tij):

0	6.4147	0
6.4147	-4.0477	0
0	0	0

- Pressure – Error = 5.359%
  - Simulated (SPAM) Max Pressure, at Top Center Particle = 10.0525 GPa
  - Calculated (Hertz) Max Pressure, at Top Center Particle = 9.9896 GPa
- Weight – Error = 2.2053%
  - Simulated (SPAM) Max Pressure, at Top Center Particle = 5.9842 kN
  - Calculated (Hertz) Max Pressure, at Top Center Particle = 5.8552 kN

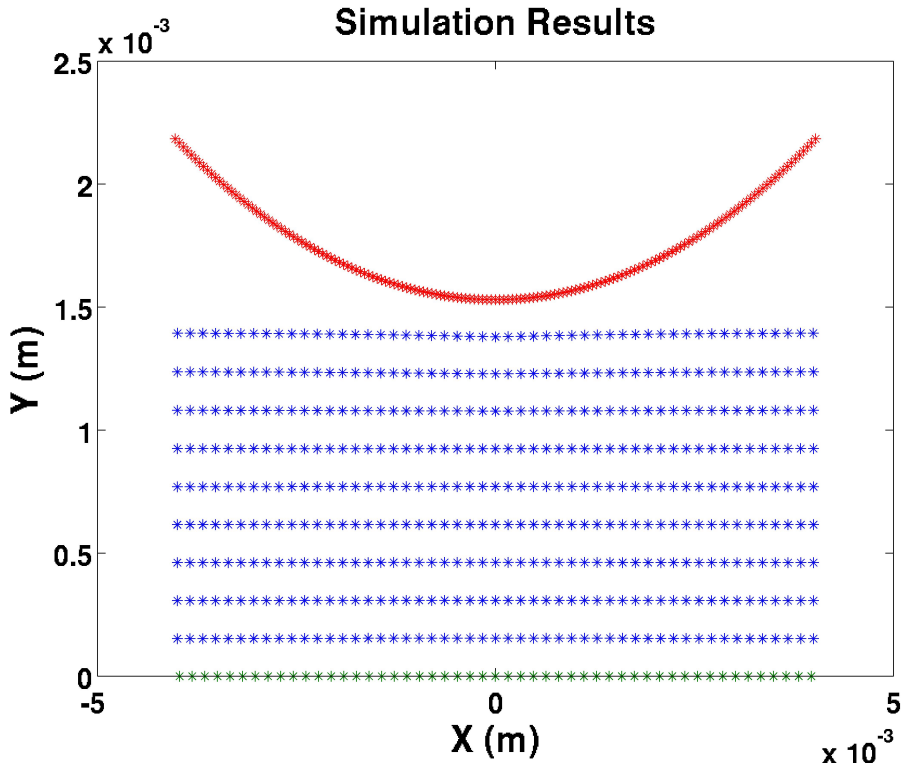
Simulation Results
x 10^-3
2.5
2
1.5
1
0.5
0
Y (m)
-5
0
5
X (m)
x 10^-3

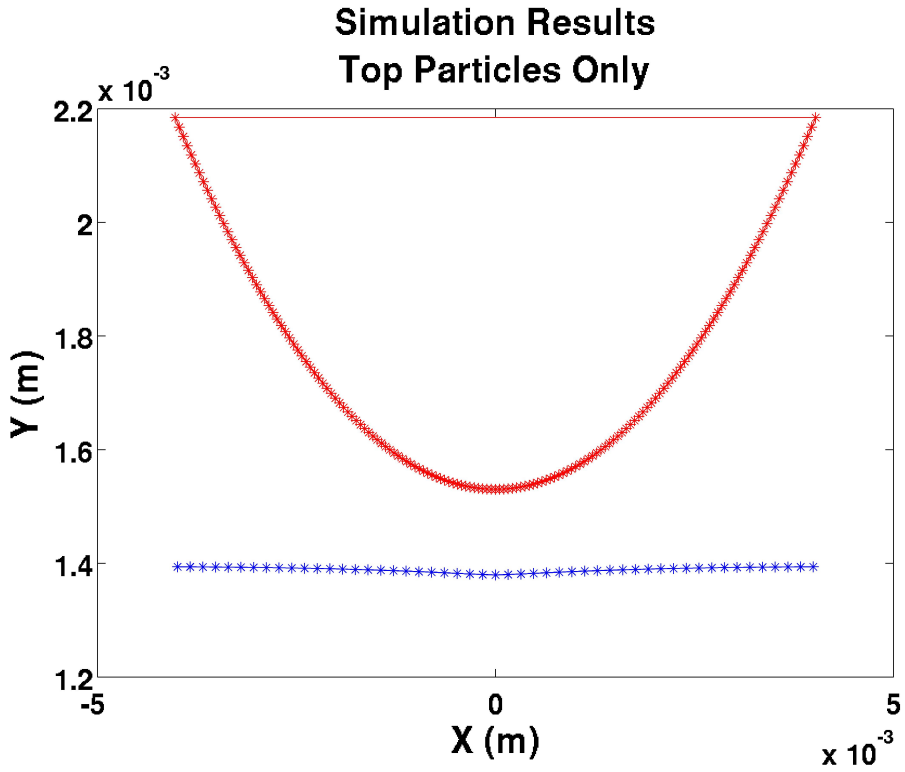
Simulation Results
Top Particles Only
x 10^-3
2.2
2
1.8
1.6
1.4
1.2
Y (m)
-5
0
5
X (m)
x 10^-3

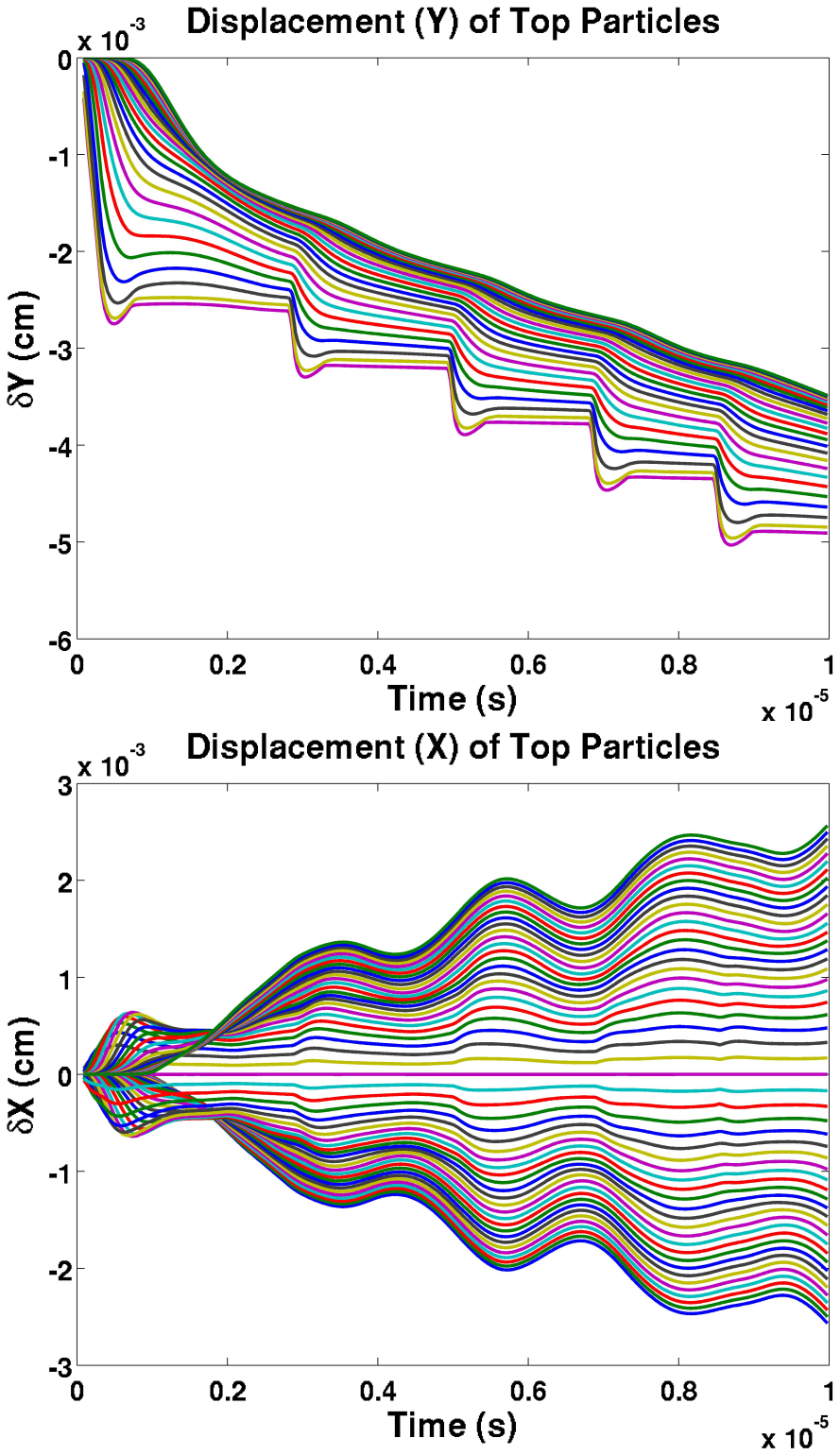
Displacement (Y) of Top Particles
x 10^-3
0
-1
-2
-3
-4
-5
-6
δY (cm)
0
0.2
0.4
0.6
0.8
1
Time (s)
x 10^-5
Displacement (X) of Top Particles
x 10^-3
3
2
1
0
-1
-2
-3
δX (cm)
0
0.2
0.4
0.6
0.8
1
Time (s)
x 10^-5

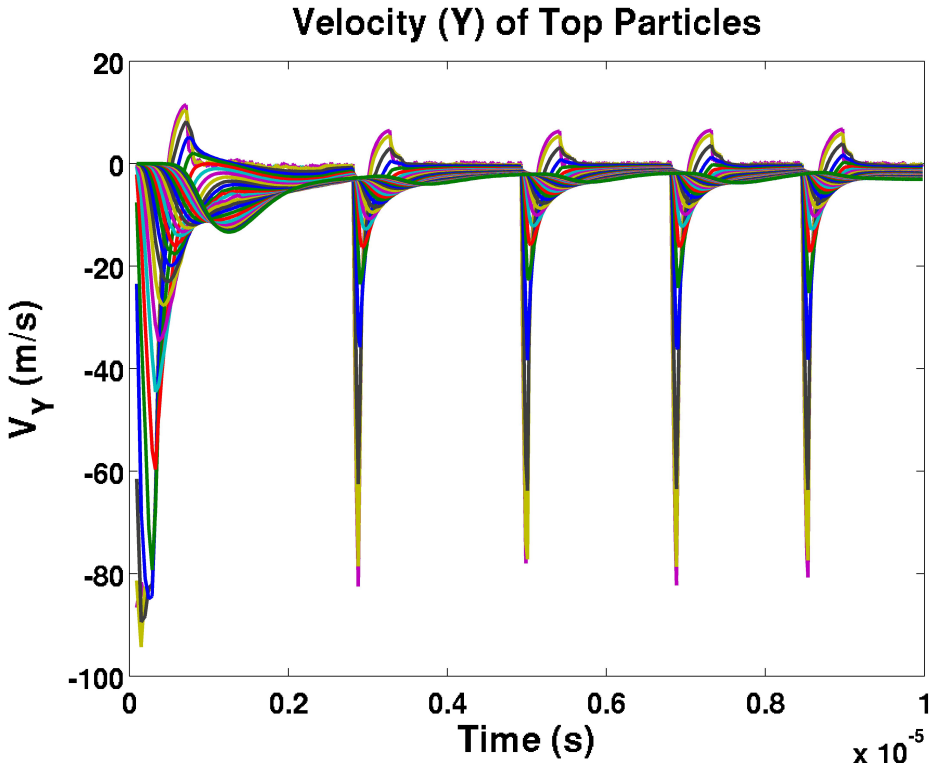
Velocity (Y) of Top Particles
20
0
-20
-40
-60
-80
-100
V_Y (m/s)
0
0.2
0.4
0.6
0.8
1
Time (s)
x 10^-5

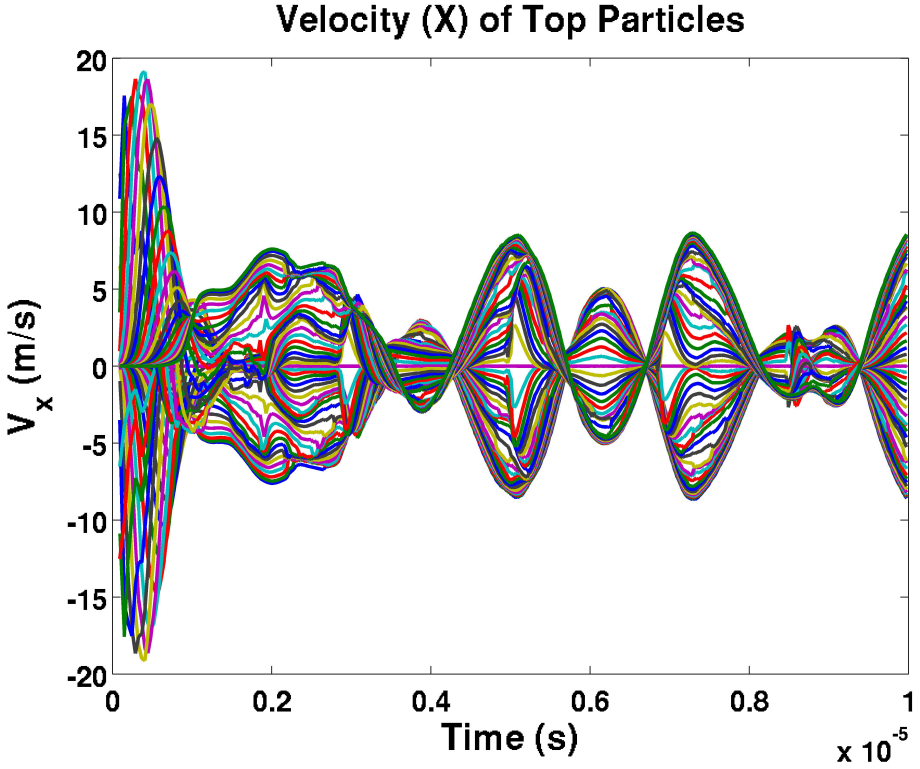
Velocity (X) of Top Particles
20
15
10
5
0
-5
-10
-15
-20
V_x (m/s)
0
0.2
0.4
0.6
0.8
1
Time (s)
x 10^-5

R = 20 meters, L = 12.25 m, H = 2.5 m, dX = 0.25 m 51 * 10 Particles

Disk Deflection (m)	Contact Length (m)	Weight – SPAM (GN)	Weight – Hertz (GN)	Max T22 – SPAM (GPa)	Max T22 – Hertz (GPa)
0.0412	1.2828	6.5983	7.3621	7.3071	7.2952
0.0505	1.4206	8.9462	8.7679	7.8587	8.0784
0.0595	1.5420	11.1197	10.5022	8.6718	8.7690
0.0684	1.6532	13.0201	12.4286	9.5720	9.4015
0.0773	1.7566	14.8473	14.5197	10.5241	9.9897

Disk Deflection (m)	% Error (Weight)	% Error (Max T22)
0.0412	10.3750	0.1624
0.0505	2.0330	2.7202
0.0595	5.8792	1.1079
0.0684	4.7594	1.8128
0.0773	2.2565	5.3490

R = 30 meters, L = 18.375 m, H = 3.75 m, dX = 0.375 m 51 * 10 Particles

Disk Deflection (m)	Contact Length (m)	Weight – SPAM (GN)	Weight – Hertz (GN)	Max T22 – SPAM (GPa)	Max T22 – Hertz (GPa)
0.0618	1.9242	14.8477	16.5667	7.3080	7.2952
0.0758	2.1308	20.1331	19.7297	7.8595	8.0783
0.0893	2.3130	25.0249	23.6305	8.6721	8.7689
0.1027	2.4798	29.3003	27.9638	9.5721	9.4013
0.1159	2.6349	33.4118	32.6699	10.5244	9.9895

Disk Deflection (m)	% Error (Weight)	% Error (Max T22)
0.0618	10.3760	0.1758
0.0758	2.0448	2.7087
0.0893	5.9011	1.1036
0.1027	4.7793	1.8172
0.1159	2.2708	5.3543

R = 40 meters, L = 24.5 m, H = 5.0 m, dX = 0.50 m 51 * 10 Particles

Disk Deflection (m)	Contact Length (m)	Weight – SPAM (GN)	Weight – Hertz (GN)	Max T22 – SPAM (GPa)	Max T22 – Hertz (GPa)
0.0824	2.5657	26.3945	29.4497	7.3074	7.2952
0.1010	2.8411	35.7889	35.0722	7.8588	8.0784
0.1191	3.0840	44.4844	42.0097	8.6720	8.7689
0.1369	3.3063	52.0851	49.7116	9.5717	9.4013
0.1546	3.5132	59.3943	58.0780	10.5241	9.9896

Disk Deflection (m)	% Error (Weight)	% Error (Max T22)
0.0824	10.3741	0.1670
0.1010	2.0437	2.7179
0.1191	5.8907	1.1050
0.1369	4.7745	1.8127
0.1546	2.2665	5.3505

R = 50 meters, L = 30.625 m, H = 6.25 m, dX = 0.625 m 51 * 10 Particles

Disk Deflection (m)	Contact Length (m)	Weight – SPAM (GN)	Weight – Hertz (GN)	Max T22 – SPAM (GPa)	Max T22 – Hertz (GPa)
0.1030	3.2070	41.2442	46.0171	7.3078	7.2951
0.1263	3.5513	55.9236	54.8013	7.8590	8.0783
0.1488	3.8549	69.5117	65.6398	8.6720	8.7689
0.1711	4.1329	81.3883	77.6770	9.5720	9.4013
0.1932	4.3916	92.8097	90.7467	10.5240	9.9896

Disk Deflection (m)	% Error (Weight)	% Error (Max T22)
0.1030	10.3718	0.1730
0.1263	2.0480	2.7142
0.1488	5.8988	1.1050
0.1711	4.7779	1.8153
0.1932	2.2735	5.3501

R = 0.2 inches, L = 0.1275 inches, H = 0.025 inches, dX = 0.0025 inches 51 * 10 Particles

Disk Deflection (mm)	Contact Length (mm)	Weight – SPAM (N)	Weight – Hertz (N)	Max T22 – SPAM (GPa)	Max T22 – Hertz (GPa)
0.0105	0.3258	425.3947	475.1323	7.3094	7.2953
0.0128	0.3608	576.8719	565.7163	7.8591	8.0785
0.0151	0.3917	716.9652	677.5850	8.6720	8.7690
0.0174	0.4199	839.5070	801.8216	9.5718	9.4014
0.0196	0.4462	957.3682	936.7987	10.5245	9.9897

Disk Deflection (mm)	% Error (Weight)	% Error (Max T22)
0.0105	10.4682	0.1937
0.0128	1.9719	2.7160
0.0151	5.8118	1.1066
0.0174	4.7000	1.8124
0.0196	2.1957	5.3537

R = 0.3 inches, L = 0.1913 inches, H = 0.375 inches, dX = 0.0038 inches 51 * 10 Particles

Disk Deflection (mm)	Contact Length (mm)	Weight – SPAM (kN)	Weight – Hertz (kN)	Max T22 – SPAM (GPa)	Max T22 – Hertz (GPa)
0.0157	0.4888	0.9572	1.0689	7.3087	7.2952
0.0192	0.5412	1.2980	1.2728	7.8590	8.0785
0.0227	0.5875	1.6132	1.5246	8.6721	8.7691
0.0261	0.6299	1.8889	1.8042	9.5721	9.4014
0.0294	0.6693	2.1541	2.1079	10.5250	9.9898

Disk Deflection (mm)	% Error (Weight)	% Error (Max T22)
0.0157	10.4565	0.1853
0.0192	1.9760	2.7177
0.0227	5.8130	1.1058
0.0261	4.6973	1.8153
0.0294	2.1928	5.3577

R = 0.4 inches, L = 0.2550 inches, H = 0.5 inches, dX = 0.005 inches 51 * 10 Particles

Disk Deflection (mm)	Contact Length (mm)	Weight – SPAM (kN)	Weight – Hertz (kN)	Max T22 – SPAM (GPa)	Max T22 – Hertz (GPa)
0.0209	0.6517	1.7066	1.9001	7.3076	7.2955
0.0257	0.7216	2.3128	2.2632	7.8605	8.0784
0.0302	0.7833	2.8727	2.7115	8.6760	8.7687
0.0348	0.8398	3.3629	3.2089	9.5768	9.4012
0.0393	0.8923	3.8344	3.7489	10.5296	9.9894

Disk Deflection (mm)	% Error (Weight)	% Error (Max T22)
0.0209	10.1859	0.1663
0.0257	2.1896	2.6967
0.0302	5.9464	1.0570
0.0348	4.7990	1.8678
0.0393	2.2794	5.4081

R = 0.5 inches, L = 0.3188 inches, H = 0.625 inches, dX = 0.0063 inches 51 * 10 Particles

Disk Deflection (mm)	Contact Length (mm)	Weight – SPAM (kN)	Weight – Hertz (kN)	Max T22 – SPAM (GPa)	Max T22 – Hertz (GPa)
0.0262	0.8146	2.6590	2.9695	7.3092	7.2952
0.0321	0.9021	3.6060	3.5358	7.8593	8.0785
0.0378	0.9792	4.4818	4.2352	8.6726	8.7690
0.0435	1.0498	5.2477	5.0117	9.5723	9.4015
0.0491	1.1155	5.9843	5.8552	10.5250	9.9896

Disk Deflection (mm)	% Error (Weight)	% Error (Max T22)
0.0262	10.4552	0.1921
0.0321	1.9856	2.7127
0.0378	5.8221	1.1000
0.0435	4.7098	1.8169
0.0491	2.2053	5.3590

R = 0.2 inches, L = 0.25 inches, H = 0.025 inches, dX = 0.0025 inches 101 * 10 Particles

Disk Deflection (mm)	Contact Length (mm)	Weight – SPAM (kN)	Weight – Hertz (kN)	Max T22 – SPAM (GPa)	Max T22 – Hertz (GPa)
0.0102	0.3224	0.4040	0.5156	8.0164	7.2189
0.0124	0.3551	0.6047	0.6508	9.1878	7.9494
0.0146	0.3852	0.7897	0.7912	10.2975	8.6234
0.0168	0.4129	0.9484	0.9431	11.4494	9.2449
0.0190	0.4385	1.0611	1.1126	12.7192	9.8172

Disk Deflection (mm)	% Error (Weight)	% Error (Max T22)
0.0102	21.6538	11.0477
0.0124	7.0836	15.5788
0.0146	0.1923	19.4141
0.0168	0.5628	23.8462
0.0190	4.6256	29.5609

R = 0.3 inches, L = 0.375 inches, H = 0.0375 inches, dX = 0.00375 inches 101 * 10 Particles

Disk Deflection (mm)	Contact Length (mm)	Weight – SPAM (kN)	Weight – Hertz (kN)	Max T22 – SPAM (GPa)	Max T22 – Hertz (GPa)
0.0154	0.4836	0.9090	1.1601	8.0157	7.2188
0.0186	0.5326	1.3602	1.4642	9.1877	7.9493
0.0219	0.5777	1.7765	1.7801	10.2968	8.6233
0.0252	0.6194	2.1337	2.1220	11.4491	9.2449
0.0284	0.6577	2.3872	2.5033	12.7189	9.8172

Disk Deflection (mm)	% Error (Weight)	% Error (Max T22)
0.0154	21.6425	11.0386
0.0186	7.1023	15.5783
0.0219	0.2067	19.4061
0.0252	0.5482	23.8431
0.0284	4.6363	29.5575

R = 0.4 inches, L = 0.5 inches, H = 0.05 inches, dX = 0.005 inches 101 * 10 Particles

Disk Deflection (mm)	Contact Length (mm)	Weight – SPAM (kN)	Weight – Hertz (kN)	Max T22 – SPAM (GPa)	Max T22 – Hertz (GPa)
0.0205	0.6449	1.6161	2.0623	8.0156	7.2188
0.0248	0.7101	2.4182	2.6031	9.1875	7.9494
0.0292	0.7703	3.1581	3.1648	10.2971	8.6234
0.0336	0.8258	3.7930	3.7726	11.4494	9.2449
0.0379	0.8770	4.2438	4.4502	12.7185	9.8172

Disk Deflection (mm)	% Error (Weight)	% Error (Max T22)
0.0205	21.6366	11.0375
0.0248	7.0994	15.5758
0.0292	0.2121	19.4090
0.0336	0.5425	23.8448
0.0379	4.6367	29.5541

R = 0.5 inches, L = 0.625 inches, H = 0.0625 inches, dX = 0.00625 inches 101 * 10 Particles

Disk Deflection (mm)	Contact Length (mm)	Weight – SPAM (kN)	Weight – Hertz (kN)	Max T22 – SPAM (GPa)	Max T22 – Hertz (GPa)
0.0256	0.8061	2.5255	3.2234	8.0182	7.2187
0.0311	0.8877	3.8447	4.0651	9.1820	7.9499
0.0366	0.9629	4.9896	4.9451	10.2974	8.6234
0.0420	1.0322	5.9783	5.8977	11.4560	9.2443
0.0474	1.0961	6.6832	6.9584	12.7286	9.8165

Disk Deflection (mm)	% Error (Weight)	% Error (Max T22)
0.0256	21.6513	11.0749
0.0311	5.4199	15.4984
0.0366	0.8983	19.4129
0.0420	1.3672	23.9251
0.0474	3.9553	29.6661

Appendix H

TABULATED DATA

Concentration Data

Date: 16 Feb 2013 R.H.: 12.5% T: 79.6°F

Nano-Diamond

	Diam 1 (mm)	Diam 2 (mm)	Avg (mm)	Vol net removed (mm^3)	COF (Mean)	0.0079
lower bearing 1	0.539	0.55	0.5445	1.21	COF (StDev)	0.0015
lower bearing 2	0.562	0.565	0.5635	1.3		
lower bearing 3	0.525	0.502	0.5135	0.90802971		
Average:	0.5420	0.5390	0.541	1.139		
			0.047	0.180		

Comments:

Date: 13 March 2013 R.H.: 14.4% T: 81.4°F

Nano-Diamond 2

	Diam 1 (mm)	Diam 2 (mm)	Avg (mm)	Vol net removed (mm^3)	COF (Mean)	0.0015
lower bearing 1	0.567	0.582	0.5745	1.3	COF (StDev)	0.0020
lower bearing 2	0.608	0.601	0.6045	1.66		
lower bearing 3	0.568	0.545	0.5565	1.11		
Average:	0.5810	0.5760	0.5785	1.357		
			0.042	0.206		

Comments:

Date: 24 Feb 2013 R.H.: 16.4% T: 80.2°F

50/50

	Diam 1 (mm)	Diam 2 (mm)	Avg (mm)	Vol net removed (mm^3)	COF (Mean)	0.0070
lower bearing 1	0.599	0.616	0.6075	1.78	COF (StDev)	0.0020
lower bearing 2	0.539	0.542	0.5405	1.08		
lower bearing 3	0.593	0.567	0.58	1.6		
Average:	0.5770	0.5750	0.576	1.487		
			0.058	0.245		

Comments:

Concentration Data

Date: 25 Feb 2013 R.H.: 14.7% T: 79.9°F

50/50

	Diam 1 (mm)	Diam 2 (mm)	Avg (mm)	Vol net removed (mm^3)	COF (Mean)	0.0056
lower bearing 1	0.608	0.55	0.579	1.15	COF (StDev)	0.0011
lower bearing 2	0.659	0.633	0.646	1.92		
lower bearing 3	0.642	0.596	0.619	1.97		
Average:	0.6363	0.5930	0.615	1.680		
			0.055	0.274		

Comments:

Date: 26 Feb 2013 R.H.: 20.3% T: 80.2°F

25/75

	Diam 1 (mm)	Diam 2 (mm)	Avg (mm)	Vol net removed (mm^3)	COF (Mean)	0.008221396
lower bearing 1	0.634	0.619	0.6265	2.12	COF (StDev)	0.001180752
lower bearing 2	0.59	0.593	0.5915	1.59		
lower bearing 3	0.579	0.582	0.5805	1.53		
Average:	0.6010	0.5980	0.600	1.747		
			0.040	0.186		

Comments:

Date: 26 Feb 2013 R.H.: 17.8% T: 81.0°F

25/75

	Diam 1 (mm)	Diam 2 (mm)	Avg (mm)	Vol net removed (mm^3)	COF (Mean)	0.0197
lower bearing 1	0.625	0.622	0.6235	1.92	COF (StDev)	0.0025
lower bearing 2	0.614	0.605	0.6095	1.62		
lower bearing 3	0.602	0.605	0.6035	1.79		
Average:	0.6137	0.6107	0.612	1.777		
			0.017	0.085		

Comments:

Concentration Data

Date: 27 Feb 2013 | R.H.: 25.9% | T: 79.9°F

1 to 8

	Diam 1 (mm)	Diam 2 (mm)	Avg (mm)	Vol net removed (mm^3)	COF (Mean)	0.0367
lower bearing 1	0.67	0.67	0.67	2.7	COF (StDev)	0.0013
lower bearing 2	0.63	0.62	0.625	1.21		
lower bearing 3	0.69	0.69	0.69	2.95		
Average:	0.6633	0.6600	0.662	2.287		
			0.050	0.411		

Comments:

Date: 12 March 2013 | R.H.: 34.2% | T: 84.1°F

1 to 8

	Diam 1 (mm)	Diam 2 (mm)	Avg (mm)	Vol net removed (mm^3)	COF (Mean)	0.0200
lower bearing 1	0.67	0.68	0.675	2.83	COF (StDev)	0.0029
lower bearing 2	0.66	0.69	0.675	2.26		
lower bearing 3	0.67	0.69	0.68	2.46		
Average:	0.6667	0.6867	0.6767	1.697		
			0.004	0.170		

Comments:

Factor wear by 0.6743

Date: 1 March 2013 | R.H.: 15.5% | T: 80.5°F

Mineral Oil

	Diam 1 (mm)	Diam 2 (mm)	Avg (mm)	Vol net removed (mm^3)	COF (Mean)	0.0250
lower bearing 1	0.618	0.605	0.6115	1.74	COF (StDev)	0.0056
lower bearing 2	0.619	0.624	0.6215	1.88		
lower bearing 3	0.608	0.623	0.6155	1.69		
Average:	0.6150	0.6173	0.6162	1.770		
			0.008	0.056		

Comments:

Concentration Data

Date: 12 March 2013 R.H.: 33.0% T: 83.0°F

Mineral Oil

	Diam 1 (mm)	Diam 2 (mm)	Avg (mm)	Vol net removed (mm^3)	COF (Mean)	0.0127
lower bearing 1	0.668	0.659	0.6635	2.34	COF (StDev)	0.0041
lower bearing 2	0.66	0.66	0.66	2.38		
lower bearing 3	0.6	0.604	0.602	1.49		
Average:	0.6427	0.6410	0.6418	2.070		
			0.054	0.243		

Comments:

Date: 14 Feb 2013 R.H.: 16.8% T: 80.0°F

Mineral Oil

	Diam 1 (mm)	Diam 2 (mm)	Avg (mm)	Vol net removed (mm^3)	COF (Mean)	0.0030
lower bearing 1	0.662	0.659	0.6605	2.38	COF (StDev)	0.0007
lower bearing 2	0.659	0.664	0.6615	2.59		
lower bearing 3	0.664	0.659	0.6615	2.59		
Average:	0.6617	0.6607	0.6612	2.520		
			0.001	0.048		

Comments:

Date: 14 Feb 2013 R.H.: 18.9% T: 79.9°F

Mineral Oil

	Diam 1 (mm)	Diam 2 (mm)	Avg (mm)	Vol net removed (mm^3)	COF (Mean)	0.0000
lower bearing 1	0.63	0.67	0.65	2.25	COF (StDev)	0.0007
lower bearing 2	0.61	0.62	0.615	1.83		
lower bearing 3	0.68	0.69	0.685	2.77		
Average:	0.6400	0.6600	0.6500	2.283		
			0.054	0.206		

Comments:

Temperature

Oil	Temp	Trial #	Ball 1- Horizontal	Ball 1- Vertical	Ball 2- Horizontal	Ball 2- Vertical	Ball 3- Horizontal	Ball 3- Vertical	Average
MO	29	1	0.66	0.66	0.66	0.66	.61	0.63	0.65
MO	44	1	.659	0.65	.636	0.65	.66	0.7	0.67
MO	51	1	.66	0.70	.67	0.69	0.74	0.71	0.71
MO	59	1	.72	0.71	.74	0.74	0.73	0.71	0.72
MO	67	1	.69	0.65	0.72	0.73	.66	0.67	0.69
ND	29	1	.647	0.64	.630	0.63	.609	0.59	0.62
ND	44	1	.585	0.55	.565	0.545	.550	0.548	0.55
ND	51	1	.553	0.553	.582	0.585	.573	0.576	0.57
ND	59	1	.622	0.622	.662	0.667	.673	0.679	0.66
ND	67	1	.70	0.69	.74	0.73	.74	0.74	0.72
MO	29	2	0.67	0.71	.68	0.7	.64	0.64	0.68
MO	44	2	0.644	0.64	.69	0.71	.68	0.69	0.67
MO	51	2	.75	0.76	.73	0.74	.69	0.69	0.73
MO	59	2	.72	0.74	.77	0.77	.80	0.82	0.78
MO	67	2	.63	0.64	.60	0.61	.62	0.64	0.63
ND	29	2	0.6	0.6	0.59	0.59	0.59	0.6	0.60
ND	44	2	0.68	0.68	0.66	0.66	0.69	0.69	0.68
ND	51	2	.582	0.582	.590	0.582	.556	0.58	0.58
ND	59	2	0.65	0.67	0.69	0.7	0.65	0.67	0.67
ND	67	2	0.7	0.69	0.66	0.66	.70	0.71	0.68
ND	51	3	0.7	0.66	.73	0.72	.70	0.68	0.69
MO	67	3	.98	0.94	.99	0.95	.98	0.93	0.94
MO	67	4	.83	0.83	.75	0.78	0.79	0.78	0.795

Temperature

Test Date	Test Date Trial #	Wear – Ball 1	Wear – Ball 2	Wear – Ball 3	Variation – Ball 1	Variation – Ball 2	Variation – Ball 3	Mean Wear	Max Error
06/18/14	6	-2.62E+06	-2.53E+06	-1.90E+06	0.006	0.006	0.034	-2.35E+06	0.034
06/18/14	5	-2.59E+06	-2.17E+06	-2.96E+06	0.01116667	0.02416667	0.01433333	-2.57E+06	0.024
06/24/14	2	-1.96E+06	-3.03E+06	-3.84E+06	0.03	0.03	0.015	-2.94E+06	0.030
06/18/14	4	-3.59E+06	-4.08E+06	-2.77E+06	0.0075	0.0175	0.0025	-3.48E+06	0.018
06/24/14	1	-2.29E+06	-3.97E+06	-2.25E+06	0.0225	0.0325	0.0275	-2.84E+06	0.033
06/18/14	1	-2.25E+06	-2.02E+06	-1.57E+06	0.024	0.0085	0.018	-1.95E+06	0.024
06/18/14	2	-1.02E+06	-9.78E+05	-9.73E+05	0.01983333	0.00733333	0.00133333	-9.92E+05	0.020
06/23/14	1	-1.09E+06	-1.42E+06	-1.26E+06	0.01833333	0.01216667	0.00316667	-1.26E+06	0.018
06/18/14	3	-2.03E+06	-2.57E+06	-2.68E+06	0.034	0.0085	0.02	-2.43E+06	0.034
06/22/14	4	-3.35E+06	-3.90E+06	-4.01E+06	0.025	0.015	0.02	-3.75E+06	0.025
06/21/14	2	-2.80E+06	-2.89E+06	-1.93E+06	0.01	0.01	0.04	-2.54E+06	0.040
06/20/14	1	-2.24E+06	-2.90E+06	-2.99E+06	0.028	0.028	0.013	-2.71E+06	0.028
06/24/14	4	-4.58E+06	-3.92E+06	-2.85E+06	0.025	0.005	0.04	-3.78E+06	0.040
06/21/14	1	-2.50E+06	-4.68E+06	-7.22E+06	0.04666667	0.00666667	0.03333333	-4.80E+06	0.047
06/24/14	3	-2.03E+06	-1.54E+06	-2.03E+06	0.005	0.025	0	-1.87E+06	0.025
06/22/14	3	-1.65E+06	-1.33E+06	-1.47E+06	0.005	0.005	0	-1.48E+06	0.005
06/22/14	2	-2.84E+06	-2.27E+06	-2.93E+06	0.00333333	0.01666667	0.01333333	-2.68E+06	0.017
06/23/14	3	-1.42E+06	-1.36E+06	-1.15E+06	0.00066667	0.00466667	0.01333333	-1.31E+06	0.013
06/22/14	1	-2.46E+06	-3.21E+06	-2.62E+06	0.01166667	0.02333333	0.01166667	-2.76E+06	0.023
06/23/14	2	-3.00E+06	-2.38E+06	-2.98E+06	0.011	0.024	0.021	-2.79E+06	0.024
07/03/14	1	-3.01E+06	-3.77E+06	-3.25E+06	0.01	0.035	0	-3.34E+06	0.035
07/04/14	1	-3.97E+06	-3.80E+06	-4.71E+06	0.02	0.03	0.015	-4.16E+06	0.030
07/04/14	2	-8.29E+06	-3.60E+06	-4.66E+06	0.035	0.03	0.01	-5.52E+06	0.035

Temperature

Surface RMS (um) 1	Surface Ra (um) 1	Surface RMS (um) 2	Surface Ra (um) 2	Surface RMS (um) 3	Surface Ra (um) 3	Avg Surface RMS (um)	Avg Surface Ra (um)
8.226	6.874	8.005	6.623	6.768	5.47	7.67	6.32
8.457	7.317	7.332	6.137	8.415	6.793	8.07	6.75
6.723	5.482	8.880	7.439	10.012	8.267	8.54	7.06
9.858	8.291	10.631	8.984	8.559	7.171	9.68	8.15
7.459	5.867	10.019	7.962	7.341	5.753	8.27	6.53
7.736	6.579	7.113	5.902	6.184	5.077	7.01	5.85
4.518	3.516	4.384	3.326	4.342	3.306	4.41	3.38
4.794	3.884	5.509	4.383	5.046	3.934	5.12	4.07
7.244	6.095	8.252	7.023	8.495	7.304	8.00	6.81
9.121	7.271	10.263	8.461	10.488	8.678	9.96	8.14
8.224	6.979	8.191	6.806	6.230	4.969	7.55	6.25
7.454	6.277	8.449	6.956	8.549	7.095	8.15	6.78
11.220	9.295	10.131	8.384	8.615	7.188	9.99	8.29
8.025	6.614	11.442	9.415	14.273	11.75	11.25	9.26
7.076	5.688	6.096	4.897	7.221	5.921	6.80	5.50
6.372	5.371	5.346	4.351	5.784	4.795	5.83	4.84
8.375	6.747	7.557	6.19	8.606	7.004	8.18	6.65
5.847	4.927	5.624	4.707	5.142	4.28	5.54	4.64
7.941	6.526	8.846	7.353	7.947	6.368	8.24	6.75
8.715	7.281	7.501	6.163	8.641	7.246	8.29	6.90
8.849	7.249	10.192	8.513	9.087	7.354	9.38	7.71
9.147	6.711	8.601	6.320	9.423	7.115	9.057	6.715
15.458	12.665	9.860	7.947	11.348	9.175	12.222	9.929

T=59C

Oil	Time (s)	Trial #	Ball 1- Horizontal	Ball 1- Vertical	Ball 2- Horizontal	Ball 2- Vertical	Ball 3- Horizontal	Ball 3- Vertical	Average
MO	10	1	.370	0.355	.358	0.341	.351	0.338	0.345
MO	60	1	.385	0.383	.383	0.370	.385	0.376	0.376
MO	120	1	.403	0.388	.424	0.424	.385	0.392	0.401
MO	300	1	.437	0.435	.435	0.430	.448	0.430	0.432
MO	1800	1	.579	0.585	.560	0.560	.602	0.616	0.587
MO	3600	1	0.720	0.710	.74	0.740	.73	0.710	0.720
ND	10	1	.348	0.335	.363	0.351	.368	0.340	0.342
ND	60	1	.374	0.363	.376	0.356	.390	0.376	0.365
ND	120	1	.371	0.361	.392	0.383	.379	0.370	0.371
ND	300	1	.455	0.446	.417	0.424	.424	0.426	0.432
ND	1800	1	.590	0.590	.556	0.550	.593	0.585	0.575
ND	3600	1	.622	0.622	.662	0.667	.673	0.679	0.656
MO	10	2	.374	0.354	.358	0.343	.363	0.349	0.349
MO	60	2	.388	0.388	.376	0.363	.372	0.370	0.374
MO	120	2	.385	0.365	.397	0.388	.381	0.367	0.373
MO	300	2	.424	0.424	.460	0.455	.444	0.437	0.439
MO	1800	2	.556	0.570	.587	0.593	.570	0.587	0.583
MO	3600	2	.72	0.740	0.770	0.770	0.800	0.820	0.780
ND	10	2	.365	0.346	.370	0.355	.355	0.335	0.345
ND	60	2	.388	0.372	.367	0.343	.385	0.361	0.359
ND	120	2	.381	0.376	.394	0.374	.408	0.406	0.385
ND	300	2	.435	0.421	.451	0.446	.430	0.444	0.437
ND	1800	2	.605	0.613	.593	0.590	.613	0.605	0.603
ND	3600	2	0.650	0.670	0.690	0.700	0.650	0.670	0.672

T=59C

Test Date	Test Date Trial #	Wear – Ball 1	Wear – Ball 2	Wear – Ball 3	Variation – Ball 1	Variation – Ball 2	Variation – Ball 3	Mean Wear	Max Error
06/30/14	2	-2.25E+004	-2.98E+004	-1.12E+004	0.018	0.005	0.000	-2.12E+04	0.018
07/01/14	1	-1.34E+005	-8.88E+004	-6.53E+004	0.008	0.000	0.004	-9.60E+04	0.008
07/01/14	2	-7.01E+004	-2.28E+005	-8.82E+004	0.006	0.023	0.013	-1.29E+05	0.023
06/30/14	3	-2.90E+005	-2.57E+005	-2.95E+005	0.004	0.001	0.007	-2.81E+05	0.007
06/30/14	1	-1.51E+006	-1.18E+006	-1.99E+006	0.005	0.027	0.022	-1.56E+06	0.027
06/18/14	4	-3.59E+006	-4.08E+006	-2.77E+006	0.005	0.020	0.000	-3.48E+06	0.020
07/02/12	1	-2.14E+003	-6.10E+003	-1.21E+004	0.001	0.015	0.012	-6.79E+03	0.015
07/02/12	2	-7.73E+004	-2.27E+004	-7.33E+004	0.004	0.001	0.018	-5.78E+04	0.018
07/02/12	3	-4.58E+004	-6.56E+004	-7.45E+004	0.005	0.016	0.003	-6.20E+04	0.016
07/02/12	4	-3.42E+005	-2.23E+005	-2.28E+005	0.019	0.012	0.007	-2.64E+05	0.019
07/02/12	5	-1.38E+006	-1.06E+006	-1.50E+006	0.015	0.022	0.014	-1.31E+06	0.022
06/18/14	3	-2.03E+006	-2.57E+006	-2.68E+006	0.034	0.009	0.020	-2.43E+06	0.034
07/04/12	7	-4.59E+004	-5.66E+003	-3.39E+004	0.015	0.002	0.007	-2.85E+04	0.015
07/04/12	6	-1.34E+005	-2.88E+004	-6.67E+004	0.014	0.004	0.003	-7.66E+04	0.014
07/04/12	5	-6.71E+004	-1.30E+005	-9.10E+004	0.002	0.019	0.001	-9.60E+04	0.019
07/04/12	4	-2.39E+005	-3.84E+005	-2.62E+005	0.015	0.019	0.002	-2.95E+05	0.019
07/04/12	3	-1.25E+006	-1.56E+006	-1.40E+006	0.020	0.007	0.005	-1.40E+06	0.020
06/21/14	1	-2.50E+006	-4.68E+006	-7.22E+006	0.050	0.010	0.030	-4.80E+06	0.050
07/02/12	6	4.08E+003	-5.72E+004	-1.32E+004	0.010	0.017	0.000	-2.21E+04	0.017
07/02/12	7	-1.02E+005	-2.69E+004	-4.03E+004	0.021	0.004	0.014	-5.65E+04	0.021
07/02/12	8	-7.37E+004	-6.27E+004	-1.69E+005	0.007	0.001	0.022	-1.02E+05	0.022
07/02/12	9	-2.57E+005	-3.30E+005	-2.97E+005	0.009	0.012	0.000	-2.94E+05	0.012
07/02/12	10	-1.63E+006	-1.50E+006	-1.71E+006	0.006	0.011	0.006	-1.61E+06	0.011
06/22/14	1	-2.46E+006	-3.21E+006	-2.62E+006	0.012	0.023	0.012	-2.76E+06	0.023

T=59C

Surface RMS (um) 1	Surface Ra (um) 1	Surface RMS (um) 2	Surface Ra (um) 2	Surface RMS (um) 3	Surface Ra (um) 3	Avg Surface RMS (um)	Avg Surface Ra (um)
0.434	0.253	0.537	0.328	0.280	0.174	0.42	0.25
1.440	1.042	1.052	0.715	0.787	0.56	1.09	0.77
0.715	0.55	1.896	1.486	0.905	0.674	1.17	0.90
2.170	1.75	1.964	1.555	2.152	1.777	2.10	1.69
6.158	5.075	5.144	3.994	7.299	6.011	6.20	5.03
9.858	8.291	10.631	8.984	8.559	7.171	9.68	8.15
0.130	0.096	0.162	0.123	0.207	0.161	0.17	0.13
1.043	0.729	0.378	0.26	0.854	0.602	0.76	0.53
0.547	0.41	0.677	0.535	0.872	0.648	0.70	0.53
2.361	1.990	1.754	1.451	1.809	1.48	1.97	1.64
5.671	4.722	4.731	3.849	6.125	5.187	5.51	4.59
7.244	6.095	8.252	7.023	8.495	7.304	8.00	6.81
0.67	0.43	0.146	0.10	0.590	0.34	0.47	0.29
1.510	1.05	0.419	0.27	0.937	0.62	0.96	0.65
0.742	0.54	1.250	0.96	1.024	0.76	1.01	0.75
1.865	1.51	2.656	2.24	1.946	1.64	2.16	1.79
5.502	4.61	6.136	5.13	5.779	4.80	5.81	4.85
8.025	6.614	11.442	9.415	14.273	11.75	11.25	9.26
0.253	0.19	0.935	0.58	0.385	0.25	0.52	0.34
1.184	0.82	0.454	0.33	0.528	0.37	0.72	0.51
0.882	0.67	0.689	0.51	1.521	1.18	1.03	0.78
1.909	1.58	2.287	1.89	2.206	1.80	2.13	1.76
6.322	5.26	5.942	4.82	6.573	5.50	6.28	5.19
7.941	6.526	8.846	7.353	7.947	6.368	8.24	6.75

T=51C

Oil	Time (s)	Trial #	Ball 1- Horizontal	Ball 1- Vertical	Ball 2- Horizontal	Ball 2- Vertical	Ball 3- Horizontal	Ball 3- Vertical	Average
MO	10	1	.365	0.355	.353	0.331	.366	0.353	0.35
MO	60	1	0.382	0.366	.375	0.363	.392	0.385	0.37
MO	120	1	0.379	0.351	.416	0.402	.396	0.376	0.38
MO	300	1	.446	0.448	.444	0.426	.433	0.433	0.44
MO	1800	1	.628	0.600	.582	0.598	.616	0.586	0.59
MO	3600	1	.66	0.700	.67	0.690	0.740	0.710	0.71
ND	10	1	.352	0.345	.363	0.352	.349	0.334	0.34
ND	60	1	.372	0.361	.394	0.381	.379	0.361	0.37
ND	120	1	.381	0.376	.403	0.406	.390	0.397	0.39
ND	300	1	.448	0.430	.433	0.428	.419	0.415	0.42
ND	1800	1	.627	0.630	.596	0.605	.613	0.610	0.62
ND	3600	1	.553	0.553	.582	0.585	.573	0.576	0.57
MO	10	2	.358	0.352	.361	0.352	.352	0.336	0.35
MO	60	2	0.385	0.370	.365	0.349	.390	0.381	0.37
MO	120	2	.394	0.374	.392	0.376	.406	0.394	0.38
MO	300	2	.430	0.424	.446	0.437	.444	0.444	0.44
MO	1800	2	.579	0.599	.602	0.613	.556	0.579	0.60
MO	3600	2	.75	0.760	.73	0.740	.69	0.690	0.73
ND	10	2	.354	0.336	.361	0.347	.363	0.358	0.35
ND	60	2	.383	0.374	.370	0.347	.376	0.349	0.36
ND	120	2	.394	0.385	.412	0.403	0.392	0.372	0.39
ND	300	2	.436	0.428	.465	0.445	.451	0.428	0.43
ND	1800	2	.602	0.602	.576	0.587	.602	0.605	0.60
ND	3600	2	.582	0.582	.590	0.582	.556	0.580	0.58
ND	3600	3	0.700	0.660	.73	0.720	.70	0.680	0.69

T=51C

Test Date	Test Date Trial #	Wear – Ball 1	Wear – Ball 2	Wear – Ball 3	Variation – Ball 1	Variation – Ball 2	Variation – Ball 3	Mean Wear	Max Error
06/26/14	3	-9.23E+03	-3.56E+03	-1.52E+04	0.014	0.004	0.013	-9.32E+03	0.014
06/26/14	2	-2.09E+04	-5.27E+04	-1.33E+05	0.000	0.005	0.015	-6.90E+04	0.015
06/26/14	1	-7.72E+04	-1.91E+05	-6.80E+04	0.012	0.032	0.009	-1.12E+05	0.032
06/25/14	3	-2.79E+05	-2.35E+05	-1.94E+05	0.011	0.001	0.003	-2.36E+05	0.011
06/25/14	1	-1.36E+06	-1.10E+06	-1.01E+06	0.019	0.005	0.006	-1.16E+06	0.019
06/24/14	2	-1.96E+06	-3.03E+06	-3.84E+06	0.030	0.030	0.015	-2.94E+06	0.030
06/27/14	1	-5.41E+03	-5.88E+03	5.69E+02	0.005	0.014	0.002	-3.57E+03	0.014
06/27/14	2	-6.03E+04	-1.12E+05	-2.49E+04	0.001	0.020	0.002	-6.58E+04	0.020
06/27/14	3	-1.02E+05	-1.50E+05	-9.46E+04	0.015	0.012	0.001	-1.16E+05	0.015
06/27/14	4	-2.55E+05	-2.25E+05	-2.19E+05	0.015	0.006	0.007	-2.33E+05	0.015
06/28/14	1	-2.05E+06	-1.50E+06	-1.82E+06	0.014	0.014	0.003	-1.79E+06	0.014
06/23/14	1	-1.09E+06	-1.42E+06	-1.26E+06	0.018	0.012	0.003	-1.26E+06	0.018
06/26/14	6	-8.94E+03	-9.19E+03	-7.05E+03	0.008	0.010	0.003	-8.39E+03	0.010
06/26/14	5	-2.91E+04	-3.50E+04	-1.11E+05	0.006	0.014	0.014	-5.82E+04	0.014
06/26/14	4	-1.28E+05	-7.27E+04	-1.36E+05	0.003	0.003	0.019	-1.12E+05	0.019
06/25/14	4	-2.28E+05	-2.95E+05	-2.87E+05	0.008	0.007	0.009	-2.70E+05	0.009
06/25/14	2	-1.40E+06	-1.84E+06	-1.23E+06	0.008	0.011	0.030	-1.49E+06	0.030
06/24/14	4	-4.58E+06	-3.92E+06	-2.85E+06	0.025	0.005	0.040	-3.78E+06	0.040
06/28/14	6	-5.37E+03	-1.08E+04	-7.84E+03	0.002	0.007	0.014	-8.01E+03	0.014
06/28/14	5	-8.10E+04	-5.68E+04	-2.85E+04	0.022	0.002	0.006	-5.54E+04	0.022
06/28/14	4	-8.10E+04	-1.69E+05	-9.42E+04	0.003	0.021	0.005	-1.15E+05	0.021
06/28/14	3	-2.74E+05	-3.33E+05	-2.99E+05	0.002	0.021	0.006	-3.02E+05	0.021
06/28/14	2	-1.69E+06	-1.33E+06	-1.58E+06	0.004	0.017	0.005	-1.53E+06	0.017
06/23/14	3	-1.42E+06	-1.36E+06	-1.15E+06	0.001	0.005	0.013	-1.31E+06	0.013
07/03/14	1	-3.01E+06	-3.77E+06	-3.25E+06	0.010	0.035	0.000	-3.34E+06	0.035

T=51C

Surface RMS (um) 1	Surface Ra (um) 1	Surface RMS (um) 2	Surface Ra (um) 2	Surface RMS (um) 3	Surface Ra (um) 3	Avg Surface RMS (um)	Avg Surface Ra (um)
0.211	0.136	0.186	0.133	0.239	0.177	0.21	0.15
0.536	0.345	0.761	0.519	1.479	1.086	0.93	0.65
0.901	0.684	1.765	1.34	0.658	0.489	1.11	0.84
2.064	1.628	1.837	1.481	1.601	1.23	1.83	1.45
5.361	4.246	4.714	3.703	4.433	3.44	4.84	3.80
6.723	5.482	8.880	7.439	10.012	8.267	8.54	7.06
0.136	0.102	0.148	0.11	0.136	0.107	0.14	0.11
0.811	0.574	1.245	0.886	0.367	0.265	0.81	0.58
1.052	0.821	1.357	1.074	0.877	0.689	1.10	0.86
1.899	1.578	1.709	1.398	1.718	1.358	1.78	1.44
7.253	6.130	6.114	5.099	6.850	5.815	6.74	5.68
4.794	3.884	5.509	4.383	5.046	3.934	5.12	4.07
0.207	0.143	0.227	0.17	0.183	0.125	0.21	0.15
0.398	0.297	0.491	0.339	1.299	0.981	0.73	0.54
1.326	1.023	0.763	0.587	1.295	1.002	1.13	0.87
1.837	1.523	2.145	1.725	2.051	1.675	2.01	1.64
5.684	4.752	6.776	5.664	5.097	4.171	5.85	4.86
11.220	9.295	10.131	8.384	8.615	7.188	9.99	8.29
0.174	0.126	0.196	0.147	0.184	0.137	0.18	0.14
0.985	0.677	0.832	0.577	0.411	0.288	0.74	0.51
0.803	0.627	1.644	1.274	1.040	0.797	1.16	0.90
2.067	1.687	2.327	1.95	2.153	1.755	2.18	1.80
6.576	5.429	5.802	4.777	6.299	5.181	6.23	5.13
5.847	4.927	5.624	4.707	5.142	4.28	5.54	4.64
8.849	7.249	10.192	8.513	9.087	7.354	9.38	7.71

Load Data

Oil	Load (lbs)	Test Date Trial #	Ball 1- Horizontal	Ball 1- Vertical	Ball 2- Horizontal	Ball 2- Vertical	Ball 3- Horizontal	Ball 3- Vertical	Average
MO	58	1	0.7	0.72	.65	0.65	.66	0.69	0.69
MO	58	5	.60	0.60	.60	0.61	.62	0.64	0.62
MO	58	1	0.61	0.61	0.66	0.68	0.62	0.64	0.64
MO	68	1	.68	0.68	.65	0.65	.61	0.61	0.65
MO	68	4	.69	0.69	.65	0.67	.59	0.59	0.65
MO	78	2	.65	0.67	.72	0.74	.72	0.72	0.71
MO	78	3	0.74	0.74	.61	0.61	.72	0.7	0.70
MO	88	4	.72	0.71	.74	0.74	0.73	0.71	0.72
MO	88	1	.72	0.74	.77	0.77	.80	0.82	0.78

Load Data

Trial #	Test Date	Wear – Ball 1	Wear – Ball 2	Wear – Ball 3	Variation – Ball 1	Variation – Ball 2	Variation – Ball 3	Mean Wear	Max Error
1	10/31/14	-3.07E+06	-2.12E+06	-2.35E+006	0.02	0.04	0.015	-2.51E+06	0.040
2	11/01/14	-1.45E+06	-1.74E+006	-2.24E+006	0.01666667	0.01166667	0.01333333	-1.81E+06	0.017
3	11/07/14	-1.75E+006	-2.66E+006	-1.93E+006	0.03333333	0.02666667	0.01333333	-2.11E+06	0.033
1	11/01/14	-2.77E+006	-2.16E+006	-1.37E+006	0.03333333	0.00333333	0.03666667	-2.10E+06	0.037
2	11/01/14	-2.95E+006	-2.15E+006	-1.20E+006	0.04	0.01	0.06	-2.10E+06	0.060
1	11/01/14	-2.44E+06	-3.70E+006	-3.69E+006	0.05	0.02	0.01	-3.28E+06	0.050
2	11/01/14	-4.18E+006	-1.46E+006	-2.66E+006	0.0425	0.0875	0.0125	-2.77E+06	0.088
1	06/18/14	-3.59E+06	-4.08E+06	-2.77E+06	0.0075	0.0175	0.0025	-3.48E+06	0.018
2	06/21/14	-2.50E+06	-4.68E+06	-7.22E+06	0.04666667	0.00666667	0.03333333	-4.80E+06	0.047

Load Data

Surface RMS (um) 1	Surface Ra (um) 1	Surface RMS (um) 2	Surface Ra (um) 2	Surface RMS (um) 3	Surface Ra (um) 3	Avg Surface RMS (um)	Avg Surface Ra (um)
8.939	7.237	7.078	5.52	7.626	6.084	7.88	6.28
5.671	4.49	6.607	5.418	7.343	5.911	6.54	5.27
6.568	5.367	8.349	6.894	6.695	5.286	7.20	5.85
8.094	6.401	7.197	5.683	5.666	4.497	6.99	5.53
8.562	6.778	7.103	5.517	4.817	3.627	6.83	5.31
7.938	6.406	9.894	8.085	10.048	8.21	9.29	7.57
10.975	9.097	5.505	4.183	8.849	7.612	8.44	6.96
9.858	8.291	10.631	8.984	8.559	7.171	9.68	8.15
8.025	6.614	11.442	9.415	14.273	11.75	11.25	9.26

Appendix I

Derivation of Relevant Equations

I.1 HEAT EQUATION

Heat Equation Derivation

The first step is to sum up, conceptually, energy generated in a one-dimensional solid [101], where

$$\dot{Q}_x - \dot{Q}_{x+\Delta x} + \dot{G} = \frac{\Delta E}{\Delta t}, \tag{I.1}$$
$$\Delta E = \rho(\Delta x A) C_P (T_{t+\Delta t} - T_t),$$
$$\dot{G} = (\Delta x A) \cdot \dot{g},$$

and this conservation of energy results in

$$\dot{Q}_x - \dot{Q}_{x+\Delta x} + (\Delta x A) \cdot \dot{g} = \rho(\Delta x A) C_P \frac{(T_{t+\Delta t} + T_t)}{\Delta t}. \tag{I.2}$$

Divide by $\Delta x A$,

$$\frac{-1}{A} \frac{\dot{Q}_{x+\Delta x} - \dot{Q}_x}{\Delta x} + \dot{g} = \rho C_P \frac{(T_{t+\Delta t} + T_t)}{\Delta t}, \tag{I.3}$$

and note from Fourier's Law of Heat Conduction [101],

$$\dot{Q} = -kA \frac{\partial T}{\partial x}. \tag{I.4}$$

Taking the limit as $\Delta x \to 0$ and $\Delta t \to 0$,

$$-\frac{1}{A}\frac{\partial Q}{\partial x} + \dot{g} = \rho C_P \frac{\partial T}{\partial t}, \tag{I.5}$$

$$\frac{1}{A}\frac{\partial}{\partial x}(k \cdot A \frac{\partial T}{\partial x}) + \dot{g} = \rho C_P \frac{\partial T}{\partial t}, \tag{I.6}$$

$$\frac{\partial}{\partial x}(k \frac{\partial T}{\partial x}) + \dot{g} = \rho C_P \frac{\partial T}{\partial t}, \tag{I.7}$$

$$\frac{\partial^2 T}{\partial x^2} + \frac{\dot{g}}{k} = \frac{\rho C_P}{k}\frac{\partial T}{\partial t}, \tag{I.8}$$

$$\frac{\partial^2 T}{\partial x^2} + \frac{\dot{g}}{k} = \frac{1}{\alpha}\frac{\partial T}{\partial t}, \tag{I.9}$$

where α (m^2/s) is the thermal diffusivity. If the heat transfer is steady-state,

$$\frac{\partial^2 T}{\partial x^2} + \frac{\dot{g}}{k} = 0. \tag{I.10}$$

Symbols

- A (m^2), surface area
- T (°C), Temperature
- ΔE (Joules), Energy
- $\dot{Q}$ (Watts), conductive energy propagation
- $\dot{G}$ (Watts), energy generation
- $\dot{g}$ (Watts/m^3), energy generation density
- ρ (kg/m^3), density
- C_P (Joules/kg·°C)
- α (m^2/s), thermal diffusivity

I.2 CONSERVATION OF MASS

Derivation

It is intuitively obvious, and provable by the conservation of mass, that the total change in the mass of a volume space must be equal to the total mass that crosses the boundary of this volume. This can be represented mathematically by [133]

$$\int_V \frac{\partial \rho}{\partial t} dV = -\int_S \rho(\mathbf{v}\cdot\mathbf{n}) dS, \tag{I.11}$$

and based on the divergence theorem,

$$\int_S \rho(\mathbf{v}\cdot\mathbf{n}) dS = \int_V div(\rho\mathbf{v}) dV, \tag{I.12}$$

and therefore

$$\int_V \frac{\partial \rho}{\partial t} dV = -\int_V div(\rho\mathbf{v}) dV, \tag{I.13}$$

$$\int_V [\frac{\partial \rho}{\partial t} + div(\rho\mathbf{v})] dV = 0, \tag{I.14}$$

$$\frac{\partial \rho}{\partial t} + div(\rho\mathbf{v}) = 0, \tag{I.15}$$

$$\frac{\partial \rho}{\partial t} + \mathbf{v}\cdot grad(\rho) + \rho\cdot div(\mathbf{v}) = 0. \tag{I.16}$$

This is one definition of the conservation of mass. The definition of the Material Derivative is,

$$\frac{D\Psi}{Dt} = \frac{\partial \Psi}{\partial t} + \mathbf{v}\cdot grad(\Psi), \tag{I.17}$$

where Ψ is an arbitrary value. Therefore, the conservation of mass can be written as

$$\frac{D\rho}{Dt} + \rho \cdot div(\mathbf{v}) = 0. \tag{I.18}$$

Symbols for Conservation of Mass Section

- ρ (kg/m^3), density
- *t* (s), time
- *V* (m^3), Volume
- *S* (m^2), Surface Area
- **v** (m/s), velocity vector
- **n**, tangential surface vector
- $\frac{D}{Dt}$, material derivative (Eqn. I.17)
- *div*, divergence
- *grad*, gradient

I.3 CONSERVATION OF LINEAR MOMENTUM

Derivation

It is intuitively obvious that the total change in the linear momentum of a volume space must be equal to the total linear momentum that crosses the boundary of this volume (traction on the surface), as well as any body forces (ex. gravity). This can be represented mathematically by [133]

$$\int_V \frac{D(\rho \mathbf{v})}{Dt} dV = \int_S \mathbf{t} dS + \int_V \rho \mathbf{B} dV, \tag{I.19}$$

and these values can all be converted to all volume integrals with the divergence theorem. The traction vector $\mathbf{t}$ can be converted to the Cauchy Stress tensor $\hat{\mathbf{T}}$, where

$$\mathbf{t} \;=\; \hat{\mathbf{T}} \cdot \mathbf{n}, \tag{I.20}$$

and thus based on the divergence theorem,

$$\int_S \mathbf{t} dS = \int_S \hat{\mathbf{T}} \cdot \mathbf{n} dS = \int_V div(\hat{\mathbf{T}}) dV, \tag{I.21}$$

and thus

$$\int_V [(\frac{D(\rho \mathbf{v})}{Dt}) - div(\hat{\mathbf{T}}) - (\rho \mathbf{B})] = 0, \tag{I.22}$$

and thus the conservation of linear momentum is defined as,

$$\frac{D(\rho \mathbf{v})}{Dt} = div(\hat{\mathbf{T}}) + (\rho \mathbf{B}) \tag{I.23}$$

Symbols for Conservation of Linear Momentum Section

- ρ (kg/m^3), density
- t (s), time
- V (m^3), Volume
- S (m^2), Surface Area
- $\mathbf{v}$ (m/s), velocity vector
- $\mathbf{B}$ (Newtons), body forces
- $\mathbf{n}$, tangential surface vector
- $\mathbf{t}$ (Pa), traction vector
- $\hat{\mathbf{T}}$ (Pa), Cauchy Stress Tensor
- $\frac{D}{Dt}$, material derivative (Eqn. I.17)
- *div*, divergence
- *grad*, gradient

I.4 NAVIER STOKES EQUATION

Derivation

Based on the derivations of the Conservation of Mass (Section I.2) and the Conservation of Linear Momentum (Section I.3), the Navier Stokes Equation for fluid flow can be derived. Throughout this effort, the fluid will consistently be considered incompressible, and thus based on the conservation of mass (Eqn. I.18), this can be represented mathematically by [133]

$$\frac{D\rho}{Dt} = 0, \tag{I.24}$$

$$\rho \cdot div(\mathbf{v}) = 0, \tag{I.25}$$

$$\frac{\partial v_i}{\partial x_i} = \frac{\partial v_j}{\partial x_j} = 0, \tag{I.26}$$

where the subscript *i* and *j* represents the Einstein notation. With this assumption, the conservation of linear momentum (Eqn. I.23) can be defined as,

$$\rho \frac{D(\mathbf{v})}{Dt} = div(\hat{\mathbf{T}}) + (\rho \mathbf{B}), \tag{I.27}$$

$$\rho(\frac{\partial v_i}{\partial t} + v_j \frac{\partial v_i}{\partial x_j}) = div(\hat{\mathbf{T}}) + (\rho \mathbf{B}), \tag{I.28}$$

By definition, the Cauchy Stress Tensor can be broken up into two parts,

$$T_{ij} = -p\delta_{ij} + T'_{ij}, \tag{I.29}$$

and these two parts include the *pressure* and the *viscous stress tensor*. The fluid will be treated as an *incompressible Newtonian fluid*; in a Newtonian fluid, also known as a *linearly viscous fluid*, the viscous stress tensor is a linear relationship with the

deformation tensor D_{ij}, which is related to the velocity gradient,

$$D_{ij} = \frac{1}{2}(\frac{\partial v_i}{\partial x_j} + \frac{\partial v_j}{\partial x_i}), \tag{I.30}$$

and if the fluid is incompressible, the viscous stress tensor would be equal to

$$T'_{ij} = 2\mu D_{ij}, \tag{I.31}$$

and thus the stress tensor is

$$T_{ij} = -p\delta_{ij} + \mu(\frac{\partial v_i}{\partial x_j} + \frac{\partial v_j}{\partial x_i}). \tag{I.32}$$

This equation can be used to find the divergence of the stress tensor to solve the conservation of linear momentum (Eqn. I.23), and thus

$$div(\hat{\mathbf{T}}) = \frac{\partial T_{ij}}{\partial x_j} = -\frac{\partial p}{\partial x_j}\delta_{ij} + \mu\frac{\partial}{\partial x_j}(\frac{\partial v_i}{\partial x_j} + \frac{\partial v_j}{\partial x_i}). \tag{I.33}$$

As the fluid is incompressible (Eqn. I.26),

$$\frac{\partial}{\partial x_j}(\frac{\partial v_j}{\partial x_i}) = \frac{\partial}{\partial x_i}(\frac{\partial v_j}{\partial x_j}) = 0, \tag{I.34}$$

and therefore the divergence of the tensor $\hat{\mathbf{T}}$ for an incompressible fluid is

$$div(\hat{\mathbf{T}}) = \frac{\partial T_{ij}}{\partial x_j} = -\frac{\partial p}{\partial x_i} + \mu(\frac{\partial^2 v_i}{\partial {x_j}^2}), \tag{I.35}$$

and by plugging in Eqn. I.35 into Eqn. I.28, the general form of the Navier Stokes Equation can be realized,

$$\rho(\frac{\partial v_i}{\partial t} + v_j \frac{\partial v_i}{\partial x_j}) = -\frac{\partial p}{\partial x_i} + \mu(\frac{\partial^2 v_i}{\partial {x_j}^2}) + (\rho B_i), \tag{I.36}$$

Symbols for Navier Stokes Section

- ρ (kg/m^3), density
- *t* (s), time
- *p* (Pa), pressure
- μ (Pa-s), dynamic viscosity
- $\mathbf{v} = v_i$ (m/s), velocity vector
- $\hat{\mathbf{T}} = T_{ij}$ (Pa), Cauchy Stress Tensor
- $\hat{\mathbf{T}}' = T'_{ij}$ (Pa), Viscous Stress Tensor
- $\hat{\mathbf{D}} = D_{ij}$, Deformation Tensor
- $\mathbf{B} = B_i$ (Newtons), Body Force
- $\frac{D}{Dt}$, material derivative (Eqn. I.17)
- *div*, divergence
- *i* and *j*, Einstein Summation
- δ_{ij}, Kroniker delta

I.5 REYNOLDS EQUATION

Derivation of Fluid Velocity

There are several assumptions that are made when deriving the Reynolds equation for lubricant fluid flow [20, 91],

- Body forces are negligible
- Pressure is constant through the lubricant film (y-direction)
- No slip at the boundary surfaces
- The lubricant flow is laminar (low Reynolds number)
- Inertia and surface tension forces are negligible compared with viscous forces
- Shear stress and velocity gradients are only significant across the lubricant film (y direction)
- The lubricant is Newtonian
- The lubricant viscosity is constant across the film (y direction)
- The lubricant boundary surfaces are parallel or at a small angle with respect to each other

To simplify this derivation, we will assume the velocity is uniform in the *x* direction, and there is no velocity in the *y* or *z* direction. If so, the pressure distribution can be defined as

$$\frac{\partial p}{\partial x} = \frac{\partial T'_{xy}}{\partial y}, \tag{I.37}$$

$$\frac{\partial p}{\partial y} = 0, \tag{I.38}$$

and as defined in Section I.4 the viscous shear

$$T'_{xy} = \mu \frac{\partial u}{\partial y}, \tag{I.39}$$

and therefore

$$\frac{\partial p}{\partial x} = \frac{\partial}{\partial y}(\mu \frac{\partial u}{\partial y}) = \mu \frac{\partial^2 u}{\partial y^2}. \tag{I.40}$$

By integrating,

$$\frac{\partial p}{\partial x} \cdot \frac{y^2}{2} + C_1 y + C_2 = \mu u, \tag{I.41}$$

and the coefficients of integration are

$$C_2 = \mu U_2, \tag{I.42}$$

$$C_1 = (U_1 - U_2)\frac{\mu}{h} - \frac{\partial p}{\partial x}\frac{h}{2},$$

$$u(y = 0) = U_2,$$

$$u(y = h) = U_1,$$

and therefore

$$\frac{\partial p}{\partial x} \cdot \frac{y^2}{2} + (U_1 - U_2)\frac{\mu y}{h} - \frac{\partial p}{\partial x}\frac{h \cdot y}{2} + \mu U_2 = \mu u, \tag{I.43}$$

$$u = (\frac{y^2 - y \cdot h}{2\mu})\frac{\partial p}{\partial x} + (U_1 - U_2)\frac{y}{h} + U_2, \tag{I.44}$$

and if there is fluid flow is in the z direction, simply substitute z for x in Eqn. I.44.

Derivation of Fluid Column

In a given volume, the fluid in must equal the fluid out, looking at both the *x*, *z*, and the sides in the *y*-direction. This can be described as,

$$Q_{x,in} + Q_{z,in} + Q_{y,in} = Q_{x,out} + Q_{z,out} + Q_{y,out}, \tag{I.45}$$

$$q_x dz + q_z dx + w_0 dx dz = (q_x + \partial q_x)dz + (q_z + \partial q_z)dx + w_h dx dz, \tag{I.46}$$

$$(\frac{\partial q_x}{\partial x}dx)dz + (\frac{\partial q_z}{\partial z}dz)dx + (w_h - w_0)dx dz = 0, \tag{I.47}$$

$$[\frac{\partial q_x}{\partial x} + \frac{\partial q_z}{\partial z} + (w_h - w_0)]dx \cdot dz = 0, \tag{I.48}$$

$$\frac{\partial q_x}{\partial x} + \frac{\partial q_z}{\partial z} + (w_h - w_0) = 0. \tag{I.49}$$

The value of q_x and q_z (if two-dimensional) is the integral of the fluid velocity from Eqn. I.44, where

$$q_x = \int_0^h u dy = |(\frac{y^3}{3} - \frac{y^2 h}{2})\frac{1}{2\mu}\frac{\partial p}{\partial x} + (U_1 - U_2)\frac{y^2}{2 \cdot h} + U_2 y|_0^h, \tag{I.50}$$

$$q_x = -\frac{h^3}{12\mu}\frac{\partial p}{\partial x} + (U_1 + U_2)\frac{h}{2}. \tag{I.51}$$

For the 1D applications of interest, where there is no flow in the y or z direction, Eqn. I.49 can be defined as,

$$\frac{\partial q_x}{\partial x} = 0, \tag{I.52}$$

$$q_z = w_h = w_0 = 0, \tag{I.53}$$

and therefore the final version of the 1D Reynolds can be generated by plugging in q_x from Eqn. I.51 into Eqn. I.52, and multiplying everything by $12{\cdot}\mu$

$$\frac{\partial}{\partial x}(h^3\frac{\partial p}{\partial x}) = 6\mu U\frac{\partial h}{\partial x}, \tag{I.54}$$

$$U = U_1 + U_2, \tag{I.55}$$

which is effectively Eqn. 2.45.

Symbols for Reynolds Equation

- ρ (kg/m^3), density
- *t* (s), time
- *p* (Pa), pressure
- μ (Pa-s), dynamic viscosity
- $\mathbf{v} = v_i$ (m/s), velocity vector
- $\hat{\mathbf{T}} = T_{ij}$ (Pa), Cauchy Stress Tensor
- q_x, q_z (m^2/s), volume flow rate (per unit length)
- w_0, w_h (m^2/s), volume rate out of film thickness (*y*) direction (per unit length)
- $Q_{in,x}$, $Q_{in,y}$, $Q_{in,z}$, $Q_{out,x}$, $Q_{out,y}$, $Q_{out,z}$ (m^3/s), volume flow rate
- C_1, C_2, constants of integration

I.6 HERTZ

Derivation

The definitions and derivations of the Hertz contact equations [9, 20, 91] assume small, elastic, static deflections. Hertz derived analytically that the pressure distribution is (repetitive from Eqn. 2.12 and 2.14),

$$P(r) = P_{Hertz} \cdot \sqrt{1 - \left(\frac{r}{a}\right)^2}, \tag{I.56}$$

$$P_{Hertz} = \frac{3}{2} P_{avg} = \frac{3}{2} \frac{W}{\pi a^2}, \tag{I.57}$$

and the deflection function,

$$\bar{u}_z(r) = \frac{\pi P_{Hertz}}{4 \cdot a \cdot E'} (2a^2 - r^2) = \delta(r) - A' x^2 - B' z^2, \tag{I.58}$$

for solids of rotation, where *A'* and *B'* are coefficients of the principle relative axis of the two surfaces. Assuming there is no ellipticity,

$$A' = B' = -\frac{1}{2} [\frac{1}{R_1} + \frac{1}{R_2}], \tag{I.59}$$

and since in the four-ball test all of the balls are identical in radius ($R_1 = R_2$),

$$\bar{u}_z(r) = \frac{\pi P_{Hertz}}{4 \cdot a \cdot E'} (2a^2 - r^2) = \delta(r) + \frac{r^2}{2 \cdot R'}, \tag{I.60}$$

where the reduced radius *R'* can be found with Eqn. 2.7 and 2.9, and the reduced Young's modulus *E'* can be found with Eqn. 2.8 and 2.10. The equation for the contact radius (Eqn. 2.11) can be found by setting $r = a$, where there is no elastic

deflection $\delta(a) = 0$,

$$\frac{\pi P_{Hertz}}{4 \cdot a \cdot E'}(2a^2 - a^2) = \frac{a^2}{2 \cdot R'}, \tag{I.61}$$

$$a = \frac{\pi R' P_{Hertz}}{2 \cdot E'} = \frac{\pi R'}{2 \cdot E'} \cdot (\frac{3}{2}\frac{W}{\pi a^2}), \tag{I.62}$$

$$a = (\frac{3}{4}\frac{R'W}{E'})^{\frac{1}{3}}, \tag{I.63}$$

and the maximum deflection δ_{Hertz} (m) from Eqn. 2.13 can be determined by setting $r = 0$,

$$\delta_{Hertz} = \frac{\pi P_{Hertz}}{4 \cdot a \cdot E'}(2a^2), \tag{I.64}$$

$$\delta_{Hertz} = \frac{\pi a P_{Hertz}}{2E'} = \frac{3}{4}\frac{W}{a \cdot E'}, \tag{I.65}$$

$$\delta_{Hertz} = (\frac{9}{16}\frac{W^2}{R' \cdot E'^2})^{\frac{1}{3}}, \tag{I.66}$$

and thus the Winkler Mattress Coefficient (Eqn. 2.5 and 2.6) can be determined by,

$$K_H = \frac{P_{Hertz}}{\delta_{Hertz}} = \frac{2E'}{\pi a} = (\frac{16E'^4}{3\pi^3 R' \cdot W})^{\frac{1}{3}}. \tag{I.67}$$

It is clear from this analytical equation that the Winkler Mattress coefficient will vary with the load. In this model, the load and Winkler Mattress coefficient are consistent throughout the entire simulation.

In order to determine the plasticity length (Eqn. 2.73), the first step is to derive the maximum deflection δ_{Hertz} as a function of the maximum pressure P_{Hertz}. The

first step is to find the Hertz contact radius *a* as a function of the maximum pressure,

$$a^3 = (\frac{3}{4}\frac{R'W}{E'}) = (\frac{3}{4}\frac{R'}{E'})(\frac{2}{3}P_{Hertz}\pi a^2), \tag{I.68}$$

$$a = \frac{\pi R' P_{Hertz}}{2E'}, \tag{I.69}$$

and therefore the deflection can be written as

$$\delta_0 = \frac{\pi a P_{Hertz}}{2E'} = \frac{\pi P_{Hertz}}{2E'}(\frac{\pi R' P_{Hertz}}{2E'}), \tag{I.70}$$

$$\delta_0 = R'(\frac{\pi}{2})^2(\frac{P_{Hertz}}{E'})^2. \tag{I.71}$$

Plastic deformation is expected to start at 60% of the yield stress [2], and therefore by setting the maximum pressure in Eqn. I.71 at 60% of the failure yield stress of the material, the yield length W_P (m) can be calculated,

$$W_P = R'(\frac{\pi}{2})^2(\frac{0.6{\cdot}G_{yield}}{E'})^2 = 0.09\pi^2{\cdot}R'(\frac{G_{Yield}}{E'})^2. \tag{I.72}$$

The initial value of $0.09{\cdot}\pi^2{\approx}0.89$ is rounded up to 1, in order to take into account the fact that there might be internal plastic flow before detectable plastic flow and wear occurs [2], which yields the exact solution for Eqn. 2.73.

Symbols for Hertzian

- $\bar{u}_z$ (m), Hertzian deflection length
- *A'* amd *B'* (m^{-1}), coefficients of the principle relative axis of the two surfaces

Appendix J

LABORATORY PHOTOGRAPHS

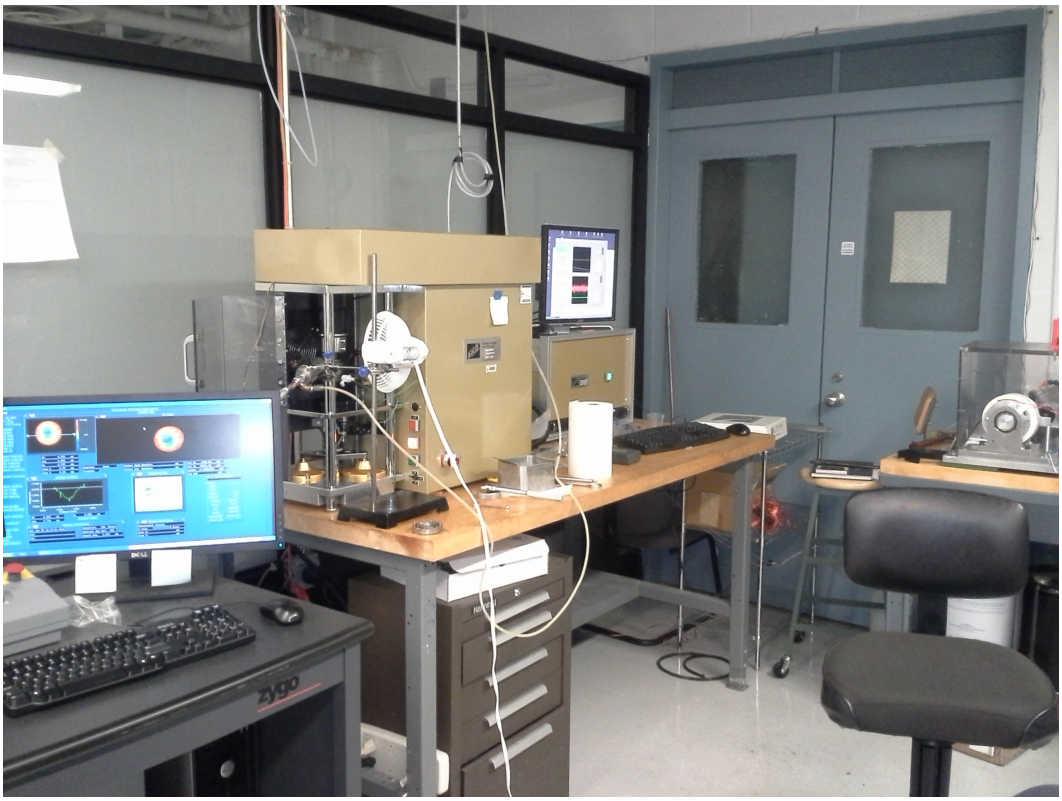

Figure J.1: Falex MultiSpecimen Test Machine, Photograph # 1

Figure J.2: Falex MultiSpecimen Test Machine, Photograph # 2

Figure J.3: Falex MultiSpecimen Test Machine, Photograph # 3

Figure J.4: Falex MultiSpecimen Test Machine, Photograph # 4

Figure J.5: Falex MultiSpecimen Test Machine, Photograph # 5

Figure J.6: Branson 1510 Ultrasonic Cleaner

Figure J.7: Zygo Corporation, Metrology Solutions Division, 3D Optical Surface Profilers, Photograph # 1

Figure J.8: Zygo Corporation, Metrology Solutions Division, 3D Optical Surface Profilers, Photograph # 2

Figure J.9: Zygo Corporation, Metrology Solutions Division, 3D Optical Surface Profilers, Photograph # 3